Selective Area Epitaxy of CdTe on Nanopatterned Substrates

BY

STEPHEN FAHEY
B.A., University of Colorado, Boulder 2002
M.S., University of Illinois at Chicago, Chicago, 2008

THESIS

Submitted as partial fulfillment of the requirements
for the degree of Doctor of Philosophy in Physics
in the Graduate College of the
University of Illinois at Chicago, 2012

Chicago, Illinois

Defense Committee:

Sivalingam Sivananthan, Advisor and Chair
Robert Klie, Physics
Yong Chang, Physics
Robert Sporken, Physics, University of Namur, Belgium
Christoph Grein, Physics
Christian Morath, Air Force Research Laboratory, NM

I dedicate this thesis to

the time-honored pursuit

of awareness

through inquiry.

Preface

The original primary goal of the research described in this thesis was to improve the crystalline quality of thin films of CdTe grown on silicon substrates by molecular beam epitaxy through lowering the dislocation loop density terminating at the surface of CdTe by utilizing a nano-patterned CdTe-Si interface. That goal has likely not been achieved in this thesis research; however, this thesis offers significant advance toward that goal, with both theoretical and experimental contributions. These contributions may be useful for condensed matter materials scientists concerned with nano-structures, lattice mismatch in thin film growth, and II-VI materials.

This thesis contains 5 outstanding new observations and developments. First is the development of a dilute etch for CdTe nano-structure cleaning. The second is the theoretical observation that silicon can potentially heat fast enough to destroy nanoscale CdTe structures on its surface during conventional molecular beam epitaxy procedures. The third is the first demonstration of selective area growth of CdTe against silicon nitride mask by molecular beam epitaxy. The fourth is the experimental observation that carbon deposit can be used as a CdTe mask for selective area molecular beam epitaxy. The fifth is the observation and characterization of CdTe selective growth and coalescence from a nano-scale array of CdTe seeds by molecular beam epitaxy. Each of these points will be expanded upon in the following pages, including a development of historical and scientific context relevant to the essential new observations and developments reported here.

It is my hope that this thesis may aide in the future development of long-wavelength infrared detectors, II-VI semiconductor technology applied to photovoltaic energy conversion of solar energy to electricity, x-ray/gamma-ray detectors, and the general advancement of materials science at small length scales.

Acknowledgements

I am in debt to many people for the successful completion of this thesis. Prof. Sivananthan for his specific words of leadership and pursuit of quality, Robert Sporken for his dedication keen insight and experience, Prof. Grein for his numerous elegant guiding scientific comments and questions, Richard Kodama for his patience and breadth of knowledge, Prof. Robert Klie for his pragmatic approach to obtaining excellent results, Charlie Becker for sharing his experience with molecular beam epitaxy, Prof. Aratyn for his guidance of the physics department, Ramana Bommena, Mike Carmody, Thomas Seldrum for helping wave the flag of global warming warning, Ramesh Dhere and Neelkanth Dhere for CdTe solar cell presentations in Physics 481 and interesting discussions, Runzhe Tao, Qiao Qiao, Yoobum Huo, Jin Hwan Park, Eric Colegrove, Alex Brown, Brian Kaster, Suleyman Tari, Ke-Bin Low, Alan Nicholls, Kristina Jarosius, Dmitry Pridachin, Xiaojin Wang, Natalie Krzyzanowski, Jason Bury, Salvador Robles, Jing Song, Yesim Anter, the UIC physics department professors and staff, Kevin Lynch, Bob Kurdydyk, Rick Frueh, Supridi (Tony) Charoenrath, Curt Cornell, Paul Varkey, Prof. Inder Batra who encouraged me to accept the fellowship that later fueled my independent studies, all my exceptional physics instructors of the past, all the students that I have instructed and interacted with especially for their instruction of me and their inspirational views of the world, Richard Ratliff for his guidance and inspiration, and finally my family whose genuine support of me has been instrumental in my development and comfort for many years.

TABLE OF CONTENTS

FIGURES

TABLES

EQUATIONS

ABBREVIATIONS

AFM	Atomic Force Microscopy
BEP	Beam Equivalent Pressure
FIB	Focused Ion Beam
FT-IR	Fourier Transform Infrared
FWHM	Full Width at Half Maximum
IR	Infrared
LPE	Liquid Phase Epitaxy
LWIR	Long Wavelength Infrared
MBE	Molecular Beam Epitaxy
ML	Monolayer
MOCVD	Metal Organic Chemical Vapor Deposition
MWIR	Mid-Wavelength Infrared
RHEED	Reflection High Energy Electron Diffraction
SEM	Scanning Electron Microscopy
SL	Superlattice
STM	Scanning Tunneling Microscope
SWIR	Short Wavelength Infrared
TD	Threading Dislocation
TDD	Threading Dislocation Density
TEM	Transmission Electron Microscopy
UHV	Ultra High Vacuum
XPS	X-Ray Photoelectron Spectroscopy
XRD	X-Ray Diffraction

1 Introduction

1.1 Historical Context and Motivation

$Hg_{1-x}Cd_xTe$ has been established as the leading IR detector absorber material. The alloy is novel, as it can be tuned as a function of the Cd fraction "x" from ~1.5eV bandgap at 293K to -0.15eV at 293K, while changing the lattice constant by less than 0.6% [1]. The bandgap of the alloy, as a function of x and temperature, T is given below [2].

$$E_{gap} = - 0.302 + 1.93x – 0.81x^2 + 0.832x^3 + 5.35*10^{-4}(1-2x)T$$

Equation 1

The formula for energy gap versus x in Equation 1 is plotted below for T=300K (dashed) and T=77K (solid orange).

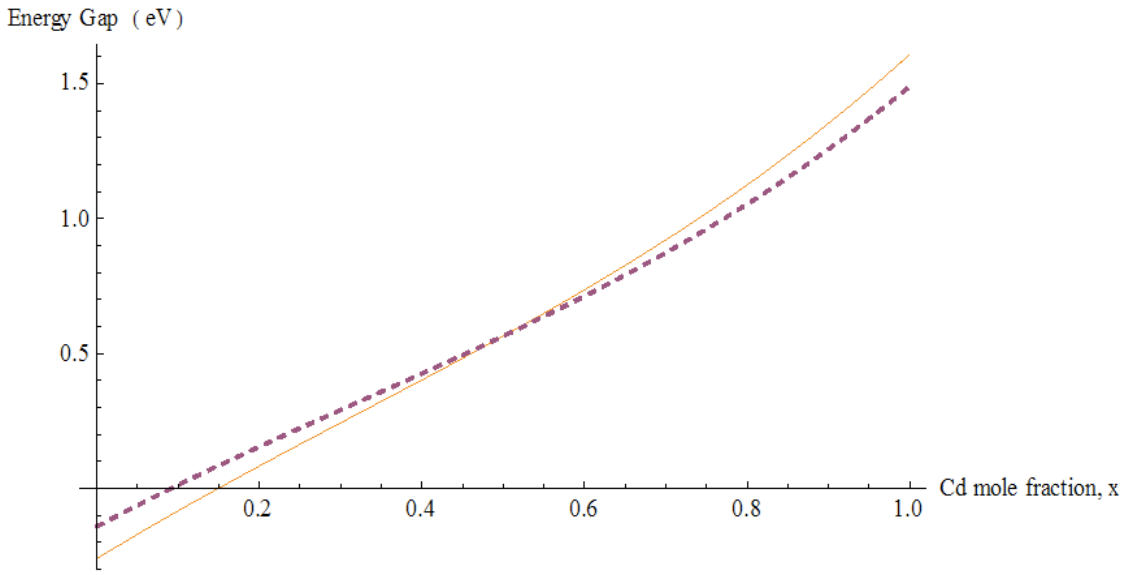

Figure 1 The energy band gap of $Hg_{1-x}Cd_xTe$ is shown as a function of alloy fraction, x. The solid curve was calculated at 77K, and the dashed curve at 300K; after reference [2].

Thus, $Hg_{1-x}Cd_xTe$ can be used as a detector absorber for wavelengths above ~775nm; including the SWIR (~1-2.5μm, 1.24-0.5eV), MWIR (2.5-6μm, 0.5-0.21eV), LWIR (6-15μm, 0.21-0.08eV), and VLWIR (15-20μm, 0.08-0.06eV) bands in the IR part of the electromagnetic spectrum. In principle any longer wavelength could also be detected, however, the longer the wavelength, the more challenging it is to realize a high performance detector, due to the signal-to-noise reduction at longer wavelengths.

The applications of IR sensors abound, from monitoring blood flow, to improving visibility through fog (with SWIR); but some of the most valuable applications are at longer wavelengths. For example, at room temperature the maximum wavelength of gray body radiation is at ~10μm (in the LWIR, with considerable transmission through the atmosphere), thus such detectors have clear practical application in security; namely, in civilian law enforcement and in the military. In addition, IR sensors have been used in remote gas-sensing applications to identify certain species of gases quantitatively. For

example, gases related to global climate monitoring and prediction can be sensed remotely from space, in the UV to LWIR, including H_2O, CO_2, CH_4, and O_3 [3]. Such remote sensing can also be used to locate and monitor industrial plumes, and to study volcanic activity remotely with long-wavelength FT-IR [4]. Some of the most intriguing uses of IR remote sensors have been found in astronomy, where an IR-equipped telescope was used to find and study the supermassive black hole at the center of the Milky Way galaxy (equivalent to $\sim 4 \times 10^6$ solar masses[1]), whose IR emission has some temporal structure which is not fully understood [5]. Researchers have in fact discovered similar massive black holes at the centers of many other galaxies[2]. Lastly, the ability to sense longer wavelengths of electromagnetic radiation is directly coupled with the largest length scale which humanity has ever consciously measured within the universe ($\sim 10^{23}$m). Studying objects at such great distances is aided by IR sensor technology, due to the apparent increased doppler redshift of radiation emanating from what is currently assumed to be a uniformly expanding universe; described by Hubble's law [6]:

$$v = H_0 \cdot d$$

Equation 2

where v is the recessional velocity of a celestial object at distance d from earth, and H_0 is Hubble's constant, equal to 22 ± 2 km/sec*million-light-years.

[1] The mass of the black hole was determined by tracing the paths of the surrounding stars for several years.
[2] It is interesting to note that according to Stephen Hawking, there is one possible future Nobel Prize lurking in the field of astrophysics for the clear observation of Hawking Radiation emanating from a black hole. However, that may require finding a black hole outside of a galaxy.

Due to the finite propagation speed of light, looking at light having originated from objects at greater distances, serves as a probe into the distant temporal past of the universe; thus experimentally probing that realm is helping to shape more accurate theoretical models of the evolution of the universe [7, 6], thought to be 14 billion years old. The newest IR space sensor, the James Webb space telescope, will peer back to only 200-300 million years after the big bang. In part due to such applications, it is important to push the existing state of the art IR detector technology to longer wavelengths and higher performance. One avenue to do this is to improve understanding and control of current detector materials. At the same time, it is desirable to reduce the cost of fabricating a high performance, large area detector.

Currently the highest performance $Hg_{1-x}Cd_xTe$ detectors are typically grown by MBE or LPE on $Cd_{1-y}Zn_yTe$ substrates. Such substrates can be nearly lattice-matched to $Hg_{1-x}Cd_xTe$ at any x value, thereby allowing for high crystalline quality $Hg_{1-x}Cd_xTe$ epilayers to be grown on them, dating back as far as 1981 [8]. In fact, $Cd_{0.96}Zn_{0.04}Te$ is exactly lattice matched to $Hg_{0.8}Cd_{0.2}Te$ with only ~ 3.5% thermal expansion coefficient mismatch [9]. CdZnTe is also largely transparent to IR, allowing for back-side-illuminated IR detector architectures; although for space applications it is useful to remove the CdZnTe substrate to reduce x-ray and gamma-ray induced noise. Unfortunately, CdZnTe is difficult to grow as a single crystal in bulk form, compared to other materials like silicon. One of the challenges is to keep the alloy ratio correct over a large volume, while avoiding the formation of Te inclusions. The difficulty of the bulk growth process for CdZnTe has resulted in the wafers formed from such growth being available commercially at ~ 20,000 times higher cost than silicon wafers, and with

maximum area ~ 14 times smaller (about $7 \times 7\,\mathrm{cm}^2$) [9]. In addition, silicon is less brittle, has a lower defect density (by a factor of ~ 100), and has an identical thermal expansion coefficient to the read out integrated circuits used in state of the art IR focal plane arrays (made on silicon). One is naturally led, therefore, to the question of whether an alternative substrate for HgCdTe epilayer growth could, or could not, be realized using silicon as the base or substrate material. For example, one may wonder if HgCdTe/CdZnTe/Si IR devices could match the high performance of HgCdTe/CdZnTe IR devices.

In practice, the answer to that question is sometimes; as equivalent-performance detectors have been fabricated on Si for the SWIR and MWIR spectral regions, but not for LWIR [10]. In the case of LWIR HgCdTe detectors on Si, devices have been fabricated, but the pixel operability is significantly worse than similar detectors fabricated on CdZnTe substrates [11]. It is currently postulated that threading dislocations (TD's) present in the active areas of the HdCdTe pixels on Si, can become activated in some cases (see Figure 2), allowing them to make some pixels inoperable; where this activation is believed to be through gettering or channeling of impurities to or along the dislocation cores, which are generally lower density regions of an otherwise perfect crystal, and subsequently short-circuiting the detector pixel p-n junction [12, 13]. It is possible that the TD's act as impurity "pipe lines" which allow contaminants from the Si to diffuse into the detector pixels' volumes [14].

The indirect correlation of the TD's to the performance of a given pixel diode manifests itself in the R_oA figure of merit of the pixel; which is the dynamic resistance at zero applied bias multiplied by the area of the diode. If the diode is partially shorted by

the presence of activated TD's, then the R_oA value will be reduced, and the leakage current increased when the diode is put under reverse bias during detector operation. In addition, the presence of TD's can reduce the minority carrier lifetime, by the introduction of electron states different from the normal perfect crystal band structure [15, 16, 17] which can act as traps or recombination centers. For a photovoltaic detector, the R_oA value is proportional to $\tau^{1/2}$, where τ is the minority carrier lifetime [18]. The R_oA value, in turn, has been seen to correlate with TD density raised to the -2 power [19]. Thus dislocations can hurt performance by reducing lifetime, and by shorting a given p-n junction.

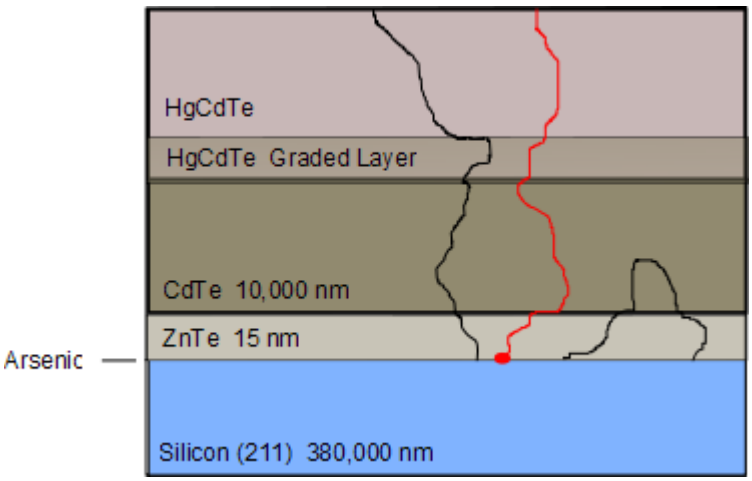

Figure 2 Schematic cross-section of HgCdTe IR absorber material grown on a CdTe-based buffer layer on Silicon. The irregular paths indicate threading dislocations typically present in such structures when grown by MBE. The red dot near the interface with the silicon is meant to indicate a contaminant volume which has "activated" the dislocation in red above it. Such activated dislocations are thought to limit long wavelength HgCdTe IR detectors on silicon. In general, not all dislocation loops, or activated dislocation loops, extend to the top surface.

The TD density in HgCdTe epilayers on Si are thought to be higher than those on CdZnTe, due to the materials mismatch, in particular the lattice mismatch in the lateral

plane of the interface. Thus, one is naturally led to consider what mechanisms are at hand to introduce lateral control over such an interface, in order to control the generation of TD's during fabrication of epilayers of HgCdTe on Si. Over the years a vast collection of work has developed in an effort to reduce the TD density in epilayers of HgCdTe on Si, without a great deal of effort to utilize lateral control, due to the small length scale of the lattice constants involved. However, the results of such efforts seem to have saturated at a maximal practically achievable quality level, characterized by TD density of $\sim 3\times10^{6}$ cm^{-2} [11, 20]. Thus efforts have shifted to more complex substrate architectures to approach HgCdTe epilayer quality achieved on CdZnTe substrates. One such method is further explored in this thesis, namely the introduction of a sub-micrometer, controlled interfacial structure at the interface between a CdTe epilayer and a typical Si wafer substrate. It is interesting to note that in other materials systems, where such lateral control has been more extensively investigated, a similar interface architecture has enabled TD reduction, and subsequently the fabrication of GaN light emitting diodes on Si substrates [21].

1.2 Overview of Nanopattern Formation Techniques

At one of the forefronts of scientific advance is the observation, formation, and understanding of structures at very small length scales. Scientists currently have awareness of subatomic particles, and some knowledge of the constituents of a nucleon, at a length scale of $\sim10^{-15}$m, but un-developed means to construct objects at that same length scale in parallel.

Zooming out, at a length scale 10^5 times larger, scientists have developed incredible means to image and manipulate individual atoms; with impressive, but scarce parallel capability. For example, single atoms can be manipulated, and small numbers of bonds made or broken, with an STM [22]; but significant parallel scaling is daunting. A different kind of example at this length scale is given by bulk crystal growth; which is essentially a massively parallel self-assembly technique. In addition, thin film crystal growth techniques such as MBE, offer the possibility to form arrays of atoms whose ordering and chemical makeup are possible to control in one spatial direction, at that length scale. From this point of view, MBE is a very powerful sub-nanometer pattern formation technique. Beyond the single small dimension, MBE also offers some ability to grow 3-dimensional nanostructures, such as Stranski-Krastanov quantum dots, although in this case the size and placement of the dots is currently difficult to fully control.

Zooming out still further, at a length scale 10^2 to 10^3 times larger, there exists a vast realm of well developed and accessible lateral nanopattern formation techniques. These can be coupled with the power of MBE vertical nanopattern formation to yield impressive 3-dimensional nanoscale structures. Currently, state of the art methods are being developed by researchers across the globe to control the MBE process laterally as well as vertically [23, 24, 25], forming nanopatterns in 3 spatial directions with wires and dots. The research presented in this thesis is part of that development, as it concerns nano-scale lateral control in the technique of MBE of CdTe on lattice mismatched substrates.

The realm of nanopattern formation techniques can be coarsely catagorized as follows:

(1) shadow mask

(2) interference

(3) imprint

(4) self-assembly

(5) direct manipulation

Several of these are listed with references in the table below for comparison (see Table 1). For all of these techniques, vertical resolution can be achieved at the atomic scale, due to the exceptional vertical length scale control of some thin film growth techniques such as MBE. In addition, it should be noted that some patterns can be used in multiple contexts; for example a given nanopattern could be used as a shadow mask or contact mask.

Technique	***Minimum lateral feature size achieved***	***Maximal lateral area limit***	***Examples***
Shadow mask	~ 10^{-7}m for MBE (diffraction limited)	system or substrate	[154] ~ 20,000nm [26] ~ 100nm
Interference	10^{-8}m	coherence-length	X-ray [27] ~ 30nm UV [28] ~ 45nm
Imprint	10^{-8}m	system or substrate	[29] ~ 10nm
Self-assembly	10^{-10}m	system or substrate	Polystyrene sphere array [30] ~ 200nm, Virus array [31] ~ 10nm, Anodized alumina [32] ~ 50nm,
Direct writing	10^{-10}m	set by writing speed	Focused ion beam (FIB) lithography [33], Electron-beam writing [34] ~ 2nm, STM writing [35] ~ 0.2nm

Table 1 Classification of some existing nano-pattern formation techniques. In the case of direct writing, the maximal pattern area is often limited by the total time required to form the pattern.

2 Experimental Systems and Techniques

2.1 Fourier Transform Infrared Spectroscopy

Fourier Transform Infrared Spectroscopy (FT-IR) is a technique used to obtain spectral information from an input optical source; including transmission and reflection data from a given sample of study. FT-IR is superior to conventional diffraction-based monochromators which utilize spatial filtering slits and blazed ruled gratings because the signal to noise is higher (by a factor of 10^2 to 10^4), and the data acquisition time is substantially reduced [36]. In combination with fast computer algorithms to calculate the Fourier Transform of the acquired discrete data [37], the FT-IR technique has become a standard for low signal-to-noise applications, particularly in the IR.

The feature of fast spectra acquisition is termed the Fellgett or multiplex advantage of FT-IR over dispersive monochromators, after Fellgett, who was the first to apply the technique to low intensity signals in astronomy applications [38]. Applications of FT-IR abound in gas sensing, where many rotational vibrational spectral signatures are in the IR [39], for example it can be used for remote sensing of greenhouse gases [40, 41, 42], and in ground-based air quality monitoring devices [43].

A typical FT-IR system is based on a four-arm interferometer with a light source, one stationary (or fixed) mirror, one movable mirror (which oscillates along the beam propagation axis at a typical velocity of ~3mm/sec), a beam splitter, and intensity detector (see Figure 3). A typical beam splitter will be KBr, and detector: DTGS TEC, as we use in this thesis.

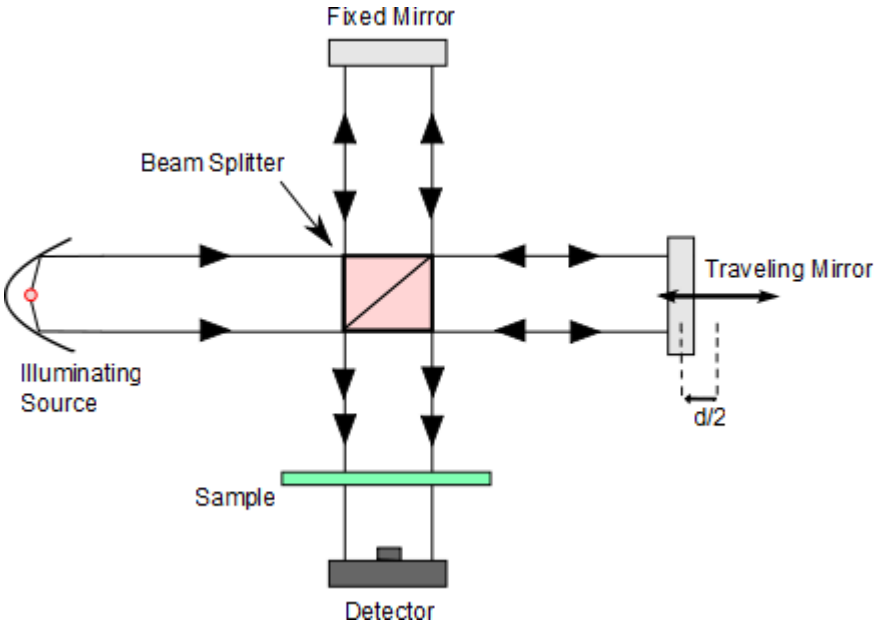

Figure 3 Four-arm interferometer with one traveling mirror; constituting a typical FT-IR system configuration.

Given a single frequency, temporally coherent illumination source, the diffraction pattern at the detector will be an Airy pattern related to the width of the optical components. The intensity at the detector, then depends on the path length difference between the two arms of the interferometer, which depends on the horizontal mirror position, δ/2, according to:

$$\frac{I(k,\delta)}{I_0} = \left| e^{i\cdot k\cdot r} + e^{i\cdot k\cdot (r+\delta)} \right|^2 = 2\left(1+\cos\left(k\cdot\delta\right)\right)$$

Equation 3

where the left-hand-side is the intensity divided by the peak intensity, and k is the magnitude of the wavevector of the radiation ($k = 2\cdot\pi\cdot\nu$ where ν is the wavenumber).

In the case of a distribution of k values within the illuminating source, the total intensity observed at the detector as a function of the moving-mirror position, δ/2, is given by:

$$I(\delta) \propto \int_0^\infty S(k) \cdot \left(1 + \cos(k \cdot \delta)\right) \cdot dk$$

Equation 4

This result can be inverted to obtain S(k) using a Fourier Transform. Utilizing the fact that S(k) and cosine are even functions, the resulting Fourier Transform pair can be expressed as follows:

$$\begin{cases} I(\delta) = I_{\delta=0} + \int_{-\infty}^{\infty} S(k) \cdot e^{i \cdot k \cdot \delta} \cdot dk \\ S(k) = \dfrac{1}{2 \cdot \pi} \int_{-\infty}^{\infty} \left(I(\delta) - I_{\delta=0}\right) \cdot e^{-i \cdot k \cdot \delta} \cdot d\delta \end{cases}$$

Equation 5

In practice the frequency range of the illumination impinging on the sample is limited by the beamsplitter properties. Before performing the Fourier Transform the data is trimmed in real space by an apodization function (we employ Happ-Genzel; other possibilities are boxcar and triangle), to eliminate artifacts arising from the turning points of the mirror's motion. In addition, a background scan is separately acquired with no sample present; and subsequently used to normalize the sample signal. The intensity versus wavenumber is fitted with user-input values for the index of refraction of the sample structure. In the case of a thin film of CdTe on silicon, one can reliably measure

the thickness of CdTe by this method, incorporating experimentally derived index values. An approximate thickness can be obtained, by assuming the index is wavenumber-independent, from the observed spacing of consecutive fringes in the data, as follows:

$$d = \frac{1}{2 \cdot n \cdot \Delta \nu}$$

Equation 6

where n is the real part of the index of refraction of the thin film, and $\Delta\nu$ is the spacing in wavenumber of consecutive maxima in the interference pattern. In our system, a useful value for n of CdTe thin films on Si, is 2.67. In this thesis we employ a spectral index fitting routine to determine CdTe film thicknesses on IR-transparent Si wafers (30-60 Ωcm), using a Thermo Nicolet Nexus model 870 FT-IR system with KBr beamsplittter and DTGS TEC detector.

2.2 Atomic Force Microscopy

2.2.1 Introduction

Microscopy is an essential and extensive technical field in science today. Any microscope essentially scatters or excites probing particles from a target specimen and subsequently determines their resultant phase space distribution (in real space and/or momentum space). The simplest, time-tested imaging device accessible to human beings is likely the human eye; an optical imaging device concept used to analyze scattered photons for at least several thousand years. However, as any blind person can attest, the

sense of touch is very powerful, and could possibly pre-date the emergence of vision in our ancestors. The incredible developments of science have added extensions to both such sensing concepts. In the optical microscope, photons are scattered and imaged using refracting or diffracting lenses; which has enabled scientists to image the planets and stars and planets of other stars and observe Brownian motion, among other things. In such a design, the angular resolution is limited by the diameter, D, of apertures in the system and the wavelength, λ, of scattering photons, and can be approximated by the Rayleigh criterion. This criterion characterizes the diffraction limit of angular resolution in a wave propagation imaging system; where ψ is the minimum angular separation in the field-of-view which can be resolved in the microscope image [44]:

$$\sin(\psi) = (1.22) \cdot \frac{\lambda}{D}$$

Equation 7

A simple case is shown in Figure 4, below.

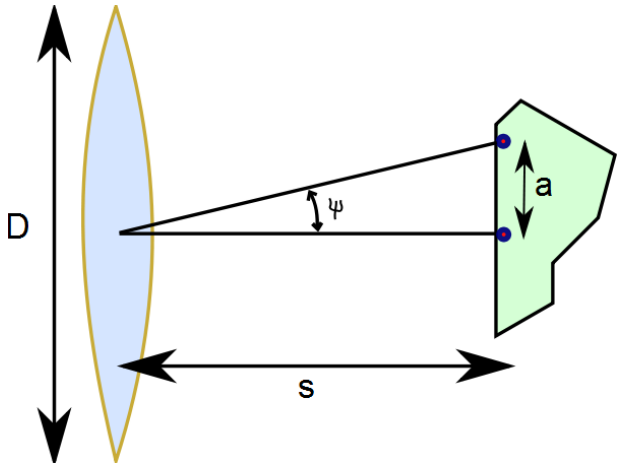

Figure 4 An example wave-propagation imaging system, with separation s, and distance between minimally separately resolvable object features given by a.

From this figure the Rayleigh criterion can be cast as below in Equation 8; from which it is clear that decreasing s will improve the theoretical resolution limit, but not necessarily the practically achievable resolution. It can be difficult to engineer a system which maintains reasonable D, but is very close to the object to be imaged; for example, the object needs to be flat and a lense may need to be achromatic and of short focal length. The realm of near-field microscopy capitalizes on decreasing s. Increasing D can be impractical from an engineering perspective, thus the Rayleigh criterion sets a practical, but not absolute, limit to the resolution of a wave-propagation-based microscope.

$$a = \frac{s}{\sqrt{\left(\frac{D}{(1.22)\cdot\lambda}\right)^2 - 1}}$$

Equation 8

The other basic, time-tested microscope concept utilizes contact between two objects; gaining information by the correlation of the two objects. This technique is also fundamentally restricted by the wavelength of probing particles; which in this case have typical de Broglie wavelength of order less than 1 Å at room temperature. Thus a contact microscope is in principle capable of atomic resolution at room temperature. Techniques have been developed to approach such resolution limits through contact. A microscope in contact with the object to be imaged, which raster scans the specimen, is considered an example of a scanned probe microscope.

The history of scanned probe microscopes dates back at least as far as the stylus profilometer [45] in the 1960's and topografiner [46] of the 1970's; which inspired the development of the first scanning tunneling microscope [47], later soliciting a Nobel Prize for enabling atomic scale resolution images within small areas of a flat sample surface, and enabling a direct rendering of a Si(111) 7×7 surface reconstruction; which was a surprising result at the time [48]. The Scanning Tunneling Microscope (STM) has the limitation of requiring a large current density to pass between the sample and probe tip, on the order of 30 A/mm^2. Such an operation regime of high current density can allow for manipulating the positions of atoms on a surface, but has the drawback of requiring a fairly conductive sample surface in order to produce stable imaging conditions. Many interesting potential sample subjects are not conductors; or rapidly develop oxidation and water surface layers in ambient conditions. This was quickly recognized and addressed by the introduction of the first Atomic Force Microscope (AFM) [49]. The first AFM utilized a STM as a feedback monitoring system for the deflection of a flexible gold foil stylus with diamond tip, as the stylus was raster scanned

over a sample surface, while tapping the surface. The AFM added the capability to image electrically insulating samples in ambient conditions, and eventually biological samples in liquids. The tapping-mode of the AFM, introduced at the advent of AFM, as opposed to contact mode, is considered a more robust technique, as it exerts less lateral force to the sample being imaged [50], and also keeps the probe tip cleaner during scanning. The AFM has even reached atomic scale resolution in practice (~ 5 Å) [51]. Both AFM and STM utilize piezoelectricity to control the scanning tips at the angstrom length scale, and fast feedback electronics with response time ~ 10^{-4} seconds [52], to maintain stable imaging conditions above a sample surface while mapping out its features approximately in real time. Modern variations of the STM and AFM abound; including conductive AFM, lateral force microscopy, and magnetic force microscopy. In addition, parallel microchip arrays of AFM's have been fabricated and high lateral scan speeds (~1 cm/sec) are being pursued [50, 53]. Also the AFM is being used to write permanent features onto surfaces at the nanometer length scale.

The AFM employed in this thesis was a Dimension 3100 Nanoscope 3D manufactured originally by Veeco (now owned by Bruker). The cantilever was silicon, with effective spring constant ~ 20 to 100 N/m, and approximate dimensions of thickness times width times length, respectively of: $4 \times 40 \times 125\,\mu m$. These values, in combination with the Young's modulus, E, of silicon, taken to be 130 GPa, can be used to estimate the cantilever effective spring constant, k (valid for small deflection), using the following relation [52].

$$k = \frac{E \cdot w \cdot t^3}{4 \cdot l^3}$$

Equation 9

This value of the spring constant is related to the estimated amplitude of thermal fluctuations experienced by the cantilever; given by the following[54].

$$z = \sqrt{\frac{4 \cdot k_B \cdot T}{3 \cdot k}} \approx \frac{0.074}{\sqrt{k}} \; ; \qquad [nm]$$

Equation 10

where k_B is the Boltzmann constant (equal to 1.38×10^{-23} J/K), T is the temperature in degrees Kelvin, and k is the spring constant in units N/m. Substituting 20 N/m for k, gives a z value of 0.2 Å, thus spontaneous thermal fluctuations do not preclude the feasibility of atomic-scale AFM resolution at room temperature. Rather, the practical limits of AFM resolution are typically related to the tip shape issues. A given image acquired by AFM is in general a convolution between the sample features and the tip shape. The features of the tip shape which influence image acquisition are generally characterized on large length scale by sloping sidewalls of the tip, and on the small length scale, by the nominal maximum radius of curvature of the tip point. As the tip scans across the sample, all real surface features will acquire a lateral broadening due to the tip shape, in relation to their relative size and shape (see Figure 5). In the limit of a very sharp and high aspect ratio sample feature, the sample will image the tip, rather than the

tip imaging the sample; that is, under those conditions the acquired image will reflect the tip, rather than sample, features.

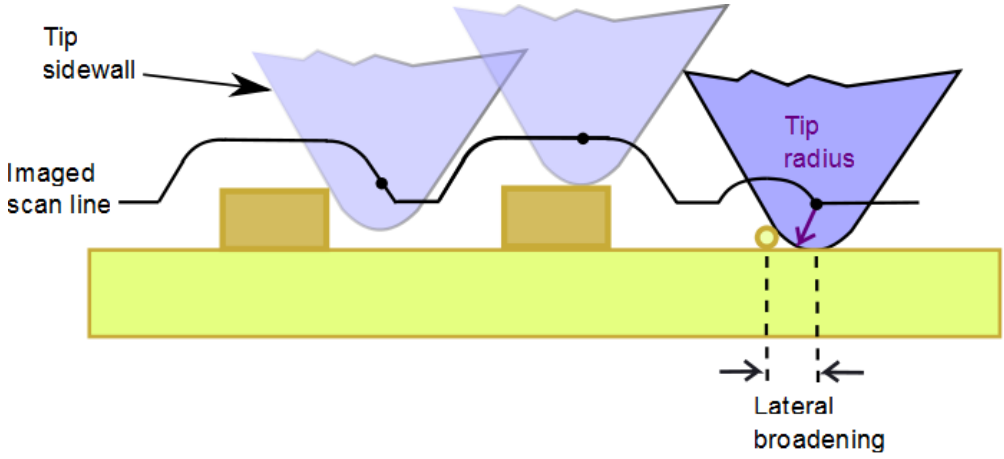

Figure 5 An idealized tip is shown at three locations while mapping the surface features of a sample by maintaining constant contact with the sample surface. An idealized AFM scan line always contains artifacts from the convolution of the tip and sample features, as shown here; including the tip sidewall angles and tip point radius of curvature. In general, the vertical resolution is far superior to the lateral resolution. The vertical resolution is typically not limited by the piezoelectric actuators or data acquisition card (which set a typical limit of 0.3 Å); rather, the vertical resolution is limited by the imperfect vibration isolation system, resulting in typical values being larger than ~ 1Å.

It is clear from Figure 5 that given tip-shape-limited resolution, the lateral and vertical resolutions will differ substantially. In practice the lateral is less than ~10nm, whereas the vertical may be on the order of angstroms. In light of the Rayleigh criterion, the AFM resolution is seen to be of the order of an x-ray imaging microscope[3]. Electron microscopes can exceed even this resolution.

[3] It should be noted that x-ray based microscopes have the draw-backs of limited optical component choices, and sample modification or destruction by the high photon energy. A key distinction is that the AFM utilizes a single, massive, high momentum probe; whereas an x-ray microscope uses many high kinetic energy probing particles.

In tapping mode operation, as the AFM tip traces a scan line, it will be driven to oscillate vertically in Figure 5, making intermittent contact with the sample, at most, at the bottom of each swing of the cantilever. The motion of the cantilever and tip can be modeled for small amplitude deviations from equilibrium by a damped driven harmonic oscillator of effective spring constant, k. The damped driven harmonic oscillator is well described by Marion and Thornton [55]. The resultant cantilever motion is shifted in time with respect to the driving force; has a resonant frequency; and can be characterized by the quality factor. The typical resonant frequency of a cantilever used in this thesis was ~300kHz. The damping, proportional to β in the force law, directly results in the phase shift, as seen in the following expression for the phase shift, δ, under the model assumed here; where the angular frequency is denoted ω , and ω_0 is the resonant angular frequency:

$$\delta = \tan^{-1}\left(\frac{2\cdot\omega\cdot\beta}{\omega_0^2-\omega^2}\right)$$

Equation 11

The interaction of the tip with the sample can be modeled as occurring primarily through the damping factor, which shifts the phase of oscillation and also clearly affects the amplitude of oscillation. The damping results from the collision of the tip and sample imparting energy to the sample; which is dependent upon the potential energy between tip and sample. At large separation, the neutral tip and sample atoms can attract by the correlation of spontaneous dipole fluctuations in the charge distribution of the atoms. The attraction can be shown to scale, to leading order in perturbation theory, as R^{-6} ,

where R is the tip and sample separation [69]. At short separation, the electron clouds overlap, producing a repulsion believed to be related to the Pauli-Exclusion principle. If one assumes a scaling of the repulsion as R^{-12}, then the so-called Lennard Jones potential curve is obtained [69]. Such a curve is plotted below for experimentally fitted values relevant to Argon [69] (see Figure 6). In the case of two separate groups of atoms (for example a sample surface and AFM tip), a similar potential curve obtains, and has been confirmed through measurement [52]. In the event that the tip and/or sample are electrically charged, additional energy contributions will arise, distorting the curve in the tip-sample system. In this thesis we utilize a weak flux of alpha particle radiation from a small Polonium 210 source to ionize the sample, cantilever, and tip as well as the surrounding air, in order to electrically neutralize any fixed charge accumulation which could otherwise influence the AFM measurement results.

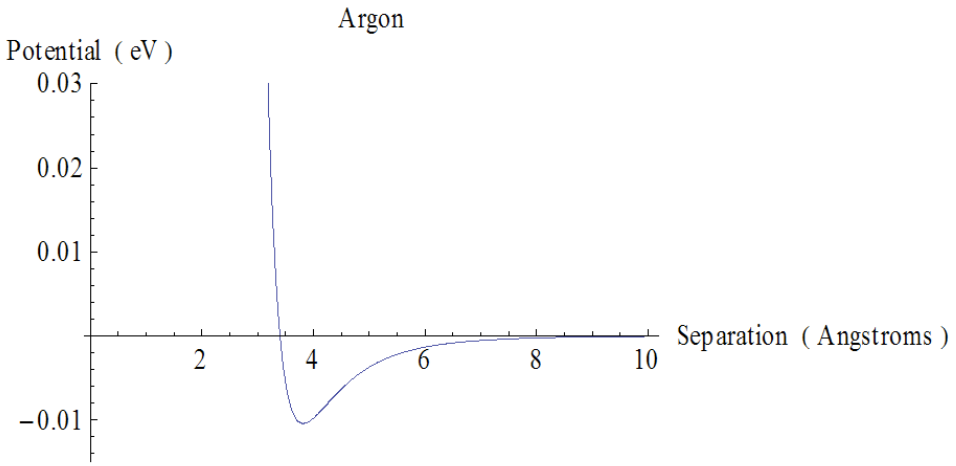

Figure 6 The Lennard Jones potential energy of two Argon atoms is shown plotted as a function of the separation between the centers of the atoms. A similar potential curve is relevant to two separate solid materials.

Such a potential curve will modify the potential between tip and sample when the AFM cantilever is maintained at fixed height, but with its tip-end allowed to flex, as shown schematically below:

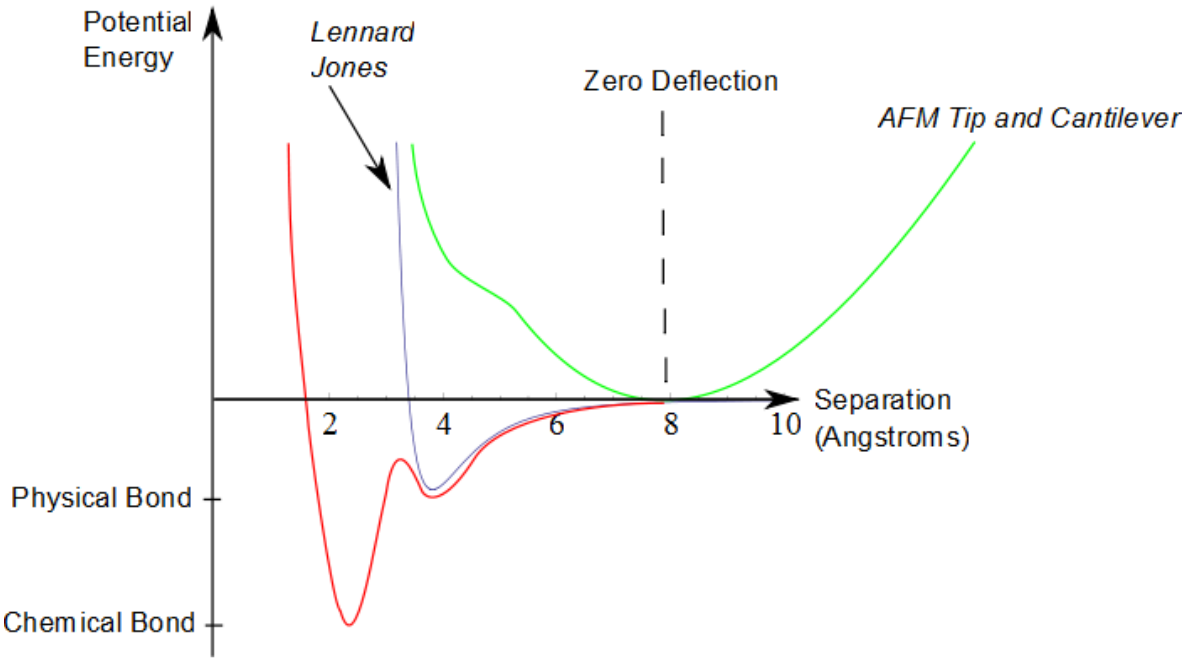

Figure 7 A schematic illustration of three fundamental possible shapes of the potential energy versus separation for an AFM tip atom and a sample surface atom. The green curve denotes the potential with the added constraint imposed by the cantilever (from the opposite end as the tip), that the equilibrium separation is ~ 8 Angstroms, denoted "zero deflection". The blue curve depicts the Lennard Jones type potential curve, exhibiting a weakly, or physisorbed, bonding state between the sample and tip atoms. The red curve depicts the more general situation in which a chemical bonding state may also exist between the tip and sample atoms.

This modification to the potential energy curve provides the essential picture of how an AFM is able to sense the presence of the sample surface under investigation. In general, the surface tip atoms could chemically bond to the surface causing artifacts in acquired data; however the technique remains robust for many samples.

In conclusion, the AFM is a powerful microscope, with short essential length scale resolution limits in the sub-nanometer regime at room temperature. In practice the tip

shape usually dominates image resolution. The lateral resolution, thus determined, is generally lower than the vertical. The interpretation of data from an AFM is essential to its proper use; as artifacts can easily be present in various forms.

2.3 Electron Microscopy

2.3.1 Introduction

The electron microscope was introduced by Ruska [56] in 1935, in direct analogy with optical microscopes (where focusing lenses, and ray tracing are applicable), but with energetic electrons as the probing particles, rather than photons. The scanning electron microscope was born of experiments observing secondary electrons emanating from a surface after bombardment with high energy primary electrons in vacuum [57, 58]. In these first devices the electron beam was not focused, and so had a width on the order of 100μm. Von Ardenne is credited with developing the first scanning electron microscope, with rastering focused electron beam, imaging via transmission of the electrons through a sufficiently thin sample [59]. While working with the first rastering electron beam transmission microscope, he proposed, but did not pursue, the idea of using secondary electrons to produce an image of a sample surface [60].

2.3.2 Theory of operation: lenses, resolution

A schematic picture illustrating the essential elements of an electron microscope are shown in Figure 8 below.

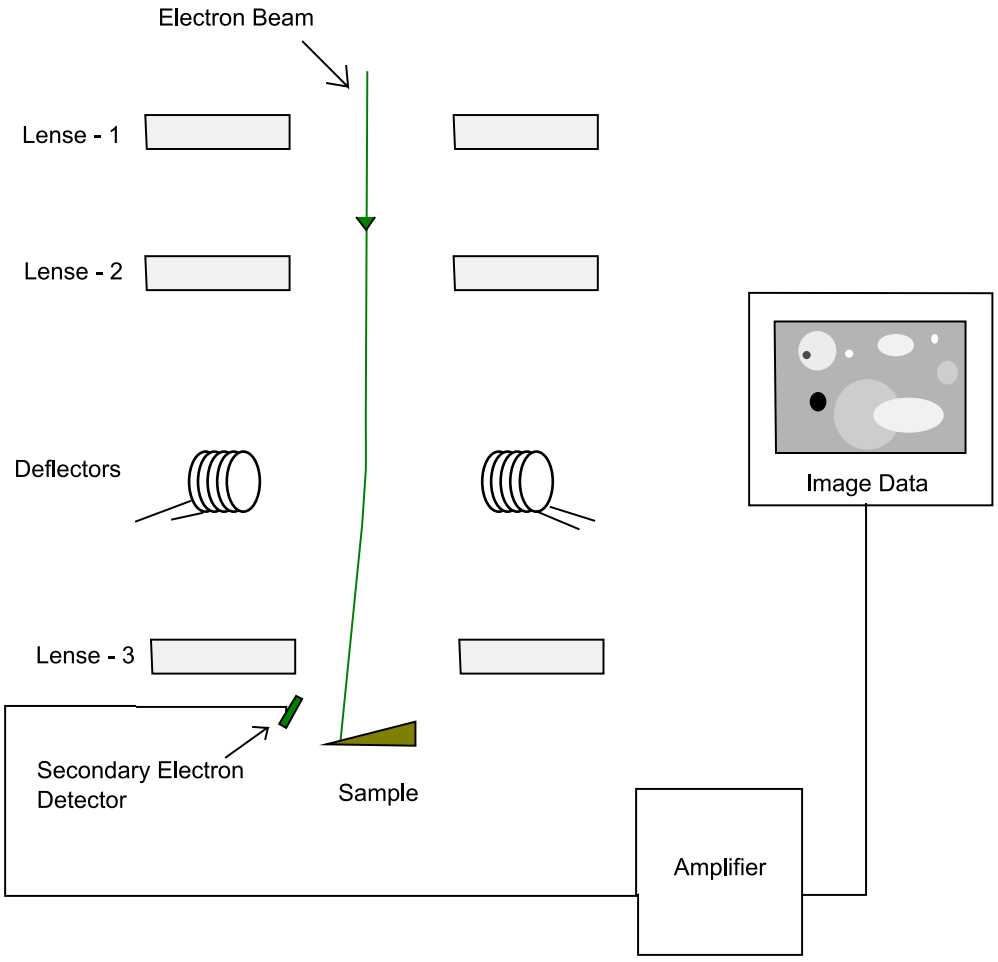

Figure 8 A schematic cross-section of a scanning electron microscope. Lenses 1 and 2 are generally condenser lenses; and beam steering is introduced lower in the column. The image data is produced by monitoring the flux of secondary electrons detected as the electron beam raster scans the sample surface.

Just as in the case of an optical microscope, the resolution is characteristically limited by the Rayleigh criterion (Equation **7**), evaluated with the de Broglie wavelength of the probing electrons. The wavelength of electrons with kinetic energy KE, is given by the relativistic expression below [56, 71]. The equality on the left should be used in favor of the corresponding classical expression when the electron energy is over ~50 keV [61].

$$\lambda_{elec} = \frac{h}{m \cdot c} \cdot \left(\frac{1}{\sqrt{\frac{2 \cdot KE}{m \cdot c^2} \cdot \left(1 + \frac{KE}{2 \cdot m \cdot c^2}\right)}} \right) = \lambda_{Comp} \cdot \sqrt{\frac{1}{\beta^2} - 1} \approx \frac{12.27}{\sqrt{V}}; \quad [\text{Å}]$$

Equation 12

where m is the rest mass of an electron (9.11×10^{-31} kg), c is the speed of light in vacuum (3×10^8 m/s), and β is the electron velocity divided by c. The right-most approximation assumes the electrons gain a KE small in comparison to their rest energy; where their KE is derived from free acceleration through electrostatic potential difference V (in volts). The full expression was used to produce the plot below, for electron wavelengths of interest in this thesis.

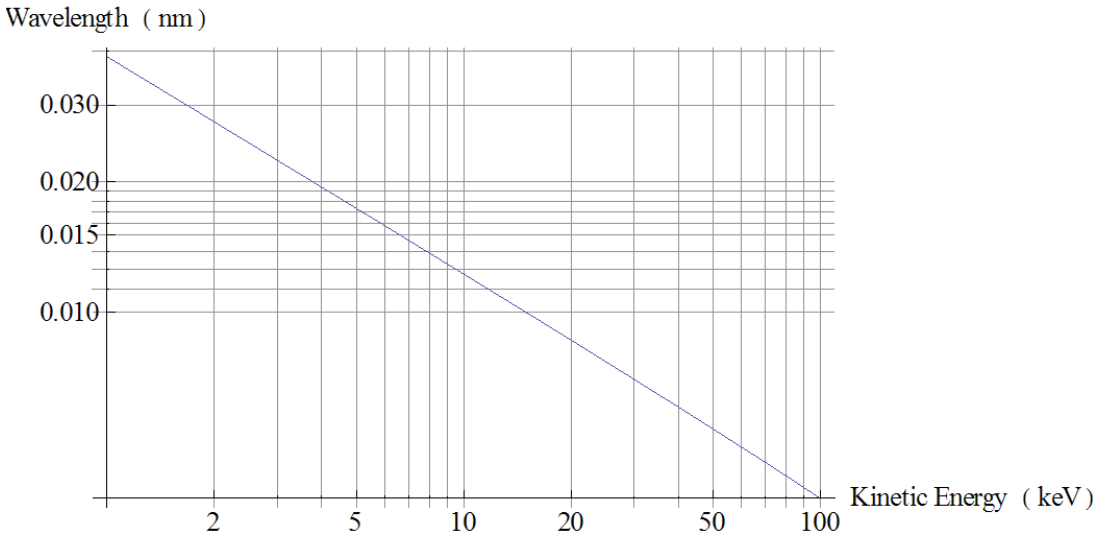

Figure 9 Relativistic electron wavelength as a function of kinetic energy.

A typical SEM may operate in the 5 to 100 keV range (and a TEM in the hundreds of keV). Thus, the relativistic electron wavelength sets a very short minimum length scale for the resolution of the SEM, at ~0.05 Å. In practice, as for AFM, the resolution is limited by other factors. In the case of the SEM the resolution is limited by lense aberration [56], and is of the order of 1 Å; which sets the scale for lateral resolution of an SEM or TEM. This significantly exceeds the resolution of the AFM, and makes atomic-scale resolution more accessible. The vertical resolution is not as small; for example when imaging is performed with secondary electrons, the depth of origin of the electrons is on the order of 5nm [62]. It should also be noted that, when secondary electrons (versus backscattered) are used for image formation; there is low atomic-number (Z) contrast in the resultant images [63].

During the imaging of a sample by SEM, a significant amount of current is imparted to the surface, of order $1A/mm^2$, or 6×10^{12} electrons/$\mu m^2 s$. The beam can heat the sample, electrically charge the sample, and catalyze reactions on the surface of the sample.

In this thesis a Hitachi S-3000N variable pressure SEM system with oil-based vacuum pump is employed to characterize the surface of patterned samples with resolved features ~ 10nm. Interestingly, the electron beam of this system is believed to have stimulated the deposition of carbon onto the samples imaged for this thesis.

2.4 X-Ray Diffraction

2.4.1 Introduction

Within the theory of quantum mechanics it is known that spatially or temporally periodic systems can change state, in momentum or energy respectively, only by multiples of some discrete smallest unit, related to Planck's constant, h, equal to 6.6×10^{-34} J*s [64]. For example, a particle interacting with a one-dimensional spatially periodic system can change its momentum only by integer multiples of h/λ in the direction of periodicity, where λ is the periodicity length of the system. In finite-volume regular arrays of atoms, approximating crystals, a similar picture plays out in the observance of scattering of x-rays from the atoms of the crystal, in that the momentum change is discrete, and similarly related to the underlying periodicity of the structure.

On the 8th of November in 1885 x-rays were discovered by Roentgen, accidentally, while he was accelerating electrons in the dark in a cardboard-shielded vacuum tube. Shortly thereafter, he began to explore their ability to penetrate solids; and discovered that they do not penetrate human bones as well as human soft tissues. He was later awarded the first Nobel Prize in Physics in 1901, for the discovery of x-rays. X-ray diffraction was then born at the hands of M. von Laue 11 years later and first published in 1912, after the discovery of divergent beams of x-rays emanating from thin crystal films [65]. M. von Laue had previously conceived intuitively that crystals should be able to diffract x-rays, much as an optical diffraction grating can diffract light. At that time, possible crystal structures had been conceived of mathematically, by considering the packing of hard spheres, but it was not known for certain that a given crystal's periodicity

could be measured with x-rays at room temperature, due to the estimated influence of thermal motion of atoms on phase sensitive reflections [66]. In the same year, father and son Bragg began working out many crystals' structures through x-ray diffraction, by viewing the conditions for constructive interference, viewed in terms of reflective regularly spaced crystal planes. Over the next year they observed that some predicted constructive interference conditions were not seen experimentally, while others were; and were able to account for this with the "structure factor" [65, 70]. Bragg's essential relation for constructive interference (reflection of x-rays) from consecutive planes spaced, d, apart, can be expressed:

$$2 \cdot d \cdot sin(\theta) = n \cdot \lambda$$

Equation 13

where θ is the angle of incoming x-rays with respect to the sample surface, λ is the x-ray wavelength, and n is a counting number. In practice, it is useful to recast this equation as follows:

$$2 \cdot d_{(hkl)} \cdot sin(\theta) = \lambda$$

Equation 14

where $d_{(hkl)}$ is the spacing between consecutive planes with Miller Indices (hkl). For cubic crystals of cube side length a, the (hkl) plane spacing is given by:

$$d_{(hkl)} = \frac{a}{\sqrt{h^2 + k^2 + l^2}}.$$

Equation 15

The above equations predict possible diffraction maxima for a given cubic crystal, but do not specify the relative intensity of different maxima. Such depends on more detail about the scattering, including polarization [65]; but more importantly, the placement and density of scattering material within the cubic cell.

A given periodic structure in space is called a crystal. A crystal can be most easily described in terms of a lattice of points generated by the set of all translation vectors of the form below, where f, g and h are integers, and $\vec{a}_1$, $\vec{a}_2$ and $\vec{a}_3$ are primitive vectors:

$$\vec{T} = f \cdot \vec{a}_1 + g \cdot \vec{a}_2 + h \cdot \vec{a}_3$$

Equation 16

plus a basis of structure corresponding to each lattice point. Such an array is also periodic with respect to certain, rotations as well. The possible perfect crystal structures that can be realized in three dimensions can be classified according to sets of symmetry operations (including linear translations and rotations) which leave the crystal indistinguishable before and after transformation, termed space groups.

In nature, there appear to be no perfect spatially periodic objects; however some objects do show repeating properties at some length scale; which are commonly referred to loosely as “crystals”. An example of such a crystal is a macroscopic volume of CdTe,

in which the coordination and bonding arrangements of all the constituent atoms is regular in length and direction, except at the surfaces, where distortions will typically be present (surface reconstructions). CdTe is typically found in nature with two slightly different crystal structures: zinc blende and wurtzite (that experimented-with in this thesis was zincblende). The zincblende structure is composed of two face-centered-cubic (fcc) lattices, offset by a quarter the cube diagonal, with Cd atoms occupying one fcc lattice, and Te the other. This crystal structure can be viewed as one fcc lattice plus a basis of two atoms offset a quarter diagonal, attached to each lattice point.

Due to the inverse relation between momentum and wavelength, it is useful when considering scattering problems to construct a transformation between the real space periodicity of a crystal with real space lattice, and an inverted, or reciprocal lattice. This is then helpful in framing scattering problems. Within the reciprocal lattice, all points are accessible through reciprocal lattice vector translations of the type:

$$\vec{G} = u \cdot \vec{b}_1 + v \cdot \vec{b}_2 + w \cdot \vec{b}_3$$

Equation 17

where u, v , and w are integers, and $\vec{b}_1$, $\vec{b}_2$, and $\vec{b}_3$ are the primitive reciprocal lattice vectors of the reciprocal space, related to the real-space lattice vectors and primitive cell volume, V, by the following equations:

$$\begin{cases} \vec{b}_1 = \dfrac{2\cdot\pi}{V}\cdot\vec{a}_2\times\vec{a}_3 \\ \vec{b}_2 = \dfrac{2\cdot\pi}{V}\cdot\vec{a}_3\times\vec{a}_1 \\ \vec{b}_3 = \dfrac{2\cdot\pi}{V}\cdot\vec{a}_1\times\vec{a}_2 \end{cases}$$

Equation 18

Consider x-ray radiation incident upon a crystalline material. The electric field of the propagating x-ray will couple to the positive and negative charge in the crystal and scatter to different directions, changing its wave vector k, depending on the appropriate cross-sections for scattering. It is an elegant and useful theorem of diffraction that states that the change in wave vector, k, in such a process, must be equal to a reciprocal lattice vector, G, as defined above. This is another expression of the initial statement of this section: that the change in momentum must be directly related to a multiple of the inverse periodicity of the system in some direction; which can be written in terms of Planck's reduced constant ($\hbar = 1.05\times10^{-34}$ J*sec)[4]:

$$\Delta\vec{p} = \hbar\cdot\Delta\vec{k} = \hbar\cdot\vec{G}$$

Equation 19

In considering the scattering from the electrons and nuclei of the material, it can be shown that the scattering due to the nuclei is insignificant in comparison to the

[4] Thus the typical form of Bragg's Law can be viewed in terms of quantized possible momentum transfer: $\hbar\cdot2\cdot\pi\cdot\left(\dfrac{2\cdot\sin(\theta_{hkl})}{\lambda}\right) = \hbar\cdot2\cdot\pi\cdot\dfrac{1}{d_{hkl}}$.

electron scattering, as follows. The following equation gives the total power radiated by an accelerated point charge, e, where c is the speed of light in vacuum (3×10^8 m/s), m is the mass of the point particle, and $\frac{dp_\mu}{d\tau}$ is the covariant momentum change with respect to proper time [104].

$$P = -\frac{2}{3\cdot c^3}\cdot\left(\frac{e}{m}\right)^2\cdot\left(\frac{dp_\mu}{d\tau}\cdot\frac{dp^\mu}{d\tau}\right)$$

Equation 20

The above equation can be used to approximate the relative contributions of electrons and nuclei, of a given atom, to the scattering of any impinging electromagnetic radiation with the following ratio:

$$\frac{P_{electrons}}{P_{nuclei}} \approx \frac{Z\cdot\left(\frac{e}{m_{electron}}\right)^2}{\left(\frac{Z\cdot e}{2\cdot Z\cdot m_{proton}}\right)^2} = 4\cdot Z\cdot\left(\frac{m_{proton}}{m_{electon}}\right)^2 \approx Z\cdot10^7$$

Equation 21

Where Z is the number of protons (and also the number of electrons) on the atom under consideration, e is the charge carried by an electron (1.6×10^{-19} C), and the masses are

labeled[5]. Thus, typical materials will exhibit on the order of 10^8 times more x-ray scattering from the electrons in the material, as compared to the nuclei.

Therefore if one assumes many-body effects are negligible when x-rays scatter from a material, then their wave vector must change, and so must their frequency, according to the Compton formula of x-ray scattering by a single electron. The Compton formula gives the relationship between incoming wavevector magnitude, k, and outgoing-scattered wavevector, k', as follows [104]:

$$\frac{k'}{k} = \frac{1}{1 + \frac{\hbar \cdot \omega}{m \cdot c^2} \cdot \left(1 - \cos\left(\theta\right)\right)}$$

Equation 22

Where $\hbar$ is the reduced Planck's constant (1.05×10^{-34} J*s), ω is the angular frequency of radiation, c is the speed of light in vacuum (3×10^8 m/s), m is the mass of the charged particle, and θ is the angle of deviation of the incident photon from its initial path after scattering. It is interesting to note that the charge of the massive target particle does not enter into this formula; thus when applied to an electron, this equation constitutes one of the rare experimentally testable relations involving an electron's mass independently of its charge-to-mass ratio. The equation can be recast in terms of wavelength as:

$$\lambda' - \lambda = \frac{h}{m \cdot c} \cdot \left(1 - \cos\theta\right)$$

Equation 23

[5] The mass of the nucleus is approximated here to be the sum of the number of protons times twice the mass of a free proton.

Where h is Planck's constant (6.6×10^{-34} J*sec); and the quantity $\frac{h}{m\cdot c}$ is the de Broglie wavelength [67] associated with the rest mass of the scattering particle, known as the Compton wavelength. For an electron, this wavelength is 0.024 Å, thus the scattering of electromagnetic radiation by electrons can be assumed to be nearly elastic. Thus we have motivated the following reasonable assumptions: that in x-ray scattering in crystalline materials, the scattering can be accounted for by considering only elastic scattering from only the electron density in the material.

Furthermore, it can be safely assumed that the real part of the index of refraction of a typical crystalline material scattering x-rays of wavelength ~2 Å is unity [68]; and that the imaginary part of the index will not strongly influence the scattering kinematics.

It is helpful to decompose the scattered x-rays from a material's electron density, according to the following development. Denote the scattered electric (or magnetic) field amplitude as F. Then, when considering scattering from a crystal, F takes the following form at the Bragg condition (Equation 19), as an integral over only electron density within the unit cell, multiplied by the number, N, of illuminated unit cells [69]:

$$F_{\vec{G}} = N \int_{\substack{unit\\cell}} n(\vec{r}) e^{-i\vec{G}\cdot\vec{r}}\, dV$$

Equation 24

where $\vec{G}$ is the reciprocal lattice vector related to the specific Bragg condition. If the electron density, $n(\vec{r})$, within each of the identical unit cells, overlaps well with the phase factor containing $\vec{G}$, then the scattered amplitude will be high. The structure

factor is then given by the integral in Equation 24, and can be recast in terms of atomic form factors, f_j , as follows [69], where the index j runs over the atoms in one unit cell:

$$S_{\vec{G}} = \sum_j f_j \cdot e^{-i \cdot \vec{G} \cdot \vec{r}_j}$$

Equation 25

and where the atomic form factors are given by:

$$f_j = \int_{\substack{all \\ space}} n_j \left(\vec{r} - \vec{r}_j \right) \cdot e^{-i \cdot \vec{G} \cdot \left(\vec{r} - \vec{r}_j \right)}$$

Equation 26

and are often assumed to be properties of the elements, independent of the chemical bonding of the elements in a solid under investigation (again, with j indicating an atom within the unit cell).

It is helpful to note a simplification that arises in the case of a crystal structure viewed in real space in terms of a basis attached to a lattice of points. In that case, the sum in Equation 25 can be factored into a sum only over the lattice, times a sum only over the basis, as follows:

$$S_{\vec{G}} = \left(\sum_j f_j \cdot e^{-i \cdot \vec{G} \cdot \left(\vec{u}_j + \vec{v}_j \right)} \right) = \left(\sum_{Lattice} e^{-i \cdot \vec{G} \cdot \vec{u}_j} \right) \cdot \left(\sum_{Basis} f_j \cdot e^{-i \cdot \vec{G} \cdot \vec{v}_j} \right)$$

Equation 27

where the $\vec{u}_j$ are primitive vectors of the unit cell lattice, and the $\vec{v}_j$ are basis vectors.

The intensity of scattered radiation will be proportional to the complex modulus squared of the structure factor. Thus if for a certain $\vec{G}$, the structure factor is zero, then there will be no intensity of scattered radiation at the corresponding incident and detection angles with respect to the crystal planes. For a given crystal structure, one wishes to identify all possible Bragg scattering conditions (corresponding to $\vec{G}$ values), by considering all possible $S_{\vec{G}}$. The possible $\vec{G}$ values can be organized according to the Miller indices of the sets of planes to which they correspond, denoted (hkl). Thus, the search can be organized in terms of Miller indices. For example, silicon, germanium, and carbon exhibit a diamond lattice structure. In that structure, the evaluation of Equation 27 results in the following relative intensities, organized according to the Miller indices of the planes, and normalized by the atomic form factor of the crystal atoms, as well as the polarization factor [71]:

Diamond crystal Miller Indices (h, k, l must be *all-odd* or *all-even* in addition to the restrictions below)	*Normalized, squared structure factor* $\frac{\left\|S_{\vec{G}}\right\|^2}{\left\|f\right\|^2 \cdot \left(\frac{1+\cos^2\left(2\cdot\theta_{hkl}\right)}{2}\right)}$
$h+k+l=z\cdot 4$ (where z is an integer) (For example: (422), (026))	4
$h+k+l$ is an odd number (For example: (111), (311), (331), (115) (135) (533))	2
otherwise	0

Table 2 Relative scattering intensities for the diamond lattice, organized in terms of Miller Indices, indexing the possible crystal planes to give Bragg scattering.

The structure factor can be used, for example, to account for the selectively extinguished maxima first noticed and explained by Bragg [65, 70]. Beyond the structure factor, a given set of crystal planes at the Bragg condition may not be observable for two other reasons. The first reason is that the Bragg scattered beam may not necessarily emerge from the sample surface; making it impossible to analyze for reflection-type, as opposed to transmission-type, XRD system configurations. The second reason is that for interplanar spacing less than half the wavelength of the x-rays, one will not observe constructive interference for a large set of such planes; thus there is an upper bound to the (hkl) values of observable Bragg planes.

The conditions for Bragg scattering from crystal planes summarized in Table 2 can be used to approximate the relative intensities of Bragg peaks from a Zinc Blende crystal structure (which can be formed mathematically by displacing two fcc lattices {with differing atoms on each fcc lattice} along their diagonal, by a quarter the length of the diagonal). The only assumption needed is that the atomic form factors of Te and Cd are identical; which is indeed the case up to 6% accuracy [71]. In the table below (Table 3), Equation 25 is used to calculate the relative scattering intensities of a Zinc Blende CdTe crystal structure for Miller indices of Bragg planes of interest which give non-zero scattered intensity in the diamond structure assumption, but using differing tabulated values for the atomic form factors of Cd and Te [71]. The structure factor reported is normalized by an electron scattering process, and the result of the fcc structure factor (equal to 16). It should be noted that it is in practice generally the ratio of two structure factor values which is of interest experimentally. It should also be noted that the

polarization of the scattered beam plays a role in influencing the intensity (which is incorporated into Table 3 as well) [71]. In addition, the thermal motion of the crystal atoms tends to reduce the intensity of Bragg peaks without changing their widths; this is also incorporated into Table 3 via the "Debye-Waller" factor evaluated at 300K [69, 72]. The values in Table 3 indicate that the second strongest peak, within the set of planes considered for CdTe, is (422).

Zinc Blende CdTe crystal Miller Indices	d_{hkl} *(Å)*	*Normalized, squared structure factor :* $\frac{\left\|S_{\vec{G}}\right\|^2}{16\cdot\left\|f_{electron}\right\|^2}$	*Bragg Angle (in degrees)* θ_{hkl} *(λ=1.54 Å)*	*Normalized, squared structure factor with polarization factor :* $\frac{1+\cos^2\left(2\cdot\theta_{hkl}\right)}{2}$ *and Debye-Waller factor :* $\exp\left(\frac{-2\cdot\pi^2\cdot\left\langle u_s^2\right\rangle}{d_{hkl}^2}\right)$	*Bragg-planes-to-(211)-angle (in degrees)* $\theta_{hkl\text{-}211}$ *(λ=1.54 Å)* *Black : observable for (211)* *Gray : unobservable for (211)*
(111)	3.741	25.77	11.88	22.1	19.47, 61.87
(311)	1.954	25.77	23.21	14.8	10.02, 42.39, 60.50, 75.75
(331)	1.487	25.77	31.20	10.1	20.51, 41.47, 68.00, 79.20
(422)	1.323	51.50	35.60	16.4	0
(511)	1.247	25.77	38.13	7.3	19.47, 38.22, 51.06, 61.87, 71.68, 80.96
(531)	1.095	25.77	44.67	5.8	14.96, 34.10, 46.36, 56.49, 65.54, 73.98, 82.07
(620)	1.025	51.50	48.72	10.5	25.35, 49.80, 58.91, 75.04, 82.58
(533)	0.988	25.77	51.19	5.0	5.05, 29.35, 51.49, 60.13, 75.58, 82.85

Table 3 Relative scattering intensities for Zinc Blende CdTe, organized in terms of Miller Indices, indexing the possible crystal planes to give Bragg scattering. In the last column only relative angles less than 90^o are listed.

Within Table 3, a classification is included as to whether or not the listed Bragg conditions are observable from a large area CdTe(211) surface, such as considered in this thesis. The criterion for being observable is simply that the angle between the {hkl} family of planes and the (211) surface normal be less than the Bragg angle for at least one set of planes within the family: $\theta_{(hkl)-(211)} < \theta_{Bragg}$.

For completeness, the penetration depth of the x-rays should be taken into account. In CdTe, of stoichiometric perfect density 5.861g/cm^3, x-rays of 1.54 Å wavelength (8052 eV) will diminish in intensity exponentially with propagation distance, with a characteristic decay distance of ~7.0 μm [73]. Thus, when measuring a typical Bragg reflection, the signal obtained will be most heavily influenced by approximately the outermost 3.5 μm of material.

Another issue which arises is practice, is the influence of crystal defects on the observed position and width of diffraction peaks. Several contributions from crystal distortions will be considered below; one important contribution comes from the strain and tilt introduced into a crystal by the presence of dislocations. In this thesis, dislocations in the analyzed thin films, with some threading character, are conjectured to be the dominant XRD peak broadening mechanism. The threading character of a dislocation is quantified by the extent to which its Burgers vector is parallel to its dislocation line within the volume of the crystal; a pure threading dislocation is shown schematically below (see Figure 10).

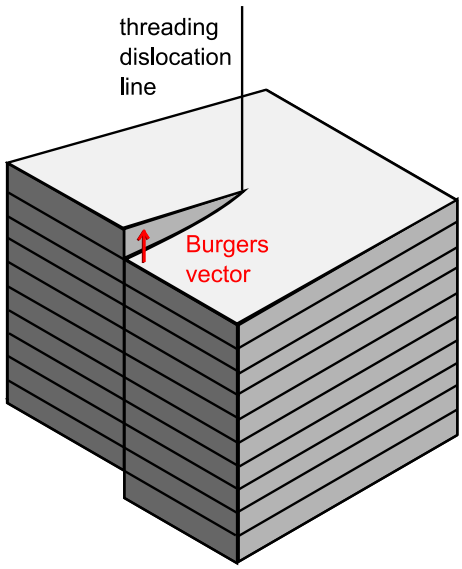

Figure 10 The distortion in the volume surrounding a pure threading dislocation is illustrated schematically, with dislocation line and Burgers vector parallel.

Various broadening contributions result in the angular Bragg condition being smeared-out into a distribution surrounding the ideal Bragg condition in angle. The intensity profile for a Bragg peak obtained in a symmetric rocking curve measurement is expected to be a convolution of a Gaussian component (Equation 28), and a Cauchy or Lorentzian (Equation 30) component [74]. The combination is known as the Voigt profile. The two functional forms arise from different broadening mechanisms: (1) Cauchy Lorentz related to state lifetime and resonance conditions; and (2) the Gaussian as a model for random error distribution about the mean measured value. The Gaussian function is given below, with full width at half maximum (FWHM) equal to β_{Gauss} :

$$I(\theta) = I(\theta_0) \cdot e^{-4 \cdot \ln(2) \cdot \frac{(\theta - \theta_0)^2}{\beta_{Gauss}^2}}$$

Equation 28

If several Gaussian functions are convolved together, the result is another Gaussian, with wider resultant width, given by the addition of the component widths in quadrature as follows:

$$\beta_{Gauss}{}^{2} = \beta_{Gauss-1}{}^{2} + \beta_{Gauss-2}{}^{2} + \beta_{Gauss-3}{}^{2} + \ldots$$

Equation 29

The Cauchy Lorentz function is given below, with characteristic width β_{Cauchy} :

$$I(\theta) = I(\theta_0) \cdot \frac{1}{\frac{\beta_{Cauchy}{}^{2}}{4} + (\theta - \theta_0)^2}$$

Equation 30

If several Cauchy Lorentz functions are convoluted together, the result is another Cauchy Lorentz function, with wider width, given by the usual addition of the component widths [74] :

$$\beta_{Cauchy} = \beta_{Cauchy-1} + \beta_{Cauchy-2} + \beta_{Cauchy-3} + \ldots$$

Equation 31

In general, the Voigt broadening mechanisms present in a general XRD rocking curve data set are related to the sample under investigation, as well as the instrument itself. In the case of CdTe/Si, it is assumed in the literature that the broadening can be

estimated from all Gaussian-type component contributions [75]. This view neglects the Cauchy Lorentzian shape contribution, but facilitates considering the net effect of multiple broadening contributions in a straight-forward, yet an approximate, fashion. Within that approximation, the total width of a given XRD rocking curve data set takes the form of a sum in quadrature over components due to, in order: intrinsic source, instrumental-filtering, sample thickness, sample curvature, sample low-angle grain structure, and sample strain fields due to dislocations:

$$\beta^2 = \beta_0{}^2 + \beta_i^2 + \beta_h{}^2 + \beta_r{}^2 + \beta_\alpha{}^2 + \beta_\varepsilon{}^2$$

Equation 32

These components are listed in the table below, for ease of reference:

β ***rocking curve width contributions***	***Description***	***Estimated value for CdTe/Si with XRD system of this thesis.***
$\sqrt{\beta_0{}^2 + \beta_i^2}$	Intrinsic source plus Instrumental-filtering	14″
β_h	Sample thickness	$\beta \approx \frac{16.97}{h}$; [for h in μm]
β_r	Sample curvature	7″
β_α	Sample low-angle grains	$\beta_\alpha{}^2 \approx 2 \cdot \pi \cdot (\ln 2) \cdot b^2 \cdot D$
β_ε	Sample dislocation strain fields	$\beta_\varepsilon{}^2 = 0.090 \cdot b^2 \cdot D \cdot \left\lvert \ln\left(2 \times 10^{-9} \cdot \sqrt{D}\right) \right\rvert \cdot \tan^2 \theta_{hkl}$

Table 4 Approximate factoring of XRD rocking curve FWHM broadening contributions, under the assumption that all factors are purely Gaussian. Note: 1” = 1 arcsec.

In the case of a 5 μm thick epilayer of CdTe on Si, the estimated contributions will take the form [75]:

$$\beta^2 = (14.9)^2 + \beta_\alpha{}^2 + \beta_\varepsilon{}^2 \qquad \left[\text{Arcsec}^2\right]$$

Equation 33

In this thesis, it can be safely assumed that the rocking curve peak data broadening can be attributed primarily to the sample itself, through the two right-most contributions in Equation 33 (due in part to the large total widths observed experimentally). The first of those two arises due to the relative tilt of microscopic domains within the crystal; which can exist only in the presence of extended defects; namely surfaces or dislocations. If the tilt distribution is assumed to be Gaussian (denoted by P), and strongly peaked in comparison with π radians, then the following expression describes the mean angular deviation, or disorientation, of the film [76].

$$\left\langle |\phi - \eta| \right\rangle = \frac{\int_{-\pi}^{\pi}\int_{-\pi}^{\pi} |\phi-\eta| \cdot P(\phi,\eta) \cdot d\phi \cdot d\eta}{\int_{-\pi}^{\pi}\int_{-\pi}^{\pi} P(\phi,\eta) \cdot d\phi \cdot d\eta} \approx \frac{\int_{-\infty}^{\infty}\int_{-\infty}^{\infty} |\phi-\eta| \cdot P(\phi,\eta) \cdot d\phi \cdot d\eta}{\int_{-\infty}^{\infty}\int_{-\infty}^{\infty} P(\phi,\eta) \cdot d\phi \cdot d\eta}$$

Equation 34

This approximate expression has been evaluated to the following result, in the case of a Gaussian distribution [77]:

$$\left\langle \left| \phi - \eta \right| \right\rangle = \frac{\beta_\alpha}{\sqrt{2 \cdot \pi \cdot \ln(2)}}$$

Equation 35

Assuming dislocations in the analyzed sample volume of Burgers vector, $\vec{b}$, arranged randomly, with area-density D (in m^{-2}), the following expression can also be obtained [76]:

$$\left\langle \left| \phi - \eta \right| \right\rangle \approx |b| \cdot \sqrt{D}$$

Equation 36

Setting Equation 35 equal to Equation 36 then gives an estimate for the rocking curve broadening contribution, β_α, due to dislocations introducing tilt into a given sample:

$$\beta_\alpha{}^2 \approx 2 \cdot \pi \cdot (\ln 2) \cdot b^2 \cdot D$$

Equation 37

Where b is the magnitude of the dislocations' Burgers vectors and D is the area-density D (in m^{-2}) of dislocations. This result is included in Table 4 for reference.

The contribution to broadening due to strain around dislocations in the film can be obtained from the following relation, assuming contribution from a random array of threading dislocations, of area-density D, each of Burgers vector b [76]:

$$\beta_{\varepsilon}^{\ 2} = 0.090 \cdot b^2 \cdot D \cdot \left| \ln\left(2 \times 10^{-9} \cdot \sqrt{D}\right) \right| \cdot \tan^2 \theta_{hkl}$$

Equation 38

Thus, under the assumptions that the total broadening of a given XRD rocking curve data set is due only to the presence of mosaic tilt (due to dislocations), and strain field effects only from threading dislocations, each with Burgers vector b, and that the dislocation network is random, one obtains the following transcendental equation relating the observed total peak width, β_{hkl}, to the dislocation density, D (in m^{-2}):

$$\beta_{hkl}^{\ 2} = b^2 \cdot D \cdot \left((0.090) \cdot \left| \ln\left(2 \times 10^{-9} \cdot \sqrt{D}\right) \right| \cdot \tan^2 \theta_{hkl} + 2 \cdot \pi \cdot \ln 2 \right)$$

Equation 39

Given values of β_{hkl}, θ_{hkl}, and b, this equation can be solved graphically for D, when D is high. When D is not high, Equation 33, Equation 37, and Equation 38 can be solved for the density. For example, using (422) of CdTe and b=0.458nm, one can manually find tens of solutions for different β_{422} magnitudes, to generate the plot and fit shown below (see Figure 11). The plot, and approximately quadratic trend, can be employed as a theoretical threading dislocation density estimator in CdTe epilayers on silicon; without graphically solving the equations above. The result of which is given below, with β_{422} in arcsec and D in cm^{-2}. It should be kept in mind that for low rocking curve peak widths, the expression below is not expected to be applicable.

$$D \approx 2470 \cdot \left(\beta_{422}\right)^2$$

Equation 40

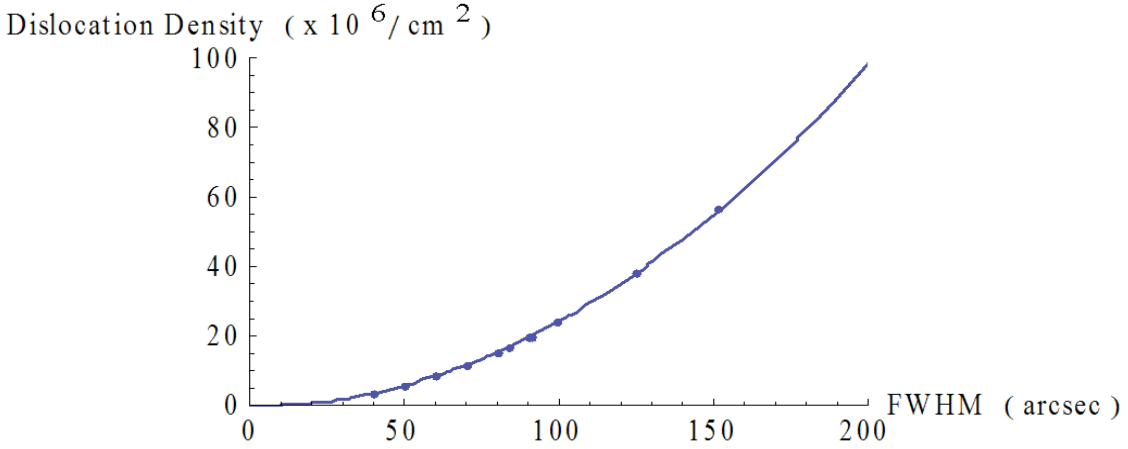

Figure 11 The dislocation density in CdTe theoretically contributes to the XRD rocking curve broadening according to the trend indicated above. The data points were obtained from solving for the dislocation density graphically, using Equation 33, Equation 37, and Equation 38.

In this thesis the XRD system utilized was a Bruker AXS Diffraktometer D8 model number 7KP2025-2DR19-0-Z high resolution single crystal X-Ray Diffraction (XRD) system, employing a Ge(220) four-bounce beam filter, vertical spatial filtering slits, and Goebel mirror before the sample, to condition the Cu $K_{\alpha\text{-}1}$ x-ray beam (see Figure 12). Rocking curves (scanning ω) were performed with this system, with x-ray tube under 40kV and 40mA operating conditions, to quantify the crystallinity of thin CdTe films on silicon substrates. The actual system also possesses a 3-bounce filter option for detection; but this feature was not utilized in the results reported in this thesis.

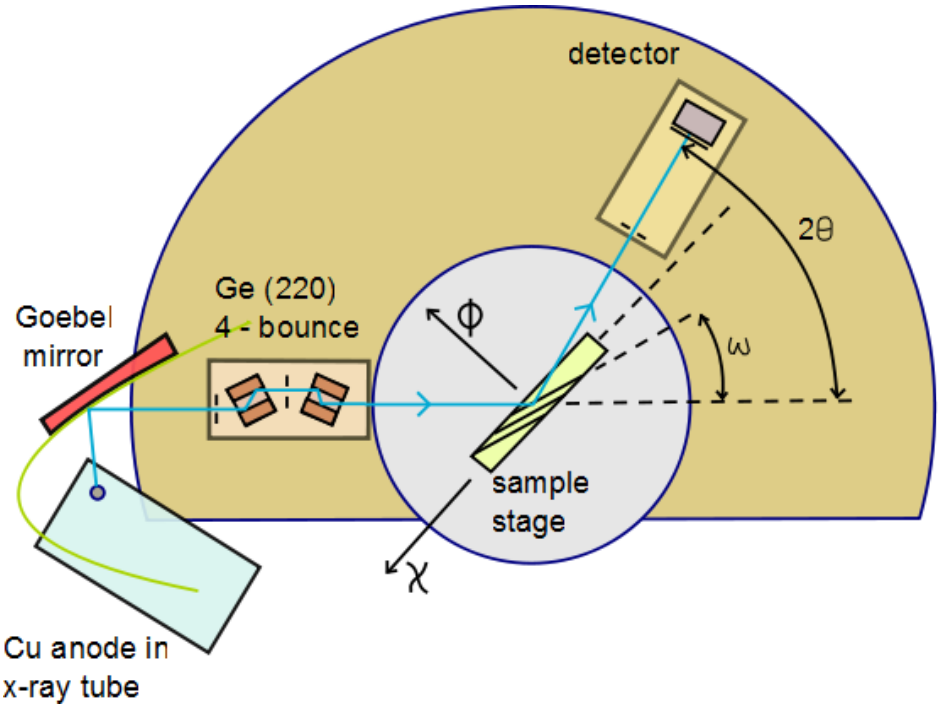

Figure 12 High resolution x-ray diffraction system. The blue line denotes the path of Cu $K_{\alpha-1}$ x-rays as they are filtered, diffracted from atomic planes within the sample, filtered again, and finally detected. The actual system also has a 3-bounce filter option at the detector.

2.5 X-Ray Photoelectron Spectroscopy

2.5.1 Introduction

The photoelectric effect was first discovered in 1887 by Heinrich Hertz; and its application to x-rays was developed first in Ernest Rutherford's lab in the early 1900's [78]. The basic picture of the photoelectric effect is a single quantum of electromagnetic field absorbed by an atom in a solid; and subsequently liberating one of its electrons from the solid. The understanding of the phenomena earned Albert Einstein the Nobel Prize in Physics [79].

2.5.2 Photoemission

The photoemission process can be described approximately by the following scenario: (1) a photon is incident upon an atom in a material, (2) the atom's electron cloud remains unchanged except for the ejection of one electron, and (3) the electron exits the material. In the case of an x-ray photon, the incident energy is sufficient to eject a core electron, characteristic of the emitting atom. If the incident x-ray photon has an energy of 1486.6eV, then it can be assumed to better than 1 part in 1000 that all the kinetic energy will be taken by the ejected photoelectron, due to the mass difference between an electron and typical nuclei[6]. In the technique of x-ray photoelectron spectroscopy (XPS), the incident x-ray photon energy is known, and the ejected photoelectron kinetic energy is measured; thus the binding energy of the photoelectron to the ejecting atom before ejection can be deduced through the assumption of the following energy conservation law:

$$E = h \cdot \nu = E_B + E_K + \phi$$

Equation 41

where E is the total energy, $h \cdot \nu$ is the x-ray photon energy, E_B is the binding energy, and E_K is the kinetic energy of the ejected photoelectron, and ϕ is the work function of the

[6] In addition, a typical incoming XPS photon of energy ~1500eV does not usually induce desorption of the surface atoms of the material under inverstigation; despite the typical surface binding energy of a surface atom being only ~2-5eV.

material in which the ejecting atom resides (this is the energy difference between the Fermi energy in the material and the vacuum energy level). The lifetime, τ_{hole}, of the remaining core hole in the ejecting atom, is related to the uncertainty of the kinetic energy of the photoelectron, $\Delta E_{photoelectron}$, via the uncertainty principle, as follows:

$$\tau_{hole} = \frac{\hbar}{\Delta E_{photoelectron}}$$

Equation 42

where $\hbar$ is the reduced Planck's constant (1.05×10^{-34} J*sec). This uncertainty results in a broadening of measured binding energy determinations, such that an ensemble statistical collection of such measurements will follow a Cauchy Lorentzian distribution (as defined in the XRD section of this thesis). A typical value for the core hole lifetime after a photoelectron is ejected from a Ag 3d state is 10^{-14} to 10^{-15} seconds [78]; which corresponds to an energy width of 0.07 to 0.7eV; whereas a typical measured value of the width of the Cd $3d_{5/2}$ core level in binding energy is ~1eV [80]. Thus, fitting data curves of photoelectron intensity versus calculated binding energy will typically necessitate a Cauchy Lorentzian shape component in addition to the typical random Gaussian shape.

The ejecting atom in the material is, in general, not electrically neutral, as it may be engaged in asymmetric bonding to its neighboring atoms in the material, whereby there is a net transfer or redistribution of electron density between the bonding atoms (of course this is not generally expected for pure elemental materials). The observed kinetic energy of the photoelectron, will thus, depend on its neighboring atoms in the material. If one assumes that all charge transfer of the valence electrons in forming bonds occurs on

shells with sizes determined by the radius of the atoms involved, then the deduced binding energy of the electron before ejection can be described as follows [78]:

$$E_B^{(i)} = E_0^{(i)} + k \cdot q^{(i)} + \sum_{j \neq i} \frac{q^{(j)}}{r_{ij}}$$

Equation 43

where $E_0^{(i)}$ is the binding energy of a free atom, $k \cdot q^{(i)}$ is the effective charge residing on the ejecting atom, and the sum runs over the charges residing on the neighboring atoms, indexed by j, at separations r_{ij} from the ejecting atom. Considering a single atom with two distinct surrounding material atoms, or chemical environments, one can consider the difference in deduced binding energies for the two surroundings using Equation 43, as follows:

$$E_B^{(1)} - E_B^{(2)} = E_0^{(1)} - E_0^{(2)} + k \cdot \left(q^{(1)} - q^{(2)} \right) + \sum_{j \neq 1} \frac{q^{(j)}}{r_{ij}} - \sum_{j \neq 2} \frac{q^{(j)}}{r_{ij}}$$

Equation 44

where (1) and (2) denote the two different surrounding chemical environments of the atom. Further, considering Equation 44 in light of Equation 41, it is clear that a difference in work function could exist between (1) and (2) in the event that (1) and (2) originate from two different materials. Partly for this reason, it is necessary to use a reference photoelectron line originating from the sample, in order to calibrate the true calculated binding energies of ejected photoelectrons (in this thesis C1s photoelectrons from adventitious carbon are employed for that purpose).

Consider an x-ray beam impinging on a material surface. The beam will penetrate a characteristic distance determined by the amplitude attenuation rate of the x-rays by absorption and scattering of the x-rays. The characteristic distance of interest is the inelastic mean free path (IMFP) of the x-rays; which depends upon the photon energy and the material in which the photons propagate. In CdTe, of stoichiometric perfect density 5.861g/cm^3, x-rays of photon energy ~1486.6eV (0.83nm wavelength) will diminish in intensity exponentially with propagation distance, with a characteristic decay distance of ~0.56 μm [73]. In the process of attenuation, the x-ray beam will excite many electrical transitions in the material; in particular, the beam is generally capable of ejecting core electrons from the atoms in the material, in proportion to a cross-section, σ, which is orbital and atom dependent. As the wavelength of the x-rays is comparable to typical interatomic bond lengths in solids, care should be taken when comparing photoelectron emission intensities between two different samples (or the same sample in different orientations with respect to the incoming x-ray beam). In addition, the ejected photoelectrons also have a typical wavelength which is less, but comparable to the interatomic spacing in materials; thus care should be taken when comparing different angular positions of photoelectron collection with respect to the x-ray bombarded material. Diffraction effects have been observed in XPS intensities by several research groups; where significant variation in the intensities of photoelectron signals is seen [81, 82, 83, 84, 85] with as much as 47% variation in the intensity, depending on the orientation of the sample. In addition, the basic photoelectron generation process cross-section has an angular intensity dependence with respect to the incoming x-ray beam, even in a randomly oriented gas of atoms or molecules. In such a gas, the dependence is

given by the following equation for the differential cross section, where θ is the angle between the ejected photoelectron propagation and the un-polarized x-ray photon propagation [86]:

$$\frac{d\sigma}{d\Omega} = \frac{\sigma}{4\cdot\pi}\cdot\left(1-\frac{\beta}{4}\cdot\left(3\cdot\cos^2(\theta)-1\right)\right)$$

Equation 45

where β is an asymmetry parameter associated with a core atomic orbital of a gas atom, and σ is the total photoionization cross-section (integrated over all solid angle), with values normalized with respect to C1s given by Scofield [87]. It follows that the above contribution to the angular dependence of the cross-section vanishes under the following condition on θ:

$$\theta = \cos^{-1}\left(\sqrt{\frac{1}{3}}\right) \approx 54.74 \qquad \text{[degrees]}$$

Equation 46

The XPS system utilized in this thesis is fixed at precisely this angle, known as the "magic angle".

Another key feature of the detection of the photoemission process is the average distance an ejected electron will travel in a host material before loosing energy through an inelastic collision (referred to as the inelastic mean free path IMFP for electrons). The IMFP is dependent on the kinetic energy of the electron [88] and the nature of the host material; thus, photoelectrons arising from distinct core states (even from the same type

of atom, in the same material) will in general have markedly different IMFP's. In the materials of interest in this thesis (for example, CdTe), the IMFP for electrons is of order 1nm to 3nm in the kinetic energy range of ~200eV to ~1500eV, respectively [89]. This is much smaller than the typical penetration depth of the impinging x-ray beam; thus the XPS technique is very surface sensitive for CdTe (and in general) [90].

2.5.3 System

The XPS system utilized in this thesis was manufactured by Surface Science Instruments, and uses a SSX-100 spectrometer. The system operates in ultra high vacuum, in order that the photoelectrons do not collide with gas molecules before reaching the detector; and also so that sample surfaces being analyzed stay clean (see MBE section on UHV). The system is schematically depicted below.

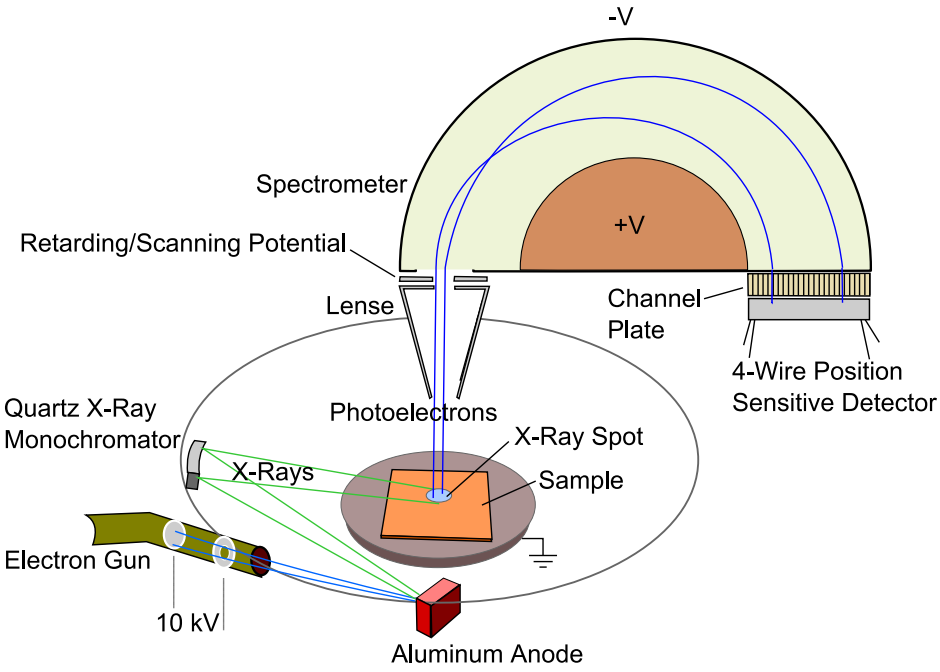

Figure 13 Schematic of the XPS system utilized in this thesis. The x-ray spot size is typically ~300 to ~600μm on the sample surface.

The essential elements are as follows: an electron gun operating at 10kV accelerates electrons onto a water-cooled Al anode, which emits K_α x-rays of intrinsic energy spread ~0.8eV to 1eV [91, 92] at central energy ~1486.6eV, which are focused by a quartz crystal monochromator onto the sample surface within a spot of diameter ~600μm and energy spread ~0.4eV [91], which ejects photoelectrons from the sample, some of which pass through the lense and spectrometer to reach the position sensitive detector, where they contribute to the recorded signal of intensity at a particular kinetic energy. The aluminum anode, quartz monochromator, and x-ray spot on the sample surface, all coincide with the Rowland circle (not shown) [91]. As mentioned previously, the angle between the in coming x-rays to the sample, and the out going photoelectrons headed toward the spectrometer, is fixed at the magic angle of 54.74^o. The angle between the sample normal and spectrometer is 53^o, dubbed the "take-off angle". During

operation the lense of the spectrometer applies a retarding potential to the incoming photoelectrons; allowing the spectrometer to scan different kinetic energy regions of the photoelectron spectrum at the 4-wire detector. Care was taken to always orient samples at the same azimuthal angle, in order to avoid the influence of diffraction on the observed intensity ratios from measurement to measurement.

2.5.4 Data fitting

A typical data set consists of photoelectron intensity as a function of binding energy. The data is generally characterized as having several strong peaks corresponding to core energy levels in the atoms analyzed, added to a more diffuse background intensity created mainly by different mechanisms of energy loss of ejected photoelectrons before they leave the sample under study. The core peaks can be fitted to a Voigt profile, and the background to a Shirley-type function within a reasonably narrow binding energy range. The total energy width of the strong core level peaks can be approximated by adding the dominant contributions to broadening in quadrature:

$$\Delta E^2 = \Delta E_{atom}{}^2 + \Delta E_{x-ray}{}^2 + \Delta E_{spectometer}{}^2$$

Equation 47

where ΔE_{atom} arises from the core hole lifetime (~0.7eV), ΔE_{x-ray} arises from the x-ray beam (~0.4eV), and $\Delta E_{spectometer}$ arises from the spectrometer (~0.6eV for $Te3d_{5/2}$

observed with the system used in this thesis). Thus the typical total width of an observed core state is expected to be ~1eV.

The intensity of photoelectrons originating from a particular core level state in a material, and detected in the XPS system, can be expressed with an infinitesimal relation as follows [93]:

$$dI_i = A \cdot I_p(z) \cdot N_i(z) \cdot S_i(z) \cdot e^{\frac{-z}{\lambda_i \cdot \cos(\theta)}} \cdot dz$$

Equation 48

where the emitting atom and orbital type is indicated by the subscript "i", the emitting atom is located a distance z from the material surface, A is the area of the x-ray spot coinciding with the spectrometer focus on the sample surface, I_p is the intensity of the x-ray beam within the analyzed volume, N_i is the number of atoms of interest per volume, S_i is the sensitivity factor of the atomic orbital of interest, and $\lambda_i \cdot \cos(\theta)$ is the IMFP of the photoelectron multiplied by the cosine of the take-off angle (53^o in the system used in this thesis). The sensitivity factor contains within it the total cross-section for an orbital, at the spectrometer lense (Equation 45), as well as the spectrometer and detector collection efficiencies; and is generally assumed to be depth-independent (z-independent). The IMFP of the photoelectrons comes into play in their escape from the sample. An idealized schematic of the photoelectron generation and escape from the vicinity of the sample surface toward the spectrometer is shown below in Figure 14. In practice it is safe to assume that I_p has no z-dependence, because the IMFP for x-rays is

very large compared to the photoelectrons. As a side note, it is also safe to assume that ~1V to 10V of fixed charge accumulation on the surface due to the photoemission process will have an influence of less than ~ 1 part in 10^3 on the observed signal.

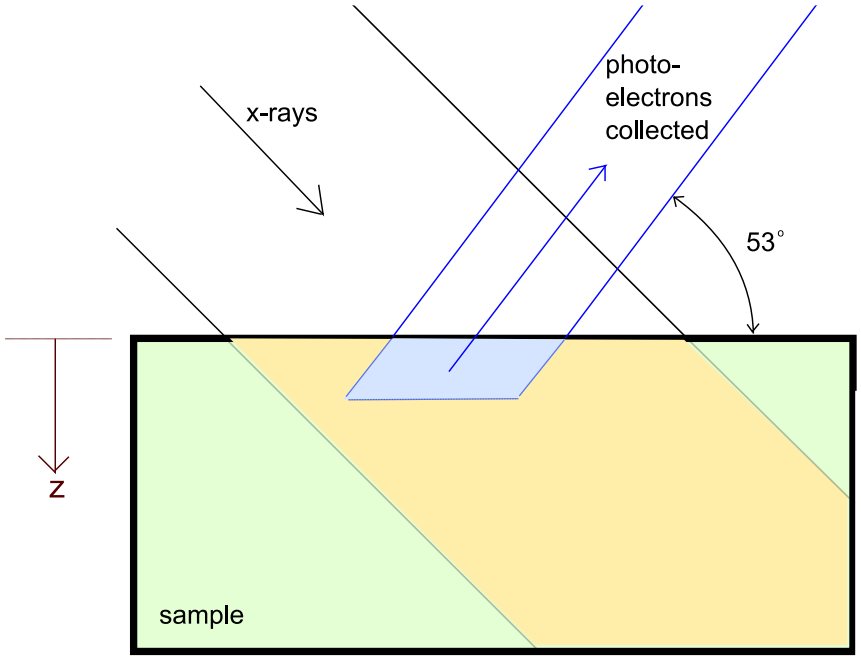

Figure 14 Schematic cross-section of the x-ray generation of photoelectrons in a sample volume, indicating the volume of generated photoelectrons which eventually may be analyzed by the spectrometer.

The total intensity observed by the detector at a particular binding energy will be the integral of Equation 48 with respect to z. In practice such integrals can be measured, however, in the absence of exact knowledge of several factors in the integral, one generally considers ratios of integrals for different core-level peaks; so that all unknown factors cancel. An example ratio would take the form here:

$$\frac{I_a}{I_b} = \frac{\sigma_a \cdot \int_0^{\infty} N_a(z) \cdot e^{\frac{-z}{\lambda_a \cdot \cos(\theta)}} \cdot dz}{\sigma_b \cdot \int_0^{\infty} N_b(z) \cdot e^{\frac{-z}{\lambda_b \cdot \cos(\theta)}} \cdot dz}$$

Equation 49

where "a" and "b" denote two different core levels, and σ denotes the cross-section for photoemission. This expression can also be experimentally determined by integrating measured photoelectron intensity data in two different regions of a spectrum, after subtracting background contributions, and correcting for the sensitivity of the spectrometer as a function of photoelectron kinetic energy. In this thesis, the background is assumed to follow the Shirley form [94] given here:

$$I_{Shirley}(E_B) = I_{E_{lower}} + B \cdot \int_{E_{lower}}^{E_B} I(E_B') dE_B'$$

Equation 50

where $I_{E_{lower}}$ is the photoelectron intensity at the lower limit of the fitting region considered (typically close in energy to a core level of interest), B is a constant for a given integral, and the integral adds infinitesimal intensity contributions from core levels. Fitting raw data with Shirley-type background and Voigt profiles for a given core level allows one to subtract off the background and compare only the integrals of different core

levels (using Equation 49). Such comparison can yield the alloy ratio of the sample surface region [93].

In this thesis a particular profile for N(z) is assumed; dubbed the "three layer model", which is depicted below:

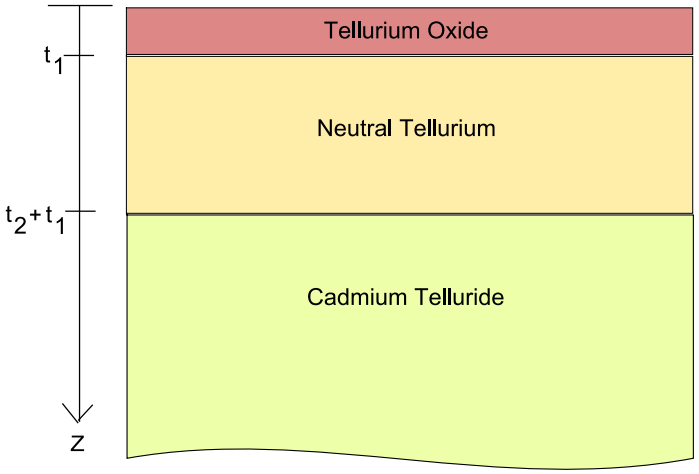

Figure 15 Three-layer model assumed in this thesis for XPS data fitting to determine distances t_1 and t_2.

This model can be used with intensity data from peak fitting of atoms in the three layers, to determine the thickness of the layers [95].

2.6 Molecular Beam Epitaxy

2.6.1 Introduction

Many techniques have been developed for crystal fabrication from non-crystalline high purity source material. Some techniques can be used to form large volume crystals, or bulk crystals; for example the Czochralski, Traveling-Heater, Solid State Recrystallization, Vertical Gradient Freeze, Chemical Vapor Transport, and Physical Vapor Transport methods; which can make use of such novel conceptions as growth in microgravity [96]. Other techniques are geared at forming thin films, from several angstroms in thickness, to tens of micrometers; for example: chemical vapor deposition (CVD), liquid phase epitaxy (LPE), metal-organic chemical vapor deposition (MOCVD), and molecular beam epitaxy (MBE). Of these techniques, the vapor-phase techniques are preferable due to ease of doped multilayer formation with abrupt interfaces; which is helpful in the formation of multi-color detectors and superlattice structures. Also, in the case of MBE versus LPE; MBE allows for a lower growth temperature, allowing better stoichiometry control and fewer Hg vacancies [97]. MOCVD requires careful control to achieve laminar gas flows, without significant reactant depletion in the carrier gas as it passes over the growing substrate. Thus, between MOCVD and MBE, MBE allows more naturally for deposition over large areas of a substrate. In addition, MBE typically allows for a lower substrate temperature during growth (thus limiting diffusion of impurities from the substrate into the growing epilayer; and limiting interdiffusion of deposited layers).

MBE systems generally consist of an ultra high vacuum (UHV) chamber, high purity solid or gaseous source material (up to "7-nine" or 99.99999% purity), a substrate holder, heaters for solid source materials and for the substrate, and cooled walls (either by water or liquid nitrogen) to reduce the pressure in the vicinity of the target crystal substrate surface (in particular, to reduce the probability of reflection of flux from the chamber walls to the substrate). The source material is heated to a temperature at which a large and steady amount of material evaporates or sublimates into the vacuum chamber; for CdTe this is typically 500 to 600^{o}C, resulting in a pressure at the top of the cell of ~10^{-5}Torr. The solid material is contained, generally, in a ceramic (pyrolytic boron nitride (PBN)) or graphite crucible, which collimates the flux of evaporating or sublimating material. If the cell is completely full, the collimated flux, J, follows the angular distribution given below; where θ is the angle with respect to the axis of the crucible, A is the crucible orifice area in cm^2, P is the cell pressure in Torr, L is the distance between the cell orifice and the sample-substrate in cm, M is the atomic or molecular mass, and T is the cell temperature in K. If the material level within the cell is significantly below the orifice opening, then the outgoing flux distribution will be more collimated, tending to be peaked in the forward direction; which typically holds, to some extent, in MBE effusion sources.

$$J = 1.12 \cdot 10^{22} \frac{A \cdot P}{L^2 \sqrt{M \cdot T}} \cos(\theta)$$

Equation 51

In the case of heated CdTe in UHV, the sublimating flux is fairly congruent (see Figure 16), consisting of $Cd + \frac{1}{2}Te_2$, where the partial pressures follow the functional form below, with “a” and “b” as parameters [98].

$$\log(P) = a - \frac{b}{T}$$

Equation 52

This expression can be recast into the more intuitive form below, in terms of a surface binding energy, E, and Boltzmann’s constant, k (equal to 1.38×10^{-23} J/K).

$$P = A \cdot e^{\frac{-E}{k \cdot T}}$$

Equation 53

The fairly congruent evaporation of CdTe enables MBE operators to use compound source material rather than elemental sources (Cd_{solid} and Te_{solid}) without reloading source material to the vacuum chamber before every deposition procedure.

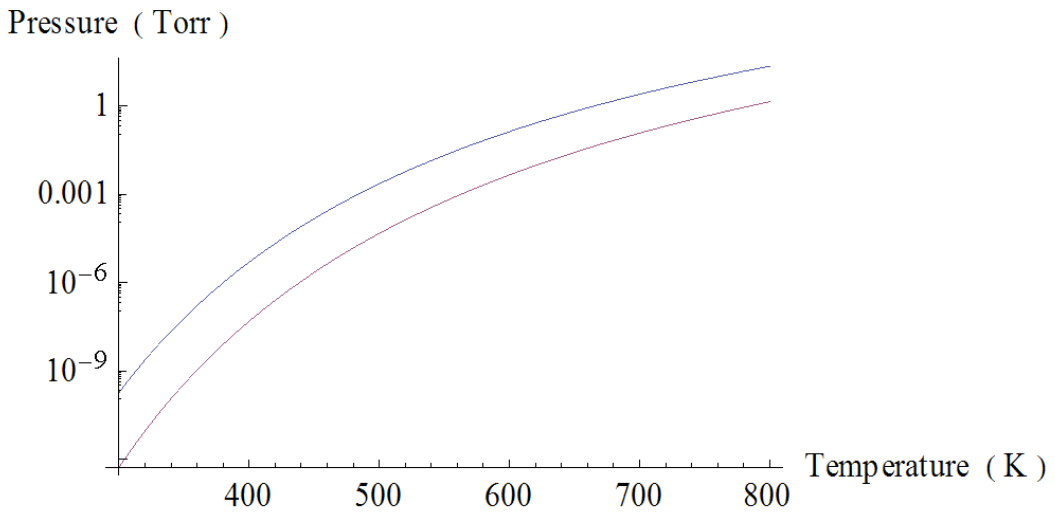

Figure 16 The vapor pressure components of CdTe in vacuum as a function of temperature are shown here. The upper blue curve is for Cd vapor, and the lower purple curve is for Te_2 . The plots were generated using the (a, b) values used for Cd and Te_2 of (5.12, 5317), and (4.72, 5960), respectively, after J.P. Faurie [98].

One of the great advantages of MBE is the ability to rapidly change the flux impinging on the substrate through the use of cell shutters. This is accomplished by heating several Knudsen effusion cells simultaneously, but selectively blocking their sublimating or evaporating outputs with mechanical shutters. This feature enables the rapid growth of a binary compound epilayer, such as ZnTe, by the technique of Migration Enhanced Epitaxy (MEE), whereby Zn and Te fluxes are alternately impinged on the sample surface with a short pause of no flux after each exposure.

With the proper choice of materials, flux, and substrate temperatures, one can easily grow a variety of single crystal films on different single crystal substrates. In particular, MBE has been established as a standard technique to grow HgCdTe thin films on CdZnTe, Si, GaAs, and Ge for subsequent IR detector fabrication.

The general physical picture of the MBE growth process involves the following features:

1) A UHV environment.
2) Temperature control of the deposition substrate, which is typically continually rotated to achieve higher time-averaged flux uniformity.
3) Incoming flux of material to the substrate surface from timed and coordinated exposures; where typically the incident flux on the sample surface is off axis from the sample normal, and the time-average is assumed fairly uniform over the sample surface area.
4) Weak bond formation of some flux constituents to the substrate into "physisorbed" states.
5) Strong bond formation of some flux constituents to the substrate into "chemisorbed" states.
6) Lateral migration of the flux constituents, and other surface species, which are bound to the substrate surface.
7) Desorption of surface species from physisorbed states.
8) Desorption of surface species from chemisorbed states.
9) Net accumulation or diminution of material on the substrate; generally dependent on flux quantity, type, substrate temperature, and surface chemical reactivity with flux constituents.

In the case of stepped substrate surfaces, the incoming flux molecules may preferentially be accumulated at the step edges on the surface, due to a higher effective bond coordination in these regions. If such a process dominates the accumulation of

incoming flux onto the substrate, then the growth is said to follow the step-flow growth mode.

2.6.2 Ultra High Vacuum (UHV) Environment

It was noted that one characteristic feature of MBE is a UHV environment. Such an environment is defined to be of pressure ~ 10^{-9} to 10^{-11} Torr, which results in a very clean environment for the substrate and growing film. At standard temperature and pressure there are approximately 2.5×10^{19} molecules per cm^3 in the atmosphere, of which about 78% are N_2 and 21% are O_2. In contrast, under UHV conditions of 10^{-9} Torr, there are approximately 10^7 molecules per cm^3, which is roughly the pressure of interplanetary space [99]. The lower density of gas molecules, by 12 orders of magnitude, results in less surface contamination during MBE processes; both the growing surface and the flux beams encounter comparatively very low contamination during the time scale of an MBE process (several days). Under such conditions the gas molecules travel great distances before colliding with other gas molecules. The mean distance a gas molecule travels before such collision can be estimated by assuming all but one gas molecule are fixed in space, and considering the density and size of gas molecules. This treatment leads to the following formula for the mean free path length of gas molecules between collisions:

$$\lambda = \frac{1}{n \cdot \sigma}$$

Equation 54

where λ is the mean free path, n is the density of gas molecules, and σ is the cross section for collision. Assuming the gas molecules are all hard spheres, σ is geometrically related to the gas molecule cross-sectional area, and thus, given by πd^2. It should be noted that the mean free path scales inversely with gas molecule density, n. When the motion of the other gas molecules is taken into consideration, and using the ideal gas law to express n in terms of pressure, P, temperature, T, and Boltzmann's constant, k, one obtains the following equation[99].

$$\lambda = \frac{k \cdot T}{\sqrt{2} \cdot P \cdot \pi \cdot d^2}$$

Equation 55

This expression indicates that the mean free path scales inversely with the pressure, given fixed temperature. Thus in vacuum system applications, typically at room temperature, the pressure is a measure of possible background contamination. A rough estimate of d for an N_2 molecule is 0.376nm [99], and about 5% smaller for O_2, giving a λ of 65nm-70nm at 300K and one atmosphere of pressure (assuming only N_2 or O_2 in the gas). In contrast, at 10^{-9} Torr, the λ for the same N_2 or O_2 molecule is 50km-55km. Thus, in a typical MBE system ~1m in diameter, operating with a background pressure of UHV, one can expect that gas molecules travel ballistically. Applying this notion, one can reason that source material molecules evaporated or sublimated toward a substrate, can be approximated to only collide with other source molecules, or the vacuum chamber walls, before colliding with the substrate. This motivates the use of liquid nitrogen

cooling of the chamber surfaces in the field of view of the substrate, in order to increase the sticking probability for gas molecules impinging on those surfaces.

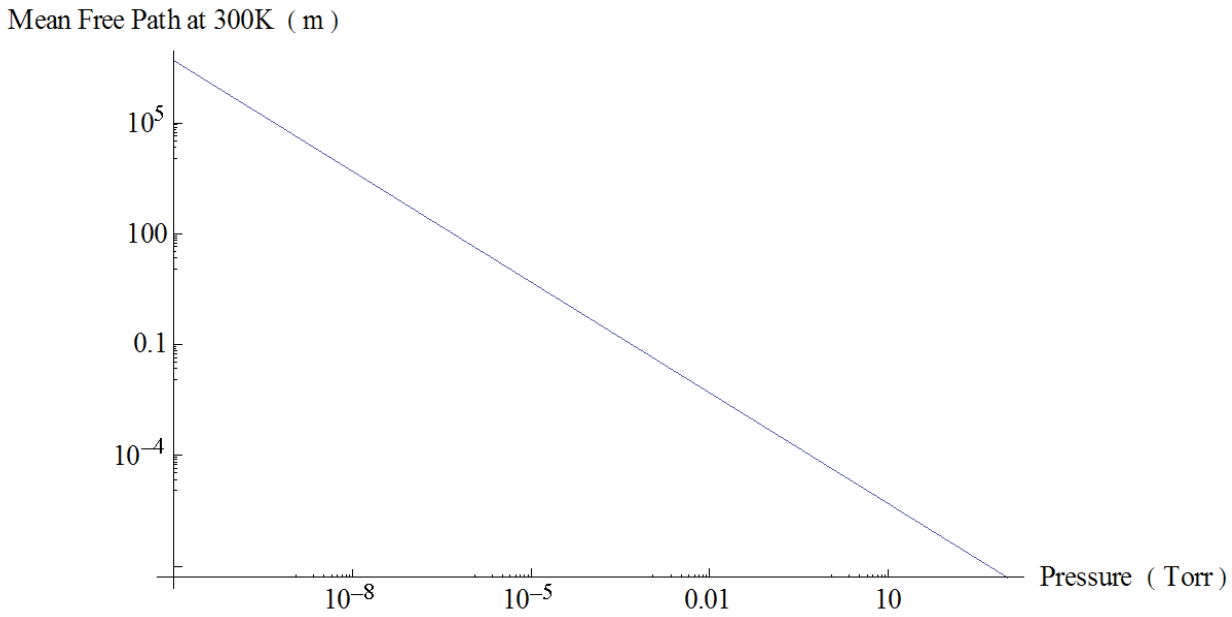

Figure 17 Here is shown a Log-Log plot of the mean free path of a N_2 molecule in a gas of N_2 near room temperature (300K), as a function of the pressure, calculated from Equation 55. The UHV environment commonly used in MBE systems is characterized by a pressure of ~10^{-10} Torr.

In the MBE system it is often useful to know the impingement rate of gas molecules on the substrate surface; either source molecules, or contamination molecules. This rate can be found from using the kinetic theory of gases to be:

$$J = \frac{n \cdot \overline{v}}{4}$$

Equation 56

where J is the number of molecules impinging per m^2*second, n is the density of the gas, and $\bar{v}$ is the mean velocity of a gas molecule, assumed to follow a Maxwell-Boltzmann distribution [99]. The flux expression can be recast in terms of the gas pressure as follows:

$$J = \frac{P}{\sqrt{2 \cdot \pi \cdot m \cdot k \cdot T}}$$

Equation 57

where P is the gas pressure, m is the mass of a gas molecule, k is Boltzmann's constant, and T is the temperature of the gas. Given that there are ~10^{15} atoms per cm^2 on a typical solid surface, we can use Equation 57 to calculate the minimum time needed to form one monolayer (ML) of deposit on the substrate from an over pressure of P, assuming all incident molecules stick and don't overlap. At a pressure of 10^{-6} Torr the time is about 2 seconds; and at 10^{-9} Torr the time is about 2000 seconds. A Log-Log plot of the time to form one ML versus pressure is shown in Figure 18.

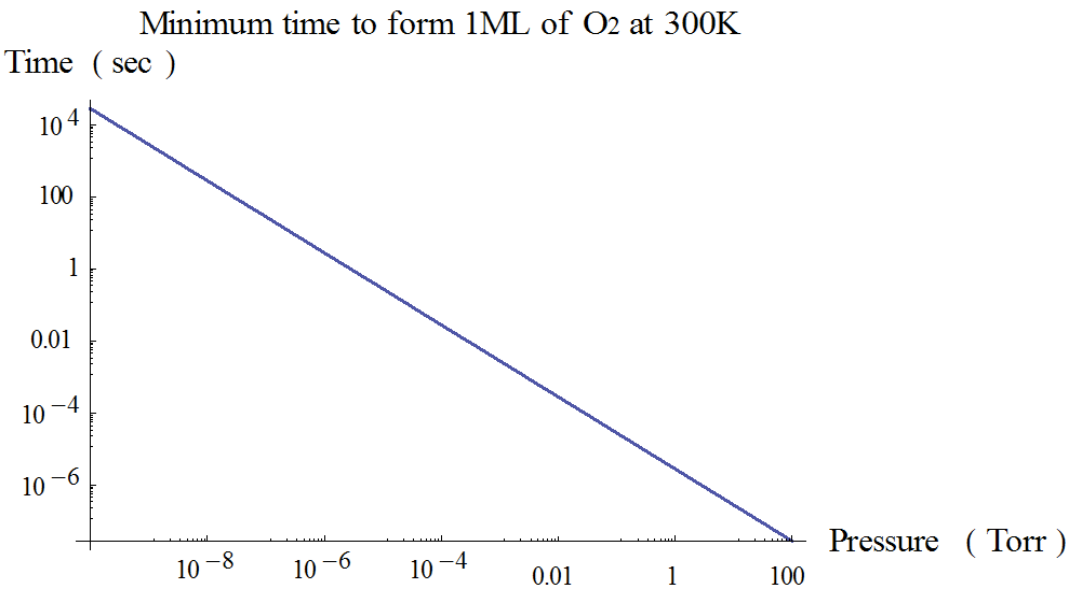

Figure 18 Log-Log plot of the minimum time needed to form one ML of deposit on a surface with an overpressure of P. The curve was calculated using Equation 57, assuming 10^{15} surface binding sites per cm^2, and gas molecules of O_2. In practice, the sticking probability is likely of order 0.1 [100], and thus extends the time for actual formation of a ML.

In practice, the substrate is usually heated to a temperature where one would expect less than unity sticking probability for incoming molecules; thus the typical practical time for the formation of a ML by MBE is longer than suggested by the analysis above, by about a factor of 10 for O_2 [100].

2.6.3 Silicon Heating

The MBE system employed in this thesis was an ISA Riber Opus 45. Some key components of this system are shown schematically in cross-section in Figure 20. In this system the substrate is heated by a resistive element, which heats a PBN diffuser behind the sample, which subsequently heats the sample and sample holder radiatively. The

molybdenum sample holder used in this thesis is shown in Figure 19 below. Samples were held by gravity in the sample holder; and the sample holder was rotated in the plane of the holder during exposure to fluxes.

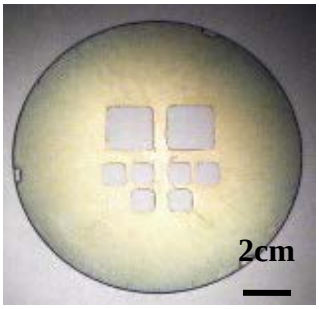

Figure 19 Growth-side view of the molybdenum sample holder employed for MBE growth reported in this thesis, with a thin film visible on the holder. The large openings accommodate 2x2cm^2 wafer pieces; and any un-occupied sample holder opening can be covered with a molybdenum blank. The color and pattern of the film indicates a reasonable flux uniformity across a given sample surface.

A computer controlled feedback loop is used to control the temperature reading of a K-type thermocouple located between the PBN diffuser and substrate; placed closer to the PBN. The location of the thermocouple junction results in the temperature reading during a typical growth procedure being on the order of 100^{o}C higher than the actual temperature of the growing surface on the substrate. A calibration was performed to correlate the measured thermocouple reading to the actual substrate temperature by connecting alloys of known melting points to the surface of 10×10 mm^2 pieces of silicon (380 μm thick and 30-70 Ωcm resistivity) in a molybdenum sample holder and observing their melting, observing the deoxidation of silicon (taken to occur at 850^{o}C substrate temperature), and by measuring the silicon surface temperature during heating and cooling with a pyrometer. The pyrometer employed was a Modline Plus 6000

manufactured by Ircon and operating at 2.0 to 2.6 μm through a Pyrex viewport window, with line-of-sight at an angle with respect to the silicon surface normal. The emissivity of silicon was taken to be 0.7 (converting to emissivity of 0.4 can be achieved by shifting the measured temperature values up by 18^{o}C). The results of the calibration are shown in Figure 21. The results have a significant amount of scatter, but provide a much more accurate estimate of the real surface temperature of silicon than the thermocouple reading. Fitting a line to the data from the melting points and deoxidation yields a calibration of sample temperature, T_s, versus setpoint thermocouple temperature, T_{tc}, both in ^{o}C, as follows:

$$T_s = 0.855T_{tc} - 58$$

Equation 58

This equation allowing the estimation of the real substrate surface temperature is important when considering comparing results with other researchers, and for calculating physical quantities, such as Boltzmann factors describing the growth process. All substrate temperatures quoted in this thesis were derived from thermocouple measurements with the above steady-state calibration (Equation 58).

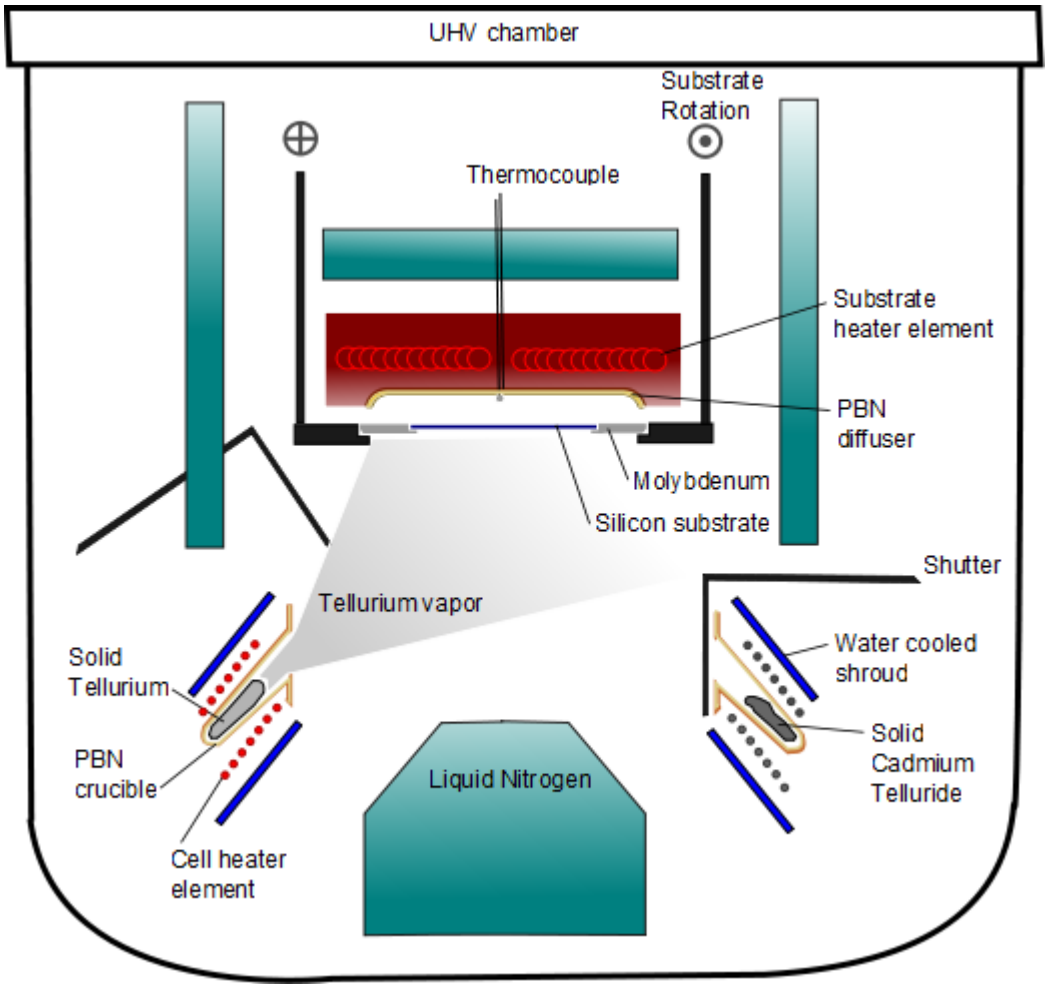

Figure 20 A schematic cross-section of the Riber Opus 45 MBE system is shown here with some key components labeled. A silicon wafer substrate is shown supported by gravity in a molybdenum sample holder; with thermocouple junction and heater near the backside of the silicon.

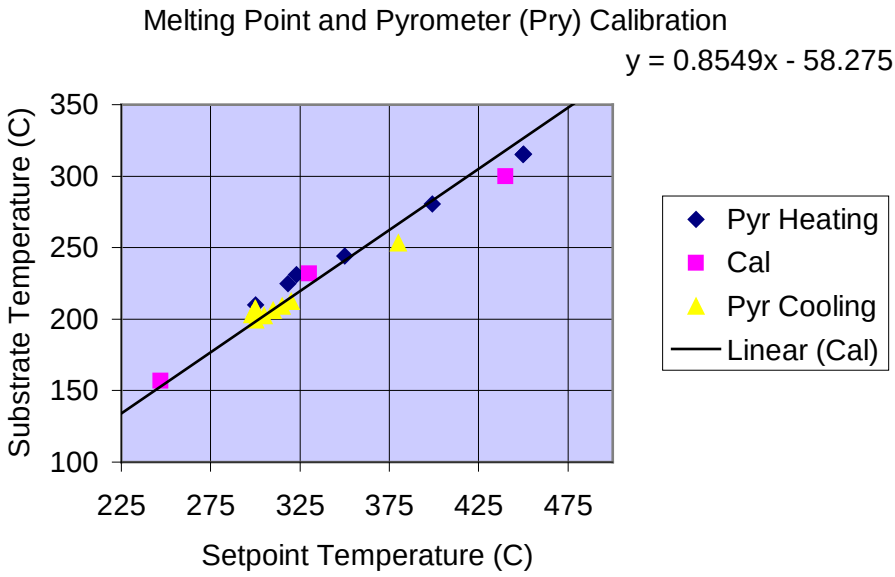

Figure 21 Temperature calibration of the Opus thermocouple reading versus silicon surface temperature. Known melting points were used for those points labeled "Cal", and other points refer to pyrometer measurements during silicon heating and cooling. The best fit line uses only the melting point data values, and the deoxidation of silicon.

In the above temperature calibration fit, sufficient time (10 minutes) was always allotted after changing the setpoint temperature, in order to allow the system to reach a steady state condition before measurements were recorded. During a given MBE procedure, however, often the system is not in a steady state; and further, it is not known a-priori whether a given silicon substrate will be higher or lower in temperature compared to the molybdenum sample holder, when out of the steady state conditions used for the temperature calibration mentioned earlier. When a procedure calls for a large increase in substrate temperature per time, it is possible that the silicon overshoots the molybdenum temperature as well as the thermocouple temperature by a significant amount. A one-dimensional radiative heat transfer model was performed in order to shed light on the situation of substrate heating, as detailed below.

In this radiative heat transfer model it is assumed that all heat transfer is through radiation in the vertical direction of Figure 20, from the heater to the molybdenum sample holder and to a silicon wafer substrate. No heat conduction was allowed in any direction; and no reflections between the heater and silicon or heater and molybdenum were allowed. The heater was modeled using Planck's law as a gray body with the appropriate uniform temperature adjusted to yield a reasonable steady-state temperature for the silicon. The emission of radiation by the silicon and molybdenum was taken to occur only downward, and modeled as two separate gray bodies. The formula used for the gray body monochromatic emissive power (in units of W/m^3) is as follows:

$$E_{gray}(\lambda,T)=\frac{2\cdot\pi\cdot h\cdot c^2}{\lambda^5(e^{h\cdot c/\lambda\cdot k\cdot T}-1)}\cdot\varepsilon$$

Equation 59

where h is Planck's constant (6.6×10^{-34} J*s), c is the speed of light in vacuum (3×10^8 m/s), λ is the wavelength of radiation in m, k is Boltzmann's constant (1.38×10^{-23} J/K), and ε is the emissivity of the gray body material surface. For a blackbody, the emissivity is unity. The background below the silicon and molybdenum was taken to be 77K.

Absorption in the silicon and molybdenum were first calculated based on empirical tabulated values of the absorption coefficient and reflectivity as a function of wavelength referenced from [101]. An infinite number of internal reflections were accounted for in the absorption, Abs, by using the formula below:

$$Abs(\lambda) = 1 - \frac{(1-R(\lambda))^2 e^{-\alpha(\lambda)\cdot t}}{1-R(\lambda)^2 e^{-2\cdot\alpha(\lambda)\cdot t}} - R(\lambda)\frac{1+(1-2\cdot R(\lambda))e^{-2\cdot\alpha(\lambda)\cdot t}}{1-R(\lambda)^2 e^{-2\cdot\alpha(\lambda)\cdot t}}$$

Equation 60

where R is the reflectivity, α is the absorption coefficient, and t is the thickness of the material. In Equation 60 the second term accounts for the transmitted radiation, and the third term accounts for the reflected radiation. The thickness of silicon was set to 0.380mm to represent a typical wafer used in MBE; and the thickness of molybdenum was set by the sample holder thickness: 1.524mm. The emissivity of silicon and molybdenum were both taken to be a constant value of 0.4. The absorption coefficient, α, governs the decay of electromagnetic wave intensity, I, with distance of propagation in the material ($I \propto e^{-\alpha\cdot z}$). At this point the temperature dependence of the emissivity, absorption coefficient, and reflectivity of silicon and molybdenum have been neglected; however, the temperature dependence of the absorption coefficient will be addressed in the following pages.

The absorption of the silicon and molybdenum at room temperature[7], as a function of wavelength are shown below in Figure 22.

[7] The data is derived from multiple references with the Handbook of Optical Constants Volume I. The majority of the original sources were located and confirmed to be room temperature measurements.

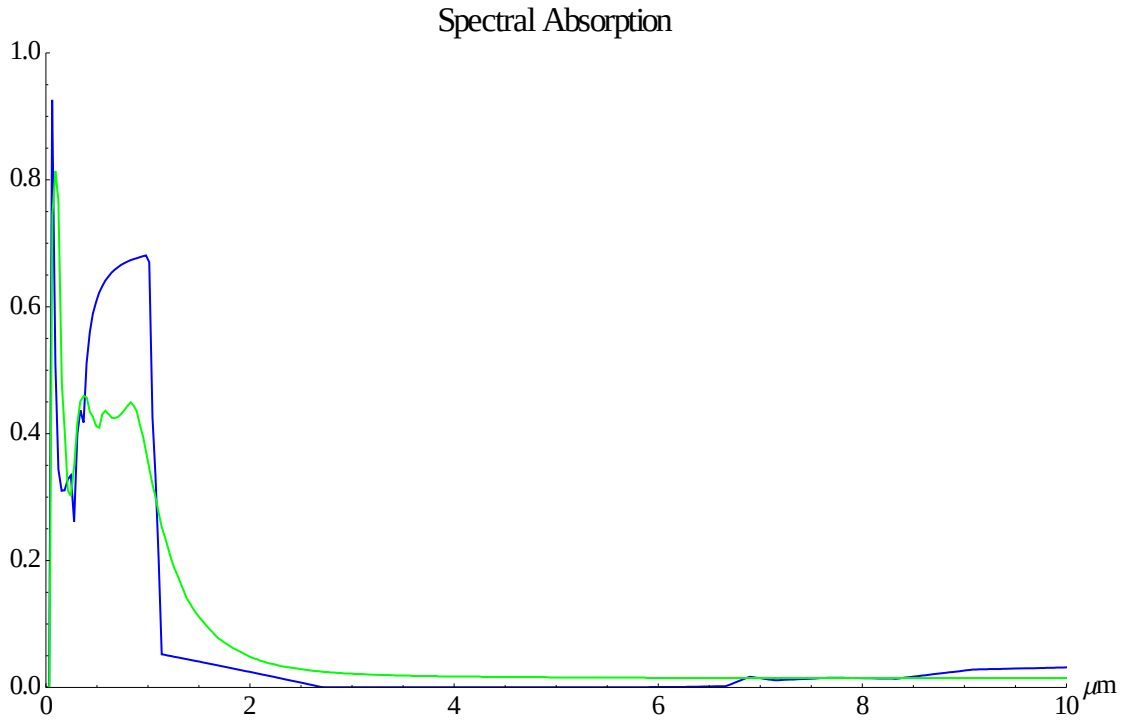

Figure 22 Spectral absorption of 0.38mm thick silicon (shown in blue), including an infinite number of internal reflections, and based on empirical data is shown here. In addition, spectral absorption of 1.5mm thick molybdenum (shown in green), including an infinite number of internal reflections, and based on empirical data is shown here.

The actual absorption, however, can change markedly in a semiconductor, as a function of temperature, due to the temperature dependence of the free carrier concentration. For an intrinsic semiconductor in equilibrium, the free carrier density, N_i (in units cm^{-3}), is the same for electrons and holes, and is given by the following temperature-dependent equation [102]:

$$N_i = 4.9 * 10^{15} \cdot \left(\frac{m_{de} m_{dh}}{m_0^2} \right)^{3/4} \cdot \sqrt{M_C} \cdot T^{3/2} \cdot e^{\frac{-E_g}{2 \cdot k \cdot T}}$$

Equation 61

where, m_{de} and m_{dh} are the density of states effective masses for electrons and holes respectively, m_0 is the mass of a free electron (taken to be 9.11×10^{-31} kg), M_C is the number of conduction band minima (6 for silicon), T is the temperature in kelvin, k is Boltzmann's constant, and E_g is the energy gap of the semiconductor. The density of states effective mass differs from simply the electronic effective mass (denoted by m*), because it includes an average over different possible conduction-band-type masses (in three principal crystal directions) and valence-band-type masses, including light holes (m_{lh}) and heavy holes (m_{hh}), as follows [102]:

$$m_{de} = \left(m_1^* \cdot m_2^* \cdot m_3^*\right)^{1/3}$$

Equation 62

$$m_{dh} = \left(m_{lh}^{*\,3/2} + m_{hh}^{*\,3/2}\right)^{2/3}$$

Equation 63

In the case of silicon these values were assumed to be 1.1 and 0.58 times m_0 for electrons and holes, respectively [103]. The energy gap of silicon is also temperature dependent, and taken to scale as follows [102]:

$$E_g = 1.169 - \frac{\left(4.9*10^{-4}\right)\cdot T^2}{T+655}$$

Equation 64

where E_g is in units of eV, and T is in units of degrees kelvin.

Thus, as an intrinsic semiconductor's temperature is increased, the free carrier concentration of electrons and holes increases exponentially. Any free carriers present can absorb incident electromagnetic radiation. We can account for this temperature dependent free carrier absorption contribution through the following development. First consider the complex index of refraction of an electromagnetic wave propagating in a medium, with real part, n, and imaginary part, k, as follows [104].

$$\tilde{n}(\omega) = n(\omega) + i \cdot k(\omega)$$

Equation 65

The complex index is related to the complex permittivity, ε, and the permittivity of free space, ε_0, by the following:

$$\tilde{n}(\omega) \approx \sqrt{\frac{\varepsilon(\omega)}{\varepsilon_0}}$$

Equation 66

where the approximation comes in assuming the magnetic permeability of the medium is the same as that of free space. The permittivity and index of refraction can be expressed more naturally in terms of the plasma frequency, defined as follows:

$$\omega_p \equiv \frac{N \cdot e^2}{m^* \cdot \varepsilon_0}$$

Equation 67

where N is the free carrier concentration in m^{-3}, e is the charge of an electron (1.6×10^{-19} C), and m^* is the effective mass of each free carrier. In terms of the plasma frequency, the index of refraction can be recast as follows:

$$\begin{cases} n(\omega) \approx 1 - \dfrac{(\omega_p \cdot \tau)^2}{1 + (\omega \cdot \tau)^2} \\ \alpha(\omega) = \dfrac{2 \cdot \tau}{c} \cdot \dfrac{{\omega_p}^2}{1 + (\omega \cdot \tau)^2} \end{cases}$$

Equation 68

where c is the speed of light in vacuum (3×10^8 m/s), τ is the mean scattering time, or relaxation time, within the Drude picture of electrical conduction, and α is simply related to k of Equation 65 by the following relation:

$$\alpha(\omega) = \frac{4 \cdot \pi \cdot k(\omega)}{\lambda}$$

Equation 69

The Drude model has been shown to predict the complex index of Silicon well at ~2.8mm wavelength, and is thought to apply beyond that realm [105]. Typical angular frequencies of radiation of interest for absorption considered in this thesis are of order

10^{15} Hz (corresponding to ~ 10^{-6}m wavelength), and typical scattering times, τ , for carriers in silicon above room temperature are of order 10^{-13} seconds, so we can assume $(\omega\tau)^2 >> 1$, in the case of silicon. Under that assumption we obtain the following:

$$\alpha(\omega) \approx \frac{2}{c \cdot \tau} \cdot \left(\frac{\omega_p}{\omega} \right)^2$$

Equation 70

Introducing the temperature-dependent mobility, μ, with explicit temperature dependence indicated, and linked to τ :

$$\mu(T) = \frac{e \cdot \tau(T)}{m^*}$$

Equation 71

the Equation 70 can now be recast as follows, with explicit wavelength, λ, and temperature, T, dependencies shown:

$$\alpha(\lambda, T) \approx \frac{e^3 \cdot \lambda^2 \cdot N(T)}{2 \cdot \pi^2 \cdot c^3 \cdot (m^*)^2 \cdot \varepsilon_0 \cdot \mu(T)}$$

Equation 72

In this expression both N, and μ are significantly temperature dependent for a typical semiconductor, like silicon, within the temperature range of interest in this thesis (~300K

to ~600K). Due to the complexity of modeling and limited available data, the temperature dependence of m^* has not been taken into account in this thesis. The temperature dependence of the mobility can be modeled by considering contributions to scattering of mobile carriers from both ionized impurities, and acoustic phonons. Those processes scale with temperature and effective mass differently, as shown below [102]:

$$\mu_{acoustic-phonon} \propto \frac{1}{\left(m^*\right)^{5/2} \cdot T^{3/2}}$$

Equation 73

$$\mu_{ionized-impurity} \propto \frac{T^{3/2}}{N_I \cdot \sqrt{m^*}}$$

Equation 74

$$\frac{1}{\mu_{average}} = \frac{1}{\mu_{acoustic-phonon}} + \frac{1}{\mu_{ionized-impurity}}$$

Equation 75

where N_I is the ionized impurity concentration. Experimental values for the temperature exponent for the average mobility of electrons and holes in silicon are -2.6 and -2.3, respectively [103], indicating the presence of other scattering mechanisms in addition to the two mentioned above. This is one indication of the value in using an empirical relation to model the free carrier absorption in a real material.

The electron free carrier absorption in intrinsic silicon is expected to obey the following dependence on temperature and wavelength (assuming $N=N_i$ of Equation 61; incorporating the temperature dependence of the silicon bandgap given by Equation 64; and expanding the factors within the exponential with respect to temperature about 300K):

$$\alpha_{Si}(\lambda,T) \propto \lambda^2 \cdot T^{4.1} \cdot e^{-6981/T}$$

Equation 76

A similar expression is expected to hold for the case of free hole absorption, but with a different constant of proportionality, and different power of temperature. The total free carrier absorption is then obtained by the sum of the two absorptions: one due to free electrons, and one due to free holes [106]; which should be valid to a first approximation, but in principle is not correct, as it assumes no coulomb coupling or other non-zero correlation between electrons and holes. In the interest of obtaining results in our heat transfer model which are as accurate and useful as possible, we appeal to the use of a reasonable empirical relation for the total free carrier absorption; which combines electron and hole contributions; and other possible factors not accounted for thus far. This relation is given here in m^{-1} [107]:

$$\alpha_{Si}(\lambda,T) = \left(4.15*10^{-3}\right) \cdot \lambda^{1.51} \cdot T^{2.95} \cdot e^{-7000/T}$$

Equation 77

The above relation is expected to be a good approximation to the total free carrier absorption in lightly doped silicon in the wavelength range 1.5 to 5 μm, and the temperature range 400°C to 700°C. We use it in our model of silicon heating from 300°C to 600°C, by incorporating it into the spectral absorption data shown in Figure 22 through addition of the absorption coefficients. For reference, several representative values of temperature were chosen to plot Equation 77 below, as a function of wavelength (see Figure 23).

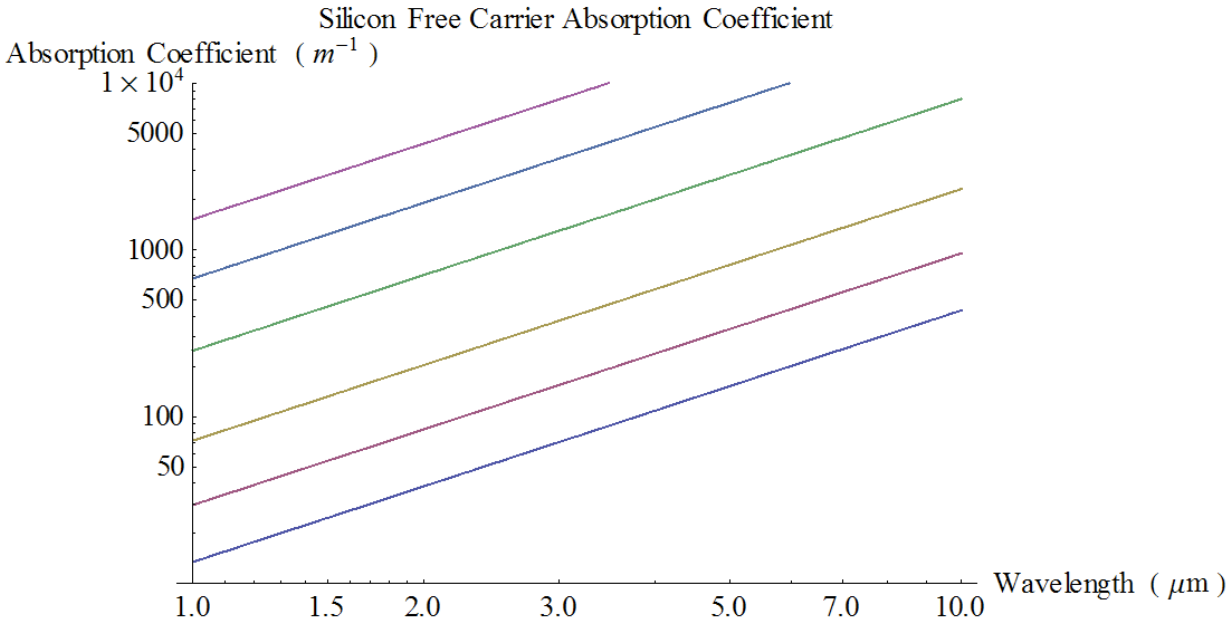

Figure 23 Contribution to the silicon absorption coefficient from free carrier absorption model for silicon at several representative temperatures. Based on the semi-empirical result of Equation 77. From top to bottom the temperatures used to generate the curves were: 653, 583, 509, 431, 383, and 345°C.

The total absorption for silicon, including the free carrier absorption, at 600K is shown below (Figure 24). It should be noted that the reflection is approximated to be temperature-independent within the model.

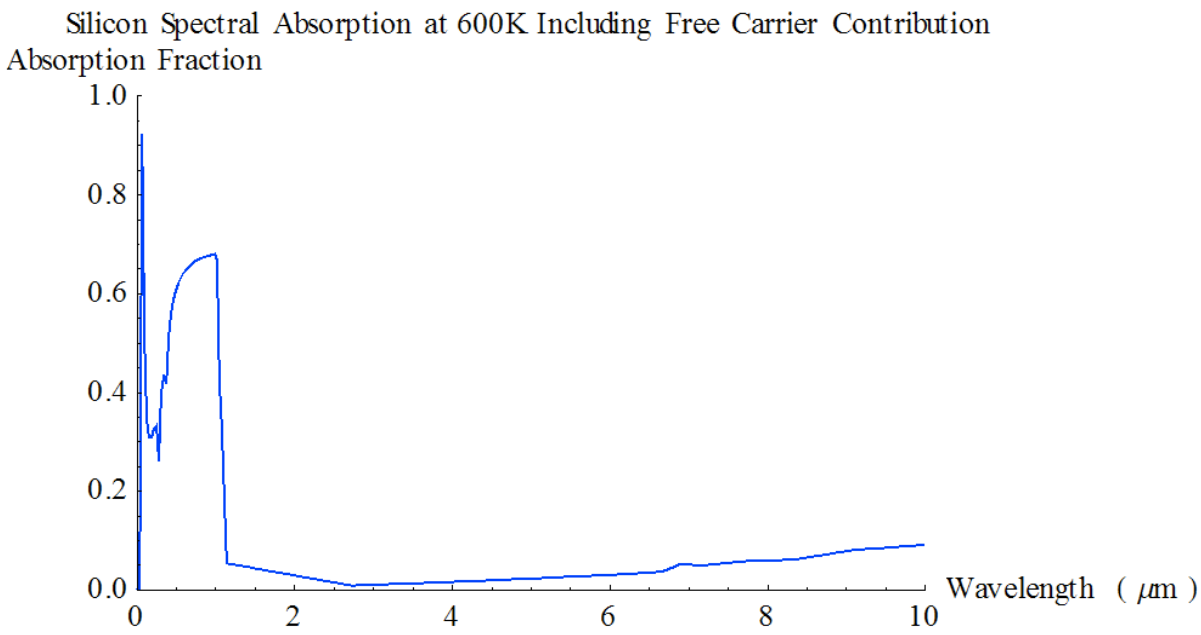

Figure 24 Spectral absorption of 0.38mm thick silicon; including an infinite number of internal reflections; incorporating free carrier absorption contributions from electrons and holes; and based on empirical data.

In the case of the molybdenum sample holder, a temperature-dependent free carrier absorption contribution was also considered in our heating model. For molybdenum it can be assumed that there is only one carrier type (electrons). The assumption $(\omega\tau)^2 >> 1$ used for silicon is now *not* valid in the case of molybdenum. Recasting Equation 68 in terms of temperature-dependent electrical resistivity, ρ, given by:

$$\rho(T) = \frac{m^*}{N \cdot e^2 \cdot \tau(T)}$$

Equation 78

results in an expression for absorption for molybdenum applicable to the realm of temperature and wavelength considered in this thesis, as follows:

$$\alpha(\lambda,T)=\frac{2}{c\cdot\varepsilon_0\cdot\rho(T)}\left(\frac{1}{1+\left(\frac{2\cdot\pi\cdot c\cdot m}{\lambda\cdot e^2\cdot N\cdot\rho(T)}\right)^2}\right)$$

Equation 79

In this expression, the value of N was taken to correspond to 2 free electrons per molybdenum atom. Using 10.28g/cm^3, 95.94g/mol and Avogado's number ($6.02\times10^{23}\,\text{mol}^{-1}$), a free electron density in molybdenum of $1.29\times10^{29}\,\text{m}^{-3}$ is obtained. Temperature-dependent resistivity data was obtained from [103], and modeled as linearly dependent on temperature as shown in Figure 25.

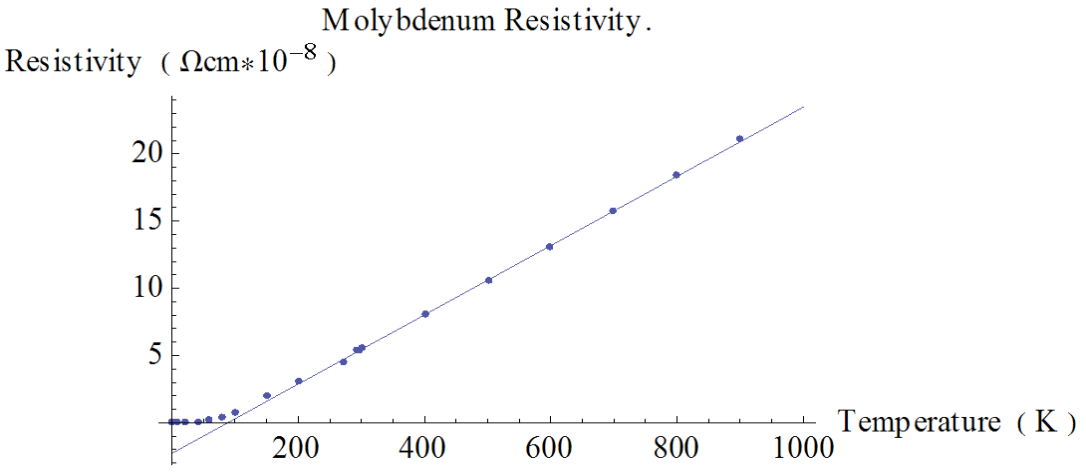

Figure 25 Molybdenum resistivity versus temperature data is displayed here; originating from [103]; with the trendline used to model the temperature dependence of resistivity of molybdenum in this thesis.

The incorporation of this free carrier absorption into the total spectral absorption of the molybdenum sample holder did not contribute appreciably to the absorption of the material (this is believed to be due to the high reflectivity of the molybdenum). In subsequent pages here, the free carrier absorption in the molybdenum has been approximated to be temperature independent. In addition, the reflectivity is also approximated to be temperature independent.

A numerical solver was used in Mathematica to solve for the temperature as a function of time for the silicon and molybdenum under constant heater power (although, for constant heater power there does exist a cumbersome closed-form solution involving an inverse function of -2arctan[t]+ln[1-t]-ln[1+t]). In preparation of solving, a numerical integral was performed for the absorption in each material multiplied by the heater spectrum (see Figure 26), over wavelengths of interest for the sample holder and silicon wafer. The temperature of the heater was set so as to reach a steady-state silicon wafer temperature value relevant to CdTe MBE growth. The formula in the argument of those integrals was obtained from the multiplication of the heater spectrum with the absorption spectrum of each material, and are plotted below for reference (see Figure 27).

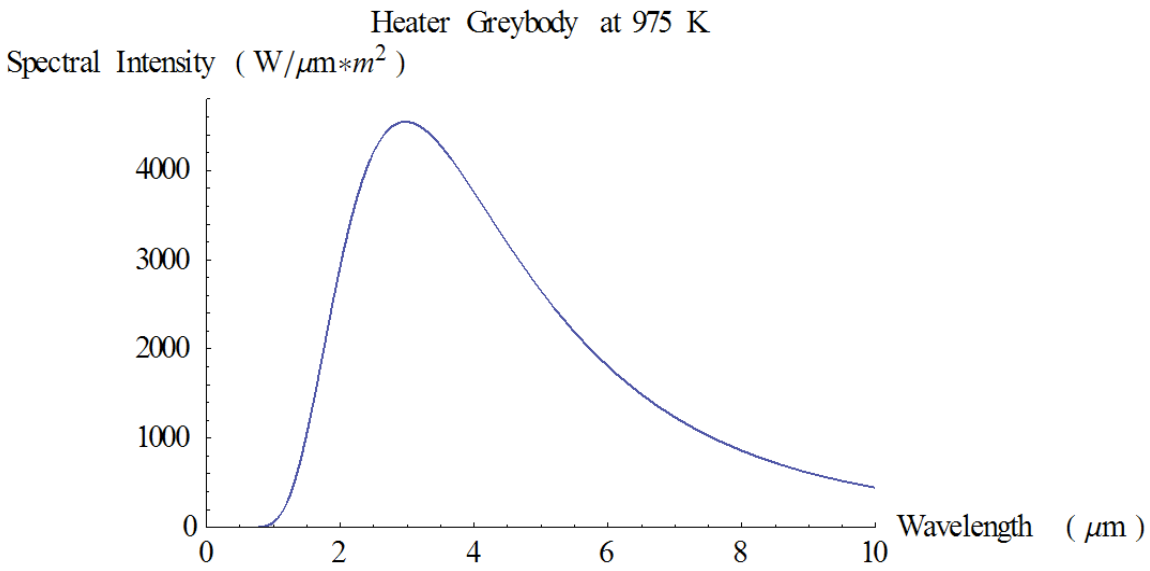

Figure 26 Heater grey-body spectrum used for modeling spectral density of radiation imparted to the silicon wafer and molybdenum sample holder. The equation describing this curve is given by Equation 59.

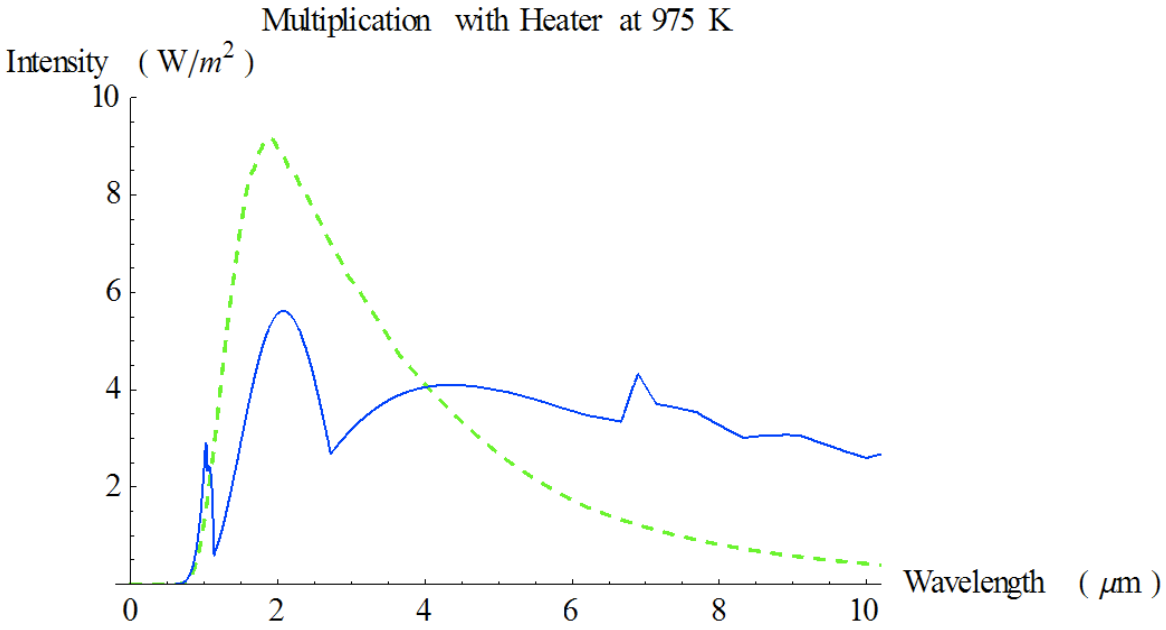

Figure 27 Multiplying the spectral absorption by the heater spectrum results in the two curves here; where the silicon wafer curve is in solid blue, and the molybdenum sample holder curve is in dashed green.

Each time step of the solver then added thermal energy due to the absorption of heater radiation ($flux_{heater}$) and 77K background ($\sigma \cdot \varepsilon \cdot A \cdot T_{background}^4$), although the background was negligible under normal conditions, and subtracted radiation due to the emission of the silicon or molybdenum away from the heater ($\sigma \cdot \varepsilon \cdot A \cdot T(s)_{background}^4$), where σ is the Stefan-Boltzmann constant of 5.669×10^{-8} W/m^{2}K^4, ε is the emissivity of the material, A is the area of the material, and T is the temperature of the material in degrees Kelvin. A schematic of the calculation geometry is shown in Figure 28. The temperature of the silicon and molybdenum objects were obtained by dividing their thermal-energy contents by the product of heat capacity (denoted c), taken to be 712, and 251 J/kg∗K, respectively, and mass (denoted m), respectively (see Equation 80). Finally, for the silicon wafer and for the molybdenum sample holder, Equation 80 was solved in each case to obtain the temperature of the object as a function of time.

$$\int_0^t \left(flux_{heater} + \sigma \cdot \varepsilon_{background} \cdot A \cdot T_{background}^4 - \sigma \cdot \varepsilon \cdot A \cdot T(s)_{object}^4 \right) \cdot ds = c \cdot m \cdot T(t)$$

Equation 80

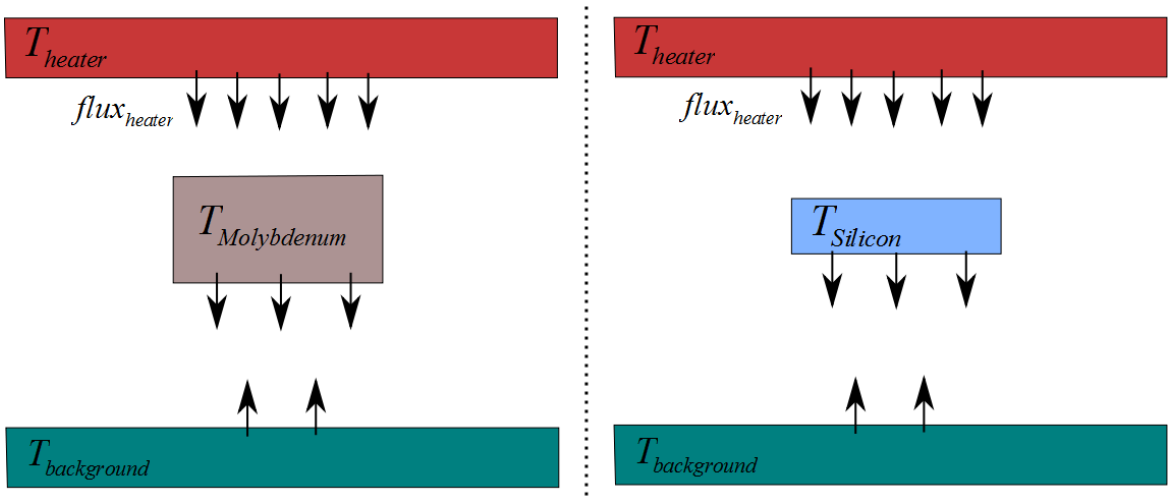

Figure 28 A schematic of the heater calculation geometry is shown here. The molybdenum and silicon are uncoupled, and can differ in emissivity, absorption, thickness, density, and heat capacity. The heater, object (molybdenum or silicon), and background are assumed to always remain at uniform, well-defined temperatures.

From Equation 80 it can be intuited a-priori that the relative change in temperature of each object will scale closely with the emissivity and the product of heat capacity, thickness, and density; but will not scale with the area, because the $flux_{heater}$ term is directly proportional to area, as is the mass, m. The values of the product $c \cdot m$ for the silicon wafer and molybdenum sample holder are: 2.9, and 31.7 J/K, respectively; dividing by area gives $c \cdot \rho \cdot t$, equal to 630.4 and 3909.4 J/K*m^2, respectively, with ρ denoting density. Thus, it is seen from these values that the sample holder requires ~6 times more heat energy than the silicon to change in temperature by the same amount, assuming identical emissivity values; however, the two materials have different absorption. Thus the sample holder could heat more slowly than the silicon wafer, or vice versa; thus the relative paths of the silicon wafer and the molybdenum sample holder, during heating, still cannot easily be determined a-priori. The actual solver results shed

light on this situation, in that the solution shows the sample holder does respond to temperature setpoint changes more slowly than does the silicon wafer (see Figure 29).

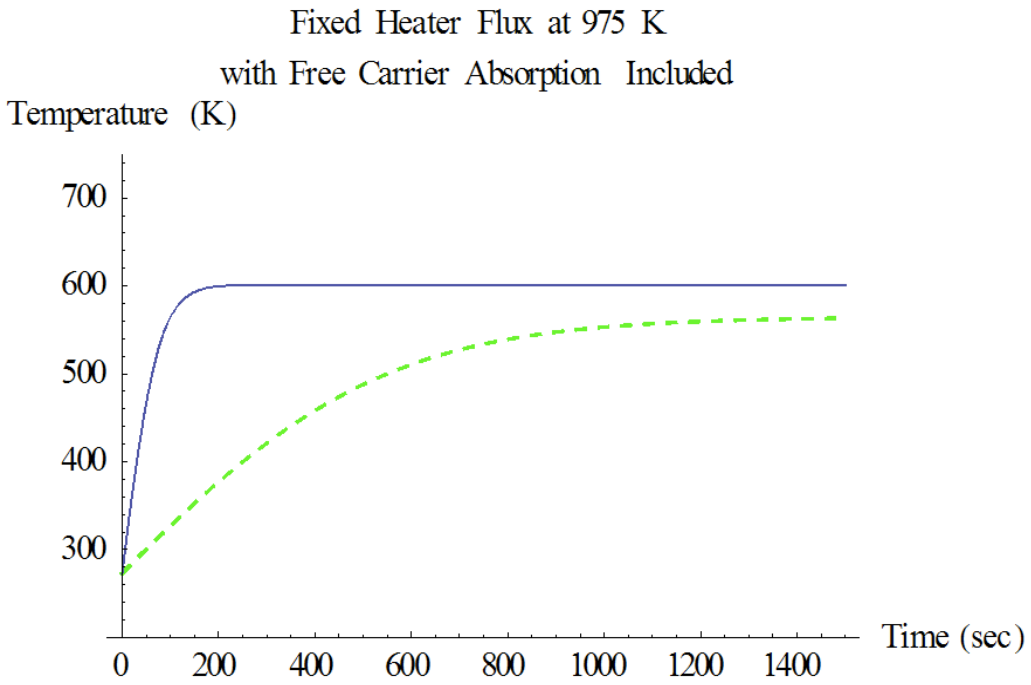

Figure 29 Temperature versus time solver solutions for the silicon wafer (blue) and the molybdenum sample holder (dashed green). The heater flux was held constant to generate these solutions. It is clearly seen that the silicon wafer temperature responds faster than the molybdenum sample holder. The path of the thermocouple temperature is not known for small times, but must be ~100^{o}C higher than the silicon for large times.

This is an important result. It implies that the thermocouple reading could be significantly lower than the silicon temperature during heating. This observation is in contrast with the result of the temperature calibration in the steady state, mentioned earlier; where the silicon was found to be lower in temperature than the thermocouple by ~100^{o}C. Thus, the initial heating of the silicon is a unique part of the MBE process, which needs special consideration. In an actual MBE system, a typical temperature control loop for heating the sample and sample holder is very likely to temporarily increase the heater output power to high values when large increases in setpoint

temperature are called for, in order to reach steady-state temperatures rapidly. Even in the case of a smooth ramping of the setpoint temperature, the heater power may fluctuate considerably while attempting to maintain the setpoint temperature of the ramp.

Under conventional MBE growth procedure conditions it is not uncommon to allow the sample heater to reach high power levels temporarily, in order to rapidly increase the sample temperature. An example situation is the heating of room temperature silicon to 300^{o}C, where the sample heater power may temporarily reach over three times the minimum required value of power, in order to reach the setpoint temperature of 300^{o}C rapidly. The previous result implies that the fast response of silicon may result in an overshoot of the intended silicon temperature setpoint, before the molybdenum or thermocouple reach their steady state values. In fact, it is possible that the silicon overshoots its steady-state temperature while being heated, and simultaneously, that the thermocouple shows no overshoot of its steady-state value.

To model the effects of this behavior approximately, the solver described was used with various increased heater flux values applied for the first 60 sec of heating, followed by the same heater flux used to generate the solutions in Figure 29. The results of a 60 second double and quadruple heater flux during initial heating are shown in Figure 30 (a) and (b), respectively. It is clearly seen that the silicon, under temporary high heat-flux conditions, initially overshoots the steady state temperature value to which it settles later. This model prediction of temperature overshoot of silicon substrates is also in qualitative agreement with experimental results obtained from heating GaAs substrates in vacuum [108].

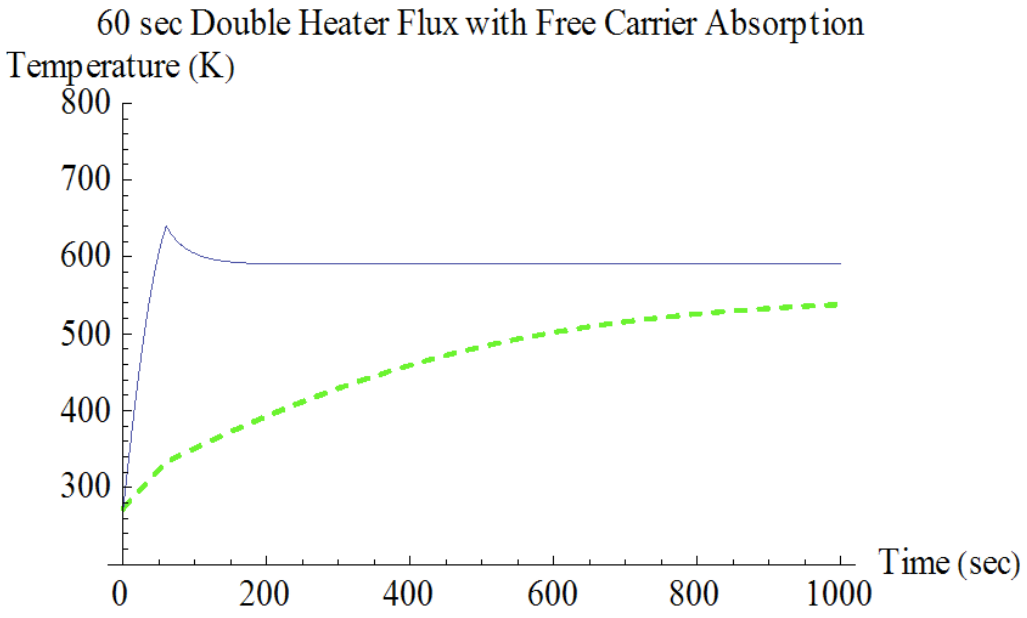
60 sec Double Heater Flux with Free Carrier Absorption
Temperature (K)
800
700
600
500
400
300
0
200
400
600
800
1000
Time (sec)

(a)

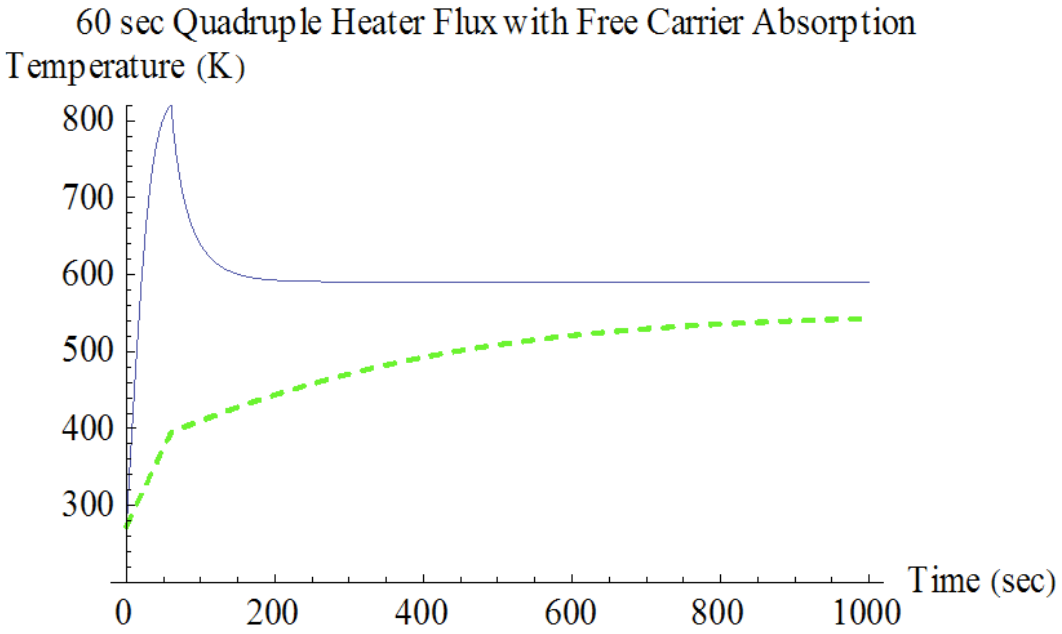
60 sec Quadruple Heater Flux with Free Carrier Absorption
Temperature (K)
800
700
600
500
400
300
0
200
400
600
800
1000
Time (sec)

(b)

Figure 30 Temperature versus time solver solutions generated with the first 60 seconds involving double (a) and quadruple (b) the minimum heater flux required to reach the steady state solutions at long time values. The silicon wafer solutions are in solid blue, and the molybdenum sample holder solutions are in dashed green. Kinks are readily apparent in the curves at 60seconds when the heater power was reduced instantly to the steady state value. It is clearly seen that the silicon solution not only initially possesses a higher temperature than the sample holder, but also overshoots the final steady state value by over 40^{o}C. The final steady state temperatures of the Si and Mo may or may not agree with the actual MBE system.

Usually, a short overshoot of substrate temperature is not a difficulty in MBE growth procedures; however, if nano-scale features are present on the surface of the silicon, they could possibly be desorbed by such an overshoot. Our radiative heat transfer model results, described above, can be used in conjuction with some additional information about the typical CdTe bonding energetics at the CdTe surface, to estimate the magnitude of desorption during such an overshoot, as described in the following paragraphs.

It has been published that CdTe(111)B desorbs at less than 18nm/hr in vacuum, when at temperatures below 310^{o}C [109], however the desorption rate is known to increase exponentially with temperature. In an effort to obtain a desorption rate relevant to the Opus MBE system used in this thesis, a sample of CdTe/ZnTe/Si(211) was etched in HBr:H_2O_2:H_2O (5:1:90) for 1 sec, and slowly heated to 310^{o}C, where it was held for 58 hours. Before and after etching and heating, the epilayer thickness was measured by FT-IR, and found to have decreased in thickness at an average rate of 2.76nm/hour during the 58 hours of dwell at high temperature (see Figure 31). The etching step itself was estimated to have removed < 8nm of material, based on a measured etch rate at room temperature [110].

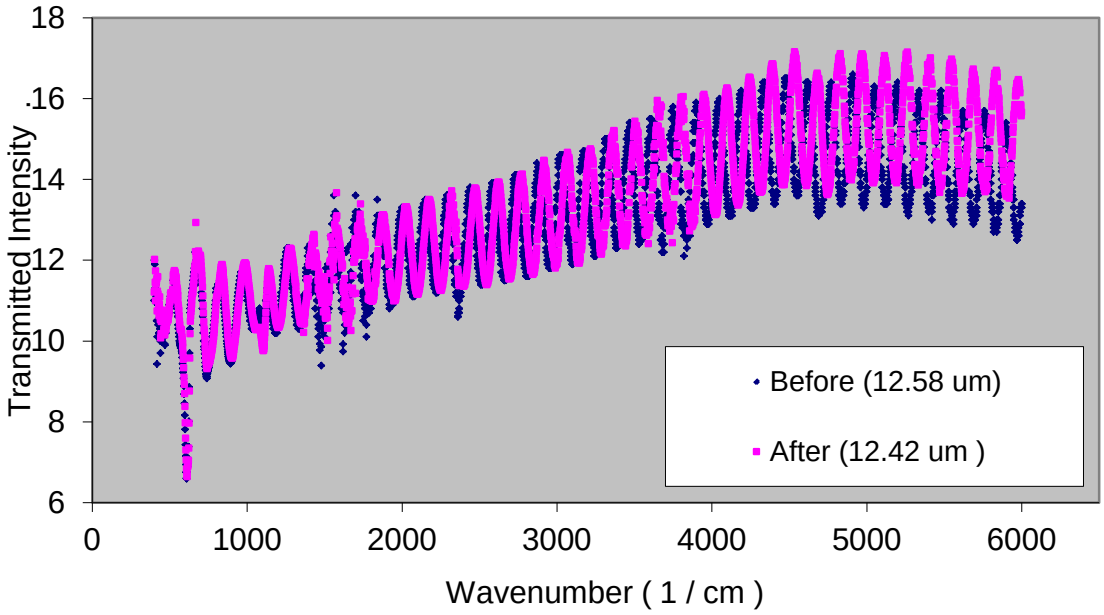

Figure 31 FT-IR data is shown here for a $2 \times 2\,\mathrm{cm}^2$ sample of CdTe/ZnTe/Si(211), etched in HBr:H_2O_2:H_2O (5:1:90) for 1 sec, and heated to 310^{o}C for 58hours. The resulting 160nm reduction in thickness corresponds to a desoption rate of 2.76nm/hour. The darker (blue) curve was acquired before etching or heating.

We can extrapolate to desorption rates at different temperatures if the activation energies and pre-exponential factors for the desorption processes are known. These factors are difficult to calculate exactly based on first principles; without techniques such as density functional theory. However, they can be estimated from fitting the experimental data of the temperature dependence of the CdTe homoepitaxy growth rate, or observing desorption with electron diffraction from the sample surface [111, 112, 113].

Data of the MBE growth rate of CdTe on CdTe(100) and CdTe(111)B are reproduced here in semilog plots below (see Figure 32), in each case, it is clear that a good model of the curve requires at least two exponential activation energies, as there are

two distinct linear regions clearly visible within each data set; thus the simplest physical model that will fit the data reasonably well is of the form here:

$$R(T) = R_0 - P \cdot e^{\frac{-E_P}{k \cdot T}} - C \cdot e^{\frac{-E_C}{k \cdot T}}$$

Equation 81

where R(T) is the vertical growth rate as a function of substrate temperature, T; P and C are positive pre-exponential constants; E_P and E_C are activation energies; and k is Boltzmann's constant. Dividing through by R_0 gives an equation for the sticking coefficient as a function of substrate temperature.

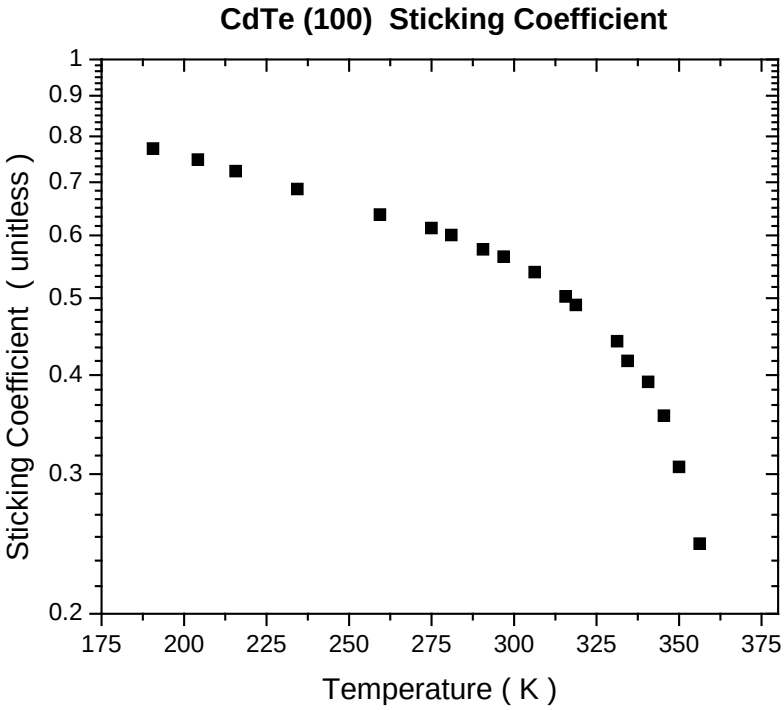
CdTe (100) Sticking Coefficient
Sticking Coefficient (unitless)
Temperature (K)
1
0.9
0.8
0.7
0.6
0.5
0.4
0.3
0.2
175
200
225
250
275
300
325
350
375

(a)

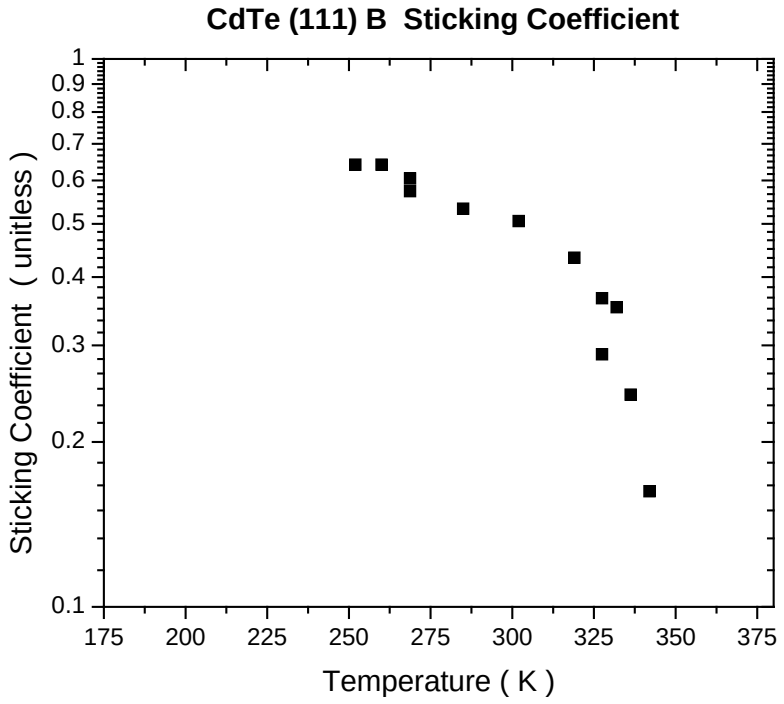
CdTe (111) B Sticking Coefficient
Sticking Coefficient (unitless)
Temperature (K)
1
0.9
0.8
0.7
0.6
0.5
0.4
0.3
0.2
0.1
175
200
225
250
275
300
325
350
375

(b)

Figure 32 Experimentally measured, normalized MBE growth rate of CdTe on CdTe(100) and (111)B reproduced from references {Behr et al. [112] for CdTe(100) shown in (a), and Seldrum et al. [111] for CdTe(111)B shown in (b)}. The growth rate has been normalized to unity at zero substrate temperature, thus the data represents the sticking coefficient as a function of temperature, at fixed CdTe flux value. Each data set apparently has two approximately linear regions within the log plots; indicating the presence of at least two Boltzmann factors in a simple fit to each data set.

Forcing a fit with only one exponential factor results in a poor representation of the trend of either surface orientation (see Appendix A). A good fit is obtained by fitting with Equation 81 to the growth rate data for CdTe(100) and CdTe(111)B; which yields the following values for the sticking coefficient equation (see Table 5). It should be noted that the bulk-terminated (211) surface consists of alternating (100) and (111) surfaces, however, the (211) growth rate is not necessarily between the growth rates of those component surfaces.

CdTe MBE Growth	P/R_0	E_P ***(eV)***	C/R_0	E_C ***(eV)***	***Source***
(100)	7.44	0.14	$2.63*10^{14}$	1.89	Behr [112]
(111)B	2.16	0.14	$1.72*10^{14}$	1.88	Seldrum [111]

Table 5 Fitting parameters for CdTe sticking coefficient versus substrate temperature by MBE; derived from data of growth rate versus substrate temperature by MBE in the cases of (100) and (111)B. The P and C denote an interpretation of the fitting parameters as describing physisorbed and chemisorbed atomic bonding, respectively.

CdTe UHV Desorption	***D (nm/min.)***	E_D ***(eV)***	***Source***
(111)B	$-5.07*10^{18}$	2.21	Dubowski [109]
(211)B	$-7.94*10^{14}$	1.88	This thesis
(111)B	-	1.9 (Cd), 2.04 (Te)	Tatarenko [114]
(110)	-	1.96 (Cd), 1.23 (Te)	Tatarenko [114]
(100)	-	0.96 (Te)	Tatarenko [114]
(100)	-	{~1.3 (Cd), ~0.86 (Te)}[8]	Benson [115]
ZnTe(100)	-	1.8 (Cd)	Benson [116]

Table 6 Fitting parameters for CdTe UHV desorption rates versus substrate temperature; derived from empirical data. The rates were derived with the assumed form: $DR = D \cdot e^{\frac{-E_D}{k \cdot T}}$, where DR is the desorption rate, k is Boltzmann's constant, and T is the temperature in degrees K. The negative sign is added to the D values to remind the reader of the distinction between desorption and adsorption rate parameters, which may differ in magnitude.

[8] Values are estimated from Figure 2 of Benson et al., using the inverse temperature axis; although the two abscissa scales in their Figure 2 do not exactly correspond. The value of 7.70eV for the Te desorption activation energy quoted in the abstract of their paper is not physically reasonable.

The fit parameters of Table 5 can be interpreted as resulting from averaged physisorbed (P and E_P) and chemisorbed (C and E_C) bonding of Cd and Te atoms to the surface. The averaging is understood to be over all reasonably accessible bonding arrangements of the surface atoms and their relative likelihood of occurring. The averaging must be complicated, in part because strictly speaking, the average of two Boltzmann factors does not result in a single Boltzmann factor unless the activation energies are identical; thus it is interesting that such a good fit to the data can be obtained with only two Boltzmann factors.

The presence of two Boltzmann factors is likely not related to the presence of two incoming flux molecule types (Cd and Te_2), because good fits to the growth rate versus substrate temperature curves are obtained with two Boltzmann factors with nearly identical activation energies for both the (111) and (100) orientations. The data implies that there are two groups of characteristic processes that each have similar activation energy values within their group, somewhat independent of the crystalline orientation of the surface. The lower activation energy group dominates the growth rate curve at low substrate temperature, and the higher activation energy group dominates the growth rate curve at higher temperature. It can be reasonably speculated that these two general groups may be related to different lateral, and/or vertical, positions of the flux molecules on the surface. In addition, the normalized P and C exponential pre-factors, P/R_0 and C/R_0, may be flux-dependent [112].

Using the fit parameters in Table 5 it can be calculated that 50% of the CdTe incoming flux is incorporated during typical MBE growth at a substrate temperature of

~310°C. This means either that a large fraction of incoming atoms and molecules do not reach chemisorbed states, or that they are incorporated at rates higher than 50%, but remove other atoms in the process (flux reflection can play a role here, but likely not sputtering). However, it is not the case that bare CdTe in UHV and under no impinging flux should desorb at the same rate. Furthermore, it is not necessarily the case that a bare surface of CdTe in UHV and under no impinging flux would desorb at the chemi-desorption rate listed in Table 5.

Using only the E_C and C values for CdTe(111)B (see Table 5) one can estimate the total desorption rate of CdTe at a typical MBE growth temperature of ~310°C to be 3nm/min. This value is 10 times larger than suggested by the data of Dubowski et al. [109], also taken at ~310°C, giving 0.3nm/min; and ~100 times larger than our experimental measurement at 310°C (see Figure 31) of 0.05nm/min for the desorption rate of CdTe(211)B. The values are summarized for reference in Table 8. The values can be derived from the parameters of Table 6; where some additional desorption activation energies reported in the literature are included for comparison. The values may differ due to temperature calibration discrepancies.

At first glance, the discrepancy between the first two of these values appears to be an indicator that the desorption rate of resident surface atoms increases when bombarded with flux, under the typical conditions for MBE CdTe growth. This is a natural conclusion, as the bombardment process described, imparts momentum to the surface atoms; enabling some of them to leave the surface; constituting a sputtering process[9]. It is known that a typical ion momentum of 4 to 8×10^{-21} kg*m/s for Ar^+ ions at 49°

[9] It is interesting to contrast this scenario with that of XPS photons at ~1.5keV, which do not remove even a fraction of a ML from samples of interest. The stark contrast in these two scenarios can be understood by the role of momentum transfer in classical collisions.

incidence angle from normal, with $\sim 2.8\times10^{13}$ ions incident on the surface per cm^2 per second can be used to sputter $Hg_{0.8}Cd_{0.2}Te$ at a removal rate of 1 to 10nm/min [117]; and similarly for CdTe, a typical momentum of 5×10^{-21} kg*m/s for Ar^+ ions, with $\sim 3.1\times10^{14}$ ions incident on the surface per cm^2 per second can be used to sputter CdTe at a removal rate of 0.6nm/min [118]. In comparison, under typical CdTe MBE growth conditions of ~10nm/min growth rate, ~10 to 100 times more flux molecules are incident on the sample surface per cm^2 per second, around half of which, do not contribute to the film growth; either due to thermal desorption, reflection, or sputtering. In the following, a model is constructed to estimate the maximal amount of sputtering which could take place near the typical CdTe MBE growth conditions.

First an estimate will be made for the amount of sputtering of surface atoms in physisorbed states. As Cd is lighter than Te_2, it will leave a given CdTe source cell of a fixed temperature with higher kinetic energy than Te_2. Cd will also be more likely to be sputtered from a physisorbed surface state than Te. Thus, let one consider the upper bound in yield for the sputtering process: a single Cd atom bound to a CdTe surface in a physisorbed bond, impacted by an incoming Cd flux atom. The Cd surface atom can be approximated to be bound in a Lennard-Jones (n-6) potential of n value 12 [119, 69], with dissociation energy given by 0.15eV (see Table 5); such is plotted below (Figure 33).

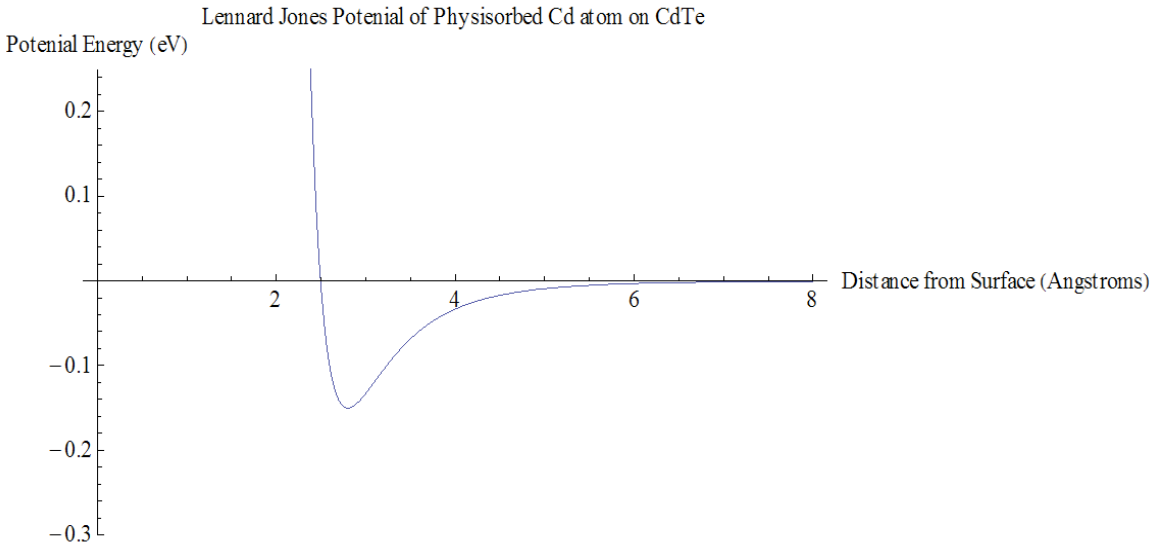

Figure 33 Lennard Jones potential energy curve with dissociation energy 0.15eV, approximating the potential energy for a Cd atom in a physisorbed bond at the CdTe surface during typical MBE of CdTe.

The probability that the surface Cd atom will be sputtered by the incoming Cd flux atom requires consideration of the density of bound energy states, with respect to energy, above the bottom of the Lennard Jones potential. The density of states can be obtained with the use of a WKB expression in quantum mechanics for number of nodes, n, of a bound eigenstate [120]:

$$\int_a^b \sqrt{2 \cdot m \cdot \left(E_n - V_{L-J}\left(x\right)\right)} \cdot dx = \left(n + \frac{1}{2}\right) \cdot \frac{h}{2}$$

Equation 82

where a and b are the classical turning points in space for the bound state, h is Planck's reduced constant, E_n is the energy of the nth bound eigenstate above the ground state, m is the mass of the Cd atom, and $V_{L-J}\left(x\right)$ is the one-dimensional Lennard-Jones potential

confining the Cd atom. The integral was numerically evaluated for E_n that were not necessarily eigenstates, in order to extract the trend in E_n versus n; the result of which is shown below (see Figure 34); where a fifth-order polynomial fit is also shown.

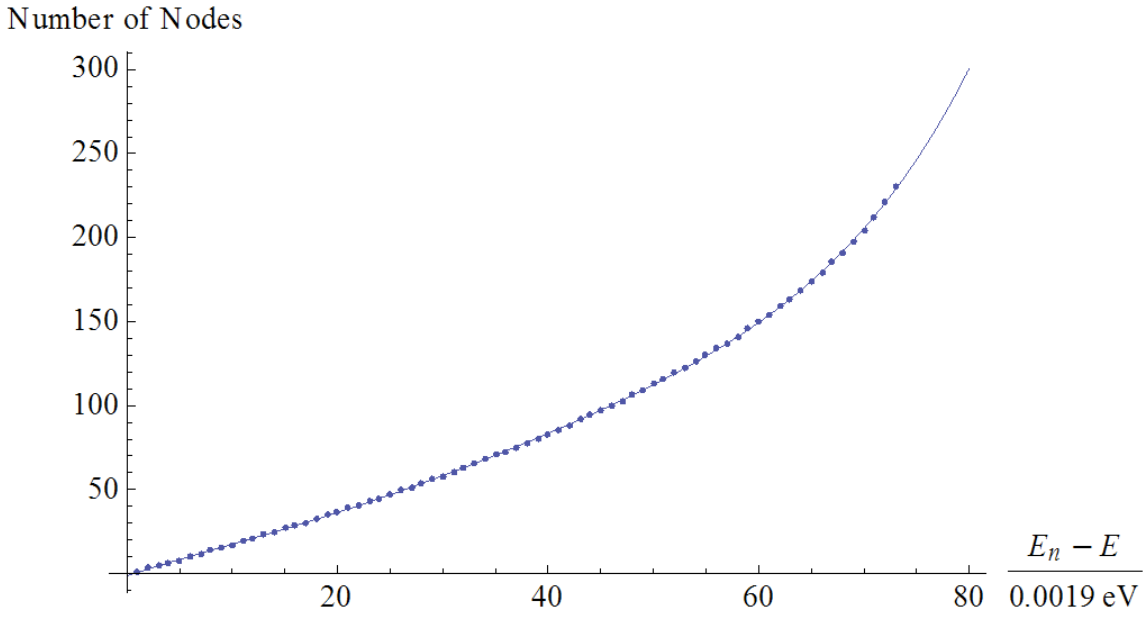

Figure 34 The trend in bound state energy (in units of 0.0019eV above the approximate ground state) versus bound eigenstate node number can be reasonably well fit to a fifth-order polynomial. The points are not necessarily eigenstates, but such are expected to be close to the general curve. The points do not continue to arbitrarily high values, because the well is of finite depth.

The fifth-order polynomial fit shown in Figure 34 was used to produce a one-dimensional energy density of states formula plotted below (see Figure 35).

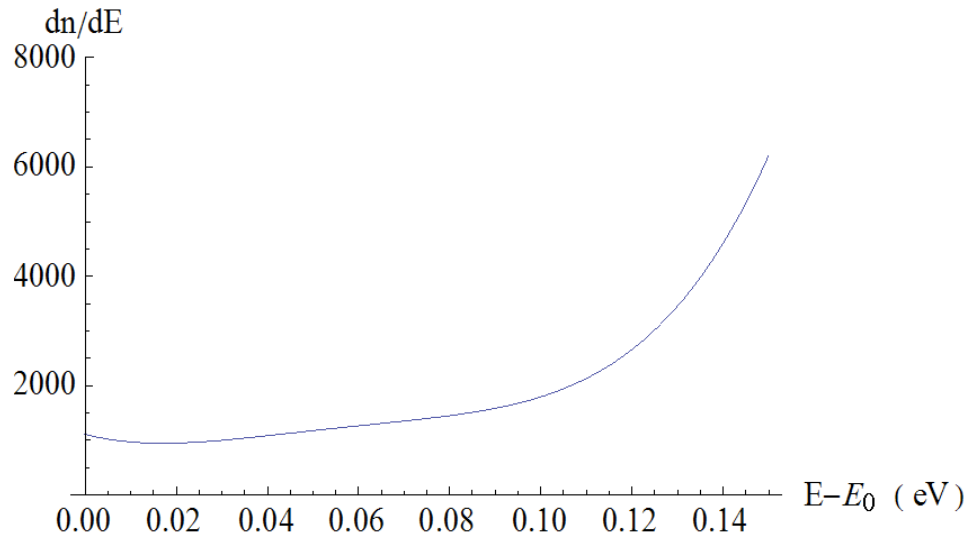

Figure 35 Approximate energy density of states (number per eV) versus energy above the approximate ground state energy, E_0, for a physisorbed Cd atom on a CdTe surface at typical MBE growth conditions. The increase of dn/dE at energy less than 0.02eV is likely an artifact of the approximation method.

The density of states was then used in conjuction with Boltzmann statistics to estimate the likely energy state of the surface Cd atom at a certain surface temperature; while the incoming Cd flux atom was taken to have a kinetic energy given by (3/2) kT, where k is Boltzmann's constant, and T is the temperature of the cell in kelvin. The final approximate result was obtained by integrating the surface atom's occupation probability (density of states times Boltzmann factor) with respect to energy, within the energy range in which the surface atom needs less energy than the total incoming atom's kinetic energy in order to desorb from the surface. The results for several surface and cell temperature combinations of interest in this thesis are summarized in the table below (see Table 7).

Cell Temperature (^oC)	*CdTe Surface Temperature (^oC)*	*Maximal sputtering desorption probability*
500	300	0.11
550	300	0.15
500	350	0.12
550	350	0.16
600	340	0.21
500	370	0.12
550	370	0.16

Table 7 Maximal approximate sputtering probability for a Cd atom physisorbed on CdTe at fixed surface temperature, impacted by a Cd flux atom originating from a cell of different fixed temperature.

The probability estimates above do not take into account the angular conditions necessary for both incoming and bound Cd atoms to leave the surface after collision; nor do they take into account the relative phase relation needed between oscillation of the surface atom and time of impact with the flux atom. Thus, the results of the above table suggest that even the most likely sputtering process, does not contribute very strongly to the overall growth process; except perhaps under extreme annealing conditions of high surface and cell temperatures. It should be noted that the sputtering process described is controlled by the physisorption activation energy, thus it may not be distinquished as a separate feature in the growth rate versus substrate temperature data fitting. Finally, the discrepancy between the first two values in Table 8 is likely primarily due to increased reflection of incoming flux, or enhanced physidesorption of surface species.

The discrepancy in the second and third values of Table 8 may be related to the stepped nature of the CdTe(211)B surface when compared with the flatter (111) surface; although substrate temperature calibration may also explain this discrepancy. The three desorption rates are shown in Table 8, for reference, and the underlying Arrhenius

relations listed in Table 6 are plotted in Figure 36, along with the Arrhenius relations associated with chemi- and phyi- desorptions during MBE growth, listed in Table 5.

Source	**Chemisorption growth rate fitting parameters: C and E_C (see Table 5)**	**Dubowski et al. [109]**	**FT-IR measurement (Figure 31 of this thesis)**
Surface	CdTe (111) B	CdTe (111) B	CdTe (211) B
Desorption Rate (nm/min.)	3	0.3	0.05

Table 8 Estimated desorption rates of CdTe(111)B and CdTe(211)B in UHV, at temperature ~310^{o}C.

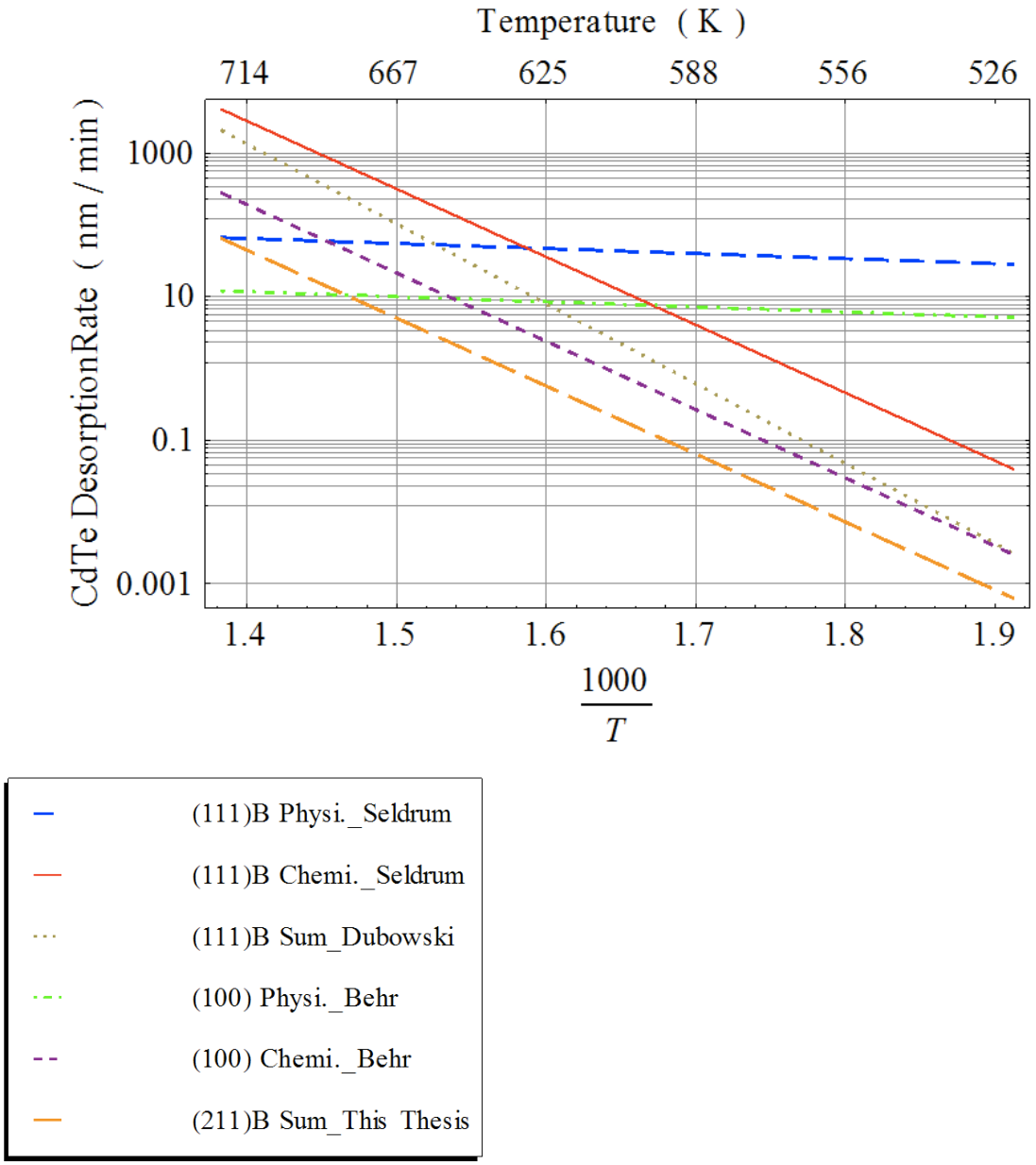

Figure 36 The estimated desorption rate Arrhenius relations of different CdTe surface orientations in Table 8 are plotted here versus inverse temperature in K. In the legend "Physi." denotes desorption from a physisorbed surface state, "Chemi." from a chemisorbed surface state, and "Sum" indicates the addition of "Physi." and "Chemi." rates. Two of the CdTe(111)B curves are based on Seldrum et al. [111]. The third CdTe(111)B curve is based on Dubowski et al. [109]. The (100) curves are based on Behr et al. [112]. The CdTe(211)B curve is based on the combination of the chemidesorption energy of the fit of Seldrum et al. and Behr et al. and the FT-IR desorption measurement of this thesis. It can be seen that at low temperature the physidesorption rate dominates. At high temperature the chemidesorption rate dominates. The two desorption rates cross at ~650K (or ~380^{o}C), around 30^{o}C higher than where the sticking coefficient goes to zero for CdTe MBE on CdTe at typical flux values used for single-crystalline growth.

The rate of CdTe desorption taken to be most relevant to the pre-heating of silicon-based substrates for the MBE growth of CdTe in this thesis is the experimentally measured value of 2.76nm/hour (or 0.05nm/min), of this thesis. This value is also coincidentally, the most conservative. Using this value, and the chemisorption activation energy E_C from the growth rate fitting on CdTe(111)B, one can obtain an Arrhenius relation with one Boltzmann factor, for the desorption of CdTe in UHV as shown below.

$$D_C(T) = -1.48\times10^{13}\cdot e^{\frac{-1.88}{k\cdot T}}$$

Equation 83

where D_C is the desorption rate from chemisorbed surface species with units nm/min, k is Boltzmann's constant, and T is temperature in K. This expression was used to quantify the total desorption of CdTe/Si during simulated pre-heating in the MBE system, when the heater flux was increased by various amounts during the first 60 seconds of heating from substrate temperature ~ 300^{o}C to ~ 600^{o}C. The expression was integrated in time to obtain total desorption losses in film thickness during the first 400 seconds of pre-heating. Two fixed silicon substrate temperatures were considered to compute the free carrier absorption: 300K and 600K. At each temperature, the heater power was adjusted to result in the silicon reaching ~600K in the steady state (long-time) condition. As shown in Figure 37 there is significant loss of CdTe, on the order of 10's to 100's of nm. It can also be seen that the free carrier absorption between substrate temperatures 300K and 600K does not appreciably change the total desorption of CdTe within the model (although the steady state temperature of molybdenum does change). In the event that

extrinsic dopants are used in the silicon substrate, there is likely also a significant desorption upon such overheating.

Thus the model indicates that a nano-scale CdTe feature present on a typical silicon wafer could easily be destroyed or detrimentally modified during initial heating to typical CdTe MBE growth temperatures. One possible modification has been observed by Transmission Electron Microscopy (TEM), for example: that CdTe nanoparticles can change from zincblende to wurtzite crystal structure when heated to sublimation temperatures of CdTe [121]. Therefore, care needs to be taken when pre-heating nanostructures of CdTe on silicon substrates to substrate temperatures typical of MBE CdTe growth. One direct path to mitigate this concern is available to the MBE grower using a resistive heater: that is the setting of an appropriate hard upper limit to the substrate heater current output, which thereby limits the maximum heater power, which limits the maximum radiative flux to the substrate. That is the approach taken in this thesis during the heating of CdTe nanostructures.

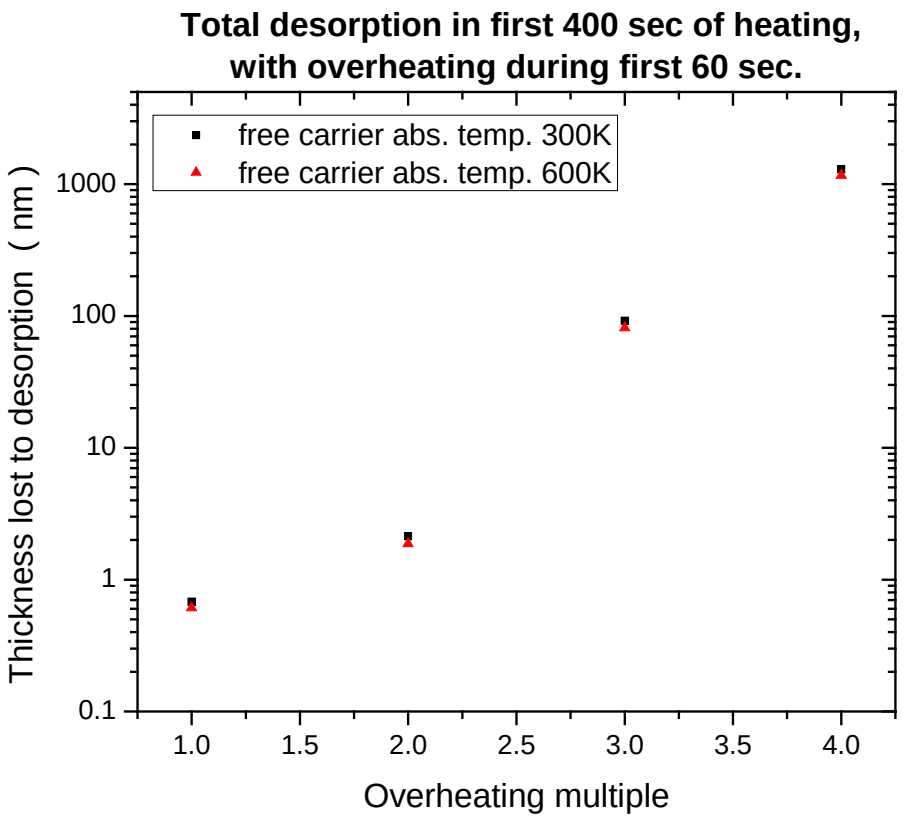

Figure 37 Estimated desorption loss of CdTe from CdTe/Si during pre-heating in MBE, using multiplied heater fluxes for the first 60 seconds of 1, 2, 3 and 4 times the minimum flux needed for the silicon to reach ~ 600^{o}C in the steady state condition. In each case, after 60 seconds the heater flux was reduced to the flux needed to reach a silicon temperature of 600K in the steady-state condition (corresponding to an overheating multiple of unity). Two silicon absorption functions were used at each heating multiple: one assuming free-carrier absorption at silicon temperature of 300K, and the other at silicon temperature of 600K. The heater temperature used was 975K and 1200K for silicon free carrier absorption temperatures of 600K and 300K, respectively. The heater power was 1.3kW and 3kW for silicon free carrier absorption temperatures of 600K and 300K, respectively. The heater emission spectrum was peaked at 3.0µm and 2.4µm for silicon free carrier absorption temperatures of 600K and 300K, respectively.

In conclusion of this section, it has been demonstrated that silicon substrate heating in typical MBE systems can result in the silicon overshooting subsequent steady state temperature values, due to the relative fast thermal response time of a silicon wafer in comparison to a typical molybdenum sample holder. This motivates the use of a hard power limit during large positive setpoint temperature changes within an MBE growth procedure for CdTe nano-structures on silicon substrates. Such could possibly be a helpful recommendation to achieve optimal results with nanostructures of different materials in the future use of MBE, or in other vacuum-based systems incorporating radiative sample heating.

In addition, an upper bound to the probable contribution of physical sputtering of CdTe during MBE growth by the incoming flux against the growing CdTe surface is estimated. The estimate suggests that the combination of reflection and desorption, in contrast to sputtering, must play a more significant role in the low incorporation rate of incoming CdTe flux typical of MBE growth of CdTe.

2.6.4 Cadmium Telluride on Silicon (CdTe/Si)

The history of crystalline films of CdTe on Si goes back as far as 1974; where single-crystalline wurtzite films were obtained on Si(111) in a background pressure of 10^{-7} Torr [122]. This work grew out of a campaign to grow thin film crystals of II-VI compounds on substrates such as Si and Ge; in which difficulty arose with sulfur reacting with silicon at a low temperature. The first CdTe single-crystalline films on Si grown by

MBE date back at least as far as 1983; where films were grown on Si(100) and (111), with indications of twin formation [123]. It was shown in 1986 that CdTe(111)B is preferred over CdTe(111)A and CdTe(100) for growth of HgCdTe, due to differences in the Hg condensation on those surfaces [124]. In 1988 it was shown that lower densities of twin defects could be obtained for growth of HgCdTe on a tilted (111)B surface, namely CdTe(211)B [125]; although there is still significant twin density near the CdTe-Si interface in such structures [126]. In 1989 Sporken et al. demonstrated that CdTe(111)B can be obtained under certain growth conditions on Si(100); and subsequently used as a substrate for HgCdTe(211)B growth [127]. During this time CdTe(211)B was established as the preferred orientation for subsequent single-crystalline HgCdTe growth.

Large area planar films of single-crystalline CdTe on Si have proven useful as alternative substrates to bulk CdZnTe for HgCdTe infrared detectors, where SWIR and MWIR detectors on Si have comparable performance to those fabricated on CdZnTe. HgCdTe/CdTe/Si detectors designed to absorb in the LWIR, however, are hampered by lattice and thermal mismatch. In particular, long-wavelength infrared (LWIR) HgCdTe detectors on Si substrates have an operability that is likely thwarted by high threading dislocation density (TDD) arising from this material mismatch [12].

It is believed by some that the lattice mismatch is more significant than the thermal mismatch for the formation of dislocations in CdTe on Si [128]. For certain thicknesses of CdTe on Si, this statement can be motivated quantitatively. The notion can be motivated by considering the lateral lattice mismatch on the (111) planes of CdTe/Si, and comparing to the known 5×6 nearly rationally commensurate registry at

the CdTe/Si interface [129], with the thermal mismatch generated after a typical MBE growth cool-down to room temperature. The comparison can be quantified with an estimate of the critical CdTe epilayer thickness as a function of mismatch [128], ε, above which dislocations will form spontaneously, as shown in Table 9. For thicknesses less than the critical thickness, the growth can be DL-free, although bearing stress due to the interface; within this regime the growth is termed coherent. In the table it is assumed that an array of interface misfit dislocations is completely confined to the interface in the case of the 5×6 registry; in this case, the growth is nearly rationally commensurate. In addition, in the table it is assumed that the thermal expansion coefficients of Si and CdTe are temperature-independent values equal to 2.6×10^{-6} K^{-1}, and 4.9×10^{-6} K^{-1}, respectively [101]. In practice, the first of these assumptions is likely not valid, because a realistic array of interface misfits will likely contain DL segments that turn up into the film, taking on threading character; however the assumption is useful in order to set an upper bound on the critical thickness. The results indicate that the lateral lattice mismatch should dominate in the formation of dislocations for CdTe(111) grown on Si(111). In the case of CdTe(211) grown on Si(211) the situation is similar along the (111) surfaces of the stepped (211) surface; however, in this case there are (100) surface planes as well. The (100) planes are thought not to introduce appreciable long-range stress or strain into the CdTe [130]; so as the film is grown thicker, the stress contribution due to the step edges will saturate without generating DL's. The thermal stress, however, could nucleate DL's if the CdTe film is grown beyond 25μm thickness; thus film thickness is limited by this value[10]. Thus, to alleviate the CdTe(211)/Si(211) mismatch thought to form ~1000 times

[10] Unless the area of the film is less than ~95nm in diameter; in which case the distortion of the film would not be sufficient to generate a single dislocation, due to the finite lower bound of possible burger's vectors.

higher dislocation densities in CdTe thinner than 25μm, compared with bulk CdZnTe(211), one should first focus attention on the lattice mismatch.

	Formula $\frac{\Delta L}{L}$	***Misfit***	***Critical Thickness*** $h_c \approx \frac{0.45}{\varepsilon^{3/2}}$ Equation 84
Bulk Lattices	$\frac{a_{CdTe} - a_{Si}}{a_{Si}}$	19.3 %	0.5 nm
5x6 Misfit Array	$\frac{5 \cdot a_{CdTe} - 6 \cdot a_{Si}}{6 \cdot a_{Si}}$	- 0.55 %	110 nm
Thermal	$\frac{e^{\alpha_{CdTe} \cdot \Delta T} - e^{\alpha_{Si} \cdot \Delta T}}{e^{\alpha_{Si} \cdot \Delta T}}$	- 0.069 %	24839 nm

Table 9 The materials mismatch of CdTe/Si involves lattice and thermal mismatch. The CdTe lattice constant is ~ 0.648nm and that of Si is ~ 0.543nm. Considering the known 5x6 registry of atoms at the typical CdTe/Si interface grown by MBE, we can see that lattice mismatch likely dominates in the formation of dislocations after the CdTe/Si is cooled from a typical MBE growth temperature of 600K, down to 300K. The thermal expansion coefficients of Silicon and CdTe were assumed to be constant values of $2.6 \times 10^{-6}\,\mathrm{K}^{-1}$, and $4.9 \times 10^{-6}\,\mathrm{K}^{-1}$, respectively [101].

As noted earlier, the apparent lattice mismatch between CdTe and Si is 19% (compressive); which is misleading, because the two crystal lattices are nearly rationally commensurate at a 5 to 6 ratio. Assuming there is a perfect array of misfit edge DL's confined near the interface between CdTe and Si, one obtains a -0.55% (tensile) mismatch (instead of compressive). This value is still significant, as any mismatch over ~2% is thought to effectively result in the formation of many DL's and the same general realm of epilayer crystalline quality [131]. The DL's that do form in CdTe on Si are thought to be largely present on the {111} planes with Burgers vectors of type $[1\bar{1}0]$.

The family {111} makes four of the particular glide planes most active for alleviation of stress in the plane of the epilayer (lateral stress). These planes intersect the (211) surface as shown in Figure 39 at an angle of 61.9 degrees with respect to the [211] direction [150]. As the epilayer is grown thicker the points of intersection of the DL's in the film with the surface of the film, naturally traverse across the film surface (no glide involved). As the DL's intersections, or ends, traverse across the surface they may encounter each other and react by fusing, annihilating, being locked in a Lomer Lock, or by repelling one another. Half the characteristic threshold separation within which two DL's may attract and move toward each other, is termed the fusion or annihilation radius. Speck et. al. [132] have used such a model, in conjuction with a classification of the possible DL's on the active family of glide planes, to predict the scaling of total DL density intersecting the film surface, as a function of film thickness; with the result being that the density is proportional to the inverse film thickness when the density is sufficiently high. In CdTe on Si, the dislocation density initially is believed to follow such a decay trend versus layer thickness, but slows down for thicker films; transitioning over to an exponential decay of the density with layer thickness [133]. Experimentally, the two trends in DL density versus epilayer thickness are observed to occur, and to reach a saturation density level; below which it has proven difficult to reduce the DL density level for CdTe/Si.

In the case of CdTe/Si for use in IR detectors the key question has been: what can be done to reduce the saturation level of DL's at the top of the film[11]? For other devices, such as solar cells, the IR question remains relevant, but an additional question may arrise: what can be done about the density of DL's within the majority of the film

[11] Or, what can be done to control the location of DL's in a device? For example: can DL's be removed from device pixels, or forced to aggregate at different locations in a device array of pixels?

volume? For IR detectors, the most obvious answer, is to grow the film thicker, but as mentioned previously, thicknesses beyond 25μm will spontaneously form DL's or cause delamination or cracking upon cooling to room temperature from a typical growth temperature.

Proposed and tested efforts to control dislocation density have included in-situ [145] and ex-situ [134] annealing, the introduction of buffer layers [129, 127], strained layer superlattice buffer layers [135, 136, 137], back-side thinned Si substrates [138], reticulated substrates, and patterned substrates. The last of these is tested under new specific conditions, reported on in this thesis.

In this thesis we draw upon established benefits of in-situ annealing and the incorporation of an interfacial ZnTe buffer layer from work of the past, while we investigate a new modified CdTe/Si interface structure to reduce the TDD in CdTe/Si, to approach bulk-grown CdZnTe quality. We anticipate that select CdTe seeding areas can be merged into a single coalesced large-area film of potentially lower TDD [139, 140], in part because remarkably positive results have been observed along these lines for GaN [141]. The primary underlying mechanism thought to be at work is the attraction of dislocation line segments to the free surfaces of the small seeding areas near the interface. Because the seeding areas are small before merging, they have a larger free surface area per volume, and thus are expected to have fewer dislocations, when compared to larger structures, such as a 3-inch wafer of CdTe on Si. A relatively inert material interfaced with CdTe can be expected to behave much as a free surface would; namely by attracting dislocation line segments to it. This is so, because it is the bonding across the interface

which transfers stress across the interface; if the interfacial bonds are weak, so will be the influence of the opposite material on the first.

For one dislocation in an isotropic continuous medium, the magnitude of the force per unit length attracting the dislocation to any free surface of the medium is expected to obey the form below (Equation 85), where it is clear there exists an analogy with the mutual force exerted between two infinitesimal current-carrying wires of electrostatics, see for example Jackson chapter 5 [104]. That analogy can only be carried so far however, as the Burger's vector does not, in general, follow the DL line direction; whereas for current carrying wires, the current vector is assumed always tangential to the wire direction, for thin wires. In addition, the image force for a current carrying wire would need to have the current in the same direction, whereas for DL's the Burger's vector for image forces is in the opposite direction. None the less, for image force calculations, one deals with the square of the Burger's vector; so provided the material is isotropic, the analogy holds for parallel DL's; and is an instructive aid.

$$F = \frac{\mu \cdot b^2}{4 \cdot \pi \cdot r}$$

Equation 85

Here μ is the elastic constant of the material, b is the dislocation burger's vector, and r is the distance from the free surface [142]. The r dependence of this formula suggests that if there exists an energy barrier to the movement of a dislocation, the dislocation will need to be sufficiently close to a free surface, in order for it to move toward that free surface, at a given temperature. Such a barrier can be envisioned as a Peierls-Nabarro

type barrier to DL glide [147]. Estimates of this threshold separation needed to attract a CdTe dislocation line segment to a nearby free surface can be obtained from half the dislocation fusion radius [143]. Practical estimates of this distance, in different material systems described in the literature, vary from 35nm [144] to 900nm [145].

It is also important to note that within the continuous medium approximation, an interface with a non-inert and stiffer material, can repel, rather than attract dislocation line segments from the interface; this is possible in CdTe at the interface to Si (when no patterning is present near the interface). This is so, because the elastic modulus of Si is approximately 3 times larger than CdTe; for comparison the same is approximately true of typical stainless steel compared to typical aluminum alloys [146]. Thus one can expect that small CdTe crystal volumes on Si would be valuable, as they could have relatively low TDD within their small volumes, when compared with large-area films of CdTe on Si.

Consider the contrast between dislocation loops in a planar film of CdTe on Si (Figure 38 (a)), versus the same loops within two small volumes of CdTe crystal on Si shown in Figure 38 (b). If the small volumes are small enough that their free surfaces are within the fusion radius of the dislocations inside them, then one would expect it is possible the dislocations would be unstable, and would thus spontaneously move to form an arrangement of lower free energy, such as is indicated in (Figure 38 (c)), provided the DL's are mobile. In that case it is seen that the dislocations have preferentially moved to the surface areas of the islands under image forces exerted on them, leaving nearly DL-free crystal within most of the two small volumes. If those two small volumes could be merged together by an isotropic crystal growth from their surfaces, one would find that

the number of DL loops intersecting the top surface of CdTe could be reduced, as indicated in Figure 38 (d). This can happen if the two Burgers vectors are in opposite directions [147] and come within twice the fusion radius of DL's. In contrast, if the Burgers vectors are not opposite the DL's cannot completely annihilate each other. Further, DL's may interact to form immobile, or sessile, DL's which are much more difficult to remove from the material.

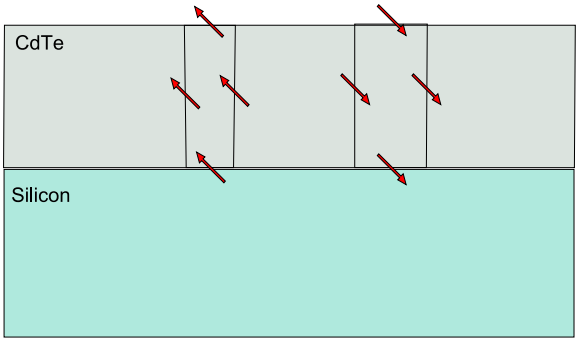

(a)

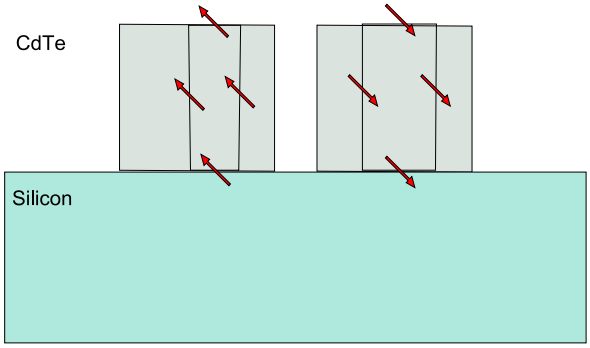

(b)

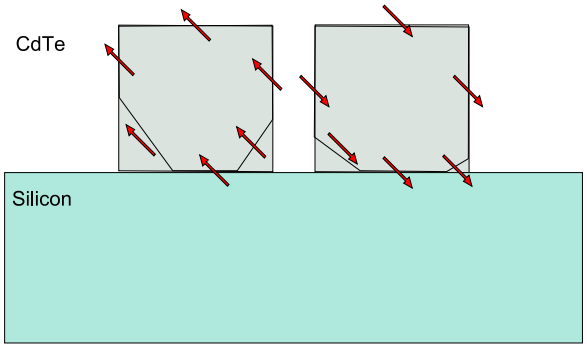

(c)

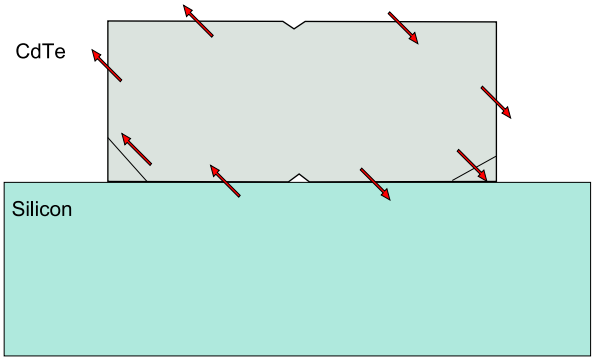

(d)

Figure 38 A schematic series of pictures illustrating the potential reduction in TDD of CdTe first within small volumes, and second within a coalesced film. A planar film of CdTe/Si is shown in (a) containing two DL loops with red arrows indicating the Burgers vectors. In (b) is a potentially unstable situation, in which the DL loops can reduce the system free energy by gliding to the side walls of the small volumes, provided they are mobile DL's. If this gliding were to take place the result may look as shown in (c). If the result in (c) was then coalesced, by uniformly growing the small crystal volumes together, then the total TDD intersecting the top CdTe surface could be reduced, as compared to the situation in (a).

Real crystals are not generally isotropic, and indeed, CdTe is not. This is important to consider in the theoretical pictures above, indicating the motion of DL's. In CdTe there are preferred directions for the formation and movement of DL's. In CdTe the DL's preferentially glide on {111} with $[1\bar{1}0]$-type Burger's vectors (of typical length 0.458nm). Thus, in asymmetric small volumes of CdTe, for example long rectangles when viewed from above, it could be apparent that DL's could show preferential glide to certain sidewalls of the small volume, rather than others, depending upon the relative orientation of the glide planes with respect to the side walls. Results in partial agreement with this line of reasoning have, in fact, been observed by Stoltz et al. [148] in the case of large HgCdTe(211) mesas, and Martinka et al. in HgCdTe(211)B on reticulated CdZnTe substrates [149], although neither mentioned this line of reasoning. A simple picture to explain the asymmetry contribution explained here is given below (see Figure 39). In Figure 39 the intersection of the active {111} glide planes with the (211) surface is indicated by a series of lines. Such lines follow the observed cross-hatch pattern seen after HgCdTe(211) growth by MBE [150]. The active glide planes intersect the sidewalls of a cube of CdTe, with top-surface oriented along [211] at angles of 35.26^{o} and 70.53^{o}; where the angle is specified between the normals of the surfaces. Thus, if a force is pulling a given DL to a sidewall, with the added constraint that the DL remain in the active glide planes (related to cross-hatch), then the resultant DL motion will likely be greater toward $[\bar{1}11]$-type side walls, rather than toward $[0\bar{1}1]$-type side walls. This asymmetry should be considered when fabricating small volumes of CdTe, with the intention of reducing their DL concentration by attraction to the sidewalls.

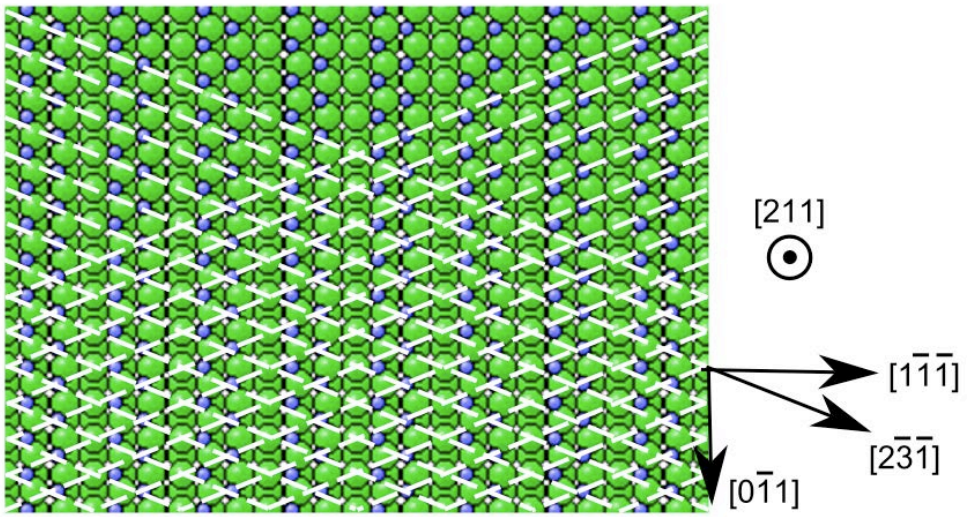

Figure 39 A schematic CdTe(211) surface is shown with lines indicating the two active types of {111} intersection angles with the surface. DL's may preferentially glide by image forces to the left and right edges in the figure, as opposed to the top and bottom. The intersection of the {111} glide planes with [211] coincides with [$\bar{2}$31] and [$\bar{2}$13] directions in the plane of the surface. Considering the 3-dimensional tilt of the glide planes with respect to the side walls gives tilts of 35.3^{o} and 70.5^{o} between the normals of the active glide planes and normals of the [0$\bar{1}$1] and [$\bar{1}$11] side walls, respectively.

Experimentally it has been reported that micro-scale islands of CdTe/Si can be made of low TDD in limited regions. Molstad et al. claim low TDD can be obtained on the top surfaces of 20μm – wide CdTe mesa regions grown on patterned Si(211) substrates [151], however they observe high TDD at the merging regions of their mesas. In addition, they coalesced their micro-scale islands into one film; which showed a significant surface corrugation due to the initial seed island separation, resulting in a height change of ~1 to 2 μm across the surface. They also observed a high TDD in the areas where islands merged. The work of this thesis can be viewed as an effort to improve upon their results, as we have coalesced smaller seeding volumes of CdTe, more closely spaced; as described in the following pages.

An idealized cross-section of our investigated nanopatterned interface structure is shown in Figure 42 (d) of the next section. The cross-section illustrates several specific possible benefits of such an interface architecture as compared to the typical traditional planar CdTe/Si interface with buffer layers; these are:

1) Reduced dislocation density: by increased localization and trapping at free and partly free surface near the interface.
2) Disconnection of impurity-activated dislocations from the CdTe top surface.
3) Trapping of impurities originating from the Si substrate[12] [152].
4) Utilization as a trap-assisted tunnel junction within a multijunction solar cell.

This thesis reports on our efforts to realize this intended architecture utilizing Selective Area Epitaxy (SAE) and coalescence; as discussed in the following pages of this thesis.

[12] This may find marked application with GaAs substrates, where substrate diffusion into CdTe epilayers is a concern for IR detector performance. Also note that 30" XRD FWHM has been reported for CdTe/GaAs by Carmody et al. at the 2011 U.S. Workshop on the Physics and Chemistry of II-VI Materials.

2.6.5 Selective Area Molecular Beam Epitaxy

Selective Area Molecular Beam Epitaxy utilizes the general technique of MBE, with the added stipulation of some level of control over the growth accumulation areas, typically as a function of lateral position on the substrate surface. This can be accomplished in several ways, two of which are highlighted here. Those two ways utilize: (1) shadow masking [153, 154, 155]; and (2) sticking coefficient control achieved with chemical patterning of the substrate surface; for example for films of InGaAs [156], GaN [194, 157, 158], GaAs [159], Si_xGe_{1-x} [172], and CdTe [160, 161, 162, 111]. Generally researchers performing SAE have utilized either geometrical or chemical structures different from the ordinary planar substrate, or both.

A similar, but distinct surface modification arises for "reticulated" substrates; where a single material is patterned to have purely geometrical surface structures that may cast significant flux shadows during MBE growth, but usually not enough to completely block growth at any area of the substrate, particularly with the common usage of sample rotation. Research on reticulated substrates has also been extensive; including GaAs substrates [163], Si [164, 165, 166, 167], and CdZnTe [168, 169]. In these cases, often the goal was similar to that of this thesis: to achieve a local reduction in DL density; and this was reported to have been achieved to some extent, within limited areas of the samples.

Shadow mask techniques are limited by diffraction of the flux molecules unless the mask is extremely close to the sample; they are also prone to accumulation of flux within the mask windows; and they may require lift-off or removal of the mask after

growth. In the case of reticulated substrates, the realization of free surface trapped near the epilayer interface to the substrate becomes more difficult to achieve while simultaneously ensuring the growth areas are small enough to have DL reduction. In addition, applications exist for large area films of low defect density; for example solar cells. Thus the second highlighted SAE technique is preferred: namely, that which achieves selectivity through the chemical nature of the surface.

In direct relevance to this thesis, Sporken et al. have demonstrated such chemical SAE of CdTe on stripes of CdTe 5μm wide, separated by 15μm of SiO_2 [160]. In this thesis we confirm SAE of CdTe against SiO_x and demonstrate for the first time SAE on smaller seeds of CdTe, of width 250nm, exposed at the base of windows in a thin overlayer of silicon nitride. In addition, we observe for the first time, the use of electron-beam induced carbon deposit as a CdTe SAE mask.

It is a general trend within the literature, that mask materials for SAE are very frequently one of the following materials: SiO_2, Si_3N_4, or carbon[13]. The reason for the success of such materials as chemical masks may be rooted in the relatively strong bonds within the materials. Thus, when a foreign molecule is incident upon such a mask surface, the physical and chemical bond formation of the molecule to the surface is weak, compared to other non-inert material surfaces. An indicator of the inert nature of a material can be obtained by considering the diatomic bond strength of the constituent atoms in isolated dimers. A table is presented below, for reference, indicating the diatomic bond energy for relevant atoms of this thesis (see Table 10).

[13] The carbon has been reported in some cases as being in diamond form, but that claim is suspect according to electron microscopy experts.

Molecule	*Dissociation Energy (eV)*
CO	11.18
SiO	8.30
C_2	6.42
SiC	4.64
SiN	4.54
SiTe	4.46
TeO	3.91
Si_2	3.22
Te_2	2.67
CdO	2.45
ZnTe	1.22
CdTe	1.04

Table 10 Diatomic molecule dissociation energies for materials relevant to SAE; after reference [101].

It is seen from the table that the typical mask materials' atoms have high diatomic bond energies in dimer forms. It is also seen that Cd and Te have relatively strong bonds to Si and O, when compared with the CdTe bond. Thus, it is somewhat surprising that SAE of CdTe is possible against SiO_2 or Si_3N_4 mask materials. It is shown in this thesis, that trace amounts of Te are present on the mask material after SAE of CdTe by MBE on these mask materials; yet the growth is still considered selective, because only a fraction of a ML accumulates on the mask materials, while at least 0.5 μm of material may accumulate on CdTe under the same growth conditions and duration.

Selective growth can only be achieved with the proper surface materials or architecture, and growth conditions. If the substrate temperature is too low or the incoming flux too high, then selectivity may not be obtained for a given substrate, and/or single crystal growth may not be obtained. Thus, there exist bounds in growth conditions for single crystalline selective growth; where incoming flux grows single crystalline material at the selected areas, and not the mask. In the case of MBE there also exists a

maximal substrate temperature bound, above which incoming flux will not accumulate appreciably anywhere on the substrate. Thus, there exists a two-dimensional window in flux and substrate temperature, within which SAE by MBE is possible.

In the case of CdTe, the maximal temperature for SAE appears somewhat dependent upon the surface crystallographic orientation. Below, is reproduced the sticking coefficient for CdTe flux on CdTe(111)B and CdTe(100) from Behr et al. and Sporken et al. [112, 113] (see Figure 40); where it is seen that CdTe(100) has a higher homoepitaxy cutoff in substrate temperature. The presence of a difference in the two curves is not very surprising, as the bulk-terminated surfaces have different surface atom bond coordination, as well as dangling bond densities. The difference in the curves comes mostly in the region where the chemisorption surface energy dominates the trend (according to the previous fitting results discussed in this thesis); thus the difference in the curves seems to originate from the difference in dangling bond densities.

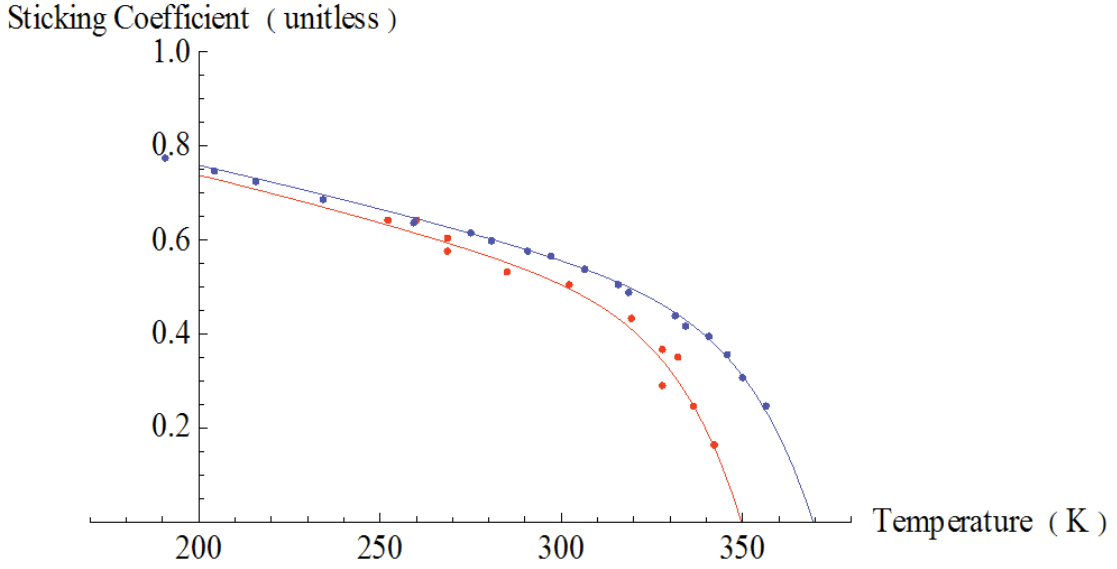

Figure 40 Sticking coefficient of CdTe flux on CdTe(111)B shown in red, and CdTe(100) shown in blue (upper curve), as a function of the substrate temperature. It is seen the CdTe(100) has a higher temperature cutoff for homoepitaxy.

In this thesis we investigate the following substrate surface with CdTe(211)B seeding regions defined geometrically and chemically with respect to a silicon nitride mask, as shown schematically in cross section below (see Figure 41).

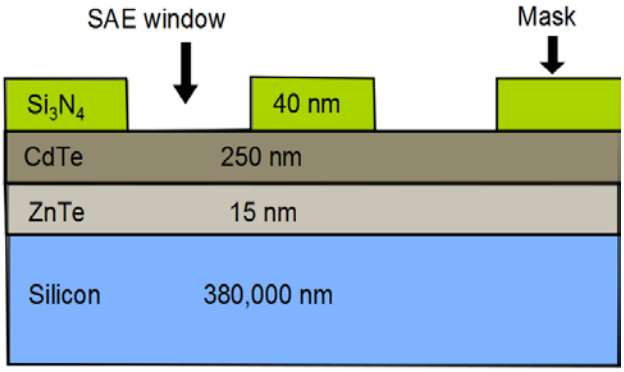

Figure 41 Schematic cross-section of a patterned sample, fabricated by reactive ion etching (RIE) and interferometric lithography. The corresponding unpatterned samples had the same cross-section except for the silicon nitride mask, which was not present. Each pair of patterned and unpatterned samples was loaded symmetrically into a Mo sample holder which was rotated in the plane of the samples, about its center during growth.

Under conditions of SAE, the following time series depicted in Figure 42 is expected to unfold. Flux accumulates selectively, islands form and blossom vertically and laterally, coalesce, and grow further. The blossoming islands should have a lower DL density within their volumes, because their size is of the order of the annihilation radius mentioned previously. When the islands merge, they may generate grain boundaries and thus, DL's; however such DL's may not be directly connected to the Si substrate, thus disabling them from channeling destructive impurities upward in the epilayer toward subsequently fabricated HgCdTe diodes.

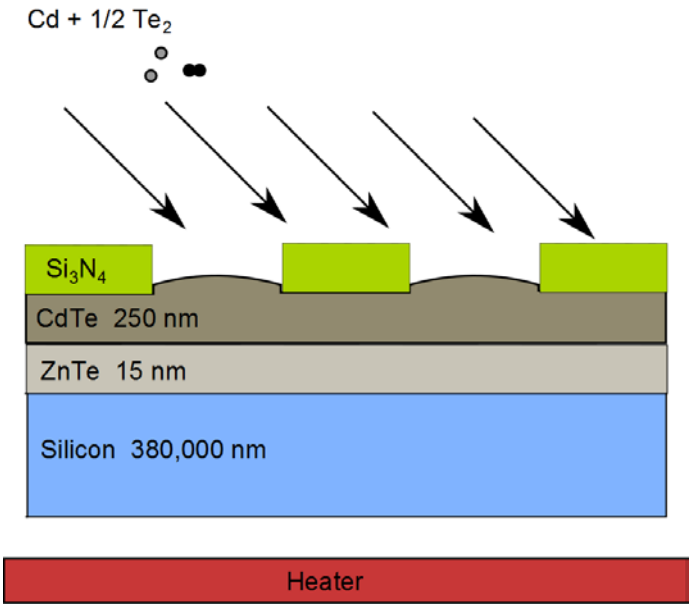
Cd + 1/2 Te2
Si3N4
CdTe 250 nm
ZnTe 15 nm
Silicon 380,000 nm
Heater

(a)

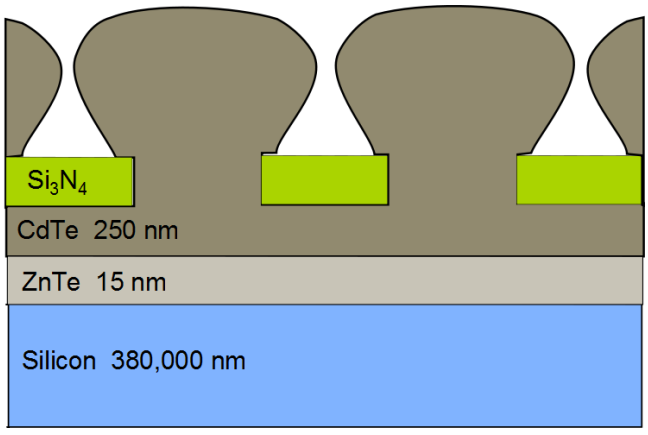
Si3N4
CdTe 250 nm
ZnTe 15 nm
Silicon 380,000 nm

(b)

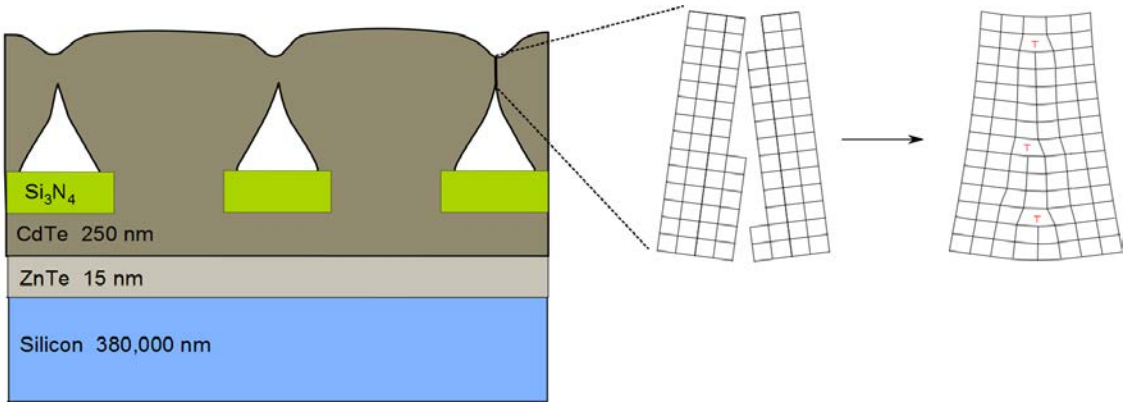

(c)

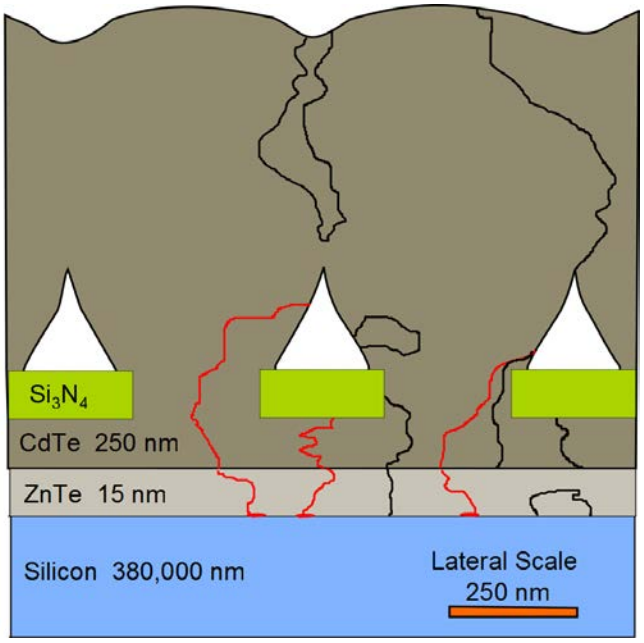

(d)

Figure 42 A schematic time series of the selective growth and coalescence of CdTe on the seeding array investigated in this thesis. Part (a) shows the initiation of the selective area growth; part (b) shows a subsequent upward and outward blossoming of each seeding area; part (c) shows an instant after the merging on neighboring islands, at which time dislocations and grain boundaries may be incorporated into the coalesced film at the areas of merging; part (d) shows a coalesced film with surface corrugation correlated to the initial seed island spacing and the lateral to vertical growth rate ratios, with dislocations that are trapped, blocked or disconnected from deleterious diffusing impurities (in red) at the silicon interface. Part (d) also shows the presence of completely free CdTe surface near the silicon, above the mask region and under the coalesced film; as well as partially free surface where the CdTe contacts the mask.

The idealized structure above also contains free CdTe surface near the interface to the silicon, where it can act to trap DL's. Also, the mask, due to its relatively inert nature, can act as a partially free surface, to attract and trap DL's. The empty volume bounded by the completely free surface can also act to attract and trap mobile impurities in the epilayer (which may originate from the substrate). Finally, the structure also has the ability to directly block DL's which terminate underneath the mask.

Such a nano-structured interface has the potential to enable higher quality LWIR HCT diodes on Si. In addition, potential may exist for higher quality CdTe/Si in general, including high efficiency single crystal solar cells [170], which in the case of III-V cells, can be limited by TDD crossing the p-n junction [171, 172].

In conclusion SAE is a well researched topic for many thin film crystalline materials; and has several common features: including chemical and geometrical structuring of a substrate surface, and the use of relatively inert mask materials. In the case of CdTe SAE by MBE a particular window in substrate temperature and flux exists; and has been demonstrated. The use of CdTe SAE in this thesis has realized a new structure with potential benefit to IR detectors and solar cells; and has introduced two new mask materials for SAE.

3 Experimental Results and Discussion

3.1 Surface Preparation

MBE is naturally a surface sensitive technique, and thus surface cleaning prior to crystal growth is essential. The common surface cleaning involves an ex-situ chemical etching of the substrate surface to remove contamination, including oxides; followed by an in-situ outgassing at elevated temperature, followed by a thermal desorption of weakly bound surface contaminants. In principle, CdTe can be cleaned in-situ by thermal means only; but requires either higher temperatures of longer hold times. An example of thermal surface cleaning of CdTe(211)B, with no pre-etching, observed by XPS, is shown below (see Figure 43). Usually one does not clean a given substrate surface by thermal heating alone; as this introduces more surface roughness than is necessary. It should also be noted that CdTe can also be cleaned in-situ with hydrogen plasma etching of the surface [93]; but this technique was not used in this thesis.

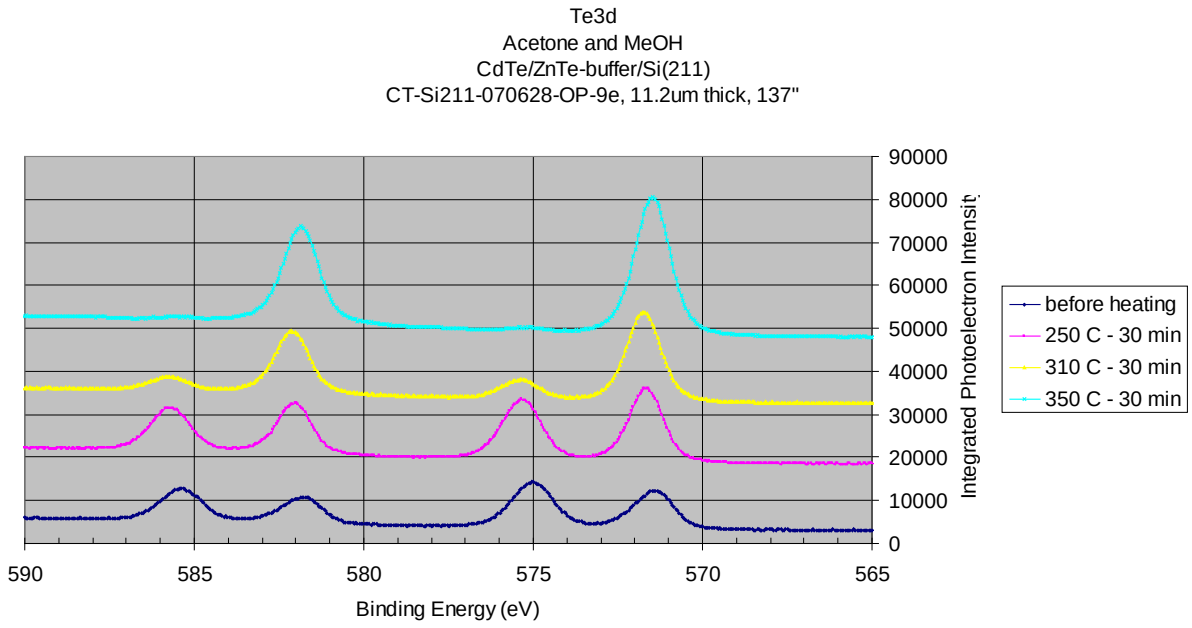

Figure 43 This XPS data demonstrates the thermal removal of surface oxide on CdTe(211)B on Si. The data shown are for $Te3d_{5/2}$ and $Te3d_{3/2}$ states; with obvious oxide present. The lowest blue curve is before any treatment, and after oxidizing in air for over one year. Each higher curve was heated to 250, 310, and 350°C, respectively; then cooled to room temperature before XPS data acquisition. At 350°C significant CdTe desorption is expected to have taken place.

For ex-situ surface etching of CdTe, acidic solutions containing HI [173, 174], HNO_3 [175], HCl:H_2O [176, 177, 178, 179], Br:Methanol [175, 180, 110], and HBr:H_2O_2:H_2O [175, 180, 110, 181, 182] are all capable of removing CdTe oxides and CdTe at a fairly controlled etching rate based on concentrations in the solution. It should be noted that it is believed that the HBr solution produces Br in solution, which preferentially etches and removes Cd over Te. Some noteworthy diatomic bond energies may be relevant, as in the case of SAE, to make relative comparisons of the qualitative strengths of different etching solutions; these are shown below in Table 11.

Molecule	*Dissociation Energy (eV)*
TeO	3.91
CdO	2.45
CdCl	2.16
CdBr	1.65
ZnBr	1.43
ZnCl	2.38
CdTe	1.04

Table 11 Diatomic molecule dissociation energies for materials relevant to surface etching/cleaning prior to MBE; after reference [101].

The values of the table above indicate, for example, that HCl solutions may etch CdTe faster than Br solutions with similar percentages of Br and HCl. This is not always the case, however; because the etching rate depends upon many processes, including the dissolution rate of reacted surface species.

In this thesis, the standard technique of ex-situ acidic wet chemical eching of our CdTe epilayers is performed in order to remove CdTe surface oxide and contamination prior to low-temperature thermal cleaning, and subsequent MBE growth in ultra high vacuum. Typical bulk CdZnTe or CdTe MBE substrates are over 100 μm thick and can be etched without careful regard for the total amount of material removed during etching, provided the resulting surface is clean and relatively smooth after preheating in vacuum to ~ 250^{o}C [183]. In the case of nano-scale CdTe seeding structures, however, a gentle etch is needed to conserve the material, and could be helpful for cleaning II-VI nano-scale structures which may be fabricated in the future.

Two wet chemical etches were employed in our SAE investigations: one HBr etch intended to minimize the surface damage layer typically formed after etching, and one HCl etch to achieve a clean or fresh surface at the expense of more surface damage. These two etches were tested on a 250nm thin, MBE-grown film of CdTe/ZnTe/Si(211)

using XPS, after the film had oxidized in air for over 1 year. The inset of Figure 44 (a) shows an SEM cross-sectional view of one piece of this test sample. Pieces from the same wafer were used for all our XPS etching studies, with each piece being etched only once.

XPS spectra from the surface of the samples were recorded using a SSX-100 spectrometer, with a hemispherical analyzer operating at constant pass energy, and a quartz-filtered monochromatic Al K_α x-ray source of photon energy hν=1486.6eV. The x-ray spot size on the sample surface was 0.5 to 1mm in width. The energy resolution in acquired data is expected to be less than 0.8eV. The pressure level in the analysis chamber was below 1×10^{-9} Torr during the measurements, with a background pressure of $\sim3\times10^{-10}$ Torr. Samples were held with spring clips to a stainless steel sample holder. Heating of the samples was performed between room-temperature data acquisition routines, with the sample holder pointed away from the spectrometer, and using a pyrometer and backside-thermocouple to monitor the sample holder temperature.

The zero of the binding energy scale was calibrated using the C 1s peak from adventitious carbon contamination at 284.5 eV. Data fitting was performed using an approximation to the convolution of a Gaussian and Lorentzian profile for each electron state detected, with Shirley background. An effort was made to use the minimum number of peak-components resulting in a good fit to the data. Resultant peak positions from fitting were compared to the XPS Database version 3.5, made available online by the National Institute of Standards and Technology (NIST) [184]. There are at least three clearly distinquishable chemical states of Te on the CdTe surfaces reported here: Te^0, Te in CdTe, and Te-oxide (Te in forms TeO_2 and TeO_3). Using the NIST database, the

binding energy for electrons in the $Te3d_{5/2}$ state is expected to be 573+/-0.3eV for Te^0, 572+/-0.2eV for CdTe, 576+/-0.4eV for TeO_2, and 577+/-0.5eV for TeO_3. Also, the binding energy of electrons in the $Cd3d_{5/2}$ state is expected to be 404.9+/-0.2eV for Cd^0, and 404.6+/-1eV for CdO. These values are listed below in Table 12 for reference.

Compound	***Electron State in Atom***	***Binding Energy (eV)***	***Standard Deviation (eV)***
Te	Te $3d_{5/2}$	573.0	0.3
CdTe	Te $3d_{5/2}$	572.6	0.2
TeO_2	Te $3d_{5/2}$	576.1	0.4
TeO_3	Te $3d_{5/2}$	577.0	0.5
Cd	Cd $3d_{5/2}$	404.9	0.2
CdO	Cd $3d_{5/2}$	404.6	1.1
C	C 1s	284.5	-

Table 12 Several electron binding energies to atoms relevant to this thesis, after reference [184].

The extent of oxidation of the sample surfaces was quantified assuming a uniform 3-layer model consisting of a Te-oxide top layer, a Te^0 intermediate layer, and a semi-infinite and uniform CdTe substrate layer underneath (see Figure 15). We approximated the mean free path of photo-electrons from $Te3d_{5/2}$ to be 2.5nm through both layers [88]. With this model the oxide over-layer thickness was calculated [93]. Scofield's photoionization cross-sections were used to calculate the Cd to Te ratio of the samples' surfaces by the normalized ratio of peak areas: $Cd3d_{5/2}$ / $Te3d_{5/2}$ [87]. The combined influence of the photoelectron mean free path and the spectrometer collection efficiency was taken to scale with photoelectron kinetic energy as $E^{0.7}$.

The sample results are detailed in the following paragraphs. The first etch solution, HBr : H_2O_2 : H_2O (0.1 : 0.16 : 300), was used to etch 250nm epilayers of CdTe/ZnTe/Si(211) for 10 sec, after a 15 min equilibration of the solution. This dilute

HBr etch was confirmed to create a small damage layer of Te^0 on the surface, 1.5nm thick, with some Te-oxide present, 0.1 nm thick. The damage layer and oxide were found to be removable by heating to 250^{o}C (see Figure 44). After HBr etching and heating to 310^{o}C, the Cd/Te ratio was found to be 0.98. The Cd content of the surface was not appreciably diminished, despite there likely being many crystal defects intersecting the film surface before etching, including twins and dislocations [129]. The amount of material removed by the etch can be estimated from a reported etch rate of HgCdTe in Kiran's thesis [110], of 680nm/30s for HBr : H_2O_2 : H_2O (10 : 1 : 60). Using that value, and assuming the etch rate is identical for CdTe as well as linear in HBr concentration, one obtains an etch rate estimate for CdTe of 0.008 nm/s (or 0.5 nm/min), for HBr : H_2O_2 : H_2O (0.1 : 0.16 : 300) which corresponds to a total CdTe removal during the 10 second etching described above of less than 1 ML. At this etch rate, one should not expect to completely remove a typical CdTe oxide in 10sec, unless the oxide etches at a faster rate than CdTe. The etch rate, is however, very approximately estimated here.

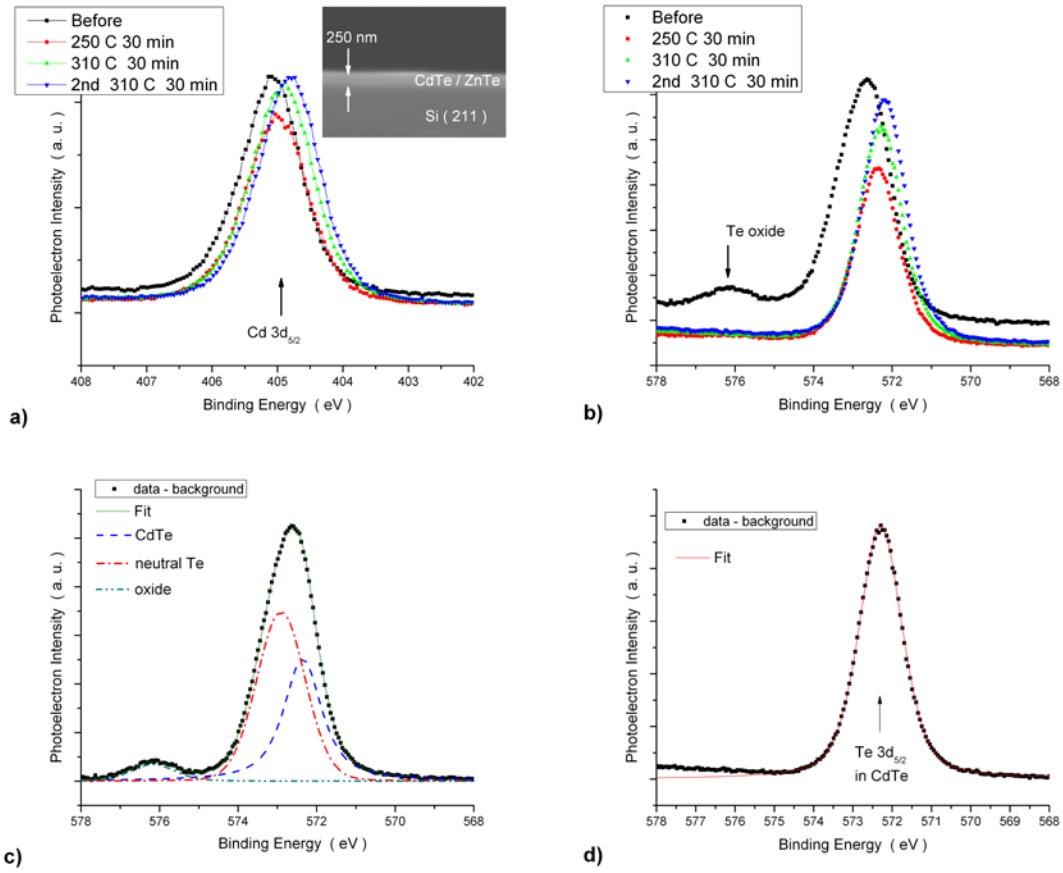

Figure 44 These plots show the result of etching and heating the surface of a 250nm thin layer of CdTe/ZnTe on Si(211) with HBr : H_2O_2 : H_2O (0.1 : 0.16 : 300) for 10 sec, after a 15 min equilibration of the solution. In the figure captions the label "before" indicates after etching and before heating. The XPS signal is mainly due to $Cd3d_{5/2}$ photoelectrons in a) and $Te3d_{5/2}$ in b). The Cd signal is not appreciably diminished or shifted in energy after heating. The Te signal can be modeled to be 1.5nm of Te^0 below 0.1nm of Te-oxide present after etching, but before heating. Parts c) and d) show the fitting results, with a contribution only from CdTe, after heating to 310°C. The fitted Shirley background has been subtracted from the data in the plots with curve fits.

The second etch solution, HCl : H_2O (11.5% HCl), was used to etch 250nm epilayers of CdTe/ZnTe/Si(211) for 1 min, after a 10 min equilibration of the solution. This HCl etch was found to produce a similar damage layer. After HCl etching and heating to 310°C, the Cd/Te ratio was found to be 0.93. The XPS data is shown for the HCl etched film in Figure 45. If one assumes that the etching rate of the HCl solution is

equal to the HCl concentration multiplied by a constant, and that the same constant can be used analogously to describe the HBr etch rate as a function of HBr concentration, then one arrives at an estimated etch rate for 11.5% HCl of ~18nm/s; far in excess of what is observed here. One possible explanation is that the dissolution of reacted surface species may play a role in slowing the etch rate by covering the surface more than in the case of the HBr etch.

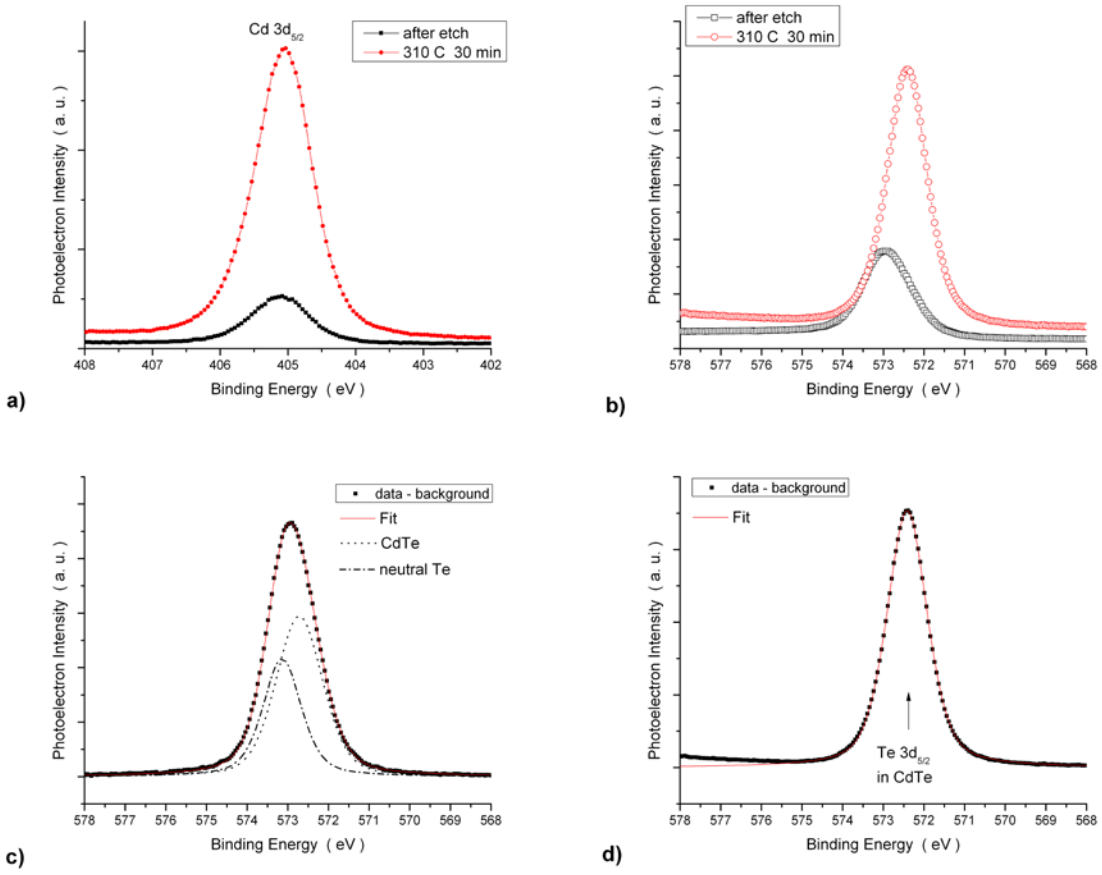

Figure 45 These plots show the result of etching and heating the surface of a 250nm thin layer of CdTe/ZnTe on Si(211) with HCl : H_2O (11.5% HCl) for 1 min, after a 10 min equilibration of the solution. The XPS signal is mainly due to $Cd3d_{5/2}$ photoelectrons in a) and $Te3d_{5/2}$ in b). The Cd and Te signals grew in intensity after heating. Fits to the data in part b) are shown in parts c) and d). The Te signal shows significant Te^0 present after etching, but only CdTe after heating to 310°C for 30 min. The fitted Shirley background has been subtracted from the data in the plots with curve fits.

In conclusion of this section, HBr and HCl acidic ex-situ surface cleaning etches for CdTe have been demonstrated to be very mild and somewhat mild, respectively. Each etch has been shown to be capable of sufficiently preparing a CdTe(211)B surface for MBE, after preheating under UHV. These etches may be useful for preparing nanostructures of CdTe, or other II-VI compounds, for MBE growth, or other processing.

3.2 Molecular Beam Epitaxy

3.2.1 Nanopatterned sample formation

Nanopatterned substrates were fabricated for the work of this thesis following the general interferometric lithography methods outlined by Hersee et al. [185]. First thin CdTe/ZnTe/Si(211) samples were prepared using established single crystalline growth procedures for CdTe(211)B on Si by MBE. The samples were then diced, coated in photoresist and exposed to two interfering laser beams (see Figure 46), such that an interference pattern was burned into the photoresist. That pattern was then transferred down into the epilayer by removing the burned photoresist and utilizing a reactive ion etch to remove CdTe in exposed areas.

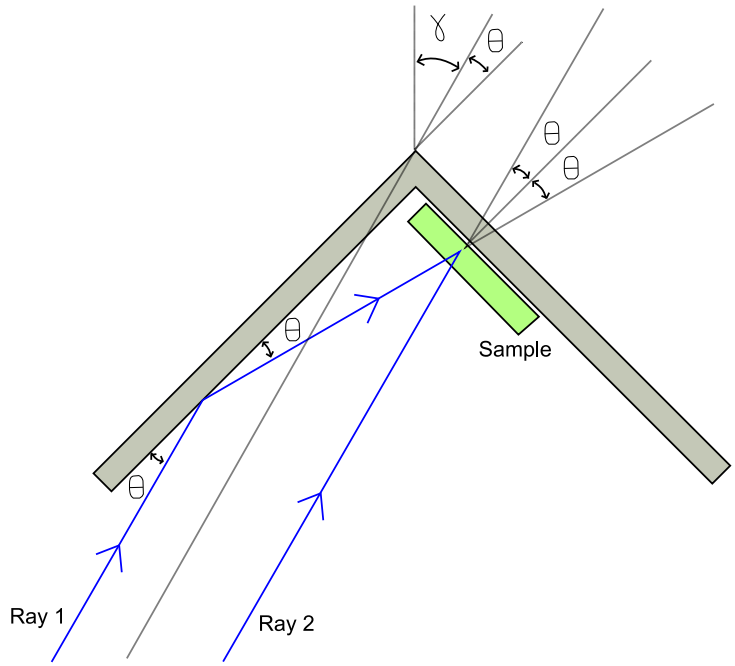

Figure 46 Schematic corner mirror configuration to cross two coherent laser beams (indicated by "Ray 1" and "Ray 2") incident on the sample surface during nanopattern formation. The angle γ can be used to tune the pitch of the resulting interference pattern on the sample surface. The sample can also be rotated about its surface normal, between laser exposures.

In such a process, the period length across the sample surface of the interferometric pattern, d, is determined by the wavelength of the laser illumination, λ, the relative propagation angle of the two beams, ψ, and the real part of the index of refraction outside the photoresist, n, as shown schematically in Figure 47 under the condition of γ=0 from Figure 46. Although the propagation direction changes for the beams within the photoresist, due to Snell's law; the wavelength also changes, resulting in the same spacing of interference fringes inside and outside the photoresist. In principle both incoming beams should be reflected before encountering the sample, to ensure equal partial polarization of each beam; thus ensuring the maximal contrast in intensity fringes of the interference pattern; however such is not necessary.

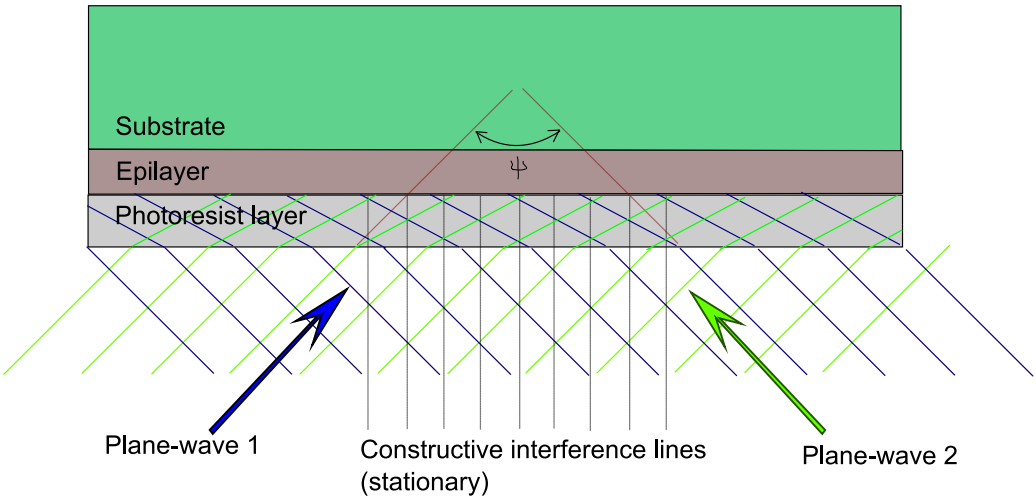

Figure 47 Interferometric lithography begins with the definition of an interference pattern in a photoresist layer, such as that shown here, resulting from two intersecting plane-waves (whose wave fronts are indicated in blue and green at one moment in time). The photoresist covers an epilayer which will later have the interference pattern transferred to it using an etch. The spacing of consecutive constructive interference fringes in the photoresist is set by the wavelength of the coherent illumination used in the two plane waves, the angle ψ, and the index of refraction on the incoming-side of the photoresist.

From the geometry of Figure 47 above, one can easily derive the relation for the pattern pitch (periodicity) as a function of the variables mentioned, as follows:

$$d = \frac{\lambda}{2 \cdot n \cdot \sin\left(\frac{\psi}{2}\right)}$$

Equation 86

Thus, in the case of the off-axis illumination shown in Figure 46, the spacing is:

$$d = \frac{\lambda}{2 \cdot n \cdot \sin\left(45^o - \gamma\right)}$$

Equation 87

By varying the angle ψ, one can produce interference patterns with periodicity no smaller than the wavelength over twice the index of refraction. By varying γ , one can in principle obtain a pattern of any larger periodicity; however the maximal laser beam diameter will limit this in practice. The fabrication of the samples reported on in this thesis utilized λ=355nm, $\gamma = 24.2^o$ ($\theta = 20.8^o$), and n~1; thus yielding a pattern pitch of ~500nm. By repeating the exposure of the photoresist to the interference pattern at multiple sample in-plane angles, a 2-dimensional array of islands was formed. Several such nanopatterned arrays were formed in thin silicon nitride layers on thin epilayers of CdTe/ZnTe on Si(211) substrates for this thesis; the surface of one is shown below in Figure 48, imaged via tapping-mode AFM. The resulting seeding window density is 4×10^8 windows/cm^2.

The quality of the patterned samples, particularly the transfer of the pattern to the correct depth, was evaluated by XPS, SEM, and AFM. This evaluation process resulted in some samples being eliminated from further experimentation.

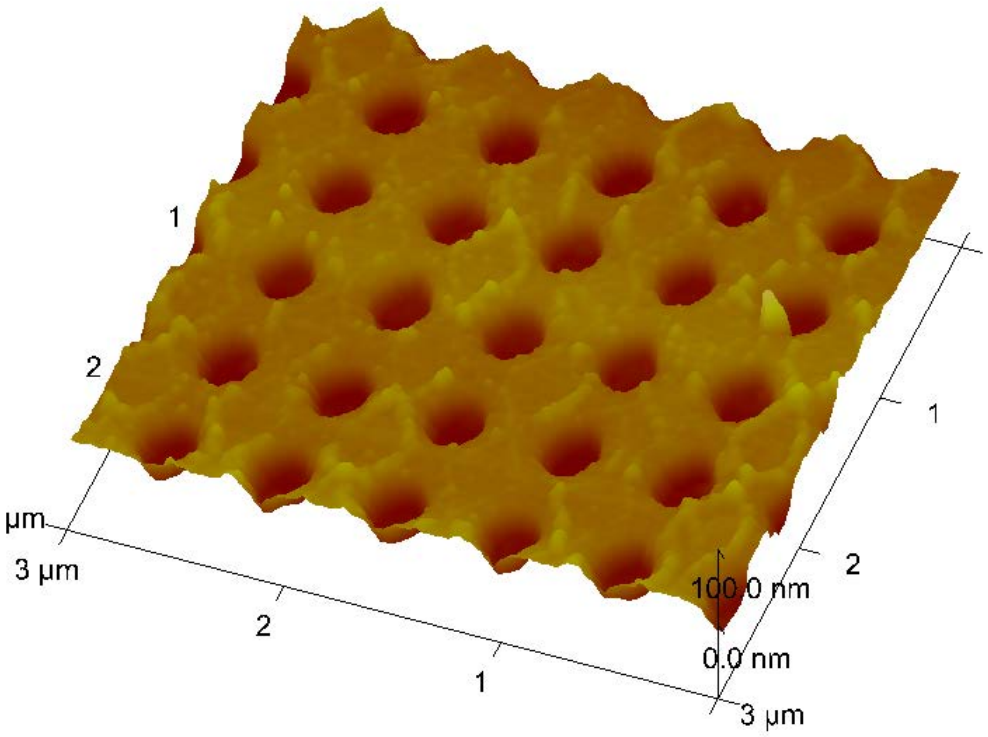
1
2
µm
3 µm
2
1
100.0 nm
0.0 nm
3 µm
1
2

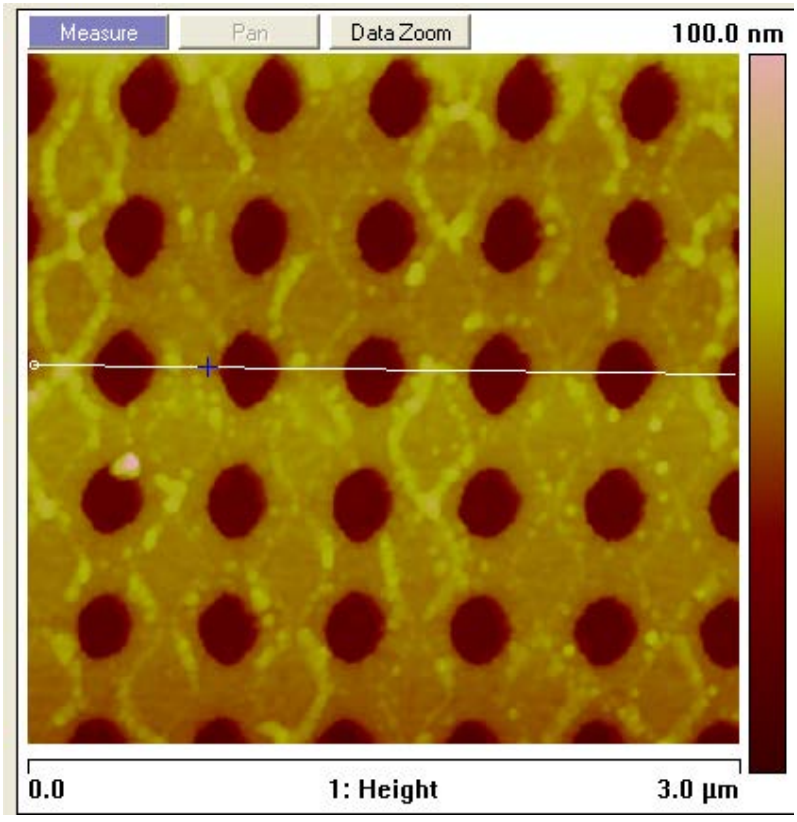
Measure
Pan
Data Zoom
100.0 nm
0.0
1: Height
3.0 µm

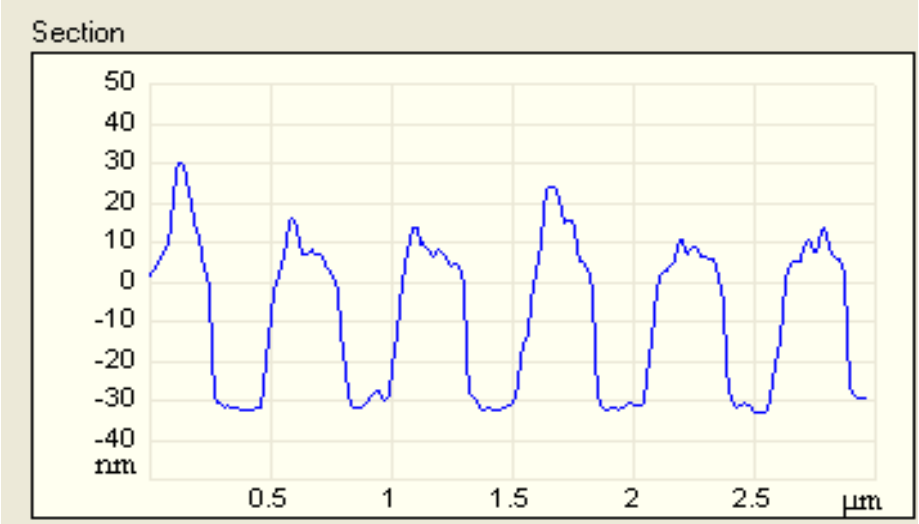

Figure 48 This figure shows tapping mode AFM height data of the center of a patterned sample of Si_xN_y mask on a 250nm epilayer of CdTe/ZnTe on Si(211) before etching or SAE. The mask thickness is approximately 40nm, and the pattern pitch is 500nm, giving a CdTe seeding window density of 4×10^8 cm^{-2}. The vertical scale in the first two image renderings spans from 0 to 100nm. The sample imaged here was used as the patterned sample of set IV, described in a later section of this thesis.

Note that a pattern pitch of 500nm is shorter than the shortest wavelength within the LWIR band divided by the real part of the index of refraction of CdTe $\left(\frac{8\mu m}{2.67} \approx 3\mu m\right)$; but not by a large amount. In a typical backside-illuminated detector on silicon with such a nanopatterned interface, the IR diode array will be no closer than ~10μm from the pattern; in this situation the first-order diffraction maxima will be present at ~60μm from the normal propagation direction [44]. As the pixel pitch may be ~20μm; diffraction could in principle be an issue for focal plane array resolution. However, diffraction is likely not an extremely significant issue, because the mask material is close in index (2.05) to the surrounding material (CdTe). It also helps that all the materials are relatively IR transparent; for example silicon nitride has a bandgap of 5eV, albeit with some LWIR absorption at 11.5-12 μm [102]. For smaller pattern pitch, diffraction should become less of an issue. Such diffraction may also possibly be used to enhance absorption in a superlattice detector.

3.2.2 Selective growth of CdTe against silicon oxide and silicon nitride

To perform SAE by MBE, one first must determine the MBE system settings which correspond to the SAE growth window conditions, as mentioned earlier in this thesis. In particular, for a given reasonable value of CdTe flux, one desires the range in substrate thermocouple temperature, corresponding to a range of real sample surface temperatures within the SAE window for CdTe against silicon oxide, or silicon nitride, or carbon, or other mask materials.

The maximum temperature at which to observe trace accumulation of CdTe on silicon oxide was determined in the MBE system used in this thesis as follows. A $2\times 2\,\mathrm{cm}^2$ piece of Si(211) wafer was cleaned ex-situ via a modified RCA process, to degrease, deoxidize, and protect the silicon surface with a thin oxide layer [186, 187]. A CdTe effusion cell was preheated. The sample was loaded to UHV, and was subsequently heated to 395^{o}C and exposed to CdTe flux of beam equivalent pressure (BEP) $\sim 5\times 10^{-6}$ Torr (approximated by assuming 10-times the ion gauge flux reading) for ~2 minutes. During the two minutes of exposure, 10kV Reflection High Energy Electron Diffraction (RHEED) [61] was used to monitor the surface (outermost ML), to detect the accumulation of any non-amorphous deposit. If no deposit was detected, then the CdTe cell was closed, and the sample cooled by 4.3^{o}C over the course of 10minutes; then the process was repeated. No change in the RHEED diffraction pattern was detected until reaching 340^{o}C. Under CdTe flux at 340^{o}C there appeared Laue rings, indicating either a one-dimensional ordered deposit on the surface, or a polycrystalline deposit. The result is shown in the lower part of Figure 49 below. Modeling the deposit as having only one spatial periodicity, we can attribute the two clear inner Laue rings observed with the following periodicities: 1.92+/-0.5nm, and 0.80+/-0.1nm. The first of which agrees very well with the observed Si facet periodicity of low temperature bare Si(211) [188]; which is given by approximately twice the bulk-terminated step edge periodicity of 0.9406nm in the $[\bar{1}11]$ direction. Thus, it is possible that incoming CdTe flux accumulates in trace amounts preferentially at step edges on the oxidized Si(211) surface, at moderately high substrate temperature. The second clearly observed ring may correspond to half the

periodicity of (337) facet sides present on the surface, with reported periodicity of $2 \times 0.785\,\text{nm}$ in the $[\bar{1}11]$ direction [188].

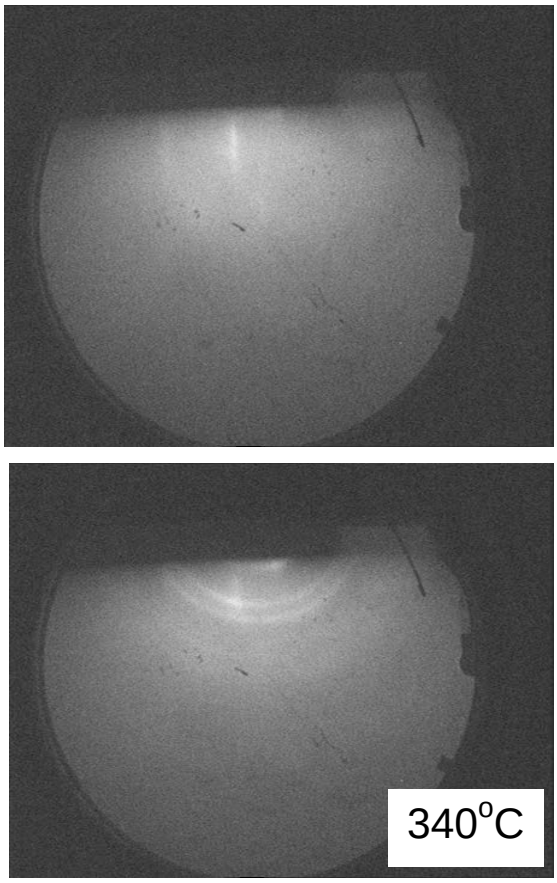

Figure 49 Observation of nucleation of CdTe flux by RHEED on RCA silicon oxide on Si(211) wafer. The top figure shows a RHEED picture of diffuse background due to the disordered silicon oxide surface, taken after exposure to CdTe flux at 344°C. At 344°C some faint spots are visible due to the underlying silicon substrate crystallinity, or a partial 2-dimensional ordering in the oxide. The lower figure shows the appearance of either a one-dimensional ordering or polycrystalline deposit, which appeared after CdTe flux exposure at 340°C; indicated by a Laue ring pattern; this is a sign that some components of the CdTe flux adhered to the surface.

It appears at first glance, that CdTe has nucleated on silicon oxide under these CdTe flux conditions, at a substrate temperature close to the maximum typical CdTe

homoepitaxy substrate temperature of ~350^{o}C; and thus that, CdTe will subsequently grow linearly with incoming flux under these conditions. However, that conclusion is false, because the deposit detected does not, in fact, allow further accumulation of CdTe; as demonstrated with the XPS data shown below (see Figure 50).

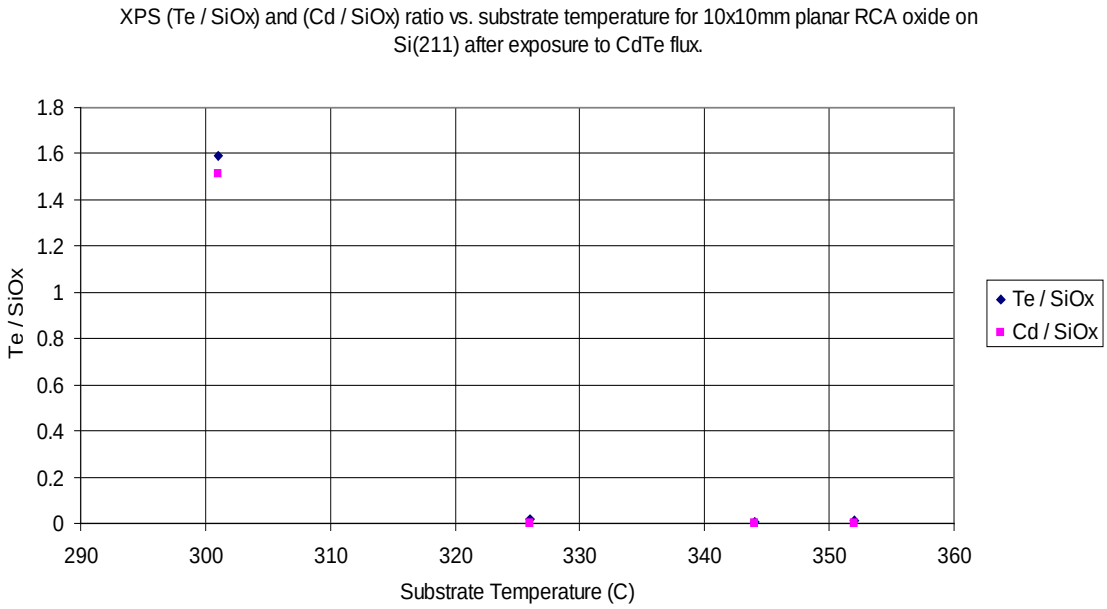

Figure 50 XPS peak ratio data shown here were acquired on RCA silicon oxide samples held at fixed substrate temperature, and exposed to CdTe flux.

In Figure 50 it is seen that although traces of deposit are present on the silicon oxide, continuous accumulation of deposit is not initiated until the substrate temperature is at least below ~325^{o}C. Thus, for this CdTe flux value, the SAE window in substrate temperature extends at least from ~325^{o}C to ~345-350^{o}C. This observation has three salient features: (1) it is a confirmation of previously reported results of SAE of CdTe against silicon oxide mask [113]; (2) it establishes the proper temperature window for SAE experimentation of CdTe with the MBE system used in this thesis; and (3) it shows

that traces of Te are to be expected on a clean, thin silicon oxide mask, even under known SAE conditions.

Silicon nitride has also been shown to be capable of acting as a CdTe SAE mask; but never before by MBE. Based on selectivity measurements for CdTe against SiO_x mask, we chose to check for selectivity of CdTe against Si_xN_y mask at a substrate temperature of 320^{o}C.

Selective growth conditions for CdTe against Si_xN_y mask were confirmed by XPS for two separate growth runs at substrate temperature T_s=320^{o}C: the first with 15 min of CdTe flux exposure on the sample and the second with 1 hour of CdTe flux, both at BEP $\sim 1.2 \times 10^{-6}$ Torr. The samples showed small amounts of CdTe on their surfaces before the experiment, due to a previous experiment. This CdTe was likely largely removed before CdTe flux exposure. The samples were etched in the dilute HBr solution, mentioned previously, for 100 sec immediately prior to loading to our MBE system, and subsequently heated to 320^{o}C. The results in the case of 15 and 60 min exposures were nearly identical. The XPS data of the 60 min exposure is shown in Figure 51, with data before etching and exposure, as well as after etching and exposure. The XPS data show a lack of appreciable CdTe deposit on the Si_xN_y ; although similarly to the case of silicon oxide, there are traces of CdTe present. This signifies conditions for selective growth, given that we can grow single crystalline CdTe on CdTe under the same conditions. If the substrate temperature were higher than ~345^{o}C, we expect that CdTe would not grow on CdTe in single crystalline form by MBE at this flux value. Therefore, similarly to the case of silicon oxide mask, there exists a substrate temperature window, from at least

320^{o}C to 340^{o}C, in which selective MBE of CdTe on CdTe and not Si_xN_y mask, is possible at this CdTe flux value.

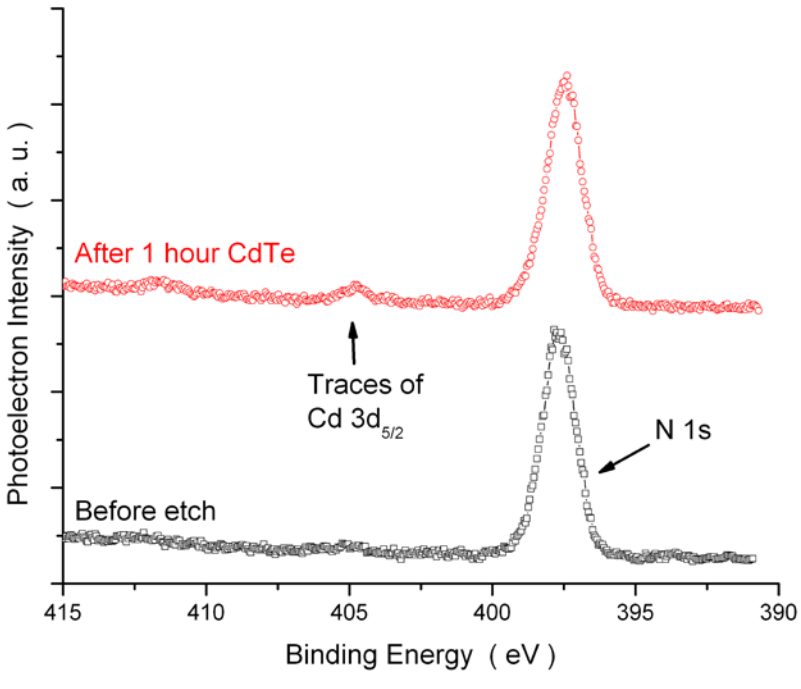
After 1 hour CdTe
Traces of
Cd 3d5/2
N 1s
Before etch
Photoelectron Intensity (a. u.)
415
410
405
400
395
390
Binding Energy (eV)

a)

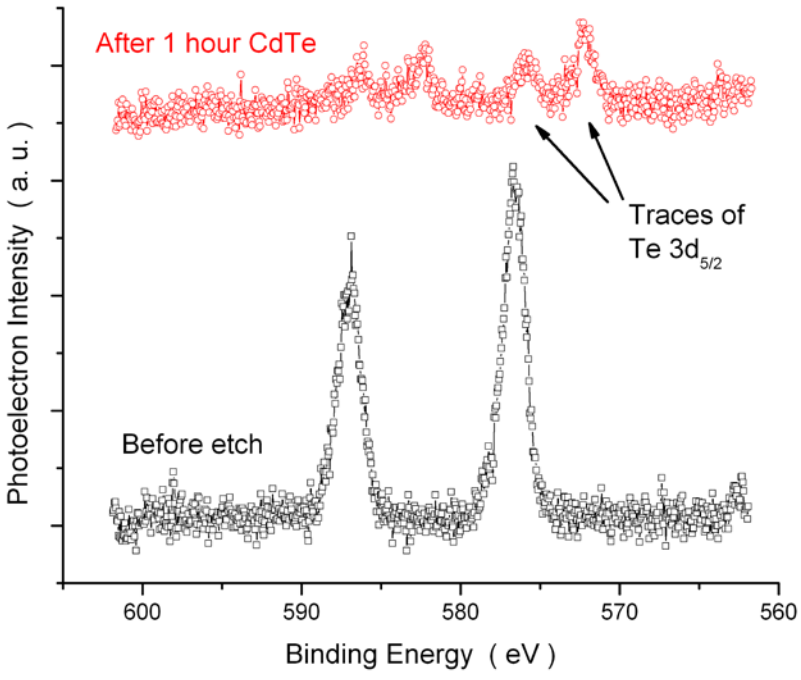
After 1 hour CdTe
Traces of
Te 3d5/2
Before etch
Photoelectron Intensity (a. u.)
600
590
580
570
560
Binding Energy (eV)

b)

Figure 51 An unpatterned sample of Si_xN_y coated with an overlayer of Te was cleaned with our HBr solution for 100 sec, and exposed to CdTe flux at a substrate temperature of 320^{o}C for 1 hour. The XPS results shown here for the Te3d and Cd3d signals before and after CdTe exposure demonstrate that no appreciable accumulation of Cd or Te has taken place.

In conclusion, SAE conditions for MBE of CdTe against silicon oxide and silicon nitride mask materials were re-established, and established, respectively, with specific conditions for the Opus 45 MBE system. This was accomplished by using a combination of RHEED and XPS analysis of the surfaces of un-patterned, masked samples. A clear observation of trace accumulation of CdTe on both mask materials, appears characteristic of the SAE window conditions; however such deposit does not preclude the feasibility of SAE.

3.2.3 Planar CdTe/ZnTe/Si(211)

The typical CdTe/Si recipe at lower temperature was tested by using a $2 \times 2\,\mathrm{cm}^2$, 250nm thin CdTe/ZnTe epilayer on Si(211) substrate, placed in the same sample holder used for all SAE studies reported here. The test used no high temperature SAE procedure; but did use a 4A substrate heater power limit during initial substate heating above 250^{o}C to deoxidize and clean the CdTe surface before growth at 211^{o}C. After pre-heating and cleaning, the main part of the growth recipe was performed with an 11A limit, and incorporated in-situ annealing cycles with repetition of the basic procedure outlined in Figure 52 below.

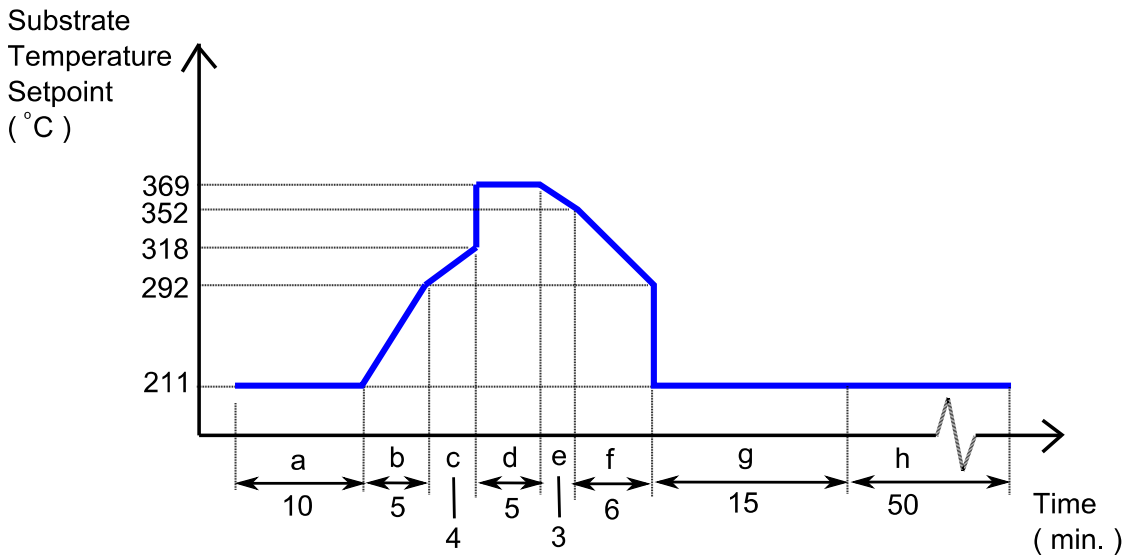

Figure 52 The substrate temperature setpoint (not thermocouple setpoint), as a function of time, is shown here for one cycle used in the thick growth of CdTe on Si in this thesis. Tellurium flux (Te_2) is incident on the sample in steps c-f. Cadmium telluride flux (Cd + Te_2) was incident on the sample surface for steps a, d , e, and h. The excursion to 369°C during step d, under CdTe and Te_2 fluxes, was intended to anneal the film, to achieve lower DL density. A typical thick growth incorporates several such cycles, with the majority of the growth occurring in steps h and a. For both planar and patterned growths, the substrate heater power was limited at 11A when performing this procedure.

The result of the test was an epilayer 8.1µm thick by FT-IR, and of 84" FWHM from CdTe (422) by XRD rocking curve measurement. The FWHM corresponds to a dislocation density of $1.7\times10^{7}\ cm^{-2}$; estimated using Equation 40. This growth result is of reasonable quality; although the result could likely be improved with fine-tuning of the growth recipe. The primary purpose of the result in the present context is to serve as a baseline from which to judge the unconventional results of planar samples grown under SAE conditions outlined in the next section.

3.2.4 Parallel growths: planar and patterned CdTe/ZnTe/Si(211)

MBE was performed on four pairs (denoted as sets: I, II, III, and IV) of $2 \times 2\,\mathrm{cm}^2$ samples of CdTe/ZnTe/Si(211), using similar CdTe flux values to the SAE determination, only T_s greater than or equal to 320^{o}C for SAE growth steps, and a 3.8A or 4A substrate heater power limit during initial heating from room temperature. Each sample pair consisted of (A): an unpatterned ~250nm thick single crystal film of CdTe/ZnTe/Si(211) with ~15nm thick ZnTe buffer, and (B): a patterned sample of ~250nm thick single crystal film of CdTe/ZnTe/Si(211) with ~15nm thick ZnTe buffer, with ~40nm silicon nitride over-layer mask incorporating an array of patterned mask holes exposing CdTe surface at the bases of the holes. Sample sets I and II involved pre-growth steps by SAE on only the patterned samples (and not the unpatterned). Sample sets III and IV had identical etching and growth conditions between the two samples within each pair for every step. Thus, the results of sample sets III and IV offer a more direct comparison of patterned versus unpatterned interface architecture. The SAE procedure duration was chosen to allow neighboring seed areas on the patterned samples, sufficient time to merge together. For some sample pairs the SAE procedure was interrupted in order to acquire SEM images of the patterned sample surface in a separate vacuum system. In such cases, the samples were re-etched and loaded to the MBE system, and heated to the proper growth temperature, before continuing the growth procedure. The completion of the total SAE procedure was then followed by a typical CdTe/Si growth recipe at lower substrate temperature, with periodic, short annealing steps at T_s=370^{o}C (see Figure 52). Before the thick growth the sample sets I, III, and IV

were heated to 237^{o}C, and set II was heated to 211^{o}C. The lower substrate temperature growth with anneals was performed on the patterned and unpatterned samples in parallel for every set of the four. In the following, the procedure for each set of samples is summarized, and results of the growth are reported. The in-plane orientation of the sample varies in the SEM images of set I; in all other sets the orientation is identical for all images of a given pair.

Sample set I had differing growth procedures for the patterned and unpatterned samples. The patterned sample underwent three SAE growth steps, with intermediate SEM analysis. In each case of SAE growth, the following steps were performed: (1) the sample temperature was ramped without any flux to 320^{o}C, (2) the sample was allowed to equilibrate under no flux, (3) the surface was exposed to CdTe flux, (4) the surface was held at 320^{o}C under no flux, and finally, (5) the sample was cooled down to room temperature under no flux. After each growth step, the sample was removed from the MBE system for SEM analysis, and re-etched with the HBr etching procedure described previously in this thesis, before re-introduction to the MBE system. The last re-introduction step was followed by a thick growth, incorporating 5 in-situ anneals (as described in Figure 52), with the unpatterned partner sample in parallel. The four growth steps' durations and estimated CdTe BEP flux values are listed below in Table 13.

Growth (SN-103d)	*Etch*	*Patt.*	*Unpatt.*	*T_s (^oC)*	*CdTe BEP (Torr)*	*CdTe Flux Duration (min.)*
1	HBr	Y	N	320^{o}C	1.6×10^{-6}	15
2	HBr	Y	N	320^{o}C	1.8×10^{-6}	15
3	HBr	Y	N	320^{o}C	1.5×10^{-6}	60
4	HBr	Y	Y	211^{o}C	1.8×10^{-6}	1320

Table 13 Growth steps for sample set I. "Patt." and "Unpatt." columns indicate if the patterned and/or unpatterned samples were present during the growth procedure. T_s indicates the substrate temperature, and the BEP of CdTe is taken as 10-times the flux gauge reading.

The patterned sample was imaged before any growth; the center of which is shown in Figure 53.

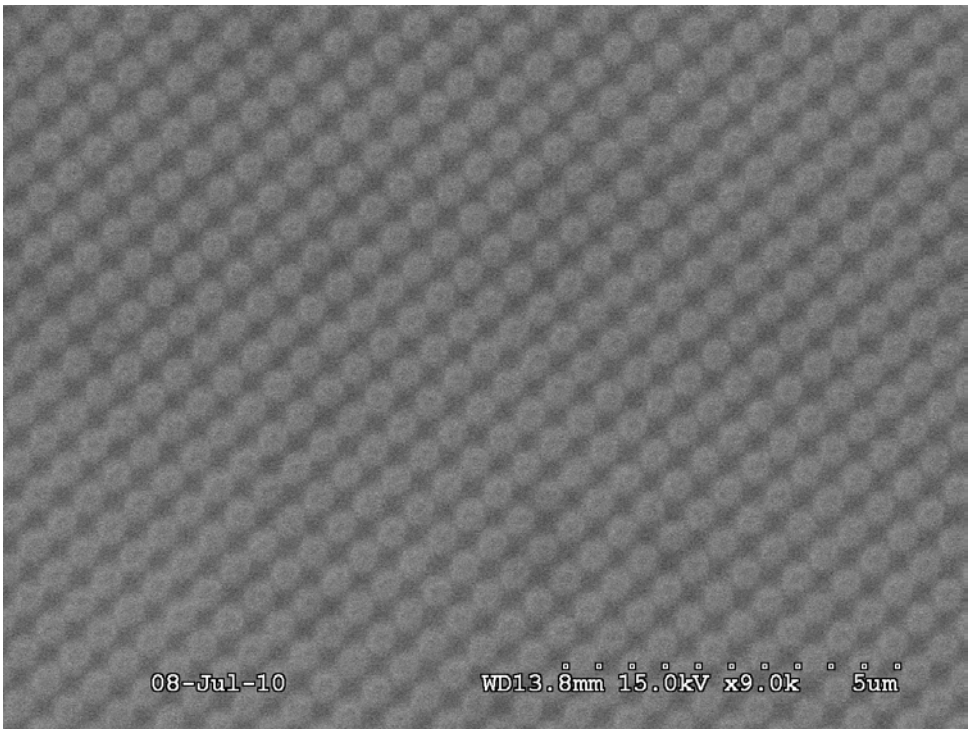

Figure 53 The approximate center of the patterned sample of set I, before any growth. The silicon nitride mask features are apparent; where CdTe is likely present in the brighter contrast regions.

After growth-1 there was a clearly noticeable change in surface morphology by SEM; as seen in Figure 54. Clearly, some CdTe has accumulated, however it appears to have done so in a mostly non-selective fashion. In addition, the growth has accumulated in nano-sized clusters, rather than as a smooth flat film of limited lateral extent. Such deposit may be single crystalline, despite the uneven surface.

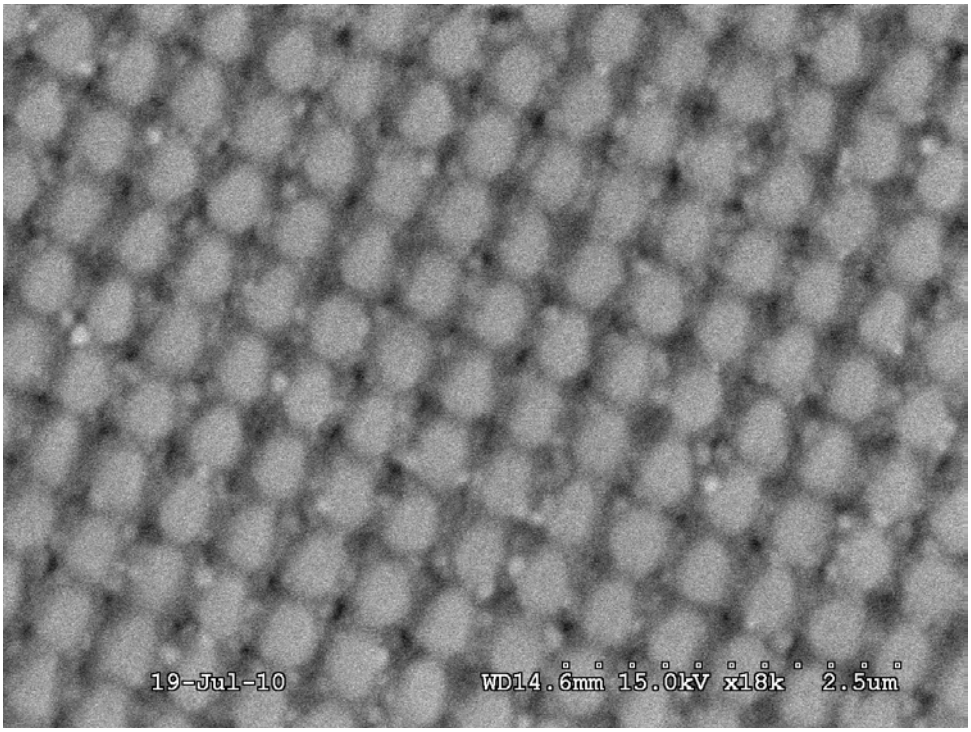

Figure 54 Patterned sample center from set I after growth-1, involving 15min of CdTe flux exposure at substrate temperature 320^{o}C. The growth is apparent as brighter contrast features in the image, and appears not to have been fully selective.

At other locations on the sample, away from the center, it appears the growth is fairly selective. For example, Figure 55 shows a region near the edge of the sample where the original silicon nitride pattern ends, likely having left a large area of planar silicon nitride devoid of holes (exposing no underlying CdTe seeding areas) in the upper part of the figure.

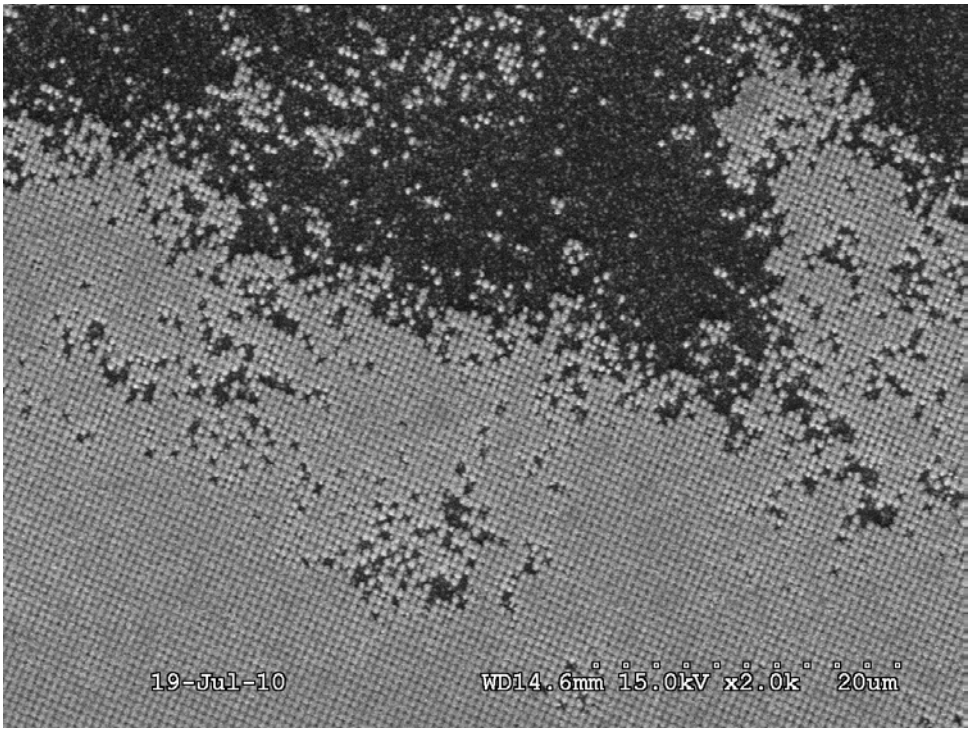

Figure 55 Patterned sample at edge of silicon nitride pattern, from set I after growth-1, involving 15min of CdTe flux exposure at substrate temperature 320^{o}C. The selective nature of the growth is more apparent in this region, although the growth still appears not to have been fully selective.

A closer view of the same type of sample region is shown in Figure 56. It can be seen,

again that the growth does not appear to be perfectly selective, but is to some extent.

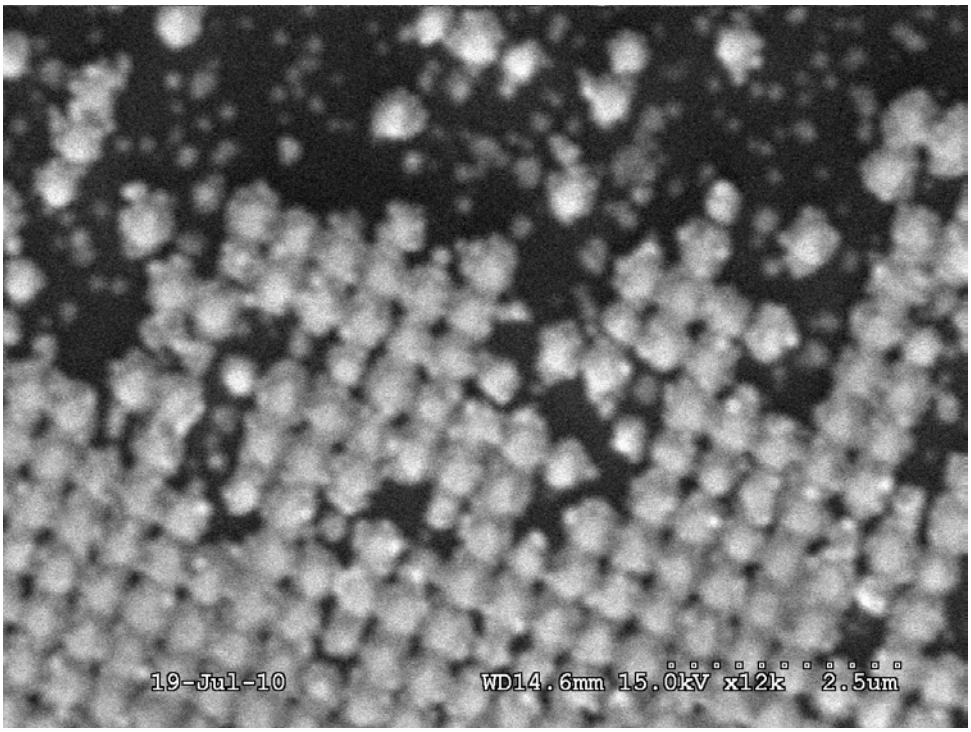

Figure 56 A magnified view of the same type of region shown in Figure 55. (Patterned sample at edge of silicon nitride pattern, from set I after growth-1, involving 15min of CdTe flux exposure at substrate temperature 320^{o}C. The selective nature of the growth is more apparent in this region, although the growth still appears not to have been fully selective.)

After growth-2, incorporating another pre-etch and heating, and 15 additional minutes of CdTe flux exposure, the surface appears to have changed again. The regions of accumulated CdTe have smoothed out considerably, and the areal density of clusters has decreased, as shown in Figure 57.

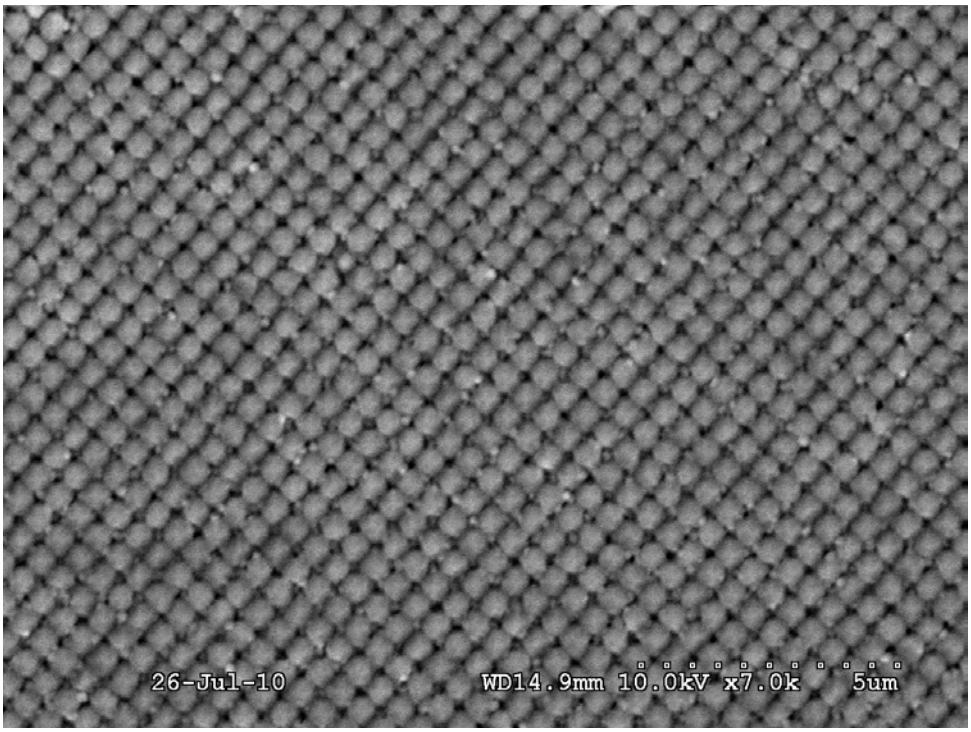

Figure 57 Patterned sample at the center, from set I after growth-2, involving 30 cumulative minutes of CdTe flux exposure at substrate temperature 320^{o}C. The islands' surfaces have become smoother, and the areal density of inter-island clusters has decreased.

During the CdTe flux exposure of growth-2, the CdTe BEP was recorded as a function of time after the shutter opening; as shown in Figure 58. It can be seen that the pressure is initially higher than its steady state value when open; which is reached within ~5 minutes. The reason for the higher initial pressure is likely that the steady state of the closed cell results in higher CdTe source material surface temperature, due to radiation, and reflection of radiation, into the cell from the shutter. In future nano-scale growth experiments it may be important to keep this feature of the typical effusion cell in mind. In SAE results quoted here (for all sample sets), the steady-state open-cell flux value is used.

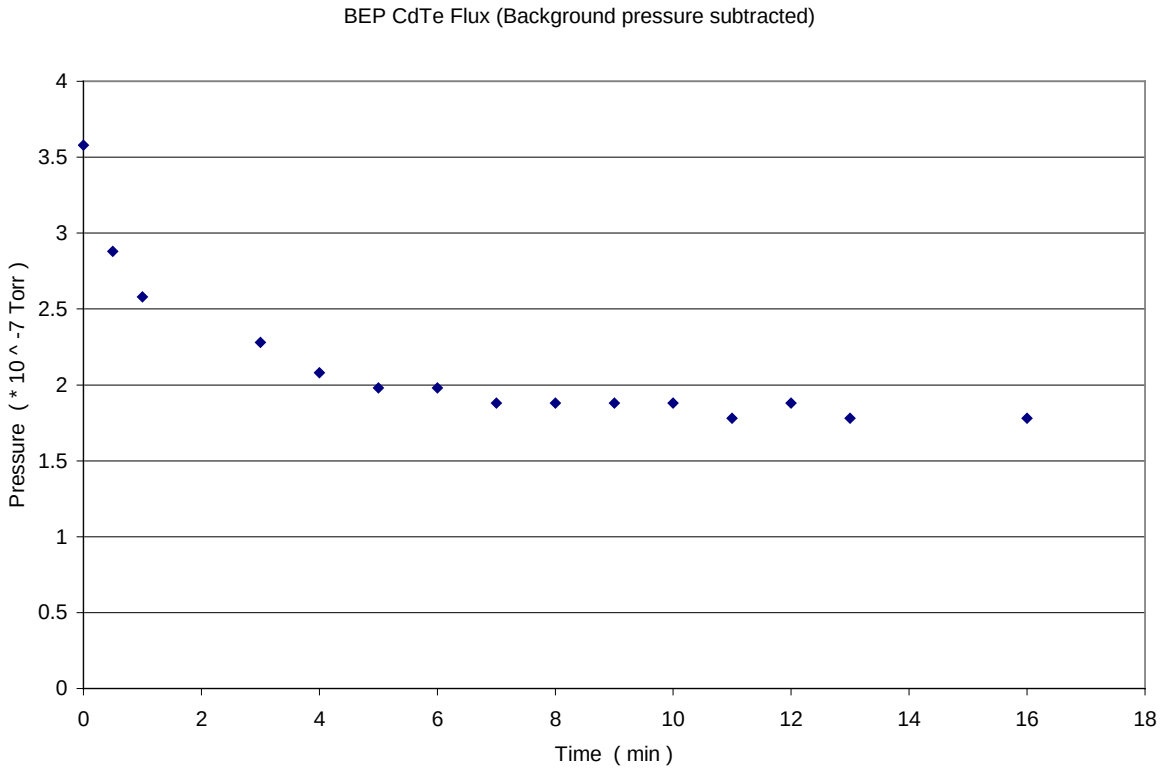

Figure 58 The BEP measured on the ion gauge flux gauge of the MBE system is shown here as a function of time after opening of the CdTe effusion cell. The CdTe effusion cell initially releases more flux during the first ~5 minutes after its shutter is opened.

After the growth-3, the islands have clearly merged together, as shown below in Figure 59.

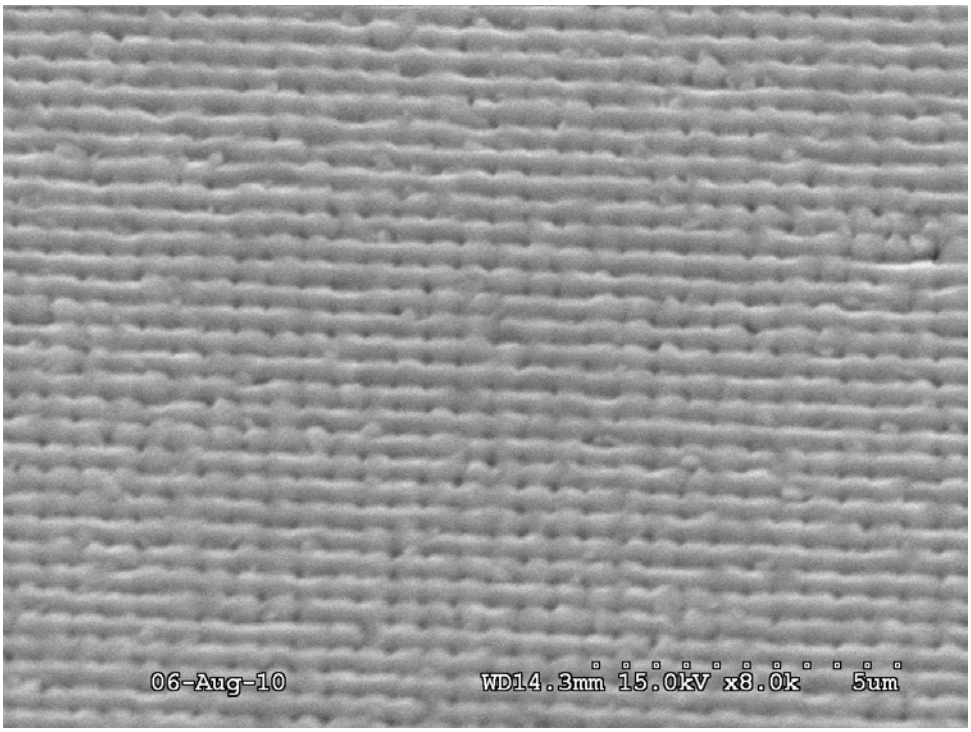

Figure 59 Patterned sample at the center, from set I after growth-3, involving 90 cumulative minutes of CdTe flux exposure at substrate temperature 320^{o}C. The islands have clearly merged together at this point, the surface has become smoother, and there is an indication of a preferred lateral merging direction (horizontal in the figure shown).

Near the edge of the patterned sample after growth-3, there is an indication of a slower growth rate on the silicon nitride mask as compared to the CdTe single crystal seeding regions; but not negligible. This can be seen in a 45^{o} tilted view of the edge of the pattern (also at the edge of the sample). In this area there were likely large-scale laser intensity fringes during the initial silicon nitride patterning process, which resulted in fringes of patterned and unpatterned regions. As shown below, the patterned regions have a larger thickness; and there appears to have been non-negligible accumulation of irregular grains between the patterned regions (see Figure 60).

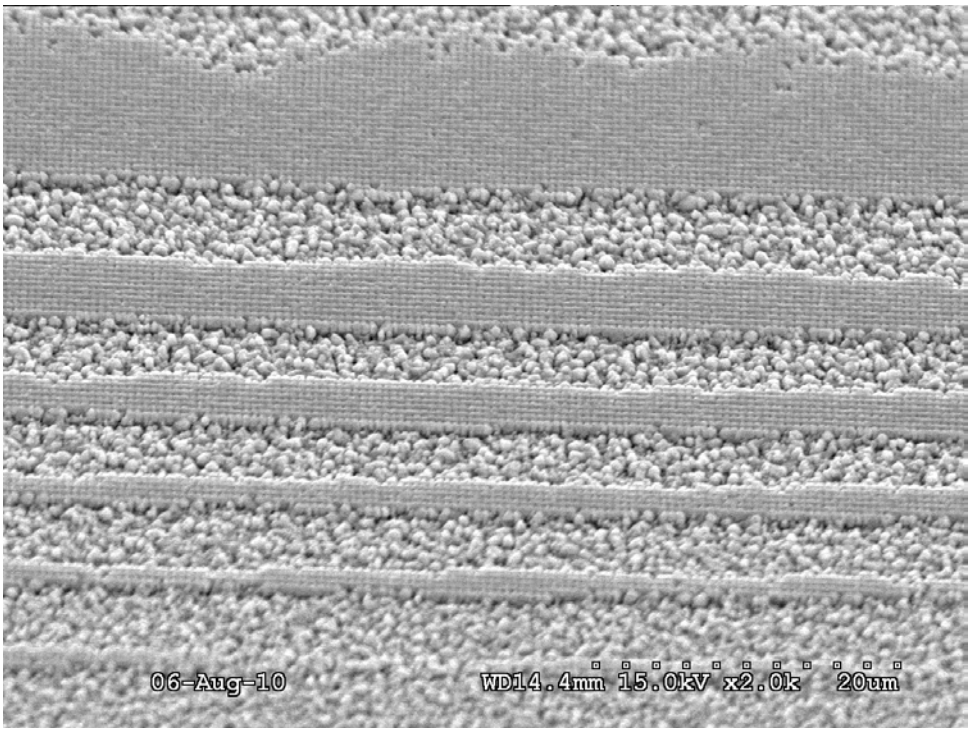

Figure 60 A 45^{o}-tilt view at the edge of the patterned sample, from set I after growth-3, involving 90 cumulative minutes of CdTe flux exposure at substrate temperature 320^{o}C. The lateral bands are likely due to large-scale interference zones present during the interferometric lithography laser exposure steps. It is likely that the rough regions have planar silicon nitride beneath them. The smoother regions appear to match the intended pattern, and are of higher height, indicating a larger growth rate compared to the irregular granular regions.

After the final thick growth on the unpatterned and patterned samples in parallel, the patterned sample surface indicates a clear lateral asymmetry in growth. This may be due to a step-flow growth mode on the (211) surface under these growth conditions. The surface is shown below in Figure 61. There is also a predominance of straight edges in the surface morphology at an angle of ~30^{o} to the apparent step-flow growth direction; these are possibly related to the sidewalls of the initial CdTe seeding windows. The angled lines do not appear related to cross-hatch, which orients along the intersection of active (111) glide planes with the (211) surface, yielding the array shown in Figure 39.

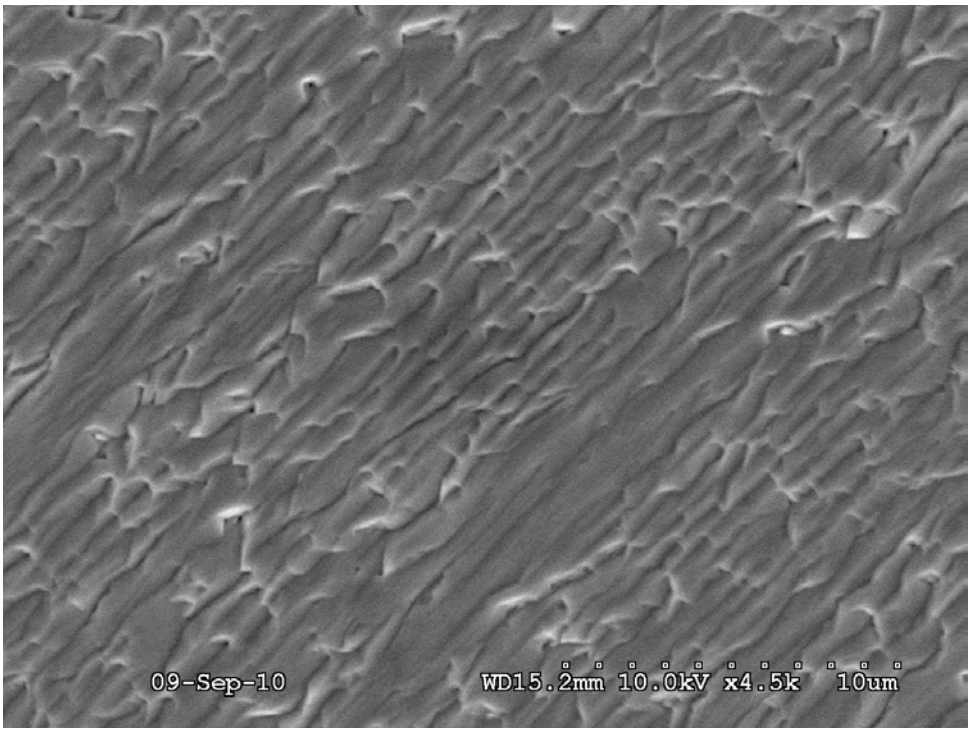

Figure 61 Patterned sample at the center, from set I after growth-3, involving 90 cumulative minutes of CdTe flux exposure at substrate temperature 320^{o}C, and growth-4 of 1320 minutes of CdTe, incorporating 5 in-situ anneals. The XRD (422) rocking curve FWHM was found to be 912" on this sample.

Sample set II also had differing growth procedures for the patterned and unpatterned samples. The patterned sample underwent one SAE growth step without the unpatterned sample, with intermediate SEM analysis before thick growth with the unpatterned sample in parallel. The SAE growth was performed at 340^{o}C, 20^{o}C higher than set I. Thus, the SAE growth was expected to be more selective than in the case of set I. The thick growth, again, incorporated 5 in-situ anneal cycles. The two growth steps are listed below with estimated CdTe BEP flux values in Table 14. The flux value for the SAE step was ~3 times higher than the typical flux value used for unpatterned CdTe on Si MBE.

Growth (SN-103f)	*Etch*	*Patt.*	*Unpatt.*	*T_s (^oC)*	*CdTe BEP (Torr)*	*CdTe Flux Duration (min.)*
1	HBr	Y	N	340^oC	2.5×10^{-6}	60
2	HBr	Y	Y	211^oC	0.9×10^{-6}	-

Table 14 Growth steps for sample set II. "Patt." and "Unpatt." columns indicate if the patterned and/or unpatterned samples were present during the growth procedure. T_s indicates the substrate temperature, and the beam equivalent pressure (BEP) of CdTe is taken as 10-times the flux gauge reading.

Before any growth the surface of the center of the patterned sample in set II was imaged by SEM, as shown in Figure 62 and Figure 63. A similar pattern is seen, as in the patterned sample of set I, as expected. After acquiring the higher magnification image below, the sample showed evidence for electron beam induced carbon deposit (as seen in the second image below). Such carbon deposit has been reported to be in a diamond-like form [197], however, we do not claim that the carbon seen here is diamond. The deposit may be graphite, polycrystalline, or completely amorphous.

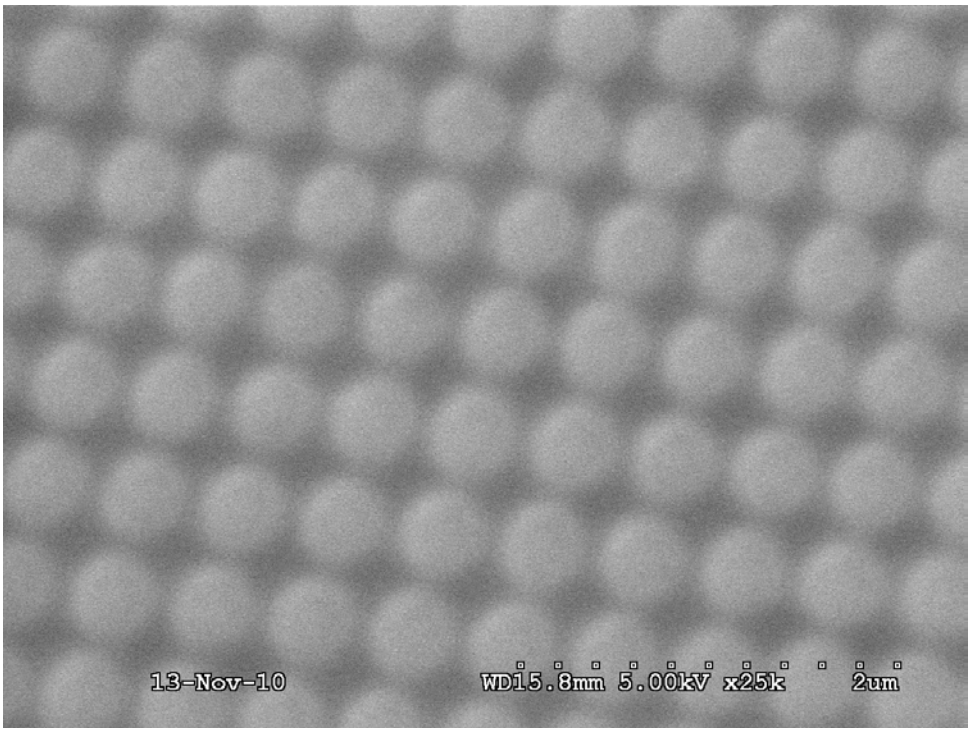

Figure 62 The approximate center of the patterned sample of set II, before any growth. The silicon nitride mask features are apparent. CdTe is likely present in the brighter contrast regions.

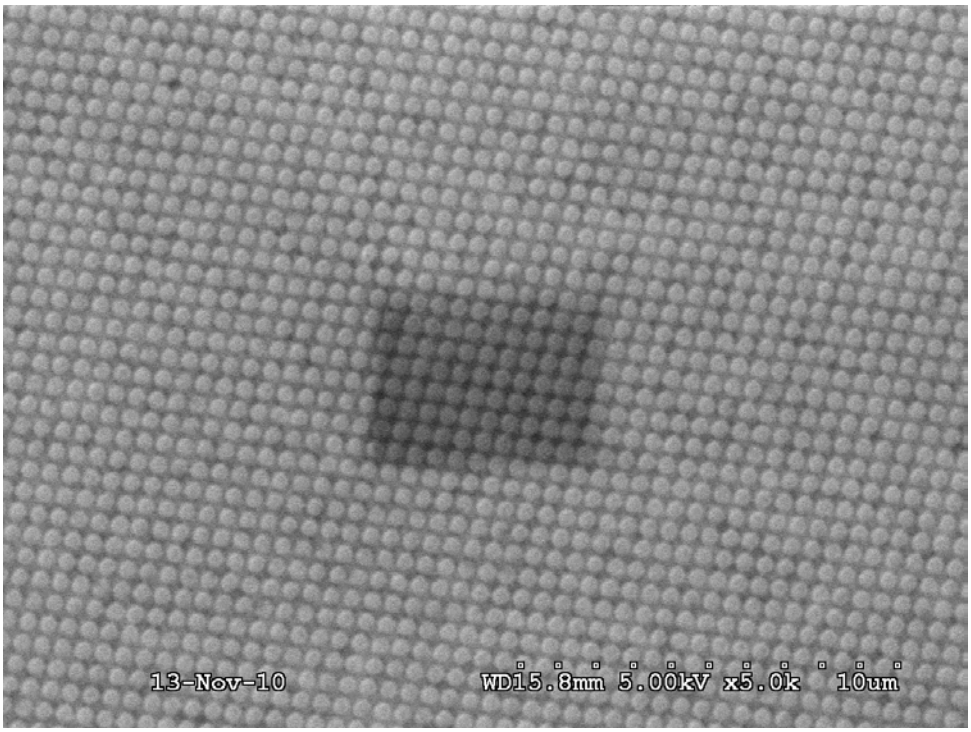

Figure 63 The approximate center of the patterned sample of set II, before any growth. The silicon nitride mask features are apparent. CdTe is likely present in the brighter contrast regions. The darker rectangle in the center of the image is likely the result of electron beam induced carbon deposit.

After the SAE growth procedure, with 60 minutes of CdTe flux, the surface morphology clearly changed, as in the case of the patterned sample of set I. The patterned sample also showed a slight asymmetry in the lateral growth direction, similarly to that seen in set I. The center of the patterned sample of set II after SAE is shown below in Figure 64. The accumulated CdTe appears single crystalline, particularly when compared with SEM images of 200nm CdTe seeds grown by vapor phase epitaxy, reported very recently [189].

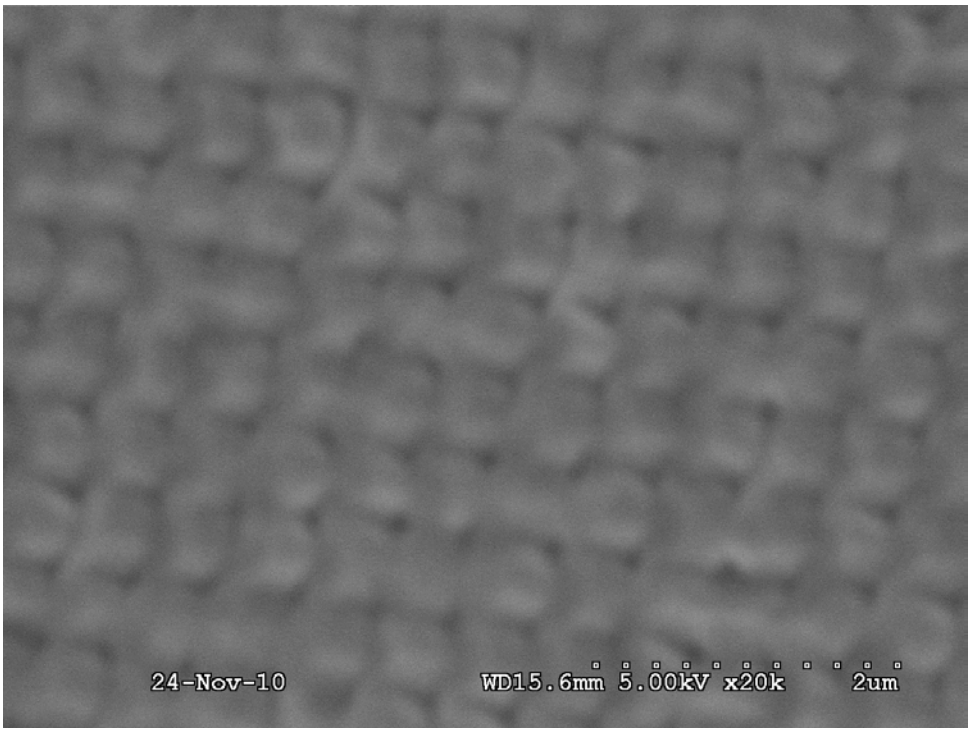

Figure 64 The approximate center of the patterned sample of set II, after the SAE growth step involving 60min of CdTe flux. The original pattern is still apparent, with a slight asymmetry in lateral growth rate. CdTe is likely present in the lighter contrast regions.

A lower magnification image of the same area is shown in Figure 65. It can be seen in this image that the previously contaminated region from the electron beam has resulted in an irregular granular deposit; perhaps containing polycrystalline CdTe.

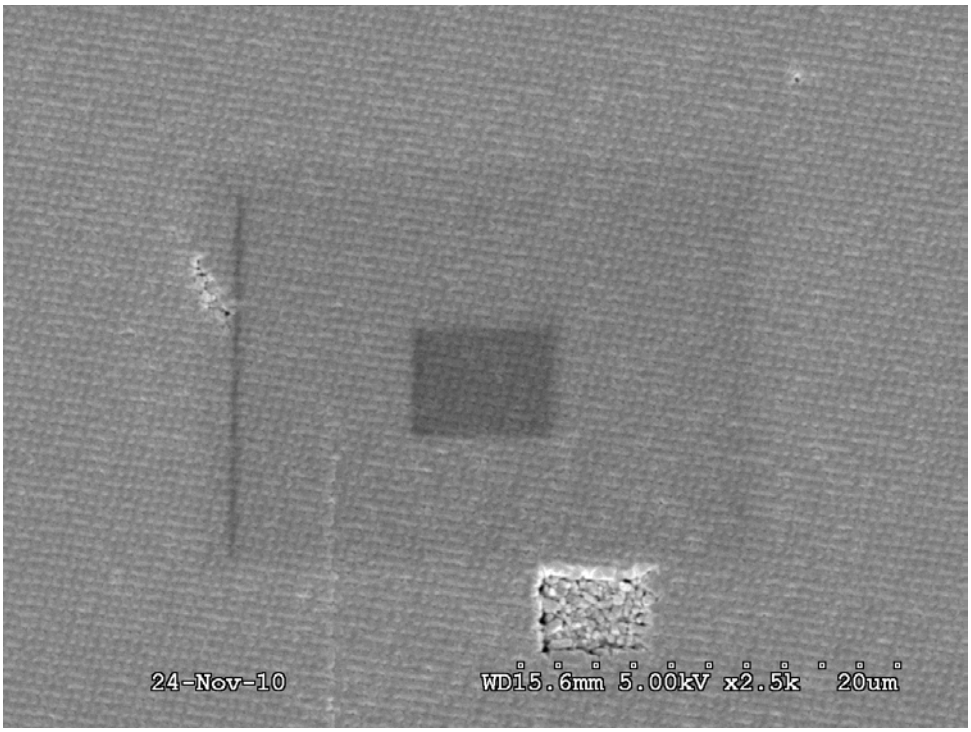

Figure 65 The approximate center of the patterned sample of set II, after the SAE growth step involving 60min of CdTe flux. The original pattern is still apparent at this length scale. The irregular granular rectangular region in the lower part of the image was the location of a previous high magnification data acquisition with the SEM; likely leaving carbon on the surface; which later possibly resulted in polycrystalline CdTe growth.

After thick growth, as in the case of set I, incorporating 5 in-situ anneal cycles; the patterned film surface center was imaged again, yielding the result shown in Figure 66 and Figure 67.

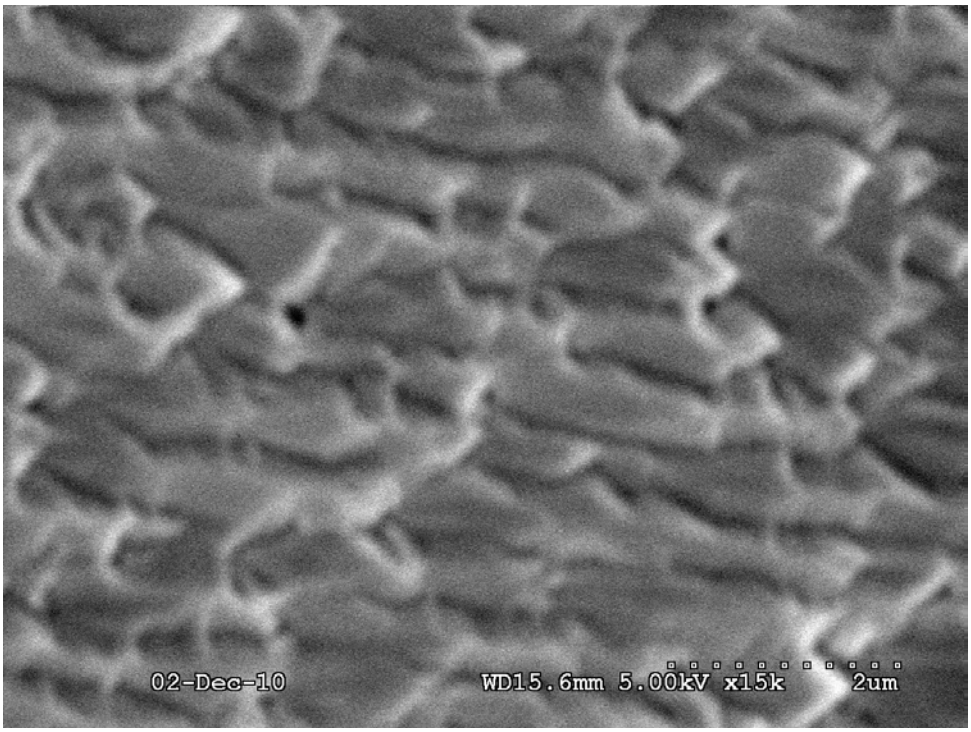

Figure 66 The approximate center of the patterned sample of set II, after the SAE growth step involving 60min of CdTe flux and the thick growth in parallel with the unpatterned sample, involving 5 in-situ anneal cycles. There is a clear indication of lateral growth asymmetry, as well as faceting possibly related to the initial CdTe seed window sidewalls. The XRD (422) rocking curve FWHM was found to be 2297" on this sample.

A lower magnification image of the same area is shown below in Figure 67.

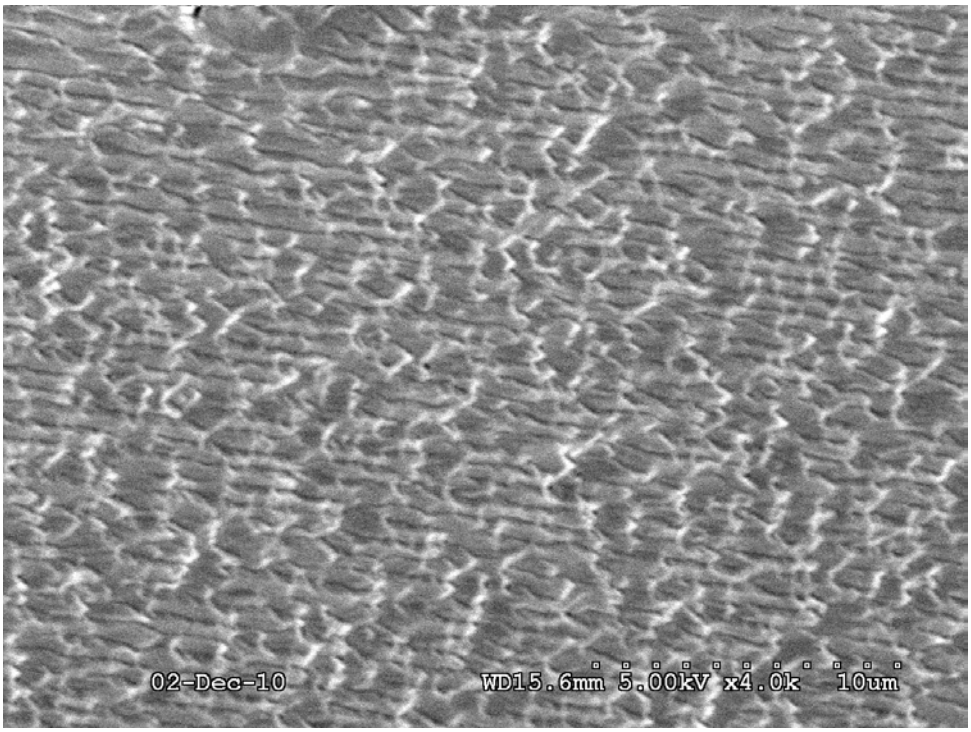

Figure 67 A lower magnification view of the same region shown in Figure 66, showing the approximate center of the patterned sample of set II, after the SAE growth step involving 60min of CdTe flux and the thick growth in parallel with the unpatterned sample, involving 5 in-situ anneal cycles. There is a clear indication of lateral growth asymmetry, as well as faceting possibly related to the initial CdTe seed window sidewalls.

The unpatterned sample from set II was also imaged after the thick growth procedure; with the result shown in Figure 68.

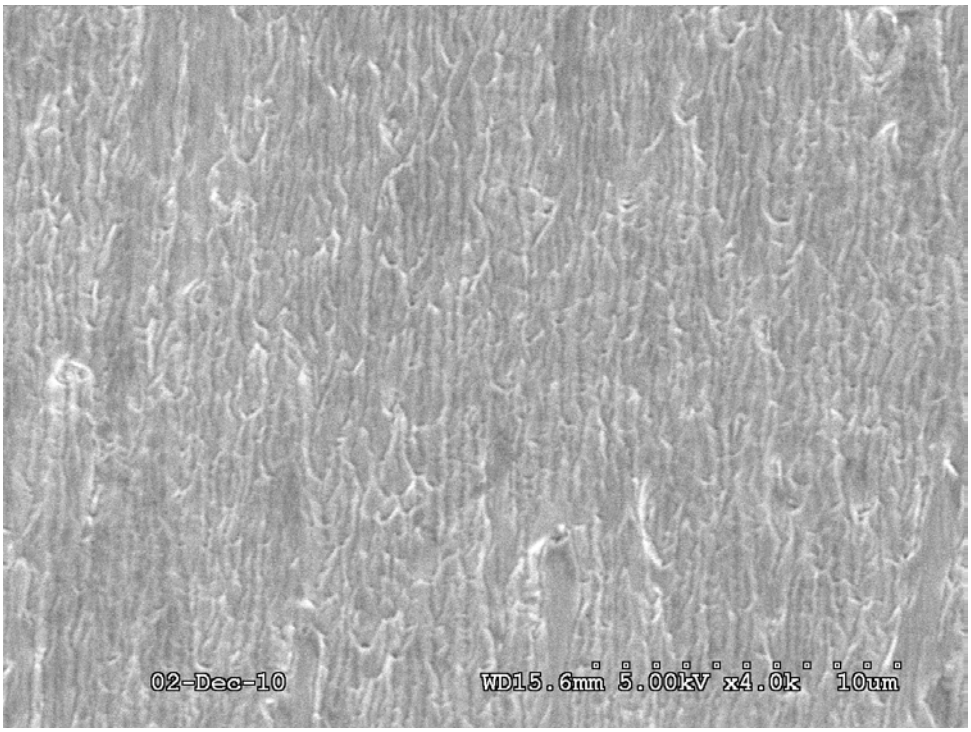

Figure 68 The approximate center of the unpatterned sample of set II, after the thick growth step involving 5 in-situ anneal cycles. There is a similar indication of lateral growth asymmetry, seen more clearly on the patterned samples.

The samples were also imaged in their centers after thick growth by AFM. The result for the patterned sample is shown in Figure 69, and the unpatterned sample is shown in Figure 70.

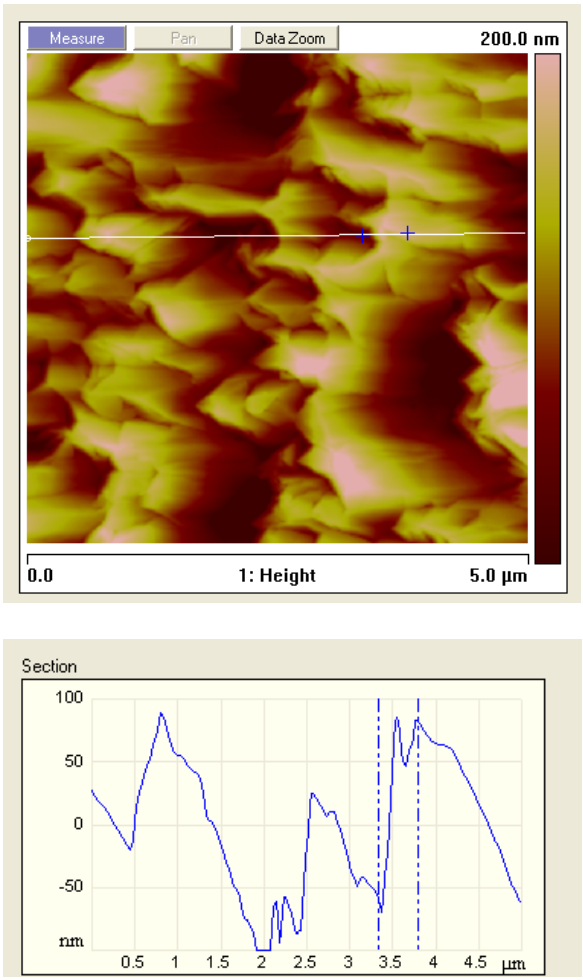

Figure 69 Patterned sample center after thick growth from set II. The peak-to-peak surface corrugation of the surface is of order 200nm.

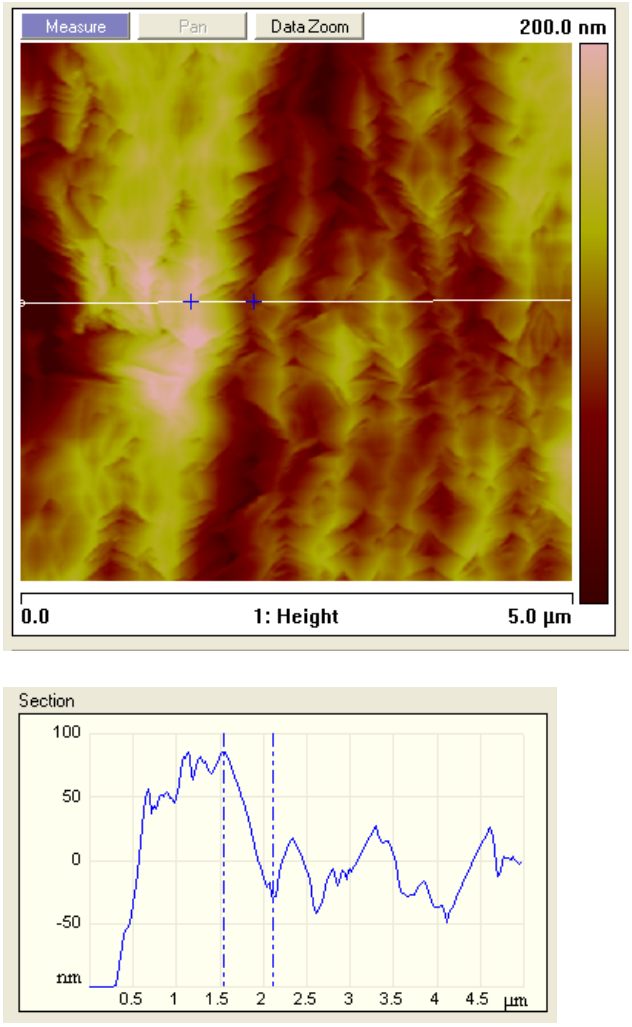

Figure 70 Unpatterned sample center after thick growth from set II. The peak-to-peak surface corrugation of the surface is of order 200nm.

In general, one would expect the patterned sample to have more corrugation. The similar values in the case of this sample set may be related to low temperature thermal cleaning.

Sample set III had all steps identical for the etching and growth procedures of the patterned and unpatterned samples. The surface cleaning and etching involved first the HBr etch mentioned earlier in this thesis, followed by the HCl etch mentioned earlier in this thesis. The sample pair underwent one SAE growth, with intermediate SEM analysis

before thick growth incorporating 5 in-situ cyclic anneals. The SAE growth was performed at a slightly higher temperature of 345^{o}C; 5^{o}C higher than set II. The two growth steps are listed below with estimated CdTe BEP flux values in Table 15.

Growth (SN-102c)	***Etch***	***Patt.***	***Unpatt.***	***T_s (^{o}C)***	***CdTe BEP (Torr)***	***CdTe Flux Duration (min.)***
1	HBr followed by HCl	Y	Y	345^{o}C	0.8×10^{-6}	90
2	HBr followed by HCl	Y	Y	211^{o}C	0.9×10^{-6}	725

Table 15 Growth steps for sample set III. "Patt." and "Unpatt." columns indicate if the patterned and/or unpatterned samples were present during the growth procedure. T_s indicates the substrate temperature, and the beam equivalent pressure (BEP) of CdTe is taken as 10-times the flux gauge reading.

The patterned sample center for set III was imaged before any growth, as shown in Figure 71 and Figure 72. Once again, the electron beam has likely left a carbon deposit in the dark rectangle in the center of the second image.

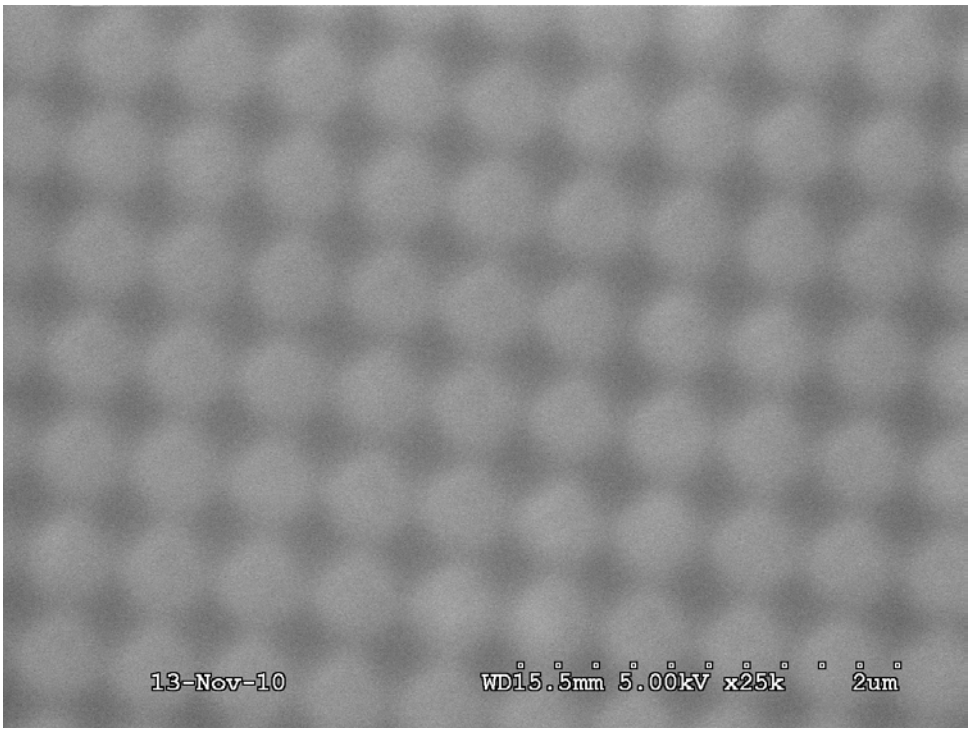

Figure 71 The approximate center of the patterned sample of set III, before any growth. The silicon nitride mask features are apparent. CdTe is likely present in the brighter contrast regions.

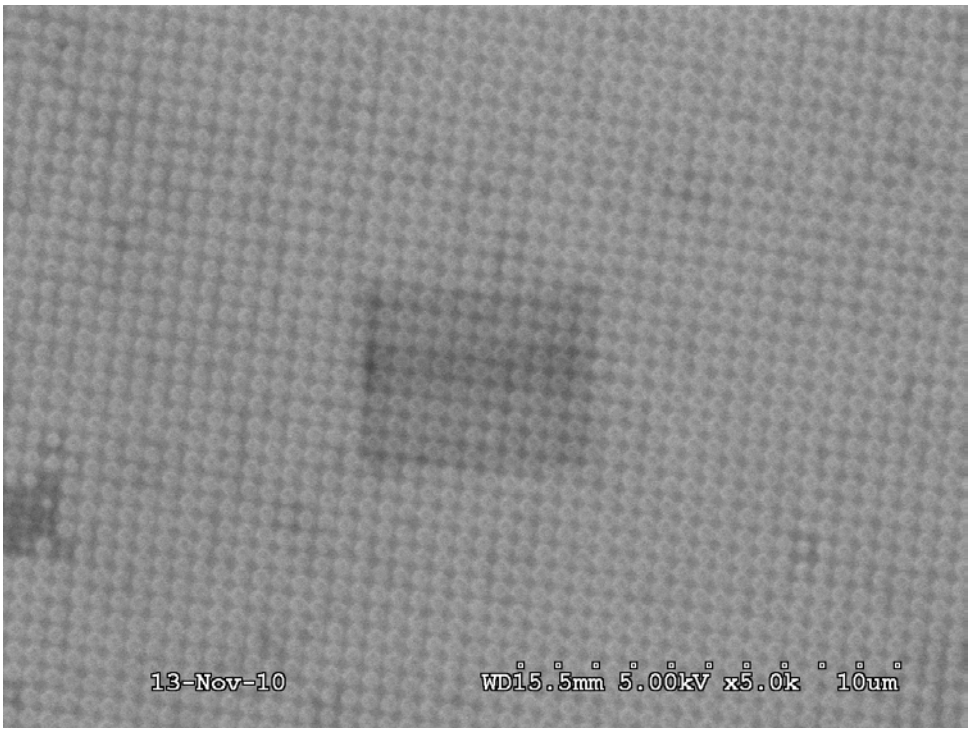

Figure 72 A lower magnification view of the same area shown in Figure 71, from the approximate center of the patterned sample of set III, before any growth. The dark rectangle was likely formed from carbon deposit induced by the SEM electron beam.

After SAE growth, the patterned sample was imaged in the center by SEM again, as shown in Figure 73 and Figure 74. There is some sidewall faceting apparent, which appears to have emerged in correlation with the initial CdTe seed window sidewall geometry. In the second figure, there appears to be no appreciable accumulation of CdTe in the rectangular area ($6 \times 4.5\ \mu m^2$) which previously was thought to have acquired an electron-beam-induced carbon coating. This result is believed to be the first reported observation of SAE of CdTe against a carbon mask [190].

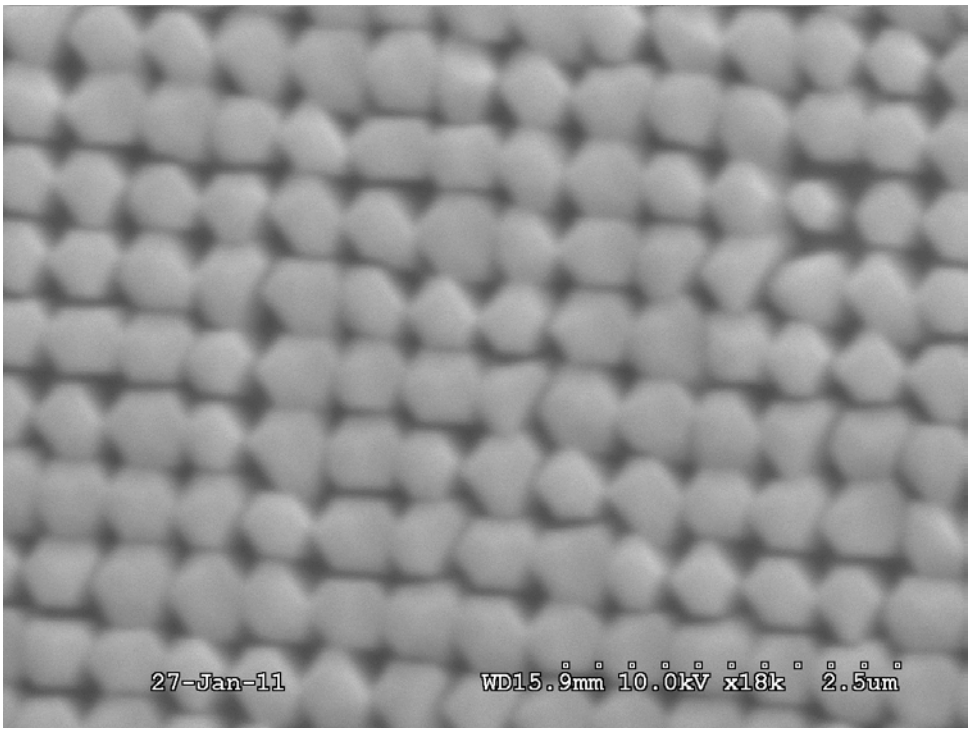

Figure 73 The approximate center of the patterned sample of set III, after SAE growth of CdTe for 90 minutes at T_s=345^{o}C. CdTe is likely present in the brighter contrast regions.

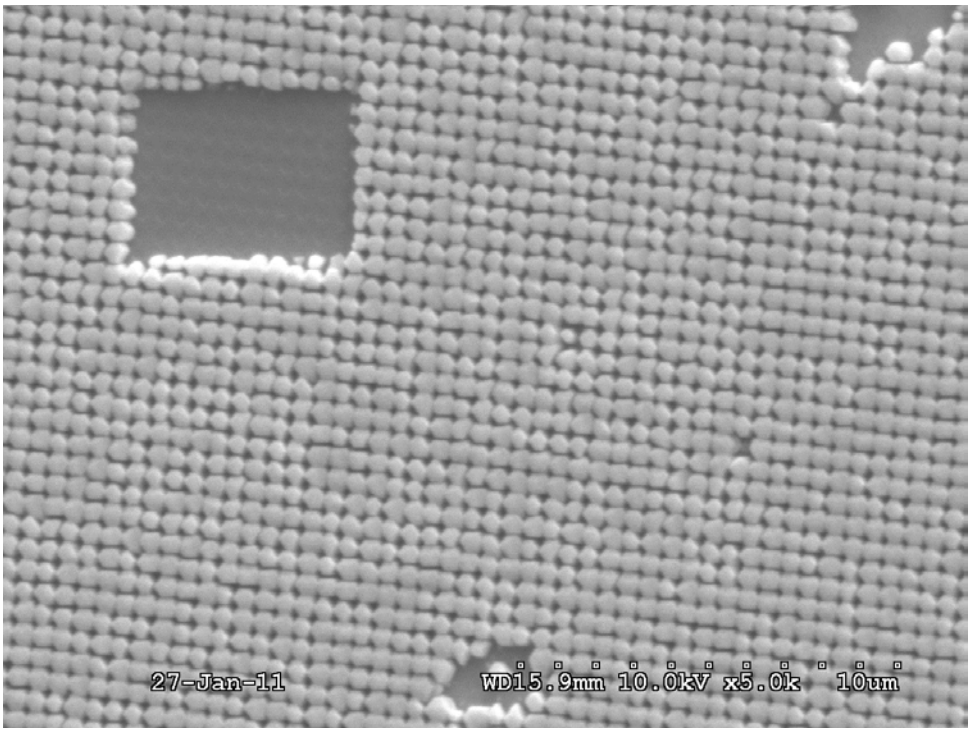

Figure 74 A lower magnification view of the same region of the patterned sample shown in Figure 73, taken in the approximate center of the patterned sample of set III, after SAE growth of CdTe for 90 minutes at T_s=345^{o}C. CdTe is likely present in the brighter contrast regions. There is a strong indicator of SAE of CdTe against the carbon deposit formed before growth-1 by the SEM electron beam within the rectangle seen here. One can also see the emergence of faceting possibly related to the initial CdTe seed window sidewalls.

A closer inspection of the carbon contaminated area shows that the original mask pattern appears to still be visible (see Figure 75). Visually following the features of that pattern over to the edges of the rectangle, where SAE of CdTe has taken place, one can see that the CdTe has accumulated selectively in the pattern areas which correspond to the darker contrast regions of the rectangle's pattern (see Figure 71). This observation is consistent with the apparent shape of the seeding windows imaged with AFM (see Figure 48). The observation suggests that the contrast between seeding windows and mask has been inverted by the process steps between imaging the sample before growth and imaging the sample after 90 min of SAE growth in this case.

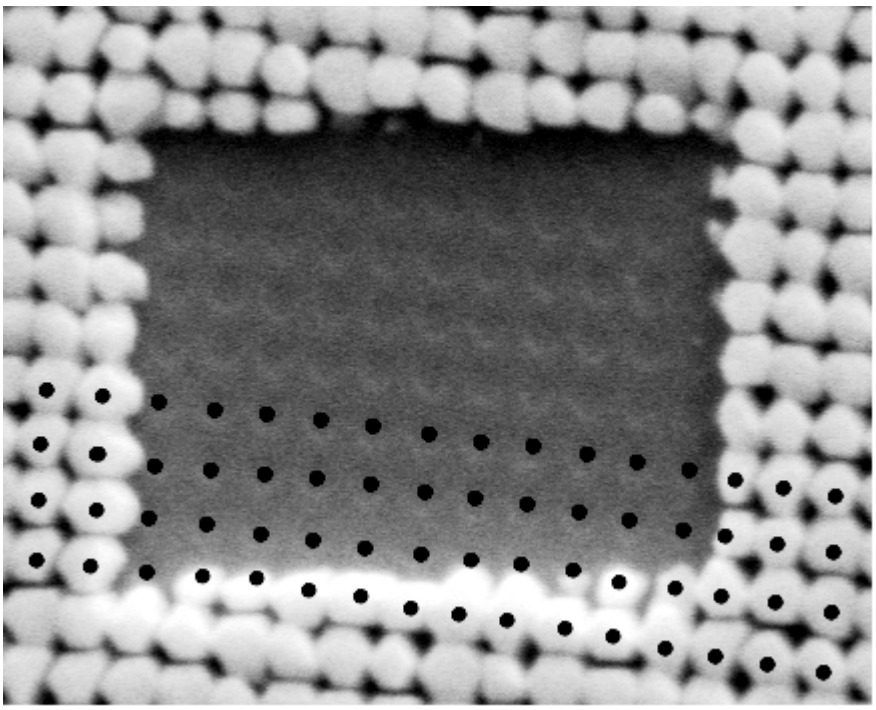

Figure 75 A zoomed-in portrayal of the image shown in Figure 74, with the image contrast artificially enhanced. CdTe is likely present in the lightest contrast regions on the perimeter of the image. Visually tracing from the pattern in the central rectangle to the edges where SAE has occurred, indicates that the relative brightness of what were once CdTe and Si_xN_y pattern features in the rectangle has now reversed. Black discs have been artificially added to the image to mark the approximate positions of the CdTe seeding regions.

The selectivity was very pronounced on this sample, which is perhaps most clear near the edge of the sample. At the edge, the pattern likely has bands of silicon nitride without the intended array of holes intended to expose underlying CdTe seeding areas. The bands were possibly formed by large length scale interference fringes from the laser used in the interferometric patterning process. In the unpatterned bands, there is no discernable deposit present, except in a few sparse seeding windows; in particular, there is no granular CdTe deposit seen in these regions; thus indicating highly selective growth conditions. It is interesting to note that the high selectivity seen here against the

patterned mask at T_s=345^{o}C, roughly coincides with the nucleation transition seen for CdTe against unpatterned silicon oxide mask, just below T_s=344^{o}C, observed by RHEED, and mentioned previously (see Figure 49). Thus, it may be that there is no trace deposit of CdTe on the mask at T_s=345^{o}C, given the flux value of 0.8×10^{-6} Torr; whereas appreciable accumulation of CdTe has occurred from the seeding windows. This implies that there may exist conditions for completely selective growth of CdTe.

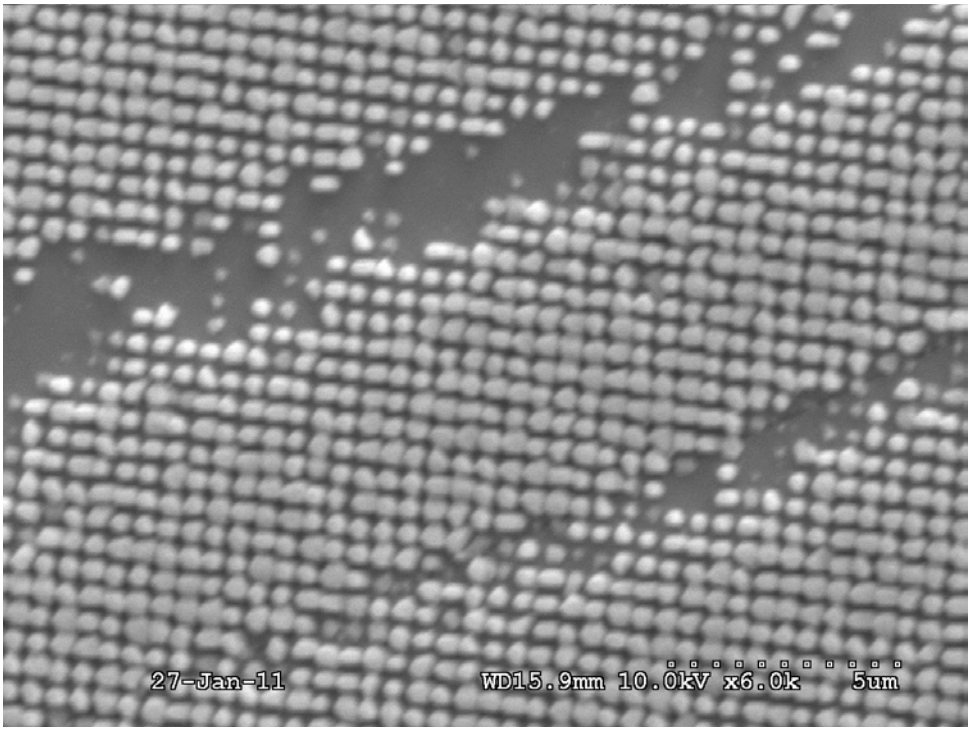

Figure 76 Near the edge of the patterned sample of set III, after SAE growth of CdTe for 90 minutes at T_s=345^{o}C. CdTe is present in the lighter contrast regions. The bands of missing islands were possibly formed by large length scale interference fringes present from the laser during interferometric lithography of the silicon nitride overlayer; which formed bands of silicon nitride without seeding window holes. Thus, in this region it is clear that the growth was highly selective, as no granular deposit is seen in the unpatterned bands.

The center of the patterned sample was imaged again by SEM after the thick growth step, incorporating 5 in-situ anneals, with the result shown in Figure 77. In that figure it is apparent that CdTe has accumulated in the carbon rectangle mentioned earlier. This observation is not too surprising, given that the thick growth procedure involves low temperature deposition at 211^{o}C; which is very likely outside the SAE growth conditions window. Near the left edge of the rectangle, the CdTe has relatively smoothly grown laterally over the carbon deposit by more than ~1μm. The lateral growth, again, is seen to be asymmetric.

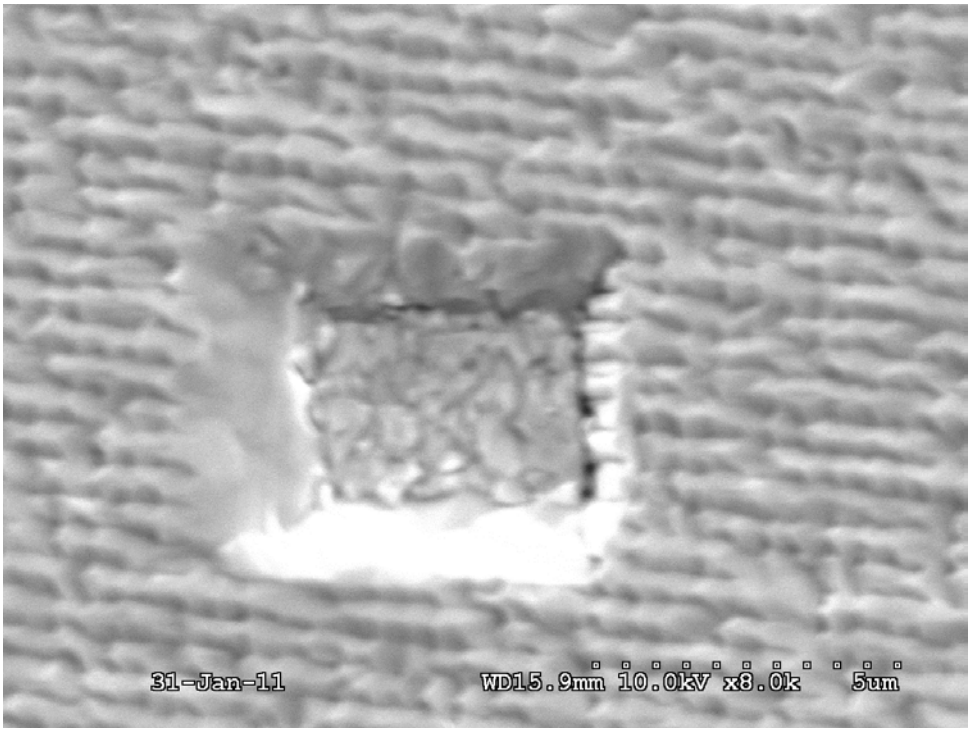

Figure 77 The center of the patterned sample from set III, after the thick growth-2, incorporating 5 in-situ anneals. It is apparent that CdTe has accumulated in the carbon rectangle identified previously. It is also apparent, upon comparison with Figure 74, that the CdTe has grown laterally into the rectangle by ~1μm from the left edge. The XRD (422) rocking curve FWHM was found to be 1047" on this sample.

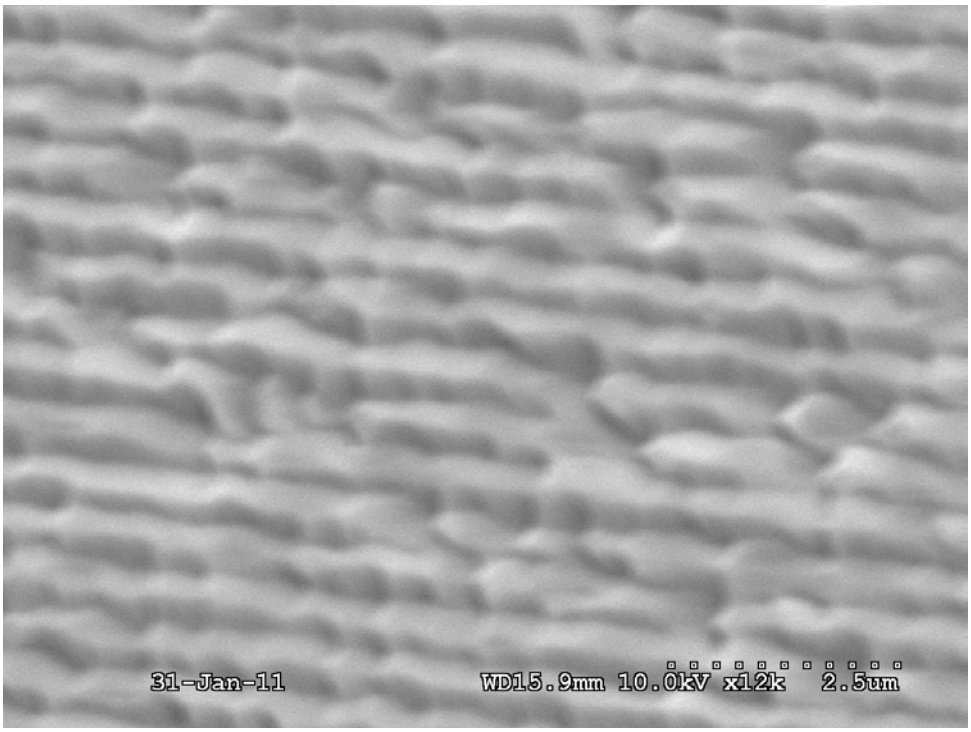

Figure 78 The center of the patterned sample from set III, after the thick growth-2, incorporating 5 in-situ anneals. The lateral island merging asymmetry indicates a lateral asymmetry in the growth rate of the CdTe.

The unpatterned sample from set III was also imaged by SEM after the thick growth; with the result shown in Figure 79. The surface appears smoother than the unpatterned sample after thick growth in set II, with no clear indication of lateral growth rate asymmetry.

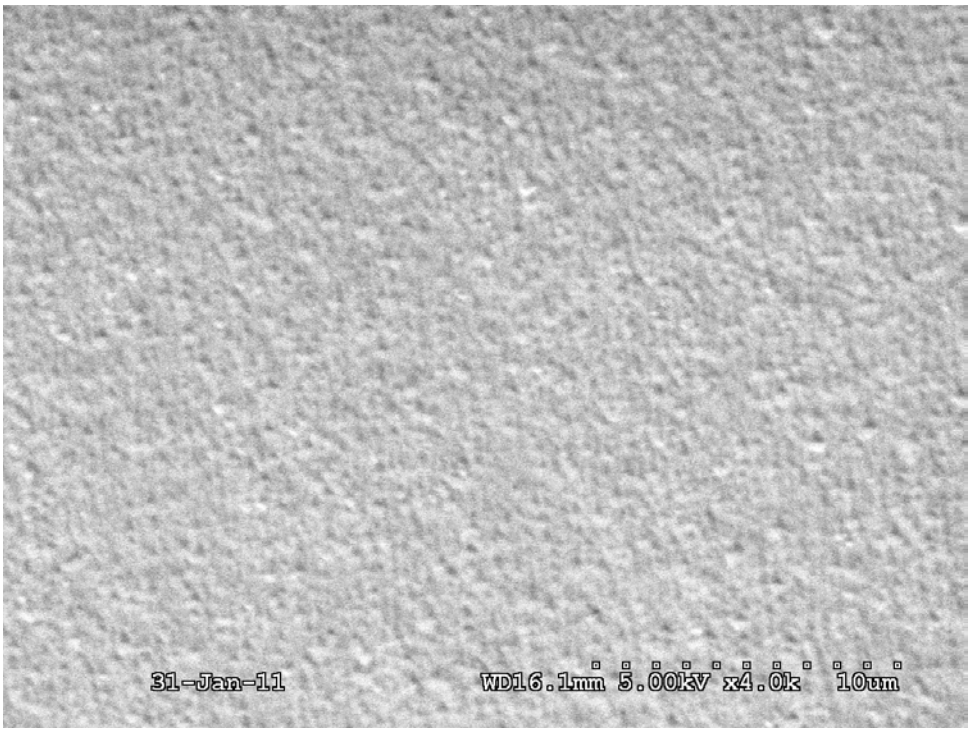

Figure 79 The approximate center of the unpatterned sample of set III, after the thick growth step involving 5 in-situ anneal cycles. There is no striking indication of lateral growth asymmetry, such as seen previously. The surface also appears smoother than the unpatterned sample of set II.

Sample set IV also involved all etching and growth steps in parallel for both the patterned and unpatterned samples. The samples were etched with only the HBr solution mentioned previously in this thesis. The growth had one SAE step at 345^{o}C, followed by removal, re-etching and introduction to the MBE system. During pre-heating for the SAE growth, the sample was exposed to Te_2 flux for the last 8.5 minutes of the pre-heating to SAE growth temperature. At the end of the SAE step, an anneal was performed (see Figure 80) in an attempt to smooth the merging of neighboring islands, and to encourage both dislocation annihilation reactions, and trapping at free surfaces to occur early in the film growth. The influence of intermediate SEM analysis, ex-situ

contamination, re-etching, and re-introduction to vacuum was eliminated from set IV, by not removing the samples from vacuum until completion of the thick growth.

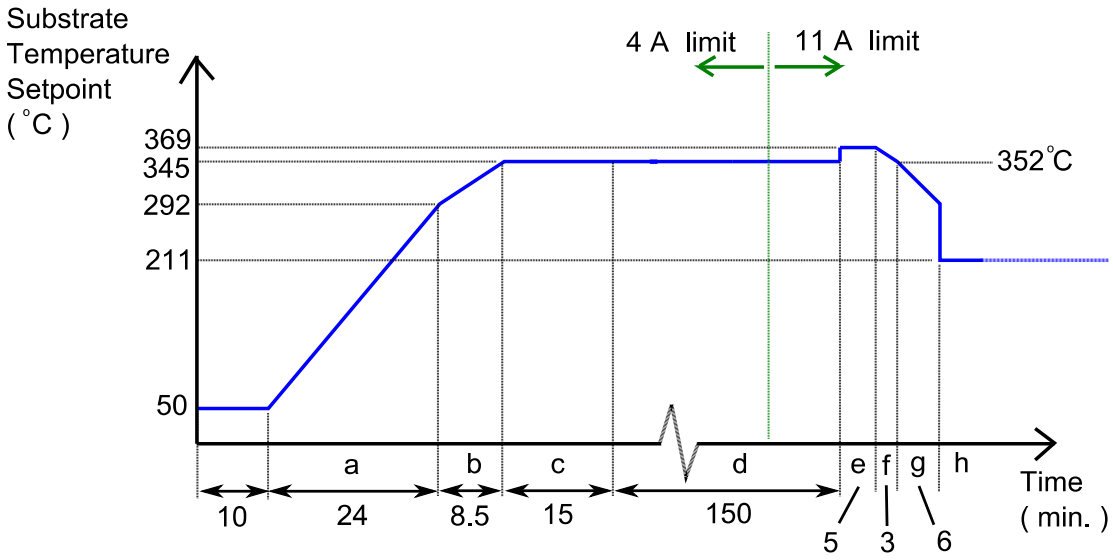

Figure 80 Growth procedure map schematic for the substrate temperature setpoint (not thermocouple setpoint) during SAE of sample pair IV. A flux of Te_2 was used during step b during preheating, as well as during steps e-g. Cadmium telluride flux was used during steps d-f in an early anneal before thick growth with 5 cyclic anneals commenced later in step h.

Sample set IV went through an identical procedure to set III, except that Te_2 flux was used during pre-heating, the samples were not removed for intermediate analysis, and the measured flux values were different. The surface cleaning and etching involved first the HBr etch mentioned earlier in this thesis, followed by the HCl etch mentioned earlier in this thesis. The sample pair underwent one SAE growth, with no intermediate SEM analysis before thick growth incorporating 5 in-situ cyclic anneals. The SAE

growth was performed at a temperature of 345°C; 5°C higher than set II. The two growth steps are listed below with estimated CdTe BEP flux values in Table 16.

Growth (SN-102b)	***Etch***	***Patt.***	***Unpatt.***	***T_s (^oC)***	***CdTe BEP (Torr)***	***CdTe Flux Duration (min.)***
1	HBr followed by HCl	Y	Y	345°C	1.1×10^{-6}	90
2	HBr followed by HCl	Y	Y	211°C	0.8×10^{-6}	725

Table 16 Growth steps for sample set IV. "Patt." and "Unpatt." columns indicate if the patterned and/or unpatterned samples were present during the growth procedure. T_s indicates the substrate temperature, and the beam equivalent pressure (BEP) of CdTe is taken as 10-times the flux gauge reading. The procedure was nearly identical to that for sample set III, except that the samples were not removed for intermediate analysis, Te_2 flux was used during pre-heating, and the measured flux values were slightly different.

The center of the patterned sample of set IV was imaged before any growth, as shown in Figure 81 and Figure 82.

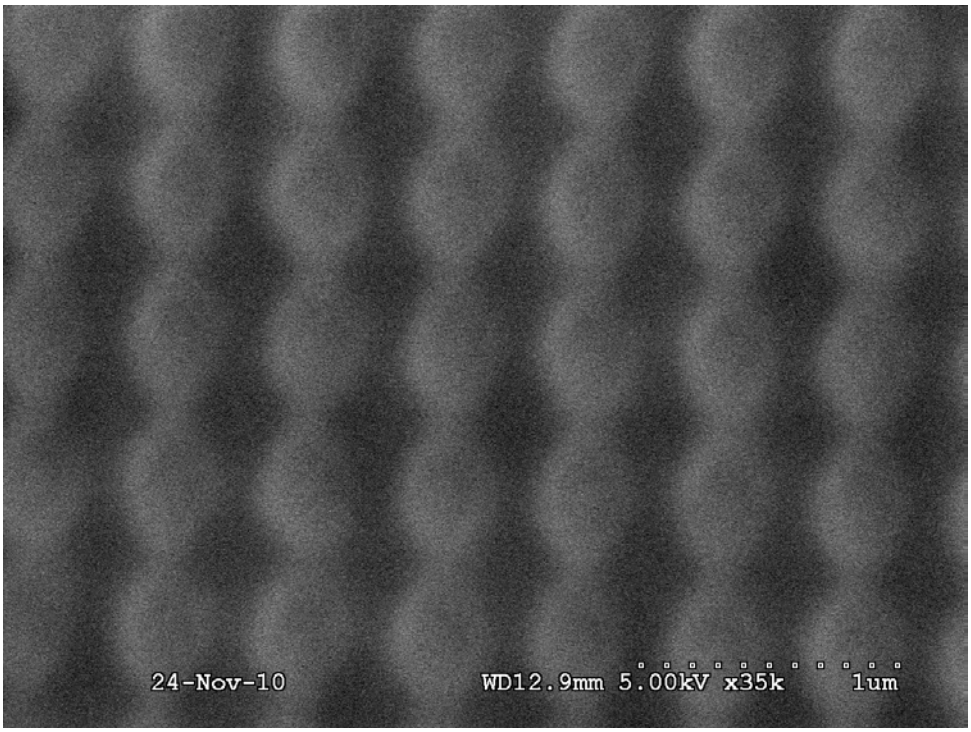

Figure 81 The approximate center of the patterned sample of set III, before any growth. The silicon nitride mask features are apparent. CdTe is likely present in the darker contrast regions. The $\left[\bar{1}11\right]$ direction of the underlying silicon substrate points left in the figure.

Figure 82 A lower magnification view of the same area shown in Figure 81, from the approximate center of the patterned sample of set III, before any growth. This image was acquired before that shown in Figure 81, thus no carbon rectangle is present. The $\left[\bar{1}11\right]$ direction of the underlying silicon substrate points left in the figure.

After SAE, the sample was imaged by SEM again as shown in Figure 83. Similarly to the previous patterned samples, this sample shows an in-plane growth asymmetry; indicating a faster lateral merging of seeding areas along the left-right orientation in Figure 83, as opposed to top-to-bottom. The in-plane orientation of the CdTe film can be inferred from the orientation of the silicon substrate, which was found by XRD from the asymmetric $\left(311\right)$ reflection. The in-plane crystal orientation is thus found to have $\left[\bar{1}11\right]$ oriented to the left in Figure 83; which is consistent with step-flow growth being the cause of smooth merging in the same direction type. In the particular case of this patterned sample, the higher degree of connected, smooth apparent merging

in the $\left[0\bar{1}1\right]$ surface orientation is likely due to the original seeding pattern which was more connected in that direction than for the other patterned samples (see Figure 81). For reference, a schematic of the (211) surface is shown in Figure 84, to aide the reader in visualizing the step-flow growth possible on this surface.

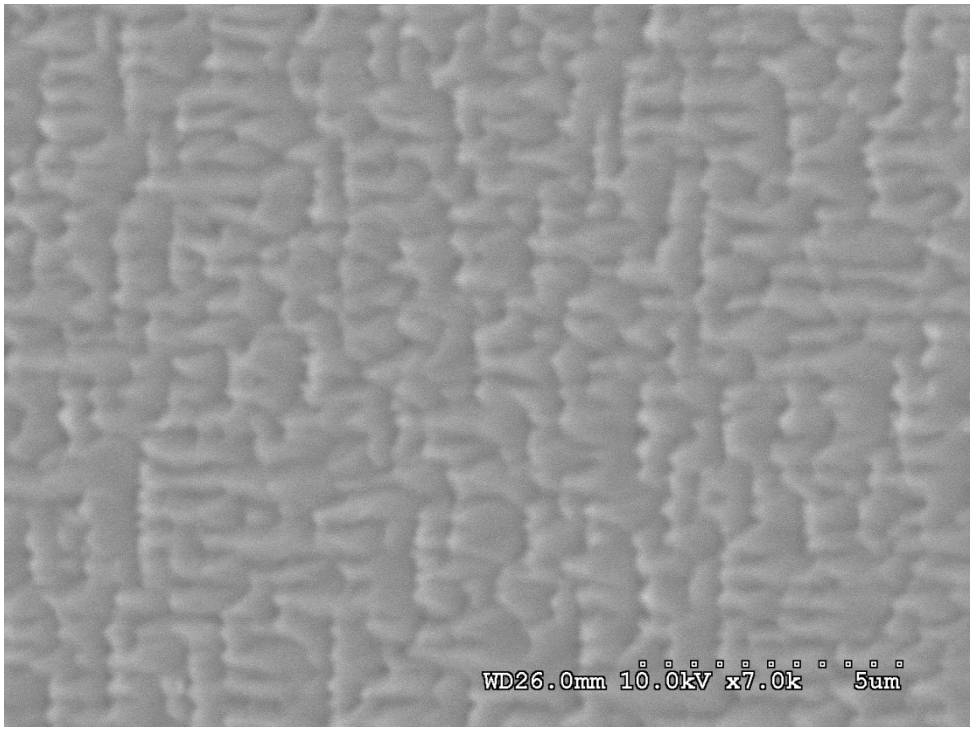

Figure 83 The center of the patterned sample from set IV, after the thick growth-2, incorporating 5 in-situ anneals. The XRD (422) rocking curve FWHM was found to be 1650" on this sample. The $\left[\bar{1}11\right]$ direction of the underlying silicon substrate points left in the figure.

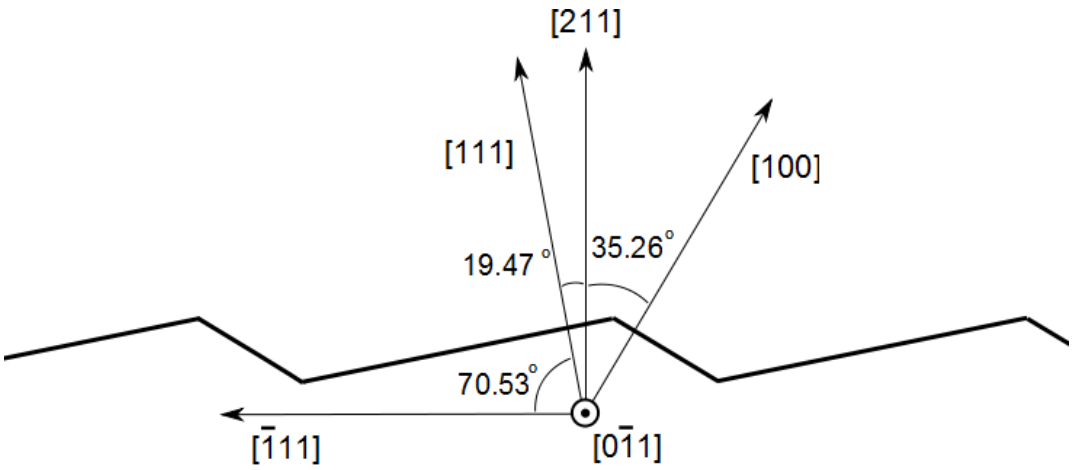

Figure 84 A schematic cross-section of the (211) surface is shown here for reference. Step-flow growth appears most likely to occur either parallel or antiparallel to the $[\bar{1}11]$ direction.

The patterned sample from set IV was also cleaved along the $[\bar{1}11]$ and $[0\bar{1}1]$ directions for cross-sectional SEM measurements along those two directions. Due to the expected step-flow growth mechanism, there is expected to be more free surface area visible/distinguishable along the $[0\bar{1}1]$ cross-section, rather than the $[\bar{1}11]$ cross-section. The observations below are consistent with that notion. In Figure 85 the cross-section parallel to $[\bar{1}11]$ is shown, where no patterned structure is apparent at the interface. In contrast, Figure 86 shows the cross-section parallel to $[0\bar{1}1]$, which indicatives the presence of free surface near the interface, spaced by the initial seed-island spacing.

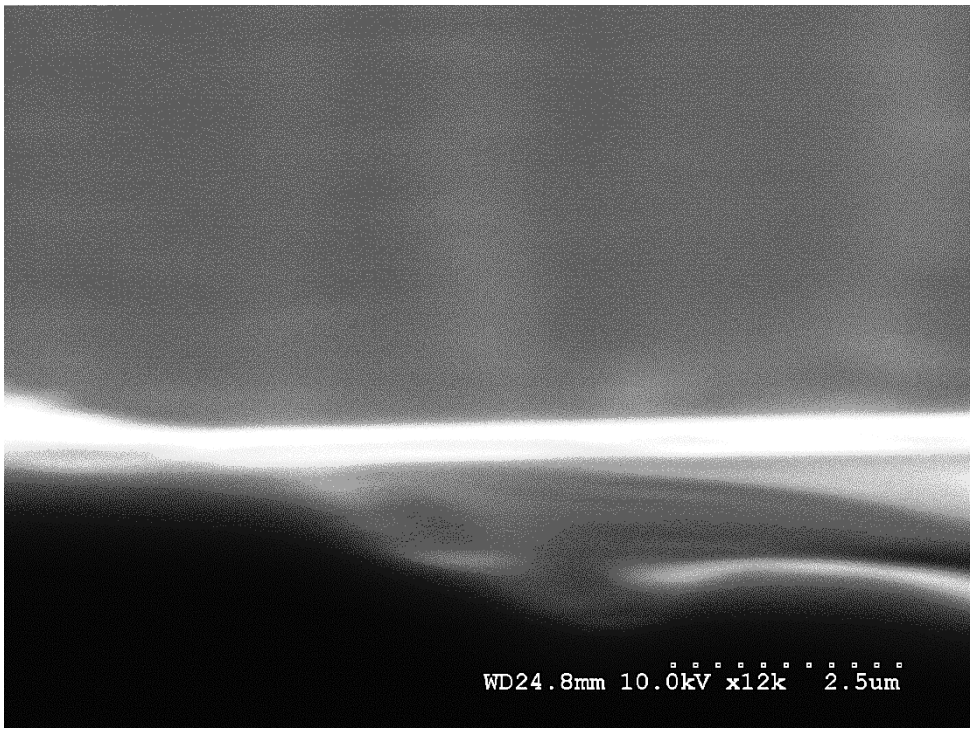

Figure 85 A cross-sectional view of the patterned sample from set IV, after the thick growth-2, incorporating 5 in-situ anneals. The surface of the cross-section contains the $[\bar{1}11]$ direction (oriented horizontally in the plane of the paper). The upper part of the image is CdTe, and the lower part is Si. No structure indicative of free surface area is visible at the interface.

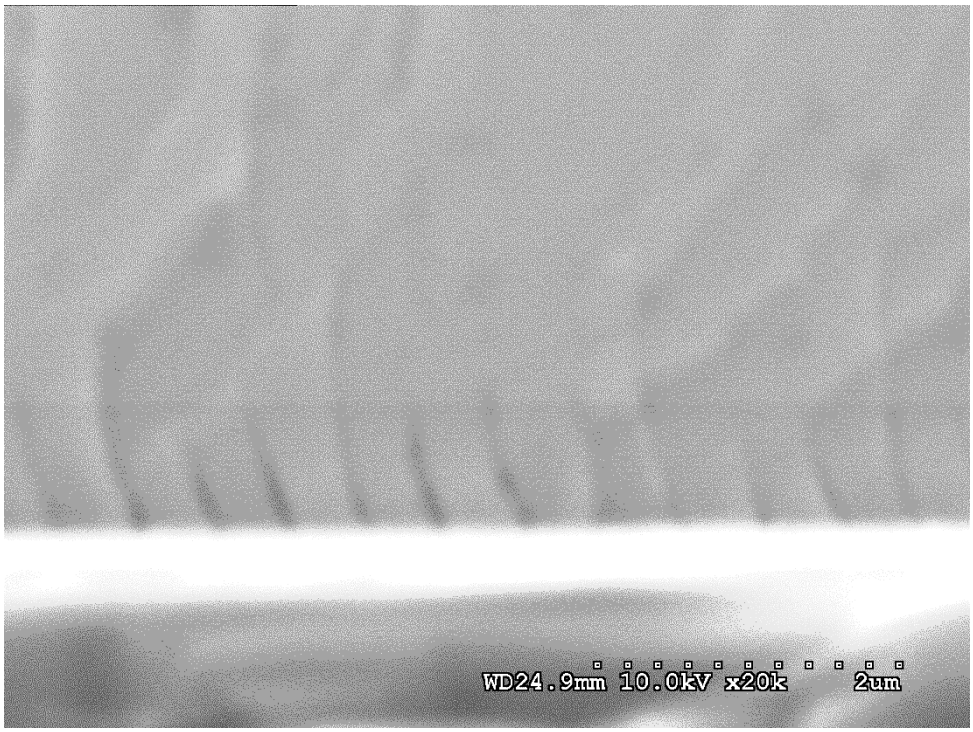

Figure 86 A cross-sectional view of the patterned sample from set IV, after the thick growth-2, incorporating 5 in-situ anneals. The surface of the cross-section contains the $[0\bar{1}1]$ direction. The upper part of the image is CdTe, and the lower part is Si. Dark contrast features indicative of free surface area are visible at the interface.

A comparison of the growth results of the four sets of patterned and unpatterned samples is given in Table 17. It should be noted that the ratio of (422) FWHM values in each case were very close to each other; although they do follow a trend with respect to the absolute value of the (422) rocking curve FWHM's. We suspect this similarity in values may be an indicator of a growth mechanism on the patterned samples that is dependent on the geometry of the seeding array, as compared to normal unpatterned growth. The calculated dislocation density in Table 17 was estimated from the (422) FWHM using Equation 40.

Set	*Etch*	*SAE T_s (^oC)*	*Thickness (μm / μm): Patt. / Unpatt.*	*(422) FWHM (arcsec / arcsec): Patt. / Unpatt.*	*Calculated Dislocation Density (cm^{-2}): Patt. / Unpatt.*
I	HBr	320	12.7 / 11.9 = 1.1	912 / 91 = 10	2.0×10^{9} / 2.0×10^{7} = 100
II	HBr	340	9.0 / 7.9 = 1.1	2297 / 454 = 5	1.3×10^{10} / 5.1×10^{8} = 26
III	HCl + HBr	345	4.5 / 5 = 0.9	1047 / 152 = 7	2.7×10^{9} / 5.6×10^{7} = 48
IV	HBr	345	9.4 / 10 = 0.9	1650 / 238 = 7	6.7×10^{9} / 1.4×10^{8} = 48

Table 17 Here is shown a summary comparison between the four sample sets; each set consisting of one patterned (Patt.) and one unpatterned (Unpatt.) sample. The thickness values were measured by FT-IR. The (422) FWHM values are from XRD rocking curves for the CdTe films. The calculated dislocation density was estimated from the (422) FWHM.

3.3 Discussion and future directions

The absolute CdTe (422) FWHM values for both sample pairs do not appear similar to the best values reported in the literature for CdTe/Si, which are ~50" to 60" [191]. This discrepancy may be in part due to the high substrate temperature used for the SAE procedure (320 to 345^{o}C). For example, it has been reported that for CdTe/ZnTe/Si(211) grown above 330^{o}C, the FWHM will exceed 200" for 8μm thick CdTe films, whereas optimal layers can be obtained at ~300^{o}C with FWHM as narrow as 70" [129]. Thus, for this research on the feasibility of patterned substrates to reduce TDD, we focus on the relative comparison of our patterned and unpatterned sample pairs. Such a relative comparison is not expected to be free from dependence on the absolute quality of the crystal growth, but should be much less so.

Focusing on the comparison of samples, it is clear that the crystalline quality of the patterned samples is significantly worse than the unpatterned samples. In the case of the patterned samples, the spacing between seeds is ~250nm and the lateral size of the seeds is also ~250nm. Thus, one can reasonably expect the seeds to be of lower dislocation density when compared to an unpatterned film of CdTe/Si of the same thickness, based on previously mentioned estimates of the fusion radius (35 to 900nm); however, the exact nature of the mechanisms of merging of neighboring islands, and subsequent growth mechanisms are not yet known. This motivates one to consider how the merging of islands may have increased the FWHM of the coalesced patterned CdTe films in comparison with the unpatterned films. In addition, the observed similarity in the ratio of patterned and unpatterned films' FWHM values supports this consideration,

despite differing surface etching, pre-heating, SAE growth temperature (T_s), thickness values, and intermediate SEM analysis interruptions between the SAE sample pairs.

One important issue for the merging of the seed islands is the presence of dislocations near the surfaces of the seeds. We note that after SAE and coalescence, and with low CdTe growth rate anisotropy, we expect there to be formed free-standing CdTe surfaces underneath the merging zones of neighboring islands similar to those described by Kwon and Lee [192]. Before the island merging, the dislocations in the small seed volumes are attracted to their surfaces, as mentioned earlier; therefore our CdTe seed islands likely have a higher density of dislocations near their surfaces compared with their interiors before merging. After the seeds merge, those dislocations previously near island surfaces may either continue to grow up further with the CdTe film, stay trapped at the free surface of CdTe near the Si or mask interface, annihilate with other dislocations from the same or neighboring islands, interact to form sessile/immobile dislocations, or react to generate more dislocations. Ideally, the pattern of islands is expected to increase the likelihood of the dislocations interacting and annihilating, or being trapped near the CdTe/Si interface by free or partially free surface. However, that appears not to have been a favored process for the samples considered here.

A second important issue for the merging of the seed islands is the lateral to vertical growth rate ratio. If the ratio is small, then a high surface corrugation will result. In the case of CdTe(211)B, it is possible for the MBE growth to proceed with step flow growth along the (111) or the (100) surface planes, thus giving a high lateral to vertical growth rate ratio in one surface direction. This is consistent with the observations reported here, of a preferential direction for smooth merging parallel to $\left[\bar{1}11\right]$. Future

samples could likely be produced of lower surface corrugation by utilizing this asymmetry. It should also be noted that a HgCdTe superlattice is also known to be capable of reducing surface roughness [193], and could likely be used to help reduce surface corrugation. In addition, it should be noted that in the case of GaN, where SAE has been very helpful in reducing DL density, the lateral to vertical growth rate ratio can be as high as 4 [194]. This motivates the exploration of stripes of CdTe seeding windows aligned with $\left[0\,\bar{1}1\right]$.

A third important issue for the smooth merging of the seed islands is the relative tilt of the islands. Rujirawat [129] reported that the tilt of the CdTe layer with respect to the Si substrate roughly followed the trend of the CdTe FWHM as a function of T_s. That is, the tilt was also minimum near T_s=300^{o}C, and away from this minimum the tilt increased by an additional 1 to 2^o for higher and lower T_s values. This variation in tilt as a function of crystal quality may play a role in our patterned sample experiments, provided that neighboring seeding areas of CdTe develop with different tilt values during the initial phases of patterned sample formation, or subsequent SAE from our patterned samples. If neighboring seeding islands have different tilt they will likely be prone to generating dislocations upon merging together during SAE, depending on the magnitude of the tilt disparity between neighboring islands. To minimize this issue, two future architectures may be helpful:

(1) smaller and closer seeding areas.

(2) a patterned mask on a thick CdTe/Si film (for example ~10μm thick). Note, however that this film ought to be thinner than ~25μm, due to the capability of

thermal mismatch in generating DL's when cooling to room-temperature after MBE growth.

The use of smaller seeds would possibly have the benefit of minimizing nearest neighbor tilt disparities; as well as the benefit of reducing the TDD in the seeding volumes, due to an increase in the side-wall surface area to volume ratio. The use of the thick film would possibly result in a more uniform tilt distribution between seeding areas before merging, in part due to lower initial dislocation density. The first architecture is well suited to possible IR detector device applications as well as solar cell applications. The second architecture is well suited to possible IR detector applications, but likely not well suited to solar cell applications.

The first proposed architecture, of smaller and closer seeds, may be difficult to achieve in large areas at a reasonable cost, due to the length scale of features needed. This thesis offers a new technique that may prove useful for fabricating such small features: the writing of carbon mask deposit by electron beam induced deposition.

It is clear from Figure 74 that we have observed an MBE growth inhibition from what we believe is carbon contamination induced by the SEM electron beam. This is not a new observation, as the electron beam is known to be capable of catalyzing chemical reactions on the surfaces of materials in vacuum, including the catalyzed deposition of carbon [195]. Such a process has been utilized to form patterns of carbon coating on a material's surface and subsequently used as a chemical mask during electrodeposition of Au to inhibit Au on the carbon-coated areas [196]. This technique of selective area carbon deposition has also been used as a negative mask for selective area porous silicon formation, whereby the carbon areas protect the underlying silicon during HF etching

[197]. Our observation of CdTe SAE against carbon makes this a possible technique to form large area carbon masked patterns for CdTe growth by MBE. The technique can expand the possible architectures for patterned CdTe samples closer to the lower estimate of half the fusion radius in CdTe (~35nm), and also closer to the lower length scale limit of the CdTe/Si interface, marked by the length scale of the 5×6 interface registry, at ~3nm.

A future investigation of interest to further elucidate the potential benefit of patterned substrates for TDD reduction in CdTe/Si would entail SEM writing thin DLC lines of various thickness and in-plane orientation on CdTe/Si, with variable inter-line spacing from sample-to-sample. It should be noted on this topic, that the spacing of lines giving the optimal results may be fairly large (mm scale) due to the density of dislocations at the top surface of a current state-of-the-art CdTe/Si (~10^7 cm^{-2}). However, the most likely optimal result will have a smaller spacing, due to the dislocation annihilation/fusion radius mention earlier. Perhaps the best result will be obtained for a mask width which exactly cancels the residual strain in the CdTe, assuming a perfect 5×6 interface registry, confined to the interface. For example, that could be achieved with two sets of 50nm-wide mask stripes of 9.09μm inter-stripe spacing. With that pattern geometry, and considering the SEM parameters needed for carbon mask formation in [197], one can estimate that a rastering electron beam delivering 30nA at the sample could deposit the pattern of mask lines at the threshold dose level of 1.5μC/cm^2 over a 1cm^2 area in ~2 min. At this rate, a 3-inch silicon wafer could be patterned in less than 2 hours.

There may be an indirect benefit from the patterned architecture reported here for the fabrication of HgCdTe devices, despite the higher FWHM and TDD on the patterned samples reported here. The Si_xN_y mask may effectively block diffusion of contaminants from 25% or more of the activated dislocations near the CdTe/Si interface (for example, fluorine). Recall that for the traditional, unpatterned interface, such dislocations could connect detrimental impurities at the CdTe/Si interface to HgCdTe diodes fabricated on the CdTe. In the patterned-interface architecture the laterally grown CdTe is free-standing above the mask, and the dislocations connecting to the CdTe/Si interface ideally may not pass the mask layer region, as they are trapped or blocked by the free surface or partly free surface and the mask itself. It is true that other dislocations may be present at the merging zones of CdTe seeding islands, but those aren't as likely to be connected to the CdTe/Si interface. This effect may help to reduce the suspected shorting of pixels by activated threading dislocations [14, 13]. However, the absolute TDD will need to be reduced below the values we have observed in this work; ideally to values in the range of $\sim 1\times10^5\,cm^{-2}$ or lower, to minimize Shockley-Read-Hall recombination in HgCdTe [198, 199]. In a similar vein, the free surface near the patterned-interface can also benefit device performance by collecting impurities which would otherwise diffuse through the bulk of the epilayer, or along dislocations in the epilayer. For example, this could be useful for epilayers of HgCdTe on GaAs or InSb; where diffusion of elements from the substrate itself can be an issue for performance of IR sensors fabricated in the HgCdTe epilayer.

4 Conclusion

We have established an appropriate dilute, wet etch for sub-micrometer-scale CdTe/ZnTe seeds and we point to the value of sample pre-heating under limited power, to minimize damage to small CdTe crystals on silicon substrates.

We have demonstrated for the first time the SAE of CdTe against Si_xN_y and likely carbon mask materials by MBE; and have observed the coalescence of CdTe against Si_xN_y mask by MBE. The coalescence is seen to have an in-plane asymmetry consistent with a step-flow growth mode of CdTe(211). The coalesced film is also seen to have small surface corrugation, related to the separation of neighboring seed islands from the patterned sample fabrication.

Using direct comparison, we have tested the feasibility of our patterned 500nm-pitch Si_xN_y and CdTe interface structure to reduce the TDD intersecting the final surface of CdTe/ZnTe/Si(211) grown by MBE. We find that our patterned substrate structure is likely insufficient to reach that goal, as the XRD FWHM from our patterned samples is ~7 times larger, and so implies the TDD is orders of magnitude higher than unpatterned growth of CdTe/ZnTe/Si(211) under identical growth conditions. To achieve a comparative reduction in TDD on a patterned substrate, the fabrication of smaller and closer seeding islands is recommended.

Future patterned sample architectures for SAE by MBE may make use of electron beam induced carbon mask deposit, to make smaller patterned features. In addition, future patterned architectures may explore the feasibility of disconnecting threading dislocations from possible mobile contaminants near the Si or GaAs interface that may

otherwise be transported to active device areas fabricated subsequently, apart from the interface to Si or GaAs; however this may not be beneficial for HgCdTe/CdTe/ZnTe/Si(211) devices unless the absolute TDD is also reduced.

Appendix A: Sticking Coefficient versus Temperature Fitting with One Exponential.

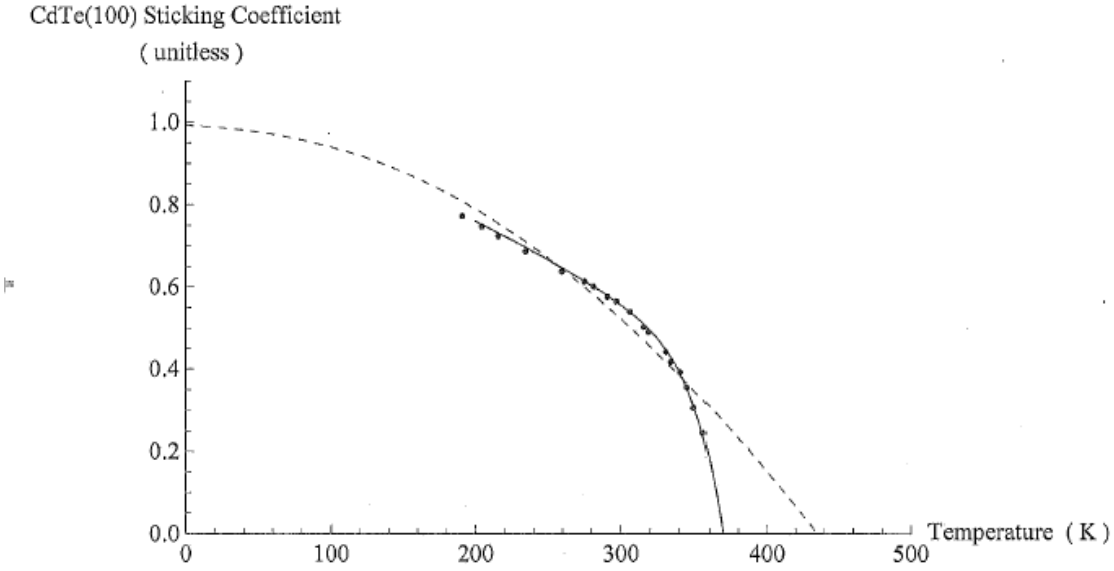

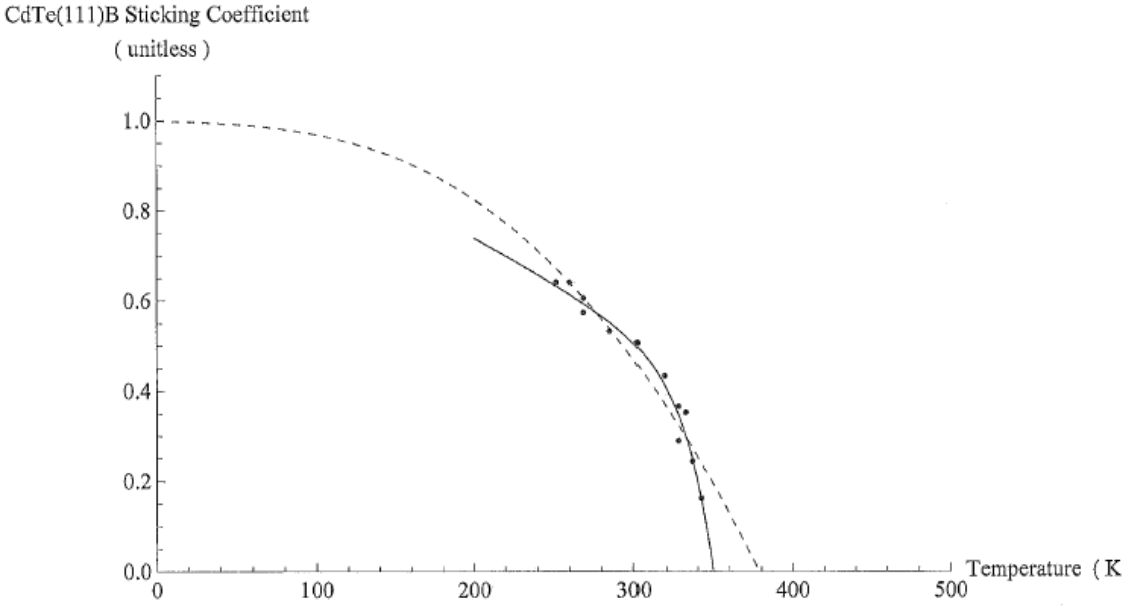

WORKS CITED

[1] P. Capper, Properties of Narrow Gap Cadmium-Based Compounds, EMIS Datareviews Series No. 10 (Institution of Electrical Engineers, London, 1994).
[2] G.L. Hansen, J.L. Schmitt, T.N. Casselman, *J. Appl. Phys.*, Vol.53, (1982), pp7099-101.
[3] M.N. Abedin, T.F. Refaat, et al., Proc. of SPIE 5152, Infrared Spaceborne Remote Sensing XI (2003), pp 279-288.
[4] F. Goff, S.P. Love, et al., Chemical Geology 177, No. 1-2, July 15 (2001), pp 133-156.
[5] A.M. Ghez, S.A. Wright, et. al., The Astronomical Journal 601 (2004), pp L159-162.
[6] J. Bennett et al., The Essential Cosmic Perspective, 5th edn. (Addison-Wesley, San Francisco, 2009).
[7] J.W. Beletic, II-VI invited oral presentation: The Fantastical Discoveries of Astronomy made Possible by the Wonderful Properties of II-VI Materials, The 2011 U. S. Workshop on the Physics and Chemistry of II-VI Materials (2011).
[8] J.P. Faurie, and A. Million, *J. of Crystal Growth*, Vol.64, (1981) pp582-585.
[9] P. Capper and J. Garland, Mercury Cadmium Telluride Growth Properties and Applications, Wiley, (2011).
[10] S.M. Johnson, A.A. Buell, M.F. Vilela, J.M. Peterson, J.B. Varesi, M.D. Newton, G.M. Venzor, et. al.; *J. Electron. Mater.*, Vol. 33, No. 6, (2004), pp526-530.
[11] M. Carmody, J.G. Pasko, D. Edwall, E. Piquette, et.al., *J. Electron. Mater.*, Vol. 37, No. 9, (2008), pp1184-1188.
[12] J.D.Benson, et. al.; *J. Electron. Mater.* 39, 7 (2010).
[13] L.O. Bubulac, J.D. Benson, R.N. Jacobs, et al., *J. Electron. Mater.*, Vol. 40, No. 3 (2011).
[14] M. Jaime-Vasquez, R.N. Jacobs, et al., *J. Electron. Mater.*, Vol. 39, No. 7 (2010).
[15] K. Jowikowski, A. Rogalski, *J. Electron. Mater.*, Vol. 29, No. 6, (2000), pp736-741.
[16] N.V. Sochinskii, M. Abellan, J. Rodriquez-Fernandez, et al., *Superlattices and Microstructures*, Vol. 45, (2009), pp228-233.
[17] V. Babentsov, V. Boiko, et al., *Nucl. Instr. and Meth. A.* (2010).
[18] M. Everaldo de Souza, PhD Thesis: Minority Carrier Lifetime in Hg1-xCdxTe Grown by Molecular-Beam Epitaxy; University of Illinois at Chicago, Physics Department (1991).
[19] S.M. Johnson, D.R. Rhiger, J.P. Rosbeck, J.M. Peterson, S.M. Taylor, and M.E. Boyd, *J. Vac. Sci. Technol. B* 10, No. 4, Jul/Aug (1992).
[20] L. He, L. Chen, et. al., *J. Cryst. Growth* 301-302 (2007), pp 268-272.
[21] J.W. Yang, A Lunev, et al., *Appl. Phys. Lett.* 76, No. 3, Jan 17 (2000), pp 273-275.
[22] S. Hla, and K. Rieder, *Annu. Rev. Phys. Chem.* 54 (2003).
[23] J. A. Czaban, D.A. Thompson, and R.R. LaPierre, *Nano Lett.* 9, No. 1 (2009), pp 148-154.
[24] O. Landre, D. Camacho, C. Bougerol, et al., *Phys. Rev. B* 81, 153306 (2010).
[25] Y. Shoji, R. Oshima, A. Takata, et al., *IEEE* (2010).
[26] T. Schallenburg, C. Schumacher, et al., *Phys. Stat. Sol. (b)* 241, No. 3 (2004), pp 564-567.
[27] M.C. Peckerar and J.R. Maldonado, *Proc. IEEE* 81, No. 9, Sept (1993).
[28] M. Rothschild, T.M. Bloomstein, et al., *MRS Bulletin* 30, Dec (2005).
[29] S.Y. Chou, P.R. Krauss, et al., *J. Vac. Sci. Technol. B* 15, No. 6, Nov/Dec (1997), pp 2897-2904.
[30] W. Li, J. Zhou, et al., *Nanotechnology* 19, 135308 (2008) .
[31] W.P. Kirk and M.A. Reed, Nanostructures and Mesoscopic Systems, Proc. Inter. Symposium, (Academic Press, Inc., Boston, 1992).
[32] M. Jung, S. Mho, and H.L. Park, *Appl. Phys. Lett.* 88, 133121 (2006).
[33] U. Dotsch and A.D. Wieck, *Nuclear Instruments and Methods in Phys. Research B* 139 (1998), pp 12-19.
[34] M. Isaacson and A. Muray, *J. Vac. Sci. Technol.* 19, No. 4, Jun (1981), pp 1117-1120.
[35] D.M. Eigler and E.K. Schweizer, *Nature* 344, Apr (1990).
[36] W.O. George, Infrared Spectroscopy, (Wiley, London, 1987).
[37] J.W. Cooley and J.W. Tukey, *Math. Comput.* 19, No. 297 (1965).
[38] P.B. Fellgett, *PhD Thesis*, University of Cambridge (1951).
[39] J.L. McHale, Molecular Spectroscopy, 1st edn (Prentice Hall, Upper Saddle River, New Jersey, 1999).
[40] A. Kuze, H. Suto, et al., *Appl. Optics* 48, No. 35, December 10 (2009).

[41] Y.J. Kaufman and Bo-Cai Gao, *IEEE Trans. on Geosci. and Remote Sensing* 30, No. 5, September (1992).
[42] A.S. Zachor et al., SPIE *Fourier Transform Infrared Spectroscopy* 289 (1981) pp 209-213.
[43] W.F. Herget, *SPIE Fourier Transform Infrared Spectroscopy* 289 (1981) pp 449-456.
[44] R.D. Guenther, Modern Optics (John Wiley and Sons, New York, 1990).
[45] J.B.P. Williamson, *Proc. Inst. Mech. Eng.* 182, No. 21 (1967).
[46] R. Young, J. Ward, F. Scire, *IEEE Review of Scientific Instruments* 43, No. 7 (1972).
[47] G. Binning, H. Rohrer, et al., *Phys. Rev. Lett.* 49, No. 1, July 5 (1982).
[48] G. Binnig and H. Rohrer, *Reviews of Modern Physics* 59, No. 3, Part I, July (1987).
[49] G. Binnig, C.F. Quate, and Ch. Gerber, *Phys. Rev. Lett.* 56, No. 9, March 3 (1986).
[50] T. Sulchek, R. Hsieh, et al., *Appl. Phys. Lett.* 76, No. 11, March 13 (2000).
[51] M.J. Brukman and D.A. Bonnell, *Phys. Today*, June (2008).
[52] R. Garcia and R. Perez, *Surf. Sci. Reports* 47 (2002) pp197-301.
[53] S.C. Minne, G. Yaralioglu, et al., Appl. Phys. Lett. 72, No. 18, May 4 (1998).
[54] H. Butt and M. Jaschke, *Nanotechnology* 6 (1995) pp 1-7.
[55] J.B. Marion and S.T. Thornton, Classical Dynamics of Particles and Systems, 4th edn. (Harcourt Brace and Company, Fort Worth, Philadelphia, 1995).
[56] R.G. Lerner and G.L. Trigg, Concise Encyclopedia of Solid State Physics, Section by A.V. Crewe (Addison Wesley Publishing Company, Inc., Reading, Massachusetts, 1983).
[57] M. Knoll, *Z. Tech. Physik* 16, No. 467 (1935).
[58] M. Knoll and R. Theile, *Z. Physik* 113, No. 260 (1939).
[59] C.W. Oatley, The Scanning Electron Microscope (Cambridge University Press, Cambridge Great Britain 1972).
[60] M. von Ardenne, *Z. Physik* 109, No. 553 (1938).
[61] A. Ichimiya and P.I. Cohen, Reflection High Energy Electron Diffraction (Cambridge University Press, Cambridge UK, 2004).
[62] C.W. Oatley, The Scanning Electron Microscope (Cambridge University Press, Cambridge, 1972).
[63] G.E. Lloyd, *Mineralogical Magazine 51*, March (1987) pp 3-19.
[64] L.E. Ballentine, Quantum Mechanics a Modern Development, (World Scientific, Singapore, 1998).
[65] J.M. Bijvoet, W.G. Burgers, and G.Hagg, Early Papers on Diffraction of X-rays by Crystals, (International Union of Crystallography, Netherlands, 1969).
[66] M.P. Marder, Condensed Matter Physics, (John Wiley and Sons, New York, 2000).
[67] L. de Broglie, *PhD Thesis:* Recherches sur la theorie des quanta, University of Paris, Physics Department (1924).
[68] A. Guinier, X-Ray Diffraction in Crystals Imperfect Crystals and Amorphous Bodies (Freeman and Company, San Francisco, 1963).
[69] C. Kittel, Introduction to Solid State Physics, 7th edn. (John Wiley and Sons, Inc., New York, 1996).
[70] W.H. Bragg, *Nature* 90, No. 2243, October 24 (1912).
[71] International Tables for X-Ray Crystallography, 2nd edn (Kynoch Press, Birmingham England, 1965).
[72] J.F. Vetelino, S.P. Gaur, and S.S. Mitra, *Phys. Rev. B* 5, No. 6, March 15 (1972).
[73] J.H. Hubbell, *Int. J. Appl. Radiat. Isol.* 33 (1982) pp 1269-1290.
[74] D. Balzar, Microstructure Analysis from Diffraction (International Union of Crystallography, 1999).
[75] J.D. Benson, R.N. Jacobs, et al., *J. Electron. Mater.* 37, No. 9 (2008).
[76] J.E. Ayers, *J. Crystal Growth* 135 (1994) pp 71-77.
[77] C.O. Dunn and E.F. Koch, *Acta Met. 5* (1957) 548.
[78] D. Briggs and M.P. Seah, Practical Surface Analysis by Auger and Photoelectron Spectroscopy, (John Wiley and Sons, Chichester New York, 1983).
[79] Einstein, Uber einen die Erzeugung and Verwandlung des Lichtes betreffenden heuristischen Gesichtspunkt. *Annalen der Physik* 17, No. 132 (1905).
[80] D.M. Poirier and J.H. Weaver, *Surf. Sci. Spectra* 2, No. 3 (1994).
[81] K. Siegbahn, U. Gelius et al., *Phys. Scr.* 1 (1970) pp 272-276.
[82] S. Evans, E. Raftery, J.M. Thomas, *Surf. Sci.* 89, No. 1-3 (1979) pp 64-75.
[83] T.M. Duc, C. Guillot, *Phys. Rev. Lett.* 43, No. 789 (1979).
[84] W.M. Kang, C.H. Li, and S.Y. Tong, *Solid State Commun.* 36, No. 149 (1980).
[85] S. Kono, S.M. Goldberg, N.F.T. Hall, and C.S. Fadley, Phys Rev. B 22 (1980) pp 6085-6103.

[86] D.J. Kennedy and S.T Manson, *Phys. Rev. A* 5, No. 1 (1972).
[87] J.H. Scofield, *J. Electron. Spec. and Related Phenomena* 8 (1976) pp129-137.
[88] M.P. Seah and W.A. Dench, *Surf. and Interface Anal.* 1, No. 1 (1979).
[89] J. Szajman, J. Liesegang, et al., *J. Electon. Spec. and Related Phenomena* 23 (1981) pp 97-102.
[90] National Institute of Standards and Technology, NIST Standard Reference Database 71, NIST Electron Inelastic-Mean-Free-Path Database, Version 1.1 (Secretary of Commerce, 2000).
[91] L. Wang, *PhD Thesis*: Zinc Blende MnS/ZnSe Heterojunction Valence Band Offset by X-Ray Photoemission Spectroscopy, University of Illinois at Chicago, Physics Department (1998).
[92] K. Siegbahn, C. Nordling, et al., ESCA Atomic, Molecular and Solid State Structure Studied by Means of Electron Spectroscopy (Almqvist and Wiksells Boktryckeri Ab ,Uppsala 1967).
[93] L.S. Hirsch, Master's Thesis, Preparation of Substrates for Semiconductor Growth Using Atomic Hydrogen, Eberly College of Arts and Sciences of West Virginia University, Physics (1998).
[94] D.A. Shirley, *Phys. Rev. B* 5, No. 12, June 15 (1972).
[95] R. Sporken et al., *J. Electron. Mater.* 38, No. 8 (2009).
[96] P. Capper, Bulk Crystal Growth of Electronic, Optical and Optoelectonic Materials, 1st edn. (John Wiley and Sons Ltd, West Sussex, England, 2005) ISBN: 0-470-85142-2.
[97] O.K. Wu, D.N. Jamba, and G.S. Kamath, *J. Crystal Growth*, Vol. 127, (1993), pp365-370.
[98] J.P. Faurie, *Prog. Crystal Growth and Charact.*, Vol. 29, (1995), pp 85-159.
[99] A. Chambers, Modern Vacuum Physics, Chapman and Hall/CRC Boca Raton (2005).
[100] C. Fulk, *PhD Thesis*: PbSnSe(211)/CdTe(211)B/Si(211) Interfaces; University of Illinois at Chicago, Physics Department (2007).
[101] W.M. Haynes and D.R. Lide, Handbook of Chemistry and Physics, 88th edn. (CRC Press Taylor and Francis Group LLC, Boca Raton, (2008).
[102] S.M. Sze and Kwog K. Ng, Physics of Semiconductor Devices, 3rd edn. (Wiley-Interscience, Hoboken, 2007), ch. 1.
[103] W.M. Haynes and D.R. Lide, Handbook of Chemistry and Physics, 91st edn. (CRC Press Taylor and Francis Group LLC, Boca Raton, 2010), sec 12, pp. 80-80.
[104] J.D. Jackson, Classical Electrodynamics, 3rd edn. (John Wiley and Sons, Inc., New York, 1999).
[105] E.D. Palik, Handbook of Optical Constants Vol. I (Academic Press Inc., Orlando, 1985).
[106] J.C. Sturm and C.M. Reaves, *IEEE Transactions on Electron Devices*, Vol. 39, No. 1, January, pp81-88 (1992).
[107] P. Vandenabeele and K. Maex, *J. Appl. Phys.*, Vol. 72, No. 12, 15 December, pp 5867-5875 (1992).
[108] Z. Wang, S.L. Kwan, T.P. Pearsall, J.L. Booth, B.T. Beard, S.R. Johnson, *J. Vac. Sci. Technol. B*, Vol. 15, No. 1, Jan/Feb (1997).
[109] J.J. Dubowski, J.M. Wrobel, and D.F. Williams, *Appl. Phys. Lett.*, Vol. 53, No. 8, 22 August, pp 660-662 (1988).
[110] R. Kiran, *PhD Thesis*: Optimization of the Hg1-xCdxTe Surface and its Characterization by Electrical and Optical Techniques; University of Illinois at Chicago, Physics Department (2008).
[111] T. Seldrum, R. Bommena, et al., *J. Vac. Sci. Technol. B*, 26, No. 3, May/June (2008).
[112] T. Behr, T. Litz, A. Waag, G. Landwehr, *J. Crystal Growth*, 156 (1995) pp 206-211.
[113] R. Sporken, D. Grajewski, et al., *J. Electron. Mater.* 29, No. 6 (2000).
[114] S. Tatarenko, B. Daudin, D. Brun, et al., *Phys. Rev. B*, 50, No. 24 (1994).
[115] J.D. Benson, B.K. Wagner, et al., Appl. Phys. Lett., 49, No. 16, 20 October (1986).
[116] J.D. Benson and C.J. Summers, J. Appl. Phys., 66, No. 11, 1 December (1989).
[117] C.M. Stahle and C.R. Helms, *J. Vac. Sci. Technol. A*, 10, No. 5, Sep/Oct (1992).
[118] J. Fritsche, T. Schulmeyer, et al., *Appl. Phys. Lett.* 81, No. 12, Sept. 16 (2002).
[119] Y.P. Varshni, *Phys. Rev. A* 40, No. 4, Aug. 15 (1989).
[120] R.L. Liboff, Introductory Quantum Mechanics, 3rd edn. (Addison-Wesley, Reading Massachusetts, 1998).
[121] T. Tanigaki, Y. Kimura, et al., *J. Crystal Growth*, 260 (2004) pp 298-303.
[122] D.B. Holt and M.I. Abdalla, Phys. Stat. Sol. (a) 26 (1974) pp 507-512.
[123] Y. Lo, R.N. Bicknell, et al., *J. Appl. Phys.* 54, No. 7, July (1983) pp 4238-4240.
[124] S. Sivananthan, X. Chu, J. Reno, and J. Faurie, J. Appl. Phys. 60, No. 4, August (1986) pp 1359-1363.
[125] R.J. Koestner and H.F. Schaake, *J. Vac. Sci. Technol. A* 6, No. 4, Jul/Aug (1988) pp 2834-2839.

[126] N.K. Dhar et al., *J. Vac. Sci. Technol. B* 14, No.3, May/Jun (1996) pp 2366-2370.
[127] R. Sporken, S. Sivananthan, et. al., *Appl. Phys. Lett.* 55, No. 18, Oct 30 (1989).
[128] R.N. Jacobs, J. Markunas, J. Pellegrino, L.A. Almeida, M. Groenert, M. Jaime-Vasquez, N. Mahadik, C. Andrews, and S.B. Qadri; *J. Cryst. Growth* 310, p2960-2965 (2008).
[129] S. Rujirawat, *PhD Thesis*: The CdTe/Si(111):As Interface; University of Illinios at Chicago, Physics Department (2000).
[130] J. Oh, C.H. Grein, *J. of Crystal Growth* 193 (1998) pp 241-251.
[131] A.E. Romanov, W. Pompe, G.E. Beltz, J.S. Speck, *Appl. Phys. Lett.* 69, No. 22, Nov 25 (1996), pp 3342-3344.
[132] J.S. Speck, M.A. Brewer, J. Appl. Phys. 80, No. 7, Oct. 1 (1996) pp 3808-3816.
[133] A.J. Ciani and P.W. Chung, *J. Electron. Mater.* (2009).
[134] S. Farrell, G. Brill, et al., *J. Electron. Mater.* 39, No. 1 (2010).
[135] S. Rujirawat, L.A. Almeida, et al., *Appl. Phys. Lett.* 71, No. 13, September 29 (1997).
[136] J.L. Reno, S. Chadda, and K. Malloy, *Appl. Phys. Lett.* 63, No. 13, September 27 (1993), pp 1827-1829.
[137] Y. Chang, J. Zhao, H. Abad, C.H. Grein, and S. Sivananthan, *Appl. Phys. Lett.* 86, 131924 (2005).
[138] R.N. Jacobs, P.J. Smith, et al., *J. Electron. Mater.* 39, No. 7 (2010).
[139] R. Bommena, T.Seldrum, L.Samain, R.Sporken, S.Sivananthan, and S.R.J.Brueck; *J. Electron. Mater.* 37, 9 (2008).
[140] E.A. Fitzgerald, *J. Vac. Sci. Technol. B* 7, No. 4, Jul/Aug (1989).
[141] T.S.Zheleva, O.H.Nam, M.D.Bremser, and R.F.Davis; *Appl. Phys. Lett.* 71, 2472 (1997).
[142] J. Friedel, Dislocations (Pergamon, Oxford, 1967), pp. 44-45.
[143] J.S. Speck, M.A. Brewer, and G. Beltz; *J. Appl. Phys.* 80, 7 October (1996).
[144] G. Badano, P. Gergaud, I.C. Robin, X. Baudry, B. Amstatt, and F. Gemain*; J. Electron. Mater.* 39, 7, pp. 908-911 (2010).
[145] Y. Chen, S. Farrell, G. Brill, P. Wijewarnasuriya, and N. Dhar, *J. Cryst. Growth* 310, pp. 5303-5307 (2008).
[146] W.D. Callister, Jr., Materials Science and Engineering An Introduction, 4th edn. (John Wiley and Sons, Inc., New York, 1997).
[147] A.H. Cottrell, Theory of Crystal Dislocations, 1st edn. (Gordon and Breach Science Publishers, New York, 1964).
[148] A. Stoltz, II-VI oral presentation: Reduction of Dislocations Density by Producing Novel Structures, The 2011 U. S. Workshop on the Physics and Chemistry of II-VI Materials (2011).
[149] M. Martinka, L.A. Almeida, et al., *J. Electron. Mater.* 31, No. 7 (2002) pp 732-737.
[150] Y. Chang, C.R. Becker, C.H. Grein, et al., *J. Electron. Mater.* 37, No. 9 (2008).
[151] J. Molstad, P.Boyd, J.Markunas, D.J.Smith, Ed Smith, E.Gordon, J.H.Dinan; *J. Electron. Mater.* 35, 8 (2005).
[152] F.F. Abraham and C.R. Brundle, *J. Vac. Sci. Technol.* 18, No. 2, March (1981).
[153] T. Schallenberg, C. Schumacher, et al., *Phys. Stat. Sol.* (b) 241, No. 3 (2004) pp 564-567.
[154] Y.Y. Luo, A. Cavus, and M.C. Tamargo, *J. Electron. Mater.* 26, No. 6 (1997).
[155] Y. Luo, A. Cavus, and M.C. Tamargo, *J. Vac. Sci. Technol. B* 16, No. 3, May/Jun (1998).
[156] B. Bryskiewicz, T. Bryskiewicz, and E. Jiran, *J. Electron. Mater.* 24, No. 3 (1995).
[157] K.Y. Zang, Y.D. Wang, et al., *Appl. Phys. Lett.* 87, 193106 (2005).
[158] K.Y. Zang, Y.D. Wang et al., *Thin Solid Films* 515 (2007) pp 4505-4508.
[159] F.W. Tausch, Jr., and A.G. Lapierre, III, J. of the Electrochemical Society 112, No. 7, Jul (1965) pp 706-709.
[160] R. Sporken, D.Grajewski, Y.Xin, F.Wiame, G.Brill, P.Boieriu, A.Prociuk, S.Rujirawat, N.K.Dhar, S.Sivananthan; *J. Electron. Mater.* 29, 6 (2000).
[161] I. Bhat and R. Zhang, *J. Electron. Mater.* 35, No. 6 (2006).
[162] R. Zhang and I. Bhat, *J. Electron. Mater.* 30, No. 11 (2001).
[163] J.L. Reno, M.J. Carr, and P.L. Gourley, *J. Vac. Sci. Technol. A* 8, No. 2, Mar/Apr (1990).
[164] G. Vanamu, A.K. Datye, and S.H. Zaidi, *J. Vac. Sci. Technol. B* 23, No. 4, Jul/Aug (2005).
[165] L.A. Almeida, M. Groenert, J. Molstad, M. Carmody et al., Proceedings for the Army Science Conference (24th) Held on 29 November to 2 December in Orlando FL. (2005).
[166] B. Weng, F. Zhao, et. al., *Appl. Phys. Lett.* 96, 251911 (2010).

[167] A.J. Stoltz, J.D. Benson, M. Carmody, et al., *J. Electron. Mater.* 40, No. 8 (2011).
[168] M. Martinka, L.A. Almeida, J.D. Benson, and J.H. Dinan, *J. Electron. Mater.* 31, No. 7 (2002).
[169] D.R. Rhiger, S. Sen, E.E. Gordon, *J. Electron. Mater.* 29, No. 6 (2000).
[170] M. Carmody, S. Mallick, J. Margetis, R. Kodama, T. Biegala, D. Xu, P. Bechman, J.W. Garland, and S. Sivananthan; *Appl. Phys. Lett.* 96, 15 (2010).
[171] J.F. Geisz, D.J. Friedman, J.S. Ward, A. Duda, W.J. Olavarria, T.E. Moriarty, J.T. Kiehl, M.J. Romero, A.G. Norman, and K.M. Jones; *Appl. Phys. Lett.* 93, 12 (2008).
[172] G. Vanamu, et al., *J. Crystal Growth*, 280 (2005) pp 66-74.
[173] P. Moravec, V.G. Ivanits'ka, et al., *J. Electron. Mater.* 38, No. 8 (2009).
[174] V.G. Ivanits'ka, P. Moravec, et al., *J. Electron. Mater.* 36, No. 8 (2007).
[175] V. Srivastav, R. Pal, and H.P. Vyas, *Opto-Electronics Review* 13, No. 3 (2005) pp 197-211.
[176] Z.F. Tomashik, E.M. Lukianchuk, and V.M. Tomashik, *Semiconductor Physics, Quantum Electronics and Optoelectronics* 7, No. 4 (2004) pp 452-455.
[177] Y.S. Wu, C.R. Becker, et al., *Appl. Phys. Lett.* 60, No. 15, Apr 13 (1992).
[178] Y.S. Wu, C.R. Becker, A. Waag, et al., *Semicond. Sci. Technol.* 8 (1993) pp S293-S295.
[179] Y.S. Wu, C.R. Becker, A. Waag, et al., *J. Appl. Phys.* 73, No. 11, Jun 1 (1993) pp 7385-7388.
[180] V. Srivastav, R. Pal, B.L. Sharma, et al., *J. Electron. Mater.* 34, No. 11 (2005) pp 1440-1445.
[181] Z.F. Tomashik, V.N. Tomashik, et al., *Inorganic Materials* 42, No. 8 (2006) pp 859-862.
[182] S. Mallick, R. Kiran, S. Ghosh, S. Velicu, S. Sivananthan, *J. Electron. Mater.* 36, No. 8 (2007) pp 993-999.
[183] J. Zhao, Y. Chang, G. Badano, S. Sivananthan, J. Markunas, S. Lewis, J.H. Dinan, P.S. Wijewarnasuriya, Y. Chen, G. Brill, and N. Dhar, *J. Electron. Mater.* 33, 8, pp. 881-885 (2004).
[184] SRD 20 NIST X-ray Photoelectron Spectroscopy 3.5; http://www.nist.gov/srd/surface.cfm.
[185] S.D.Hersee, D. Zubia, X. Sun, R. Bommena, M. Fairchild, S. Zhang, D. Burckel, A. Frauenglass, and S.R.J. Brueck; *IEEE J. Quantum Electron.* 38, 8, August (2002).
[186] T. Seldrum, *PhD Thesis*: Selective Growth of CdTe by Molecular Beam Epitaxy on CdTe(211)B Microseeds and Si(100) Nanoseeds patterned on SiO_2; University of Namur, Belgium, Physics Department (2009).
[187] W. Kern and D.A. Puotinen, *RCA Rev.* 31, No. 187 (1970).
[188] D.H. Zavitz, A. Evstigneeva, et al., *J. Electron. Mater.* 24, No. 6 (2005).
[189] S. Shintri, C. Schaper, W. Sarney, P. Wijewarnasuriya, S. Trivedi, and I. Bhat, II-VI oral presentation: Vapor Phase Epitaxial Growth of (211)B CdTe and Ge on Nanopatterned Si for HgCdTe Based Infrared Device Applications, The 2011 U. S. Workshop on the Physics and Chemistry of II-VI Materials (2011).
[190] S. Fahey, R. Bommena, R. Kodama, R. Sporken, and S. Sivananthan, submitted to *J. Electron. Mater.* (2012).
[191] M. Carmody, R. Kodama, D. Lim, and J. Margetis; Invited Paper 1.1 Review of Alternate Substrate Technology for MBE Growth of HgCdTe, 2008 II-VI Workshop on the Chemistry and Physics of II-VI Materials, November 11-13, Las Vegas (2008).
[192] Ui-Hui Kwon and Won-Jong Lee; *Thin Solid Films* 445, pp. 80-89 (2003).
[193] Y. Chang, C.H. Grein, J. Zhao, S. Sivananthan, C.Z. Wang, T. Aoki, D.J. Smith, P.S. Wijewarnasuriya, V. Nathan; *J. Appl. Phys.* 100, 114316 (2006).
[194] D. Kapolnek, S. Keller, et al., *Appl. Phys. Lett.* 71, No. 9, Sept. 1 (1997).
[195] Shinji Matsui, Toshinori Ichihashi, Masakazu Baba, and Akinobu Satoh, Superlatt. Microstruct. 7, 4, pp. 295-301 (1990).
[196] T. Djenizian, L. Santinacci, and P. Schmuki, *Appl. Phys. Lett.* 78, 19 (2001).
[197] T. Djenizian, L. Santinacci, H. Hildebrand, and P. Schmuki, *Surf. Sci.* 524, pp. 40-48 (2003).
[198] T.J. de Lyon, R.D. Rajavel, J.A. Vigil, et al., *J. Electron. Mater.* 27, pp. 550-555 (1998).
[199] K. Jowikowski and A. Rogalski, *J. Electron. Mater.* 29, No. 6 (2000), pp. 736-741.